Measurement of Neutrino Interactions on Water using Nuclear Emulsion Detectors

Ayami Hiramoto

February, 2021

Department of Physics, Graduate School of Science
Kyoto University

Abstract

This thesis reports precise measurements of neutrino interactions on water using nuclear emulsion detectors to improve neutrino-nucleus interaction models.

The T2K experiment measures neutrino oscillation parameters with a precision of the world's highest level to explore the CP violation in the lepton sector. Towards a higher precision, reduction of the systematic error is crucial in addition to accumulating more statistics. One of the largest systematic error sources in the current measurement is the uncertainty on neutrino-nucleus interactions. This large uncertainty on the neutrino interactions comes from complicated nuclear effects, as well as the lack of statistics due to its tiny cross section. Although it is essential to measure the particles from the neutrino interactions to understand the nuclear effects, existing detectors do not sufficiently cover low-momentum hadrons.

Hence, we started a new experiment, NINJA, which uses nuclear emulsions to detect the particles from the neutrino interactions. We use a detector with an alternating structure of the emulsion films and water target layers. Since the nuclear emulsion has an excellent spatial resolution, this structure allows us to achieve a lower momentum threshold for protons and pions from the neutrino-water interactions. A 3-kg water target detector was exposed to an antineutrino mode beam at J-PARC, and we observed 86 candidate events of the neutrino interactions on water. Measurements of the track multiplicity and kinematics of muons, charged pions, and protons from the neutrino interactions are performed. We successfully measured protons from the neutrino-water interaction with a $200\,\mathrm{MeV}/c$ threshold. Since the proton momentum thresholds of the T2K near detectors are around $400\,\mathrm{MeV}/c$, this measurement achieved an unexplored region in the measurement of the neutrino-water interactions. In these measurements, we found a tendency to overestimate the number of charged pions in the current model. In addition, the muon distributions show slightly higher angle and lower momentum shapes than the model predictions. Although the statistics were limited, these results clearly demonstrated the capability of the emulsion detector.

We carried out a data taking with a 75-kg water target from November 2019 to February 2020. At the end of this thesis, we discuss how the NINJA measurements with these larger statistics can contribute to T2K by validating and constructing the neutrino interaction models. We performed a multivariate analysis using kinematics information including low-momentum protons, which is hardly obtained in the current T2K near detectors. As a result, we demonstrated that we can measure the cross section of a specific type of neutrino interactions which gives a large systematic error in the T2K measurement, with a 20% systematic error.

In this thesis, we demonstrated that the NINJA experiment can measure the neutrino-water interactions with a lower momentum threshold. Following the pilot run, our physics run measurements will contribute to constructing more reliable neutrino interaction models for the neutrino oscillation analysis in T2K.

Acknowledgments

I have been fortunate to work with many amazing people over the six years at the beginning of my research life.

My heartfelt gratitude goes to Prof. Tsuyoshi Nakaya, who gave me the opportunity to work on neutrino physics. He encouraged me with a lot of thoughtful advice, which always brought me new ideas. I really hope to follow his scientific insight someday. I would also like to show my deep gratitude to Prof. Atsuko Ichikawa for supporting and showing her attitude towards physics and experiments. She definitely has a huge impact on my life. I am very grateful to Dr. Tatsuya Kikawa for his detailed discussion over many topics in this thesis. He always answered my questions easily, so looking for something he does not know yet was fun.

I would like to express my appreciation to the NINJA collaboration. It was an excellent opportunity to learn about nuclear emulsion from Dr. Tsutomu Fukuda. The day we first met in Hakuba may be the beginning of this long journey. Yosuke Suzuki has worked with me for a long time, and he provided many essential data on the emulsion. I personally think the NINJA experiment would never have started without his muscle. Takahiro Odagawa is one of the most dependable NINJA friends. He is always a sharp observer, and he discussed a lot with me. I really enjoyed working with Hitoshi Oshima, who made a way to the first NINJA physics analyses together. I was impressed by his careful work. I would like to thanks Prof. Akihiro Minamino, Prof. Masahiro Komatsu, Dr. Osamu Sato, Prof. Hiroshi Shibuya, Prof. Satoru Ogawa, Prof. Shigeki Aoki, and Prof. Syoji Mikado for their helpful advice based on their wealth of knowledge and experience. I am also grateful to the NINJA colleagues, Hiroaki Kawahara, Dr. Tomokazu Matsuo, Dr. Yusuke Morimoto, Tomoki Takao, Yuji Tanihara, Mayuko Naiki, Kosaku Mizuno, Hideaki Takagi, Ina Sanjana, and Dr. Ajmi Ali for their effort in carrying out the experiment.

All of my work owes many experts in T2K. Prof. Yoshinari Hayato provided incisive comments in a wide range of fields, from the SFT electronics to neutrino interaction analysis. Advice from Prof. Masashi Yokoyama was always instructive and touching the core of my analysis. Discussion with Dr. Teppei Katori, Dr. Kendall Mahn, Dr. Sara Bolognesi, Dr. Xianguo Lu, and Dr. Stephen Dolan were essential to think about the physics potential of NINJA. I am grateful for the support and discussion on the operation and analysis of INGRID provided by Prof. Takeshi Nakadaira, Prof. Ken Sakashita, and Dr. Megan Friend. Lukas Berns kindly worked on the NINJA flux, and he also told me a lot of interesting ideas. I learned a lot of technical things while working with INGRID experts, Dr. Taichiro Koga, Dr. Naruhiro Chikuma, and Dr. Ken'ichi Kin. I would not have been able to work as an INGRID expert without the guidance by Tatsuya Hayashino. I also thank Koga-san's careful comments on the NINJA analysis even after he left T2K. I would also like to thank Dr. Benjamin Quilain and Dr. Cao Son for their continuous

support. I really enjoyed staying at Tokai with T2K friends, Keigo Nakamura, Wataru Uno, Kenji Yasutome, Soichiro Kuribayashi, Masanori Tajima, Mao Tani, Yohan Lee, and Masaki Kawaue. I will never forget Kenji's big appetite.

I am grateful to my friends that I shared my time with; Hirotaka Nagata, Jun Harada, Tomoyo Yoshida, Fabio Iacob, Georgio Pintaudi, Ka Ming Tsui, and Tomasz Bonus. I was happy to discuss with them both research and life. I really love my friends in the Kyoto group; Dr. Syunichi Akatsuka, Dr. Yosuke Ashida, Syunsuke Tanaka, Yoshie (Kageyama) Nakanishi, and Dr. Yohei Noguchi. They all are great researchers, and I owe it entirely to them that I have succeeded so far. I would also like to thank Prof. Roger Wendell, Prof. Osamu Tajima, Dr. Toshi Sumida, Hayashi-san, Tanizawa-san, Sekiguchi-san, Sasaki-san, and all the past and current members of the Kyoto High Energy Physics group.

Finally, I would like to thank my family, Moritaka Hiramoto, Hiromi Hiramoto, and Fuka-chan, for always being supportive and trusting in me. I am grateful to my beloved husband, Xing – Thank you.

Contents

Chapter 1

Introduction

The Standard Model of particle physics is one of the most outstanding achievements of physics in the 20th century, within which almost all observed phenomena in the current particle physics are described. Nevertheless, we still have open questions. For instance, the asymmetry of matter and antimatter in the universe is one of them. Equal amounts of matter and antimatter are assumed to have existed at the beginning of the universe. However, eventually, the symmetry of matter and antimatter is violated. Only matter constructs our universe, and there is a tiny fraction of antimatter. The key to figuring out the matter-antimatter asymmetry in the universe is the asymmetry in the nature of particles and antiparticles, such as CP violation. CP violation in the quark sector has been observed experimentally thus far, although it does not give a sufficient amount of asymmetry of matter and antimatter in the universe. On the other hand, CP violation in the lepton sector has never been observed yet, and the violation in the neutrino mixing is being searched for.

This chapter begins with introductions to the theoretical and experimental backgrounds of neutrino physics. Following this, the motivation of this thesis is described as well as the introductions to the T2K and NINJA experiments.

1.1 Discovery of neutrinos

A neutrino is a neutral particle with spin 1/2 that interacts only via the weak interaction except for gravity. A neutrino has one of three flavors: electron neutrino (ν_e), muon neutrino (ν_μ), and tau neutrino (ν_τ). In 1930, the existence of neutrinos was first suggested by W. Pauli to give an explanation to the continuous energy spectrum of electrons from the β decay [1], which had been at issue since the beginning of the 20th century.

The first detection of neutrinos was in 1956. Anti-electron neutrinos ($\overline{\nu}_e$) from a nuclear reactor at Savannah River Plant were detected by F. Reines and C. L. Cowan using a $CdCl_2$-doped water target sandwiched between liquid scintillator detectors [2]. In 1962, L. M. Lederman, M. Schwartz, and J. Steinberger observed the second flavor of neutrinos by the AGS neutrino experiment at Brookhaven National Laboratory [3]. In this experiment, charged pions were generated by accelerated protons impinging to a beryllium target, and muon neutrinos from the decay of the generated charged pions were detected via charged-current interactions. The third flavor of neutrinos was finally observed at the very end of the 20th century by the DONUT experiment at Fermilab [4].

They measured tau neutrinos from the decay of charm mesons using a nuclear emulsion detector. Thus far, the existence of the fourth or more types of light neutrinos is disfavored by the measurement of the decay width of the Z^0 boson resonance at LEP and SLC [5,6]. Besides, a measurement of cosmic microwave background by Planck [7] also disfavors the existence of other neutrino species.

1.2 Neutrino oscillation

In the Standard Model, neutrinos are considered massless particles. However, the observation of neutrino oscillation revealed that neutrinos have tiny masses. Below, an overview of the theory of the neutrino oscillation is given.

1.2.1 Theory of neutrino oscillation

When neutrinos are not massless, and their mass eigenstates are not identical with the flavor eigenstates, they change their flavors while flying. This phenomenon is known as the neutrino oscillation. The flavor eigenstates of neutrinos $|\nu_\alpha\rangle$ ($\alpha = e, \mu, \tau$) are expressed as a mixture of the three mass eigenstates $|\nu_i\rangle$ ($i = 1, 2, 3$):

$$|\nu_\alpha\rangle = \sum_i U_{\alpha i} |\nu_i\rangle. \tag{1.1}$$

Here, U is known as the Pontecorvo-Maki-Nakagawa-Sakata (PMNS) matrix [8], which is a 3×3 unitary matrix:

$$\begin{aligned} U &= \begin{pmatrix} U_{e1} & U_{e2} & U_{e3} \\ U_{\mu 1} & U_{\mu 2} & U_{\mu 3} \\ U_{\tau 1} & U_{\tau 2} & U_{\tau 3} \end{pmatrix} \\ &= \begin{pmatrix} 1 & 0 & 0 \\ 0 & c_{23} & s_{23} \\ 0 & -s_{23} & c_{23} \end{pmatrix} \begin{pmatrix} c_{13} & 0 & s_{13} e^{-i\delta_{\mathrm{CP}}} \\ 0 & 1 & 0 \\ -s_{13} e^{i\delta_{\mathrm{CP}}} & 0 & c_{13} \end{pmatrix} \begin{pmatrix} c_{12} & s_{12} & 0 \\ -s_{12} & c_{12} & 0 \\ 0 & 0 & 1 \end{pmatrix} \begin{pmatrix} e^{i\alpha_1/2} & 0 & 0 \\ 0 & e^{i\alpha_2/2} & 0 \\ 0 & 0 & 1 \end{pmatrix}. \end{aligned} \tag{1.2}$$

where $c_{ij} = \cos\theta_{ij}$, $s_{ij} = \sin\theta_{ij}$, and θ_{ij} is the mixing angle between two mass eigenstates, $|\nu_i\rangle$ and $|\nu_j\rangle$. The parameter δ_{CP} is the Dirac CP-violating phase, and in the case of $\delta_{\mathrm{CP}} \neq 0, \pi$, $\nu_\alpha \to \nu_\beta$ and $\overline{\nu}_\alpha \to \overline{\nu}_\beta$ ($\alpha \neq \beta$) have different oscillation probabilities. The parameters α_1 and α_2 are the Majorana CP-violating phases, which appear when neutrinos are Majorana particles [9], and they do not change the neutrino oscillation probabilities.

The Schrödinger equation describes time propagation of the mass eigenstate:

$$i\frac{d}{dt}|\nu_i(t)\rangle = \mathcal{H}_0 |\nu_i(t)\rangle = E_i |\nu_i(t)\rangle. \tag{1.3}$$

Here, $\mathcal{H}_0$ is the Hamiltonian in a vacuum, and E_i is the energy eigenvalue of the mass eigenstate. The mass eigenstate evolves as follows:

$$|\nu_i(t)\rangle = e^{-iE_i t} |\nu_i\rangle. \tag{1.4}$$

Hence, the evolution of a flavor eigenstate (ν_α) is denoted as:

$$\begin{aligned} |\nu_\alpha(t)\rangle &= \sum_i U_{\alpha i} e^{-iE_i t} |\nu_i\rangle \\ &= \sum_{i,\beta} U_{\alpha i} e^{-iE_i t} U^\dagger_{\beta i} |\nu_\beta\rangle. \end{aligned} \tag{1.5}$$

The relation between the mass (m_i) and momentum (p) of the mass eigenstate is written as $|p| \gg m_i$ in the ultra-relativistic limit. Thus, we can use the following approximation (in natural units, $\hbar$=c=1):

$$E_i = \sqrt{p^2 + m_i^2} \simeq p + \frac{m_i^2}{2E}, \tag{1.6}$$

$$t \simeq L, \tag{1.7}$$

where E and L ($= ct$) are the energy and traveling distance of the neutrino, respectively. According to Eq. 1.5 and Eq. 1.6,

$$|\nu_\alpha(t)\rangle = \sum_{i,\beta} U_{\alpha i} e^{-ipt} e^{-i\frac{m_i^2 t}{2E}} U^\dagger_{\beta i} |\nu_\beta\rangle. \tag{1.8}$$

Therefore, with the approximation of Eq. 1.7, the oscillation probability of $\nu_\alpha \to \nu_\beta$ is written as:

$$\begin{aligned} P(\nu_\alpha \to \nu_\beta) &= |\langle \nu_\beta(t) | \nu_\alpha \rangle|^2 \\ &= \delta_{\alpha\beta} - 4 \sum_{i>j} \mathrm{Re}(U^\dagger_{\alpha i} U_{\beta i} U_{\alpha j} U^\dagger_{\beta j}) \sin^2 \left(\frac{\Delta m^2_{ij} L}{4E} \right) \\ &\quad + 2 \sum_{i>j} \mathrm{Im}(U^\dagger_{\alpha i} U_{\beta i} U_{\alpha j} U^\dagger_{\beta j}) \sin \left(\frac{\Delta m^2_{ij} L}{4E} \right), \end{aligned} \tag{1.9}$$

where $\delta_{\alpha\beta} = \sum_i U^\dagger_{\alpha i} U_{\beta i}$, and $\Delta m^2_{ij} \equiv m_i^2 - m_j^2$ corresponds to a mass-squared difference. For instance, modern accelerator-based long-baseline neutrino oscillation experiments measure the following two probabilities:

$$\begin{aligned} P(\nu_\mu \to \nu_e) \simeq\ & 4 c_{13}^2 s_{13}^2 s_{23}^2 \sin^2\Phi_{31} \\ & + 8 c_{13}^2 s_{12} s_{13} s_{23} (c_{12} c_{23} \cos\delta_{\mathrm{CP}} - s_{12} s_{13} s_{23}) \cos\Phi_{32} \sin\Phi_{31} \sin\Phi_{21} \\ & - 8 c_{13}^2 c_{12} c_{23} s_{12} s_{13} s_{23} \sin\delta_{\mathrm{CP}} \sin^2\Phi_{32} \sin^2\Phi_{31} \sin^2\Phi_{21} \\ & - 2 c_{13}^2 s_{12}^2 s_{23}^2 \frac{aL}{E} (1 - 2 s_{13}^2) \cos\Phi_{32} \sin\Phi_{31} + 8 c_{13}^2 s_{13}^2 s_{23}^2 \frac{a}{\Delta m^2_{31}} (1 - 2 s_{13}^2) \sin^2\Phi_{31}, \end{aligned} \tag{1.10}$$

$$P(\nu_\mu \to \nu_\mu) \simeq 1 - 4 c_{13}^2 s_{23}^2 (c_{12}^2 c_{23}^2 + s_{12}^2 s_{13}^2 s_{23}^2) \sin^2\Phi_{32}, \tag{1.11}$$

$$a \equiv 2\sqrt{2} G_F n_e E,\ \Phi_{ij} \equiv \frac{\Delta m^2_{ij} L}{4E}. \tag{1.12}$$

Here, $\Delta m^2_{21} \ll \Delta m^2_{32}$ is assumed. The parameter G_F is the Fermi constant, and n_e is the electron density in the matter. The probability $P(\nu_\mu \to \nu_e)$ is called the ν_e appearance probability, while $P(\nu_\mu \to \nu_\mu)$ is called the ν_μ disappearance (or survival) probability. In Eq. 1.10, the signs of δ_{CP} and a are inverted for antineutrino. The first line of Eq. 1.10 is the dominant term, the second line is the CP-conserving term, the third line is the CP-violating term, and the last line is the matter effect term, which is explained later.

As written in Eq. 1.10 and 1.11, the probabilities of neutrino oscillations are described as a function of the neutrino energy, given the fixed distance L. Measuring these probabilities allows us to obtain the oscillation parameters: the mixing angles, mass-squared differences, and δ_{CP}. The CP-violating phase δ_{CP} is measured by the ν_e appearance mode because the sign of the CP-violating term in Eq. 1.10 is opposite in neutrino and antineutrino. Therefore, comparing $\nu_\mu \to \nu_e$ and $\overline{\nu}_\mu \to \overline{\nu}_e$ can probe the δ_{CP} value.

In Eq. 1.10, the matter effect appears when neutrinos travel through dense matters, such as the earth or the sun [10, 11]. Neutrinos are affected by coherent scatterings with electrons in matters. All flavors of neutrinos interact with the electrons via neutral current, while charged-current interactions occur only for electron neutrinos. The matter effect changes the oscillation probability, thus we need to take this effect into account carefully. We can measure the sign of the mass-squared difference by the matter effects, while only its absolute value can be obtained by neutrino oscillation in a vacuum. The sign of Δm^2_{21} is already known from the measurements of solar neutrino oscillation [12–14]. However, it is still unknown whether $m_1 < m_3$ (normal mass ordering, NO) or $m_1 > m_3$ (inverted mass ordering, IO). Determining mass ordering is one of the most critical subjects in neutrino physics.

In the following section, the history and current situation of neutrino oscillation experiments are introduced.

1.2.2 History of neutrino oscillation experiments

In 1968, the Homestake experiment reported that the measured flux of electron neutrinos produced by fusion reactions in the sun was about 1/3 of the expected value [15]. Since then, similar observations were reported by GALLEX [16], Kamiokande [17], GNO [13], and SAGE [18]. This deficit in the flux of the solar neutrino was at issue as the "solar neutrino problem." Results from various experiments using various detectors showed different amounts of deficits. Thus, a simple modification of the model of the solar neutrino production in the sun could not explain this problem.

A solution to the solar neutrino problem was brought by a measurement of atmospheric neutrinos using the Super-Kamiokande (SK) detector, which is a huge water Cherenkov detector. The atmospheric neutrinos come from the decay of hadrons generated by the collision of cosmic rays with the earth's atmosphere [19]. In 1998, the zenith angle distributions of charged leptons from the interactions of the atmospheric neutrinos were measured by SK [20]. Figure 1.1 shows the measured zenith angle distributions, in which the result was consistent with the case assuming the neutrino oscillation. After observing the oscillation of the atmospheric neutrinos, the oscillation of the solar neutrino was also reported [21], and it was revealed that the solar neutrino problem came from the neutrino oscillation. In addition to these measurements, Sudbury Neutrino Observatory (SNO) directly measured the oscillation of the solar neutrinos in 2001 [22]. The SNO experi-

ment detected all flavors of neutrinos from the sun using neutral current interactions on a heavy water target. While the flux of electron neutrinos was significantly smaller than the flux assuming no neutrino oscillation, it was confirmed that the total flux, including all flavors, is consistent with the expected flux from the sun. This result proved that the electron neutrinos changed their flavor to another, and the neutrino oscillation was directly confirmed.

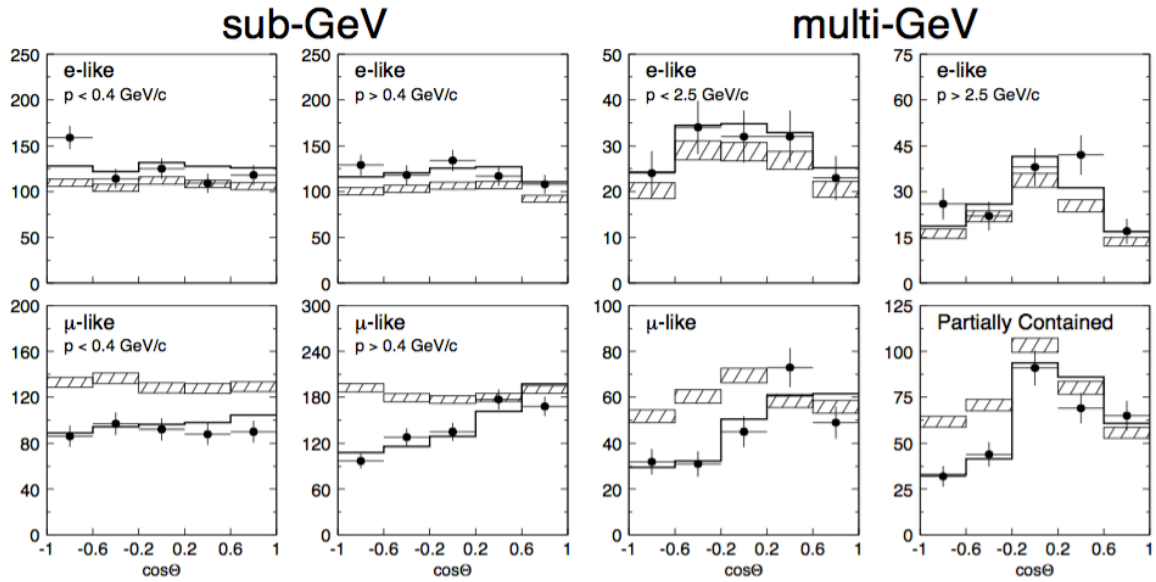

Figure 1.1: Zenith angle distributions of charged leptons from the interactions of the atmospheric neutrinos measured by SK. The hatched region corresponds to the no-oscillation case, while the bold line corresponds to the case assuming the neutrino oscillation. The distributions are consistent with the case assuming neutrino oscillation [20].

Once the evidence of neutrino oscillations was provided, neutrino oscillation experiments using artificial neutrino sources, such as reactors and accelerators, have been widely carried out as well as the measurements of the solar and atmospheric neutrinos. The neutrino oscillation parameters have been measured at various energy ranges and baseline lengths. Table 1.1 shows the current best fit values of the neutrino oscillation parameters [23]. The neutrino oscillation parameters θ_{12} and Δm^2_{21} have been measured by Homestake [15], SK [24], SNO [25], and Borexino [26] using the ν_e disappearance of the solar neutrinos. Besides, the survival probability of $\overline{\nu}_e$ from nuclear reactors measured by KamLAND [27] also constrains these parameters. The parameters θ_{23} and $|\Delta m^2_{32}|$ are measured by accelerator-based long-baseline neutrino oscillation experiments, such as K2K [28], MINOS/MINOS+ [29], T2K [30], and NOνA [31], as well as the measurements of the atmospheric neutrinos by SK [14] and IceCube [32]. These parameters are measured via the ν_μ disappearance channel. The constraint on θ_{13} was first given by the Chooz experiment [33] using reactor neutrinos. In 2011, T2K indicated that θ_{13} has a non-zero value [34] by measuring the ν_e appearance in SK. After that, the parameter was precisely measured by short-baseline reactor-neutrino experiments, such as Daya Bay [35], Double Chooz [36], and RENO [37].

In the current understanding, while the mixing angles and the mass-squared differences are determined with around 5% precision, the value of δ_{CP} is still unknown. The parameter

Table 1.1: Summary of the best-fit values of the neutrino oscillation parameters [23].

Parameter	Ordering	Best-fit$\pm 1\sigma$	3σ range
$\sin^2\theta_{12}$	NO	$0.304^{+0.012}_{-0.012}$	0.269 – 0.343
	IO	$0.304^{+0.013}_{-0.012}$	0.269 – 0.343
$\sin^2\theta_{23}$	NO	$0.573^{+0.016}_{-0.020}$	0.415 – 0.616
	IO	$0.575^{+0.016}_{-0.019}$	0.419 – 0.617
$\sin^2\theta_{13}$	NO	$0.02219^{+0.00062}_{-0.00063}$	0.02032 – 0.02410
	IO	$0.02238^{+0.00063}_{-0.00062}$	0.02052 – 0.02428
Δm^2_{21} $[10^{-5}\,\mathrm{eV}^2]$	NO, IO	$7.42^{+0.21}_{-0.20}$	6.82 – 8.04
Δm^2_{31} $[10^{-3}\,\mathrm{eV}^2]$	NO	$2.517^{+0.026}_{-0.028}$	2.435 – 2.598
Δm^2_{32} $[10^{-3}\,\mathrm{eV}^2]$	IO	$-2.498^{+0.028}_{-0.028}$	-2.581 – -2.414
$\delta_{\mathrm{CP}}[^\circ]$	NO	197^{+27}_{-24}	120 – 369
	IO	282^{+26}_{-30}	193 – 352

δ_{CP} can be measured by the ν_e appearance of the accelerator neutrinos using the values of θ_{13}, θ_{12}, and Δm^2_{21} measured by the reactor and the solar neutrino experiments. Currently, the constraints are mainly given by T2K [30] and NOνA [31], and the CP-conserving values ($\delta_{\mathrm{CP}} = 0, \pi$) are excluded with a 90% confidence level.

1.2.3 Remaining questions

There has been significant progress in the measurements of the neutrino oscillation parameters so far. The measurements of the mixing angles suggest that the PMNS matrix has much larger mixings than those in the Cabibbo-Kobayashi-Maskawa (CKM) matrix [38, 39], which describes the mixing in quarks. According to the measurements, the value of θ_{23} is very close to $\pi/4$, which corresponds to the maximal mixing. Theoretical reasons behind such structure are fascinating, and further precise determination of the matrix elements is essential to understand the structure of the PMNS matrix. Besides, the determination of the mass ordering is also necessary to close in on the mystery of the origin of such a tiny neutrino mass. Discussions about if neutrinos are Majorana particles or not are also exciting and crucial to understanding the neutrino mass, but this topic is not the scope of this thesis.

Measurement of δ_{CP} is the primary purpose of the current and future accelerator-based long-baseline neutrino oscillation experiments. The Sakharov conditions [40] require CP violation in the early universe for the solution of the matter-antimatter asymmetry. CP violations have been observed in the quark sector [41–43], that are consistent with the predictions of the Standard Model. The measured amount of CP violations so far is not sufficient to explain the matter-antimatter asymmetry. Thus, CP violation in the lepton sector could be a key. Observation of CP violation in the neutrino oscillation is anticipated.

The ongoing experiments attempting to measure the δ_{CP} value are the T2K experiment and the NOνA experiment. These experiments are complementary in measurements of the neutrino oscillation in different baseline lengths. Both experiments have been providing precise measurements of the mixing angles and giving constraints on δ_{CP}. In the following section, we focus on the T2K experiment.

1.3 Introduction of the T2K experiment

1.3.1 Overview

The Tokai to Kamioka (T2K) experiment is a long-baseline neutrino oscillation experiment being carried out in Japan [44]. Figure 1.2 shows an illustration of T2K. A high-intensity neutrino beam consisting predominantly of ν_μ ($\overline{\nu}_\mu$) is produced at Japan Proton Accelerator Research Complex (J-PARC) at Tokai. The neutrinos are measured at near detectors located in the J-PARC site and a far detector, SK, placed 295 km away from the neutrino production source.

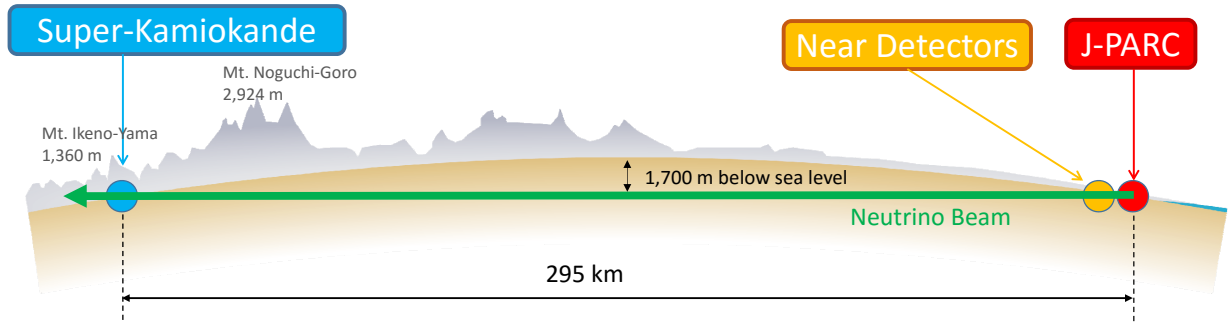

Figure 1.2: Illustration of the T2K experiment. A high intensity neutrino beam produced at J-PARC is measured by near detectors and Super-Kamiokande.

1.3.2 Current status and future prospects

In the T2K experiment, the following two measurements have been performed to extract the oscillation parameters.

- ν_e appearance channels ($\nu_\mu \to \nu_e, \overline{\nu}_\mu \to \overline{\nu}_e$): in Eq. 1.10, the dominant term involves the $\sin\theta_{13}$ value. Thus the probability of this channel gets quite small if θ_{13} is close to zero. The appearance of ν_e from the ν_μ beam was reported in 2013 with 7.3 σ significance [45], and a non-zero value of θ_{13} was also reported. After the reactor neutrino experiments measure the θ_{13} value, this channel is used to measure δ_{CP} by comparing $\nu_\mu \to \nu_e$ and $\overline{\nu}_\mu \to \overline{\nu}_e$.

- ν_μ disappearance channels ($\nu_\mu \to \nu_\mu$, $\overline{\nu}_\mu \to \overline{\nu}_\mu$): this channel is used for precise measurements of $|\Delta m^2_{32}|$ and $\sin^2\theta_{23}$. As seen in Eq. 1.11, the dominant term of the probability of this channel is relatively simple, thus $|\Delta m^2_{32}|$ and θ_{23} values can be obtained after constraining θ_{12} and θ_{13}. The precise determination of θ_{23} is also crucial for the measurement of δ_{CP} because the first term of Eq. 1.10 involves $\sin^2\theta_{23}$.

Figure 1.3 shows the latest results of these analyses, in which $|\Delta m^2_{32}|$, $\sin^2\theta_{23}$, and δ_{CP} confidence regions are shown. Although details about the results will be discussed in Sec. 2.6, note that T2K provides one of the world's most precise measurements for these parameters. The current sensitivities to the oscillation parameters are limited by the statistical uncertainty. Therefore, increasing the statistics is crucial to achieving further precise measurements. As a next-generation experiment after T2K, Hyper-Kamiokande (HK) [46] is under construction. The HK detector has an 8.4 times larger fiducial volume than SK. Besides, an upgrade of the accelerator beam power is also planned. These upgrades will significantly increase the statistics and allow us to reach the 5σ measurement of δ_{CP}. In the United States, Deep Underground Neutrino Experiment (DUNE) [47] is also planned as a next-generation after NOνA, and it will be a complementary experiment to HK.

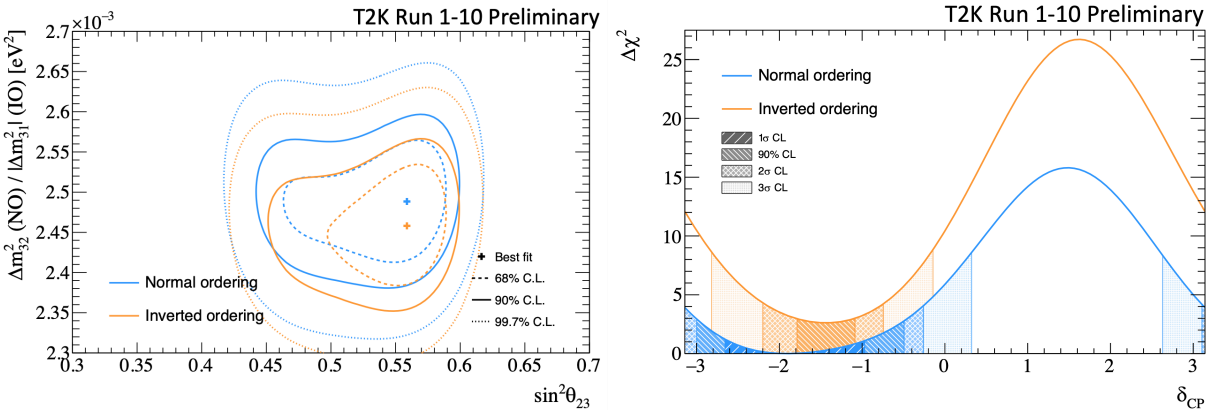

Figure 1.3: Latest results of $|\Delta m^2_{32}|$, $\sin^2\theta_{23}$, and δ_{CP} by T2K [30]. The left plot shows two-dimensional confidence level contours of $|\Delta m^2_{32}|$ and $\sin^2\theta_{23}$. The right plot is negative log-likelihood as a function of δ_{CP}. These results are obtained with constraints of θ_{13} by reactor neutrino experiments.

While the next-generation experiments promise to reduce the statistical uncertainties, the systematic uncertainties will be the dominant error sources in the future. In the current measurements, one of the dominant systematic uncertainties comes from the uncertainty in neutrino interaction modeling. Therefore, the neutrino interaction modeling is focused on in this thesis, and a new experiment to reduce the systematic uncertainties in T2K and HK is presented.

1.4 Neutrino interactions

This section describes a brief introduction of neutrino interactions. Neutrinos interact only via the weak force. An interaction mediated by $\mathrm{W}^\pm$ boson is called a charged-current interaction, and that mediated by Z^0 boson is called a neutral-current interaction.

Figure 1.4 shows diagrams of the charged-current and neutral-current interactions. The charged-current and the neutral-current are written as:

$$j^{\mu\pm} = \overline{u}\frac{-ig_W}{2\sqrt{2}}\gamma^\mu(1-\gamma^5)u \tag{1.13}$$

$$j^{\mu 0} = \overline{u}\frac{-ig_Z}{2}\gamma^\mu(g_V - g_A\gamma^5)u, \tag{1.14}$$

where g_W and g_Z are coupling strengths, u and $\overline{u}$ are Dirac spinors, γ^μ and $\gamma^5 = i\gamma^0\gamma^1\gamma^2\gamma^3$ are the Dirac matrices, g_V and g_A are the vector and axial-vector coupling constants respectively. In the neutral-current interaction, we cannot identify the neutrino flavor by the outgoing lepton. Therefore, the charged-current interactions are normally used in neutrino oscillation experiments. Neutrino interactions described in this thesis are the charged-current interactions unless otherwise specified.

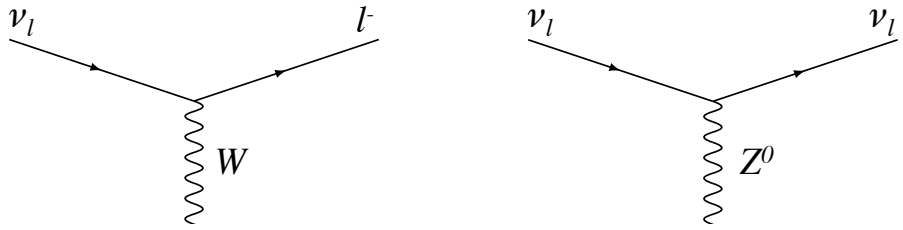

Figure 1.4: Diagrams of a charged-current (left) and neutral-current (right) interactions via weak bosons.

In neutrino experiments, we can detect neutrinos only by observing particles emitted when neutrinos interact with target materials. Since nucleons in the target materials are bounded in nuclei, the cross section of the neutrino-nucleus interactions is considered as the sum of the neutrino-nucleon interactions. The Lagrangian of the neutrino interaction on a nucleon is written as:

$$\mathcal{L} = \frac{G_F}{\sqrt{2}}\left(j_\mu^\dagger(k_l, k_l')J^\mu(k_h, k_h') + h.c.\right), \tag{1.15}$$

where $j_\mu^\dagger$ is leptonic current, J_μ is hadronic current, k_l and k_h are four-momenta of the lepton and hadron respectively. The differential cross section of the charged-current interaction can be obtained from the leptonic and hadronic currents as

$$\frac{d\sigma}{dq^2} = \frac{G_F^2\cos^2\theta_C}{32\pi^2 M^2 E_\nu^2}L_{\alpha\beta}H^{\alpha\beta}, \tag{1.16}$$

where q^2 is the square of the four-momentum transfer, M is the nucleon mass, θ_C is the Cabibbo angle, $L_{\alpha\beta}$ and $H^{\alpha\beta}$ are the leptonic and hadronic tensors respectively. While the leptonic tensor is simple within the Standard Model, the hadronic tensor is complicated since it involves QCD physics, and the cross section strongly depends on models. Besides, what we measure is not an interaction on a free nucleon but that on a bounded nucleon in a nucleus, thus nuclear physics has a significant impact. Details of the neu-

trino interactions in the energy region used in neutrino oscillation experiments will be explained in Chapter 3. Modeling of the neutrino interactions is essential for simulation of the neutrino interactions, and the uncertainties in the models are propagated to the systematic uncertainties of the neutrino oscillation analysis. For precise measurements of the oscillation parameters, constructing a precise model is crucial.

1.5 Introduction of the NINJA experiment

Several experiments are ongoing to measure and understand the neutrino interactions precisely [48, 49]. For T2K and HK, precise measurements of the neutrino interactions on water targets are especially essential. Hence we proposed a new experiment, Neutrino Interaction research with Nuclear emulsion and J-PARC Accelerator (NINJA). The NINJA experiment aims to measure neutrino-water interactions very precisely using nuclear emulsion detectors in J-PARC. The nuclear emulsion detector is a three-dimensional tracking device, which has an excellent spatial resolution owing to its high granularity. An alternating structure of nuclear emulsion films and thin water-target layers allows us to observe short tracks, especially low momentum protons from neutrino-water interactions which are hardly detected by existing detectors. Details of the NINJA experiment are described in Chapter 4. In this thesis, the first results of the neutrino-water interaction measurements using the nuclear emulsion detector are reported.

1.6 Outline of this thesis

The remainder of the thesis is organized as follows. First, Chapter 2 describes an overview of the T2K experiment. Chapter 3 introduces neutrino interaction models, which are especially important to discuss T2K and NINJA. Chapter 4 describes the experimental apparatus of the NINJA experiment, as well as data taking status of the pilot run. Chapter 5 expresses the Monte Carlo (MC) simulation. Chapter 6 describes the neutrino event reconstruction, and Chapter 7 addresses the momentum reconstruction and particle identification (PID). Chapter 8 presents the result of the first physics measurements from NINJA. Chapter 9 addresses the status of the NINJA physics run. Chapter 10 discusses the prospects of neutrino interaction modeling. Finally, Chapter 11 concludes the thesis.

Chapter 2

The T2K experiment

As introduced in Sec. 1.3, T2K is a long-baseline neutrino oscillation experiment in Japan. This chapter begins with introductions of a beamline and experimental apparatus in the T2K experiment. Following this, operations of the experiment, especially monitoring of the neutrino beam profile, are described. An overview of the oscillation analysis is then described together with the latest status and prospects of T2K.

2.1 J-PARC accelerator and the neutrino beam

The J-PARC accelerator consists of three accelerators; LINear ACcelerator (LINAC), Rapid Cycling Synchrotron (RCS), and Main Ring (MR), as shown in Fig. 2.1. H^- ions accelerated up to 400 MeV at LINAC are converted to protons at injection to RCS. These protons are accelerated to 3 GeV at RCS and injected into MR, then MR provides a 30 GeV proton beam. A proton beam spill from MR is delivered to a graphite target every 2.48 s. The beam spill has an eight-bunch structure, as shown in Fig. 2.2. Each proton bunch has about 58 ns full width, and they are separated by around 580 ns. The beam power has been increased gradually, and the highest beam power operated so far is around 513 kW as of 2020, while the designed beam power of MR is 750 kW. The data used for the main results in Chapter 8 were taken in 2017–2018, and the beam power was about 450 kW at that time.

Protons impinging on the graphite target produce hadrons, predominantly pions. A neutrino beam is produced by the decay of hadrons. Three electromagnetic horns [51] focus the hadrons into a decay volume, where the hadrons decay mainly into muons and neutrinos as follows:

$$\pi^+ \rightarrow \mu^+ \nu_\mu \tag{2.1}$$
$$\pi^- \rightarrow \mu^- \overline{\nu}_\mu. \tag{2.2}$$

In addition to the decay of pions, there are contributions from kaons, which accounts for around 5% of the neutrino flux. By changing the polarity of the electromagnetic horns, the charge of the hadrons focused by the horn is switched, and thus, either neutrino or antineutrino beam is selected. Focusing of positively charged particles is called neutrino mode, and focusing of negatively charged particles is called antineutrino mode. In contrast, negatively charged particles in the neutrino mode and positively charged particles

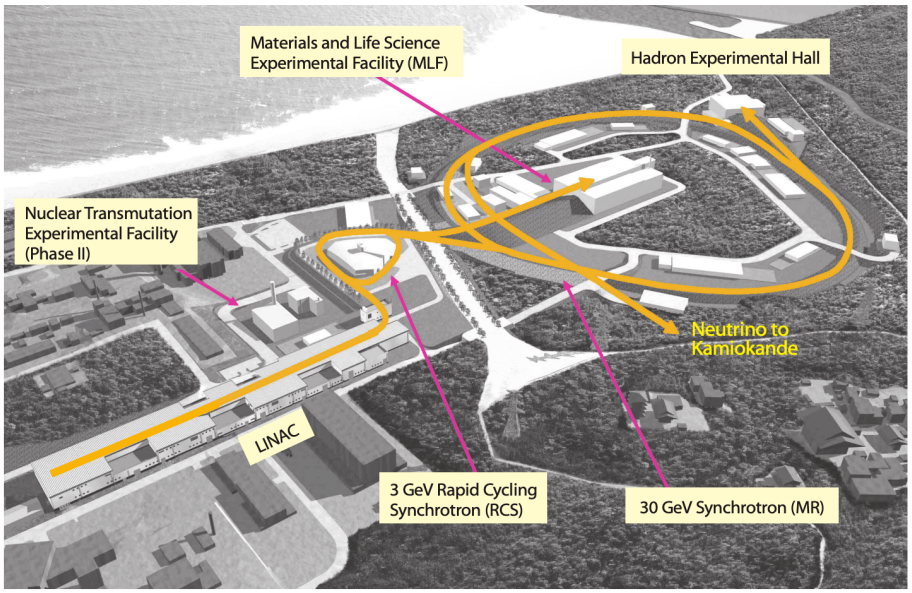

Figure 2.1: Bird's-eye view of the J-PARC facility in Tokai, Japan [50]. J-PARC consists of LINear ACcelerator (LINAC), Rapid Cycling Synchrotron (RCS), and Main Ring (MR). The proton beam is extracted from MR and delivered to a graphite target to produce a neutrino beam.

in the antineutrino mode are defocused. The neutrino mode is composed predominantly of ν_μ, and the antineutrino mode is mainly composed of $\overline{\nu}_\mu$. Figure 2.3 shows predictions of the neutrino fluxes at SK without considering the effect of neutrino oscillation. Since the horns' defocusing is not perfect, a 5%–10% amount of wrong-sign component contaminates each focusing mode. Besides the muon neutrinos, electron neutrinos are also produced by the decay of the kaons and muons. However, the amount of the electron neutrinos is around 1% of all.

Neutrinos produced by the decay of hadrons have a broad energy spectrum instead of a monoenergetic beam. Hence, T2K employs an off-axis method to obtain a narrow neutrino energy spectrum. Figure 2.4 shows the positional relation between the neutrino beamline and detectors. The far detector, SK, is located 2.5° away from the neutrino beam center. There are two types of near detectors in J-PARC: an off-axis detector ND280 and an on-axis detector INGRID. ND280 is placed at 2.5° off-axis as well as SK.

When a pion decays into a muon and a neutrino, the neutrino energy E_ν is written as

$$E_\nu = \frac{m_\pi^2 - m_\mu^2}{2(E_\pi - p_\pi \cos\theta_\nu)}, \tag{2.3}$$

where m_π and m_μ are the pion and muon masses respectively, E_π and p_π are the energy and momentum of the parent pion, and θ_ν is the angle between the incoming pion direction and the outgoing neutrino. In the T2K beamline, momentum of the parent pion is widely distributed. When $\theta_\nu = 0$, E_ν linearly increases as a function of p_π. In contrast, when a non-zero θ_ν value is assigned, a small E_ν value can be taken even if p_π gets increased. Figure 2.5 shows the neutrino energy spectrum and the oscillation probability at SK. The 2.5° off-axis setting provides a neutrino energy spectrum with a 0.6 GeV peak, which is

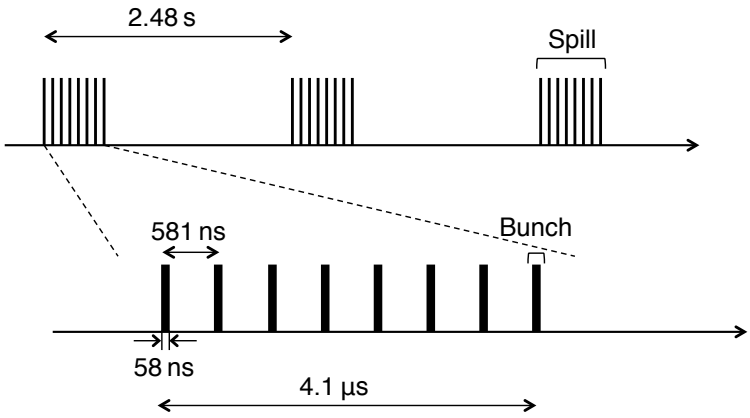

Figure 2.2: Bunch structure of the J-PARC MR spill. The proton beam spill is delivered to the graphite target every 2.48 s with an eight-bunch structure.

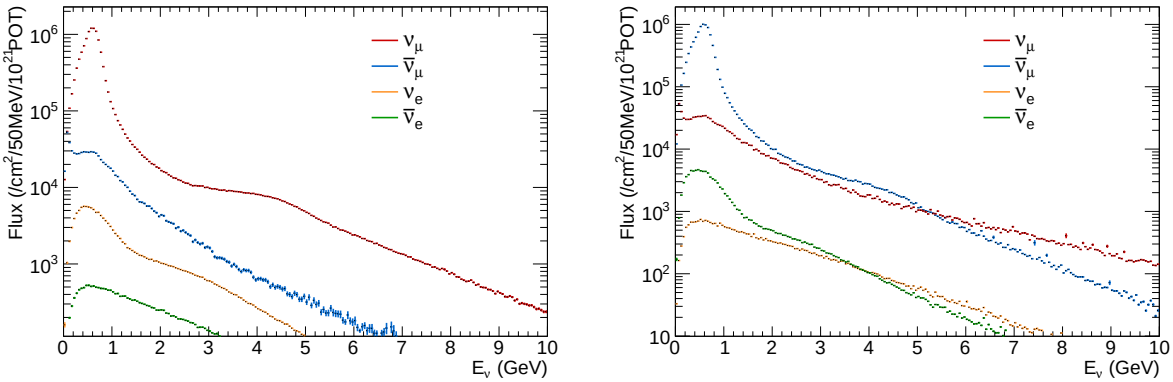

Figure 2.3: Prediction of the neutrino flux at SK without considering the effect of neutrino oscillation. The ν_μ, $\overline{\nu}_\mu$, ν_e, $\overline{\nu}_e$ components in the neutrino mode (left) and the antineutrino mode (right) are shown.

well-suited to see the effects of neutrino oscillation at SK. However, the off-axis method is susceptible to the neutrino beam direction. If the beam direction changes by 1 mrad, the peak of the neutrino energy spectrum at SK is varied by about 3%. Therefore, monitoring the neutrino beam direction with good accuracy is essential to run the experiment.

Muon monitor (MUMON) [52, 53] is a detector to measure the muons from the decay of hadrons downstream of the beam dump, which is behind the decay volume. MUMON measures the muon beam intensity and its profile. Thus, by measuring muons, the neutrino beam direction can be indirectly monitored. The MUMON detector is composed of ionization chambers and silicon PIN photodiodes, which are placed in 7×7 arrays. These two independent detectors cover a 1.5 m × 1.5 m area. MUMON is the only detector monitoring the bunch-by-bunch beam profile downstream of the graphite target. It is an essential detector for the operation of the T2K experiment to monitor the neutrino beam direction together with INGRID, which is described in the following section. MUMON has been operated since the beginning of the T2K measurement. There is an upgrade plan to use electron-multiplier-tube (EMT) detectors for a future high-intensity beam. Details of the EMT studies can be found at Ref. [54].

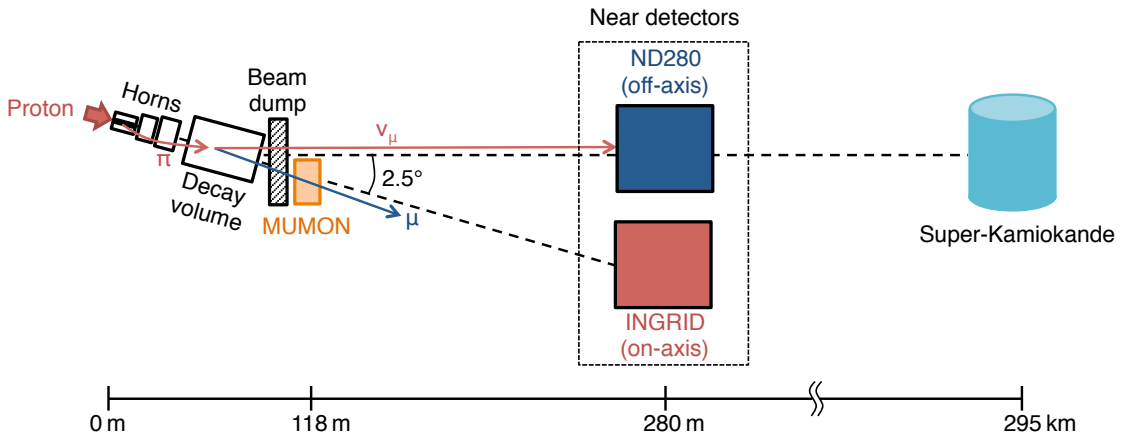

Figure 2.4: Positional relation between the neutrino beam line and the detectors. The off-axis near detectors, ND280, is located 2.5° away from the neutrino beam center as well as SK. INGRID is located as an on-axis near detector.

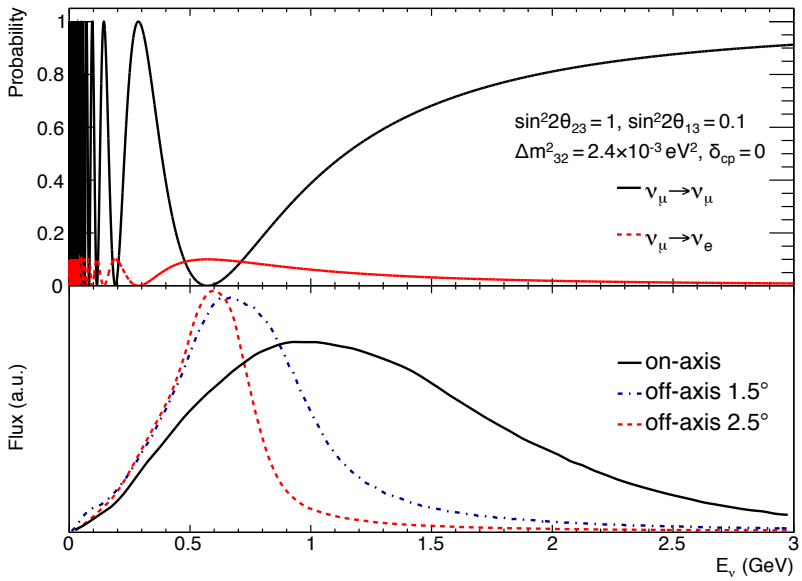

Figure 2.5: Oscillation probabilities of $\nu_\mu \rightarrow \nu_\mu$ and $\nu_\mu \rightarrow \nu_e$ at SK as a function of the neutrino energy (top), and neutrino energy spectra for different off-axis angles (bottom). T2K employs 2.5° off-axis beam. It has a spectrum with a 0.6 GeV peak neutrino energy, which is well-suited to see the effects of neutrino oscillation at SK.

2.2 Near detectors

The neutrinos delivered from the beamline are detected by the near detectors located at 280 m downstream of the graphite target. Figure 2.6 shows an illustration of the T2K near detector hall, in which two detectors are placed: the on-axis detector INGRID and the off-axis detector ND280. INGRID is placed to monitor the neutrino beam properties, and ND280 is used to predict neutrino events at SK and to study the neutrino interactions on several target materials.

2.2.1 The on-axis near detector: INGRID

Figure 2.7 shows the on-axis detector, INGRID. It consists of 14 identical modules, and they are located in a 10 m × 10 m cross-shape to measure the event rate and the profile of the neutrino beam. The beam profile needs to be monitored within 1 mrad accuracy. At the INGRID position, the 1σ width of the neutrino beam is around 5 m, which can be covered by seven horizontal or vertical INGRID modules. By fitting the numbers of neutrino events observed at the seven modules, the horizontal and vertical neutrino-beam profiles can be obtained. While MUMON measures the muons from the decay of the hadrons to indirectly monitor the neutrino beam, INGRID directly measures the neutrinos. More details of the neutrino beam measurement are described in Sec. 2.4 and Appendix 2.2.1.

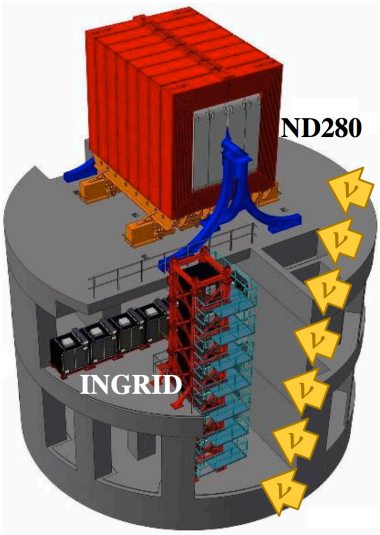

Figure 2.6: T2K near detectors located at 280 m downstream of the graphite target. ND280 is placed 2.5° off-axis, and INGRID is placed on-axis.

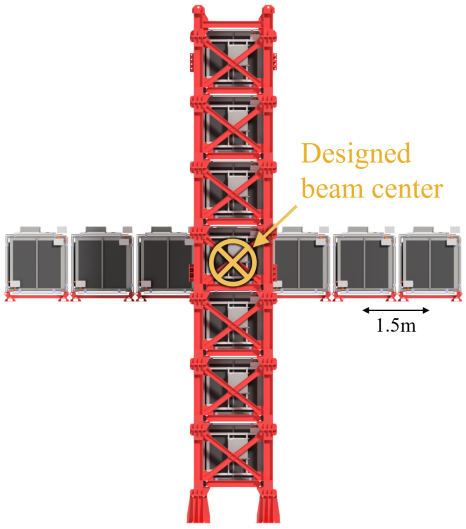

Figure 2.7: On-axis near detector INGRID: it consists of 14 modules placed along the vertical and horizontal axes. INGRID measures the neutrino event rate and the beam profile.

Figure 2.8 shows an exploded view of an INGRID module. It consists of 9 iron plates and 11 plastic-scintillator tracking planes. Each iron plate has a 6.5-cm thickness, and they are used as neutrino interaction targets. Each scintillator tracking plane consists of 24 vertical (x) scintillator bars and 24 horizontal (y) bars. The dimensions of the scintillator bar are 120 cm × 5 cm × 1 cm, and scintillation light is collected by a wavelength shifting

(WLS) fiber inserted along the scintillator. At one edge of the WLS fiber, a Multi-Pixel Photon Counter (MPPC) [55, 56] is attached using a dedicated optical connector.

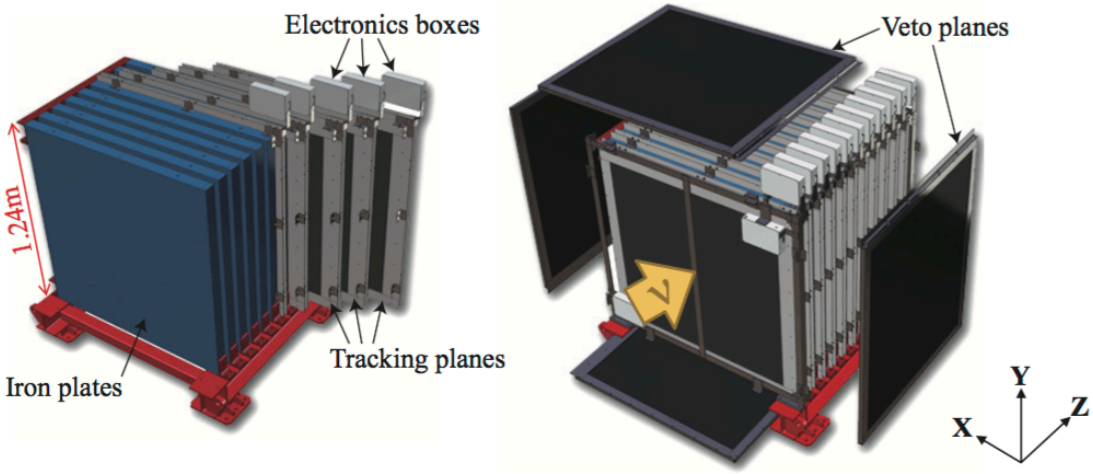

Figure 2.8: Exploded view of one module of INGRID. It has a sandwich structure consisting of iron plates and scintillator tracking planes.

Neutrino interactions occurring in INGRID are selected by tracking charged particles, mainly muons, from the neutrino interactions on iron using the scintillator tracking planes. Figure. 2.9 shows event displays of an INGRID module. A neutrino interaction occurring in INGRID and an external background from upstream of INGRID are shown. INGRID plays an essential role in the NINJA analysis described later, and its reconstruction method will be described in Sec. 6.2.

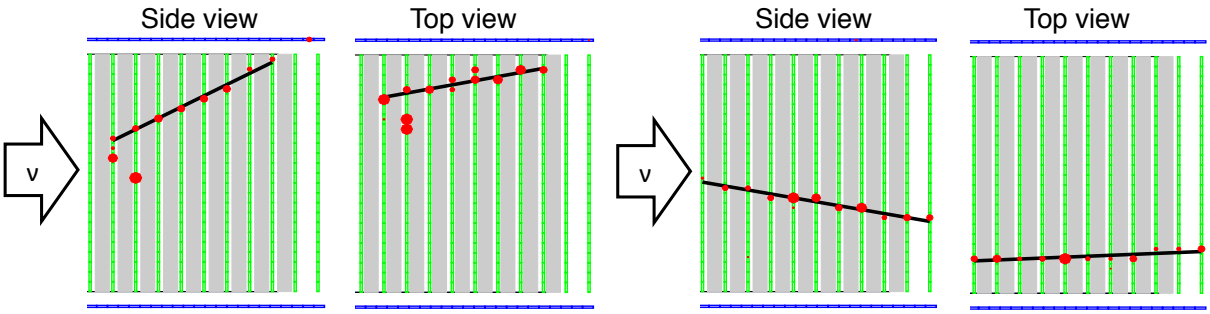

Figure 2.9: Event displays of an INGRID module for a neutrino event (left) and an external background from upstream of INGRID (right). Red circles are hits by charged particles, and their size is proportional to the observed light yield at the scintillator.

2.2.2 The off-axis near detector: ND280

Figure 2.10 shows an exploded view of the off-axis detector, ND280. ND280 is a detector complex designed to detect neutrino interactions with tracking and calorimetric information. ND280 sub-detectors are placed in a 0.2 T dipole magnet. This magnet was used for the UA1 experiment [57] and donated to T2K. ND280 is composed of the following sub-detectors.

- Pi-zero detector (P0D) [58]: P0D is a detector specialized in measuring neutral pions from the neutrino interactions, which are a significant background source of the ν_e appearance measurement at SK. P0D is located at the most upstream of ND280. It has a sandwich structure composed of tracking layers of plastic scintillators, water bags as neutrino interaction targets, and thin radiator layers made of lead or brass.
- Time Projection Chamber (TPC) [59]: Three TPC modules are installed downstream of P0D. Each module is filled with an argon-based gas mixture, and the signal is read out by MicroMEGAS [60] planes. TPCs measure the curvature of a charged particle track in the magnetic field to determine its momentum and charge sign. TPCs also measure the energy deposit along a track. Thus particle identification can be performed with the energy deposit and the measured momentum information.
- Fine Grained Detector (FGD) [61]: Two FGD modules are installed between the TPC modules. FGD is made of fine-segmented plastic scintillator bars, which have the size of $1\,\mathrm{cm} \times 1\,\mathrm{cm} \times 186\,\mathrm{cm}$. They play the role of targets as well as tracking detectors. The upstream FGD is composed of only scintillator bars, while the downstream FGD has water target layers between the scintillator tracking planes to measure neutrino interactions on water.
- Electromagnetic CALorimeter (ECAL) [62]: ECAL is placed at the outermost layer within the UA1 magnet, and it contains lead layers and scintillator layers. Electromagnetic showers are produced in the lead layers, and the energy of the electrons and gamma rays from the neutrino interactions are measured.
- Side Muon Range Detector (SMRD) [63]: Scintillator planes are inserted between iron layers of the UA1 magnet yoke to construct SMRD. SMRD is used for the tracking of high-angle escaping muons from the central detectors. SMRD also provides triggers for cosmic rays coming from the outside.

ND280 is designed to measure the neutrino interactions at the same off-axis as SK, and its measurements give constraints on the neutrino flux and the neutrino interaction uncertainties for the prediction of observation at SK. These constraints reduce the systematic uncertainty of the neutrino oscillation analysis. Besides, various cross-section measurements are provided from the neutrino events observed at ND280 [64–71]. However, low-momentum protons from neutrino interactions cannot be detected by the current ND280 detectors. Therefore, it is difficult to understand the neutrino interactions precisely. This problem is discussed in Sec. 3.4.

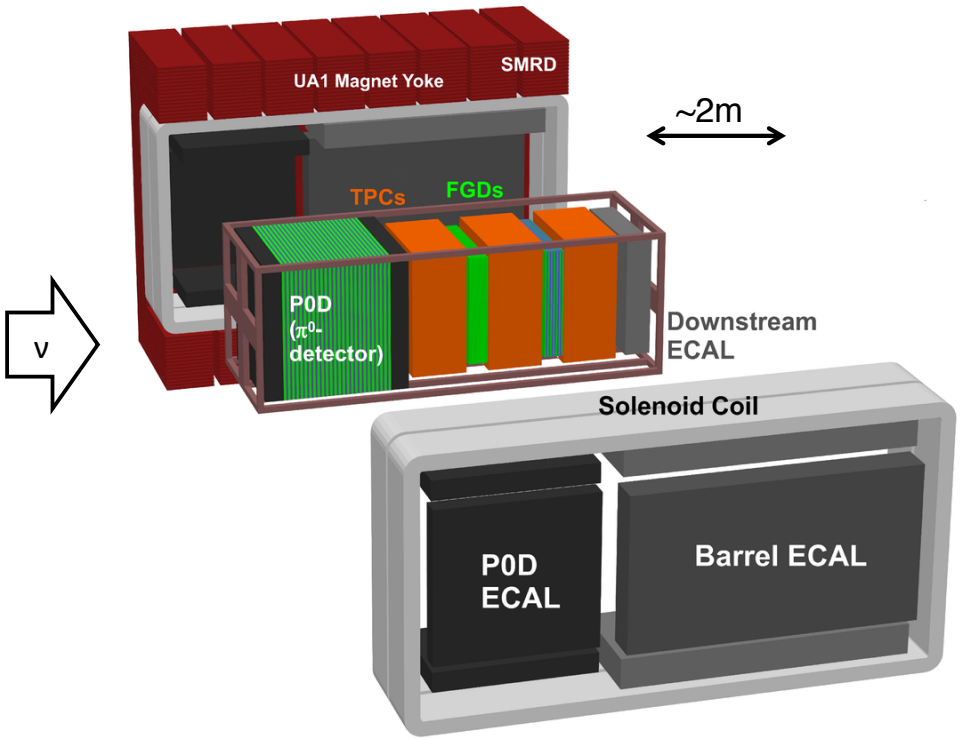

Figure 2.10: Exploded view of the T2K off-axis detector, ND280

2.3 Far detector: Super-Kamiokande

T2K uses a 50 kton water Cherenkov detector, Super-Kamiokande (SK), as the far detector. Figure 2.11 shows a schematic view of the SK detector. A cylindrical tank, 39 m in diameter and 40 m in height, is optically separated into an Inner Detector (ID) and an Outer Detector (OD). Charged particles from the neutrino interactions occurring on water emit Cherenkov light, and they are detected as ring patterns on the detector wall. The ID detects Cherenkov light from charged particles inside it with 11129 photomultiplier tubes (PMTs), while the OD identifies external backgrounds with 1885 PMTs. A separation between muon and electron tracks for identification of ν_μ and ν_e is performed using their ring shapes. The Cherenkov light from a muon forms a clear ring shape. On the other hand, the light from an electron forms a fuzzy ring due to electromagnetic showers. The particle identification, vertex reconstruction, and reconstructions of the energy and direction of a particle are obtained by fitting the PMT hit pattern of the ring.

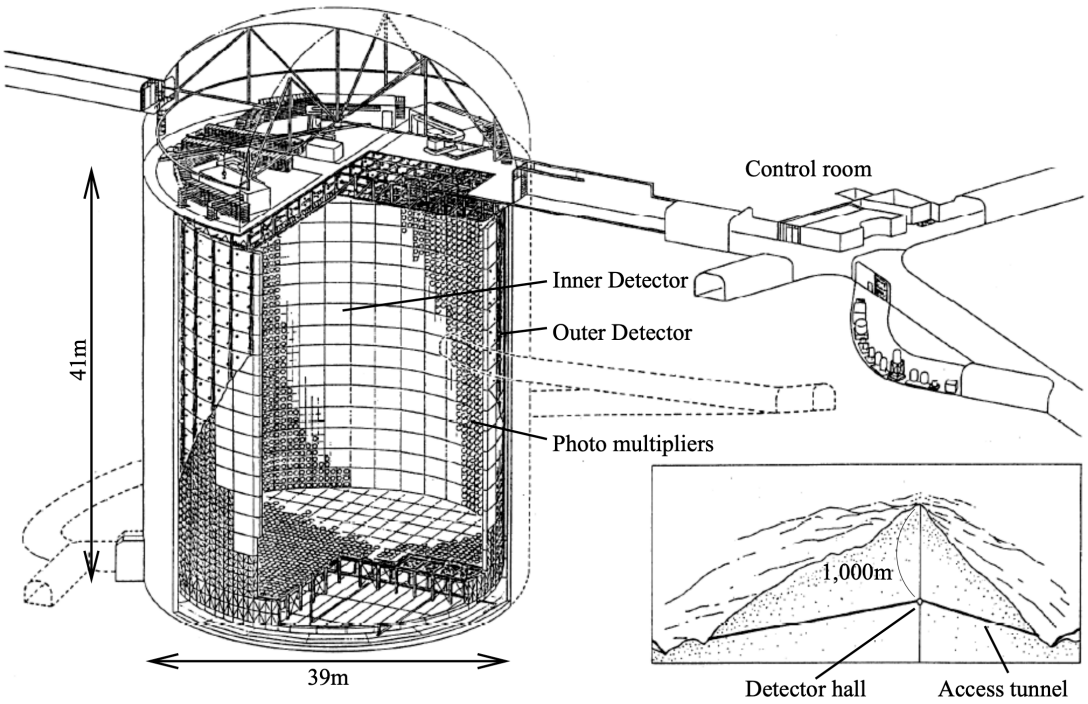

Figure 2.11: Schematic view of the Super-Kamiokande detector [72]

2.4 Measurement of the neutrino beam properties

In this section, the measurement of the beam properties by INGRID is described. As discussed in Sec. 2.2.1, INGRID monitors the event rate and the beam profile of the T2K neutrino beam. This is essential because T2K employs the off-axis method, and it is sensitive to the beam direction. The measured beam profile is used to evaluate the neutrino flux uncertainty induced by the beam direction, which is one of the most important inputs to the neutrino oscillation analysis.

The number of protons delivered to the graphite target is called as protons on target (POT). The neutrino event rate is obtained from the numbers of neutrino interactions detected in all the INGRID modules normalized by the POT measured by proton beam monitors in the beamline. Figure 2.12 shows an example of daily event rates in the antineutrino mode beam, which corresponds to the beam used for the analysis in the latter part of this thesis. The daily event rate was stable within the statistical fluctuation. Several points with large error bars correspond to short beam time due to troubles or scheduled maintenances of the accelerator.

Figure 2.13 shows the neutrino beam profiles fitted by a Gaussian function. Horizontal and vertical beam center values are obtained from the peak positions of the fitting, and beam widths are obtained from the Gaussian 1σ values. The neutrino beam direction is reconstructed from the positional relation between the graphite target and the measured beam center. A 1 mrad deviation corresponds to a 28-cm shift at INGRID. As shown in Fig. 2.13, the measured shifts are much smaller than the requirement of 1 mrad in both horizontal and vertical directions.

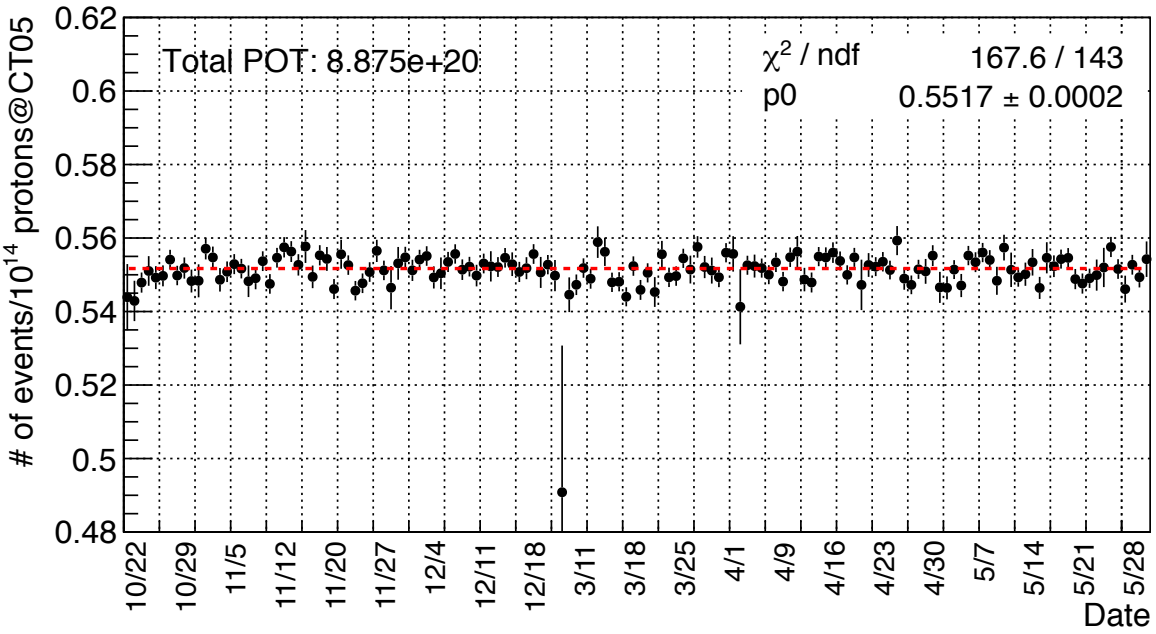

Figure 2.12: Neutrino event rate in the antineutrino mode beam measured by INGRID (example of the T2K run9 period). Vertical error bars correspond to the statistical errors, and the red broken line shows the average event rate in the period.

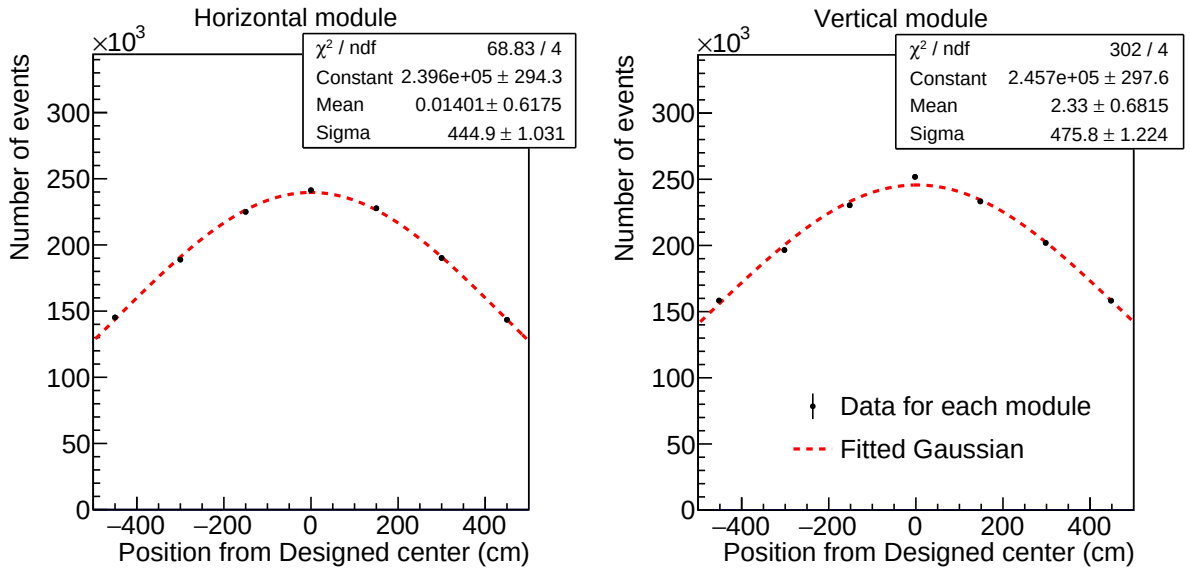

Figure 2.13: Neutrino beam profile in the antineutrino mode beam measured by INGRID (example of the T2K run9 period).

Figure 2.14 shows the measured neutrino beam properties of all the T2K runs, in which the neutrino event rate and the beam directions are shown. The measured event rate and directions are stable enough and meeting the 1 mrad requirement. INGRID has measured the neutrino beam profile together with MUMON during the decade of the T2K operation. The stable operation of INGRID and the beam profile measurement provide a basis for all physics measurements in T2K. More details and comparisons of the I NGRID measurements with MUMON and the proton beam are shown in Appendix. A.

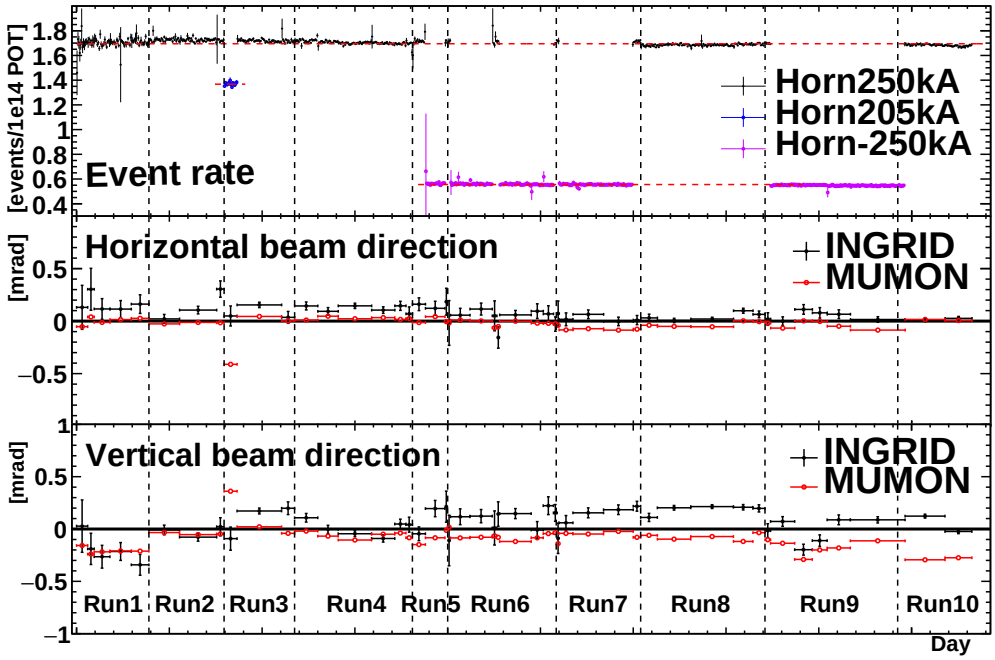

Figure 2.14: Neutrino event rate and the profile of the T2K neutrino beam over a decade.

2.5 Neutrino oscillation analysis in T2K

This section describes an overview of the T2K oscillation analysis. The neutrino beam delivered from the beamline is measured by both ND280 and SK. The number of observed neutrino interactions at ND280 (N_{near}) is written as follows:

$$N_{\mathrm{near}}(E_{\mathrm{rec}}) = \int \Phi_{\mathrm{near}}(E_\nu) \times \sigma(E_\nu) \times \epsilon_{\mathrm{near}}(E_\nu) \times T_{\mathrm{near}} \times R(E_\nu, E_{\mathrm{rec}})\, dE_\nu. \tag{2.4}$$

Here, $\Phi_{\mathrm{near}}(E_\nu)$ is the neutrino flux at ND280, $\sigma(E_\nu)$ is the neutrino cross section, $\epsilon_{\mathrm{near}}(E_\nu)$ is the neutrino detection efficiency at ND280, T_{near} is the number of target nuclei in ND280, and $R(E_\nu, E_{\mathrm{rec}})$ is a response function of ND280 describing the probability of reconstructing E_ν (the energy of a neutrino event) as E_{rec}. The measurement of neutrino interactions at ND280 constrains $\Phi_{\mathrm{near}}(E_\nu) \times \sigma(E_\nu)$ to reduce systematic uncertainty because $\Phi_{\mathrm{near}}(E_\nu)$ has a strong correlation with the neutrino flux at SK, $\Phi_{\mathrm{far}}(E_\nu)$.

The number of observed neutrino interaction at SK is written as

$$N_{\mathrm{far,e}}(E_{\mathrm{rec}}) = \int \Phi_{\mathrm{far}}(E_\nu) \times \sigma_{\nu_e}(E_\nu) \times \epsilon_{\mathrm{far,e}}(E_\nu) \times T_{\mathrm{far}} \quad (2.5)$$

$$\times P_{\nu_\mu \to \nu_e}(E_\nu) \times R_e(E_\nu, E_{\mathrm{rec}})\, dE_\nu, \quad (2.6)$$

$$N_{\mathrm{far},\mu}(E_{\mathrm{rec}}) = \int \Phi_{\mathrm{far}}(E_\nu) \times \sigma_{\nu_\mu}(E_\nu) \times \epsilon_{\mathrm{far},\mu}(E_\nu) \times T_{\mathrm{far}} \quad (2.7)$$

$$\times P_{\nu_\mu \to \nu_\mu}(E_\nu) \times R_\mu(E_\nu, E_{\mathrm{rec}})\, dE_\nu, \quad (2.8)$$

where $N_{\mathrm{far,e}}$ and $N_{\mathrm{far},\mu}$ are the numbers of observed ν_e and ν_μ events respectively, $\epsilon_{\mathrm{far}}(E_\nu)$ is the event detection efficiency at SK, T_{far} is the number of target nuclei in SK, $R_e(E_\nu, E_{\mathrm{rec}})$ and $R_\mu(E_\nu, E_{\mathrm{rec}})$ are response functions of the SK detector for ν_e and ν_μ, respectively. The parameters $P_{\nu_\mu \to \nu_e}(E_\nu)$ and $P_{\nu_\mu \to \nu_\mu}(E_\nu)$ are the neutrino oscillation probabilities of $\nu_\mu \to \nu_e$ and $\nu_\mu \to \nu_\mu$, respectively. Neutrino interactions are reconstructed as a function of reconstructed neutrino energy. Then, the neutrino oscillation parameters are extracted from a maximum-likelihood fit to the reconstructed energy spectrums of the ν_e and ν_μ events at SK.

Figure 2.15 shows the flow of the T2K oscillation analysis. Neutrino interactions at the near and far detectors are predicted by the flux and the neutrino interaction models.

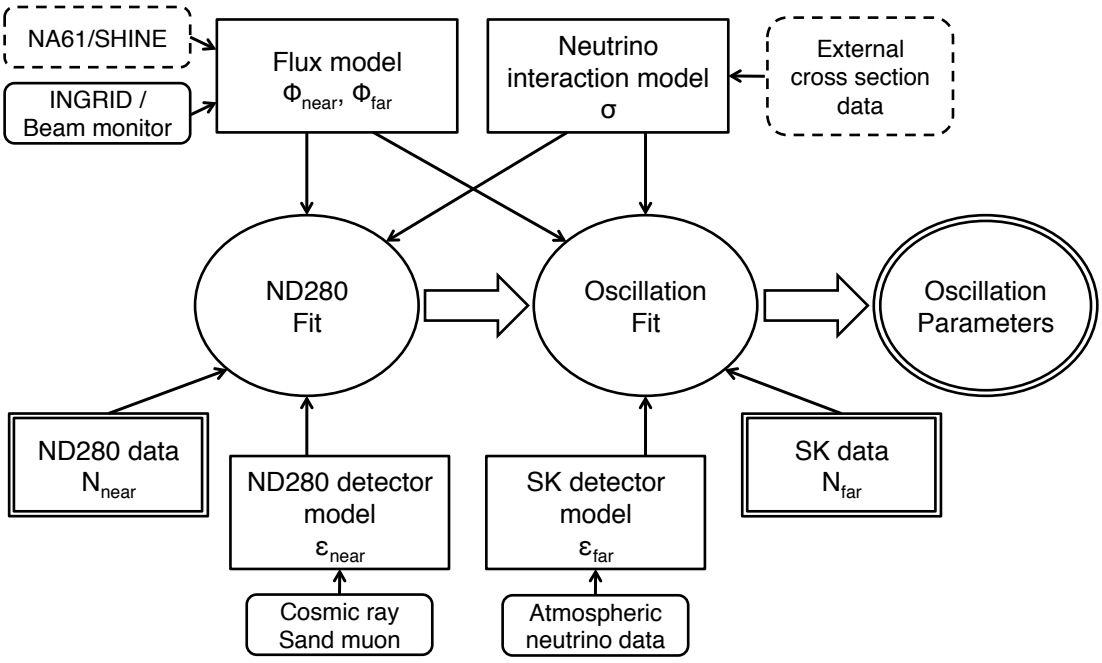

Figure 2.15: Flow chart of the T2K oscillation analysis. Neutrino interactions at near and far detectors are predicted by the flux, the neutrino interaction, and the detector models. Observed neutrino interactions at the ND280 are fitted by the prediction, and it gives constraints on the flux and the neutrino interaction parameters. Constrained parameters are propagated to the SK predictions, and the neutrino oscillation parameters are extracted.

For the flux model prediction, we use external data mainly by CERN NA61/SHINE [73–76] to constrain the uncertainty of hadron production at the graphite target, as well as the internal data from INGRID and the proton beam monitors. The neutrino interaction model is constructed based on external cross-section measurements. The ND280 detector response is modeled using control sample data, such as cosmic rays and sand muons, which are muons from neutrino interactions on the wall of the near detector hall. The SK detector response is modeled using the atmospheric neutrino data as well as cosmic ray and calibration source data. Observed neutrino interactions at the ND280 are fitted by the prediction, and it gives constraints on the flux and neutrino interaction parameters. Constrained parameters are propagated to the SK predictions, and the neutrino oscillation parameters are finally extracted by comparing the prediction and the data.

2.6 Latest results from T2K

T2K started the data taking in 2010. Data corresponding to 2.0×10^{21} POT of the neutrino mode beam and 1.6×10^{21} POT of the antineutrino mode beam were accumulated by 2020. Figure 2.16 summarizes the history of the MR beam power and the accumulated POT. Figure 2.17 shows the reconstructed energy spectra of observed ν_e and $\overline{\nu}_e$ candidate events at SK. The number of observed ν_e candidate events is larger than that of the prediction, while the opposite tendency is seen in the $\overline{\nu}_e$ candidate events. As already shown in Fig. 1.3, the latest result of δ_{CP} shows that T2K excludes CP conserved parameters (δ_{CP}=0, π) with more than 90% confidence level.

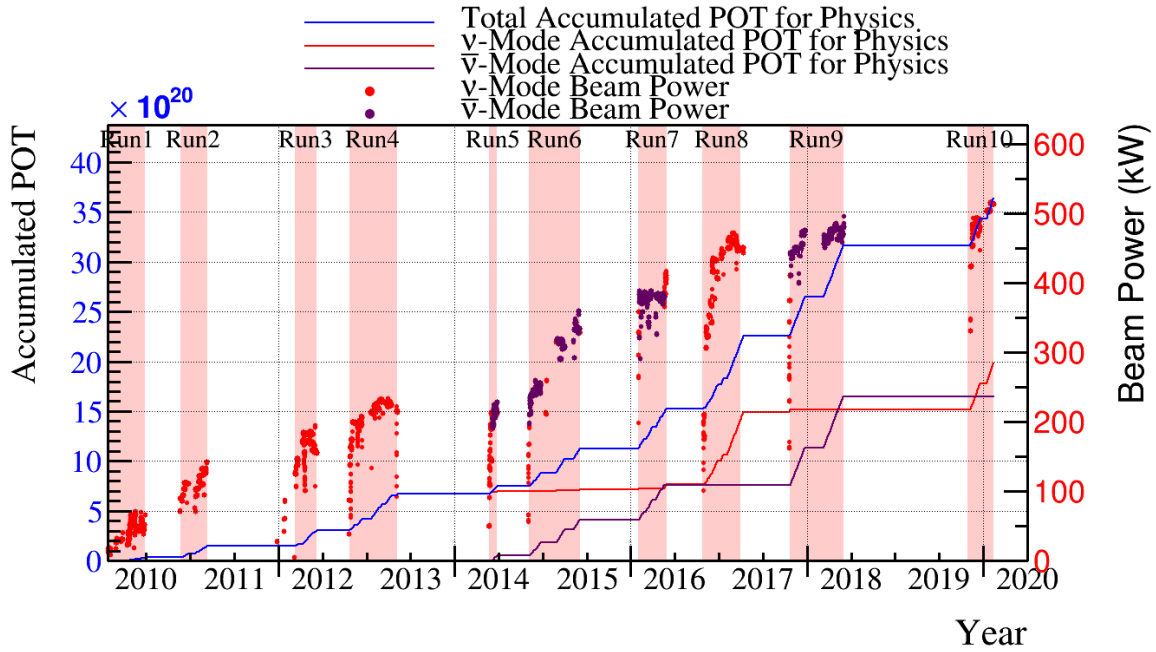

Figure 2.16: History of the beam power and the accumulated POT.

The current results are still limited by the statistical error. To achieve more precise measurements, increasing statistics is essential. An MR upgrade is planned to increase the beam intensity up to 1.3 MW by shortening the spill repetition time from 2.48 sec

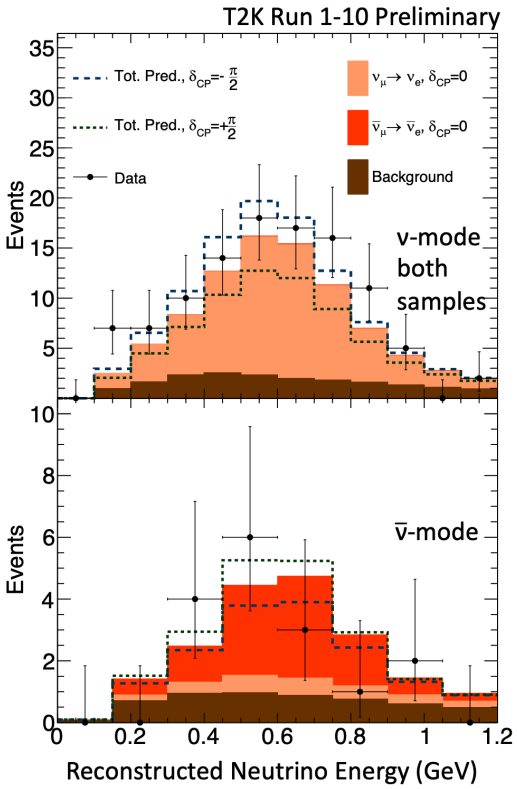

Figure 2.17: Reconstructed energy spectra of observed ν_e and $\overline{\nu}_e$ candidate events at SK. The numbers of events are measured as a function of reconstructed neutrino energy [30].

to 1.3 sec [77]. In addition, construction of HK is also ongoing. These upgrades will lead to a 5σ observation of the CP violation in the neutrino oscillation. As the statistics increase, reduction of the systematic uncertainty becomes more crucial. Table 2.1 shows the systematic error on the number of events measured at SK broken down by the error source. Observed events at SK are categorized into the following five samples:

- one electron-like ring in the neutrino mode (ν_e1R)
- one muon-like ring in the neutrino mode (ν_μ1R)
- one electron-like ring in the antineutrino mode ($\overline{\nu}_e$1R)
- one muon-like ring in the antineutrino mode ($\overline{\nu}_\mu$1R)
- one electron-like ring with one decay electron in the neutrino mode (ν_e1R+1d.e.)

The constraint by the ND280 measurement reduces the uncertainties of the flux and interaction from more than 10% to 3%. The neutrino interaction uncertainty is one of the dominant systematic errors in the current measurement. In the HK period, where the statistical uncertainty is reduced, and the systematic uncertainty becomes dominant, the uncertainty from the neutrino interaction should be reduced down to 1% level for ν_μ events, and 3% level for ν_e events. Although the flux and the cross-section uncertainties are significantly reduced after the ND280 constraint, further improvement is necessary. Besides, there are several neutrino interaction uncertainties that cannot be constrained by

ND280. These uncertainty sources also need to be reduced. In the following section, an introduction to the neutrino interactions and current problems on the interaction models are discussed.

Table 2.1: Systematic uncertainty (%) on the number of events measured at the T2K far detector. Flux+Xsec (cross section) term corresponds to the uncertainty after constrained by ND280. Each column corresponds to an event category at SK, and the last column is the error on the ratio of ν_e and $\overline{\nu}_e$ one ring events. Unconstrained parameters, such as 2p2h Edep, and IsoBkg low-p_π, are explained in Sec. 10.1.2 and Appendix F.

Error source	ν_e1R	ν_μ1R	$\overline{\nu}_e$1R	$\overline{\nu}_\mu$1R	ν_e1R+1d.e.	ν_e1R/$\overline{\nu}_e$1R
Flux+Xsec (ND constr)	2.0	2.1	2.3	2.3	4.1	1.7
2p2h Edep	0.2	0.4	0.2	0.4	0.0	0.2
IsoBkg low-p_π	0.1	0.4	2.2	2.5	0.1	2.1
$\sigma(\nu_\mu)/\sigma(\nu_e)$, $\sigma(\bar{\nu})/\sigma(\nu)$	2.6	0.0	1.5	0.0	2.7	3.0
NC γ	1.4	0.0	2.4	0.0	0.0	1.0
NC Other	0.2	0.2	0.4	0.2	0.8	0.2
SK	3.1	2.1	3.9	1.9	13.4	1.2
All	4.7	3.0	5.9	4.0	14.3	4.3

Chapter 3

Neutrino interactions

The cross section of neutrino-nucleus interactions is considerably small, thus measuring the neutrino interactions is always challenging. In the 1970s, bubble chambers were useful tools to look into neutrino interactions. The bubble chambers measured the axial-vector form factor of a nucleon by fitting data of neutrino interactions on hydrogen or deuterium [78–80]. These results were well described by models of the neutrino interactions on free nucleons. By contrast, recent neutrino-oscillation experiments employ heavier nuclei, such as carbon, oxygen, and argon. Hence, the picture of the neutrino interactions is getting more complicated due to "nuclear effects," such as correlations between nucleons and re-interaction inside the nuclear medium. In this chapter, a general description of the neutrino interactions with a nucleus is introduced as well as the importance and difficulty of understanding the nuclear effects. Following this, the status of current experiments studying the neutrino interactions is described.

Before describing the details of the neutrino-nucleus interactions, the importance of understanding the models of the neutrino interaction is emphasized again. For instance, in the T2K experiment, neutrino interaction models are necessary to predict the number of events as a function of the neutrino energy at SK for the neutrino oscillation analysis. Since the neutrino beam is not monoenergetic, we need to reconstruct incoming neutrino energies only from observed particles. Therefore, understanding and modeling how final state particles are observed in detectors after interacting in a nucleus are crucial. T2K uses NEUT [81] as a nominal simulator of the neutrino interactions. Neutrino interaction models used in NEUT are focused on in the following sections.

3.1 Neutrino interactions with a nucleus

3.1.1 Charged current quasi-elastic scattering

Figure 3.1 shows the cross sections of the neutrino interactions with a nucleus. Charged-current quasi-elastic (CCQE) interactions constitute the dominant interactions in the T2K energy range, and they are used as the primary signal in the T2K far detector.

Figure 3.2 shows diagrams of the CCQE interactions. The CCQE interaction is a two-body scattering which leaves one lepton and one nucleon in its final state: $\nu_l + n \to l + p$, where l is an electron or a muon. The incoming neutrino energy is reconstructed simply from the lepton kinematics as written as follows, when the nuclear effects are ignored:

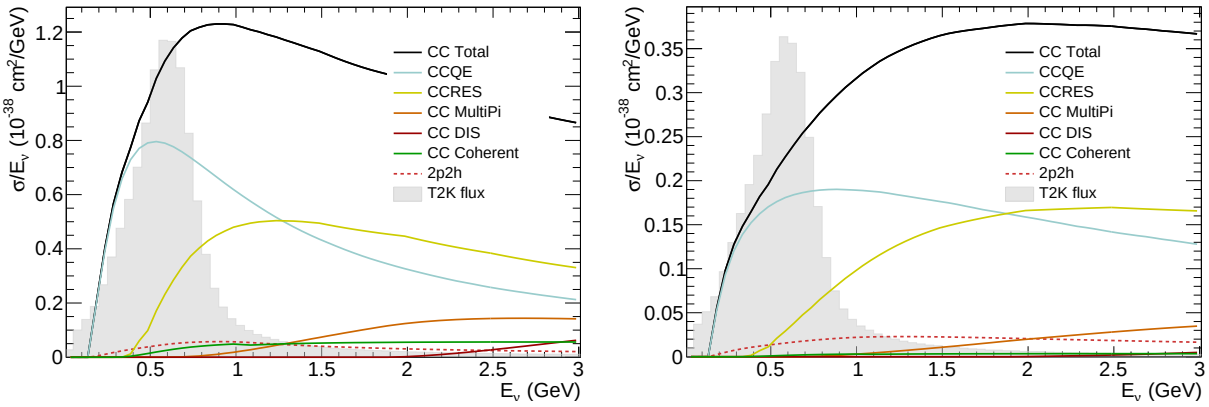

Figure 3.1: Cross sections of neutrino-oxygen interactions per nucleon, divided by E_ν, in the T2K energy range. The left plot shows the ν_μ cross section, and the right plot shows the $\overline{\nu}_\mu$ cross section. The gray histogram in the left plot corresponds to the T2K neutrino mode flux, and that in the right plot is the T2K antineutrino mode flux.

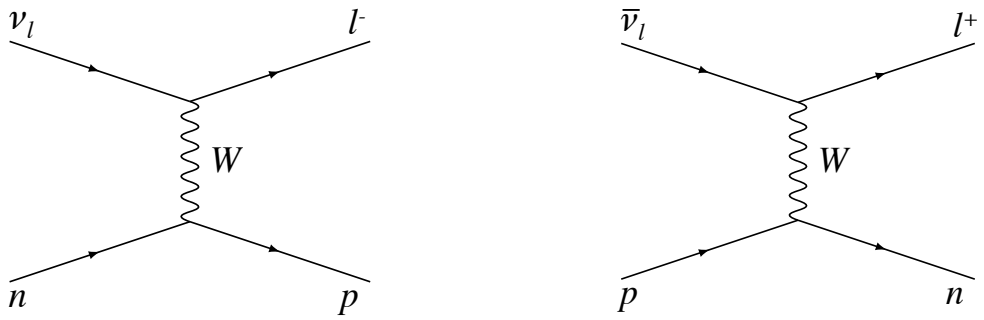

Figure 3.2: Diagrams of CCQE neutrino (left) and antineutrino (right) interactions.

$$E_\nu = \frac{m_n E_l - m_l^2/2 + (m_p^2 - m_n^2)/2}{m_n - E_l + p_l \cos\theta_l}, \tag{3.1}$$

where E_ν is the energy of the incoming neutrino, m_n and m_p are the neutron and proton masses, m_l is the outgoing lepton mass, E_l, p_l, and θ_l are the energy, the momentum, and the angle with respect to the neutrino beam direction, of the outgoing lepton respectively.

The cross section of the CCQE interaction is parametrized by a framework of Llewellyn-Smith [82], whose parameters are mostly measured by β decay experiments and electron scattering experiments. The differential cross section is given as a function of the square of the four-momentum transfer (Q^2):

$$\frac{d\sigma}{dQ^2} = \frac{G_F^2 M^2 \cos^2\theta_C}{8\pi E_\nu^2} \left[A(Q^2) \pm B(Q^2)\frac{s-u}{M^2} + C(Q^2)\frac{(s-u)^2}{M^4} \right], \tag{3.2}$$

where G_F is the Fermi coupling constant, M is the mass of a nucleon, and θ_C is the Cabibbo angle. The parameters s and u are the Mandelstam kinematic variables, and the sign $+(-)$ is for neutrinos (antineutrinos). The functions $A(Q^2), B(Q^2)$, and $C(Q^2)$ are

written by the vector (F_V^1, F_V^2), axial-vector (F_A), and pseudoscalar (F_P) form factors:

$$A(Q^2) = \frac{m_l^2 + Q^2}{M^2}\left[(1+\tau)F_A^2 - (1-\tau)(F_V^1)^2 + \tau(1-\tau)(\xi F_V^2)^2 + 4\tau(\xi F_V^1 F_V^2) - \frac{m_l^2}{4M^2}\left((F_V^1 + \xi F_V^2)^2 + (F_A + 2F_P)^2 - 4(1+\tau)F_P^2\right)\right], \tag{3.3}$$

$$B(Q^2) = 4\tau F_A(F_V^1 + \xi F_V^2), \tag{3.4}$$

$$C(Q^2) = \frac{1}{4}(F_A^2 + (F_V^1)^2 + \tau(\xi F_V^2)^2). \tag{3.5}$$

Here, $\tau = Q^2/4M^2$, and $\xi = (\mu_p/\mu_N - \mu_n/\mu_N) - 1$, which consists of the proton magnetic moment μ_p, the neutron magnetic moment μ_n, and the nuclear magneton μ_N.

The form factors express a spatial charge distribution of nucleons. Simply assuming an exponential charge distribution,

$$\rho(r) = \rho(0)\exp(-Mr), \tag{3.6}$$

a Fourier transform of the charge distribution gives a dipole form factor with an effective mass. The form factors F_V^1 and F_V^2 appear in electromagnetic interactions as well, thus the vector mass M_V is accurately determined by electron scattering experiments as M_V =0.84 GeV/c^2 [83]. According to the observations, the dipole form factor works for $Q^2 < 2\,\mathrm{GeV}^2$, while there are deviations at a higher Q^2 region. Therefore, these form factors are commonly tuned to reproduce the parameterization by BBBA05 [84].

For the other form factors, assuming the Partially Conserved Axial Current (PCAC) [85], the pseudoscalar form factor is written as:

$$F_P(Q^2) = \frac{2M^2}{Q^2 + M_\pi^2}F_A(Q^2), \tag{3.7}$$

while a dipole form factor is assumed for the axial-vector form factor:

$$F_A(Q^2) = \frac{g_A}{(1 + Q^2/M_A^2)^2}. \tag{3.8}$$

Here, M_π is the pion mass and g_A =1.267 is determined from β decay experiments accurately [86], while the value of the axial mass M_A, denoted M_A^{QE} especially for CCQE, is still a controversial topic. The axial mass $M_A = 1.026 \pm 0.021$ GeV is given from a global fit to neutrino-deuterium scattering measurements using bubble chambers [87]. However, discrepancies with the bubble chamber results have been observed in neutrino scattering measurements using heavier nucleus targets. We discuss this topic further in Sec. 3.2.

3.1.2 Resonant pion production

When the energy of the incoming neutrino is above around 400 MeV, the center of mass of the neutrino-nucleon interaction exceeds the delta baryon mass. Then, it can result in

emitting a single pion and a nucleon via a baryon resonant state. These interactions are called the resonant pion productions, and the following charged-current interactions are included:

$$\begin{aligned}
\nu_l + p &\rightarrow l^- + p + \pi^+ \\
\nu_l + n &\rightarrow l^- + p + \pi^0 \\
\nu_l + n &\rightarrow l^- + n + \pi^+ \\
\overline{\nu}_l + p &\rightarrow l^+ + p + \pi^- \\
\overline{\nu}_l + p &\rightarrow l^+ + n + \pi^0 \\
\overline{\nu}_l + n &\rightarrow l^+ + n + \pi^-
\end{aligned}$$

Example diagrams of CC resonant pion production (CCRES) are shown in Fig. 3.3. These interactions can be backgrounds for the CCQE interactions when the produced pions are not reconstructed. Moreover, this mode is recently included in the signal of T2K oscillation analysis because we can also reconstruct the incoming neutrino energy by assuming a two-body scattering with Δ instead of a nucleon in the CCQE interaction.

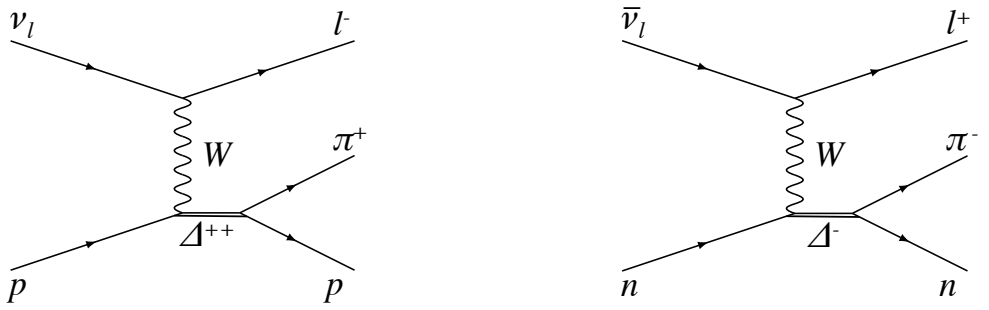

Figure 3.3: Example diagrams of CC resonant pion productions with neutrino (left) and antineutrino (right).

The Rein-Sehgal model [88] has been widely used for the resonant pion production. In this model, 18 baryon resonances that have invariant mass W <2 GeV are included as well as their interference terms. A small fraction of isospin $I = 1/2$ non-resonant background is also taken into account incoherently. Besides, since lepton mass is not considered in the Rein-Sehgal model, the lepton mass effect based on Ref. [89] is corrected in NEUT.

The resonant pion production can be expressed by a similar method to the CCQE calculation, thus form factors are used to describe it. In the T2K energy region, the $\Delta(1232)$ resonance is the dominant process. The $\Delta(1232)$ form factors based on analyses by Graczyk and Sobczyk [90] are employed. The form factors are separated into the vector and axial-vector terms similar to the CCQE form factors. The vector form factor is well determined from measurements of pion productions by electron scatterings [91], while there are two parameters not constrained enough in the axial-vector form factor: M_A^{RES} =0.95±0.15 GeV/c^2 and C_5^A =1.01±0.12, which correspond to M_A^{QE} and g_A in the CCQE interactions, respectively. The uncertainties of these parameters need to be considered carefully in neutrino interaction simulators.

3.1.3 Coherent pion production

In a coherent pion production, a neutrino scatters on a whole nucleus without knocking out any nucleon. This interaction occurs only at low momentum transfer. Thus the cross section is very small in the T2K energy region. There are two possible modes:

$$\begin{aligned} \nu_l + A &\rightarrow l^- + A + \pi^+ \\ \nu_l + A &\rightarrow \nu_l + A + \pi^0 \end{aligned}$$

where A is a nucleus. This interaction mode also leaves a single pion in the final state. Although the Rein-Sehgal [92,93] model is implemented in NEUT for the charged-current coherent interactions, they are tuned to follow the Berger-Sehgal [94] model, which shows better agreement with MINERνA results [95].

3.1.4 Deep inelastic scattering

At a high energy region where the incoming neutrino energy is more than a few GeV, the neutrino directly interacts with a quark inside a nucleon. This interaction mode is called deep inelastic scattering (DIS), and a hadron jet is produced by breaking a nucleon, as shown in Fig. 3.4.

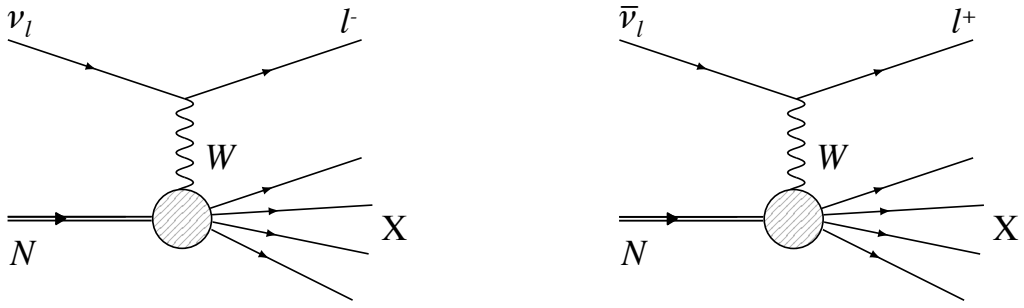

Figure 3.4: Diagrams of CC DIS interactions with neutrino (left) and antineutrino (right).

The DIS interactions are calculated using a parton distribution function (PDF), which describes the probability of finding a quark inside a nucleon. The DIS interactions have been measured using high-energy neutrino beams above a few GeV and probing the nucleon structure. These measurements are well implemented in PYTHIA [96]. Thus, in NEUT, the DIS interactions are simulated by PYTHIA for events with $W > 2\,\mathrm{GeV}$. On the other hand, there is not enough data to determine the PDF in a low energy region such as the T2K neutrino beam. In NEUT, events in $W < 2\,\mathrm{GeV}$ region are described by a "multi-pion model," where GRV98 PDF modified by Bodek and Yang [97] is used, but a 10% level uncertainty remains in this model.

3.1.5 Neutral current interaction

In a neutral current (NC) interaction, an incoming neutrino scatters off a nucleon by exchanging a Z boson without producing a charged lepton. Since observable particles

are limited to the scattered nucleons, pions, and de-excitation gamma rays, it is hard to measure the NC interactions in ND280. However, the NC interactions can be backgrounds in SK. For instance, NC single π^0 productions will be a background source for the ν_e selection when two gamma rays from the π^0 decay are reconstructed as one electron-like ring. Besides, an NC single π^+ production is categorized as a ν_μ candidate event where π^+ is miss-identified as a muon-like ring. At the T2K energy region, quasi-elastic interaction is the dominant mode in the NC interactions as well as the CC interactions.

3.2 Nuclear effects

As described in Sec. 3.1.1, the neutrino interaction model with a free nucleon well explains the experimental results of neutrino scattering using bubble chambers since they use light nuclei as their targets. However, recent neutrino experiments usually use heavier nuclei. Thus "nuclear effects" significantly present, which were invisible in light nucleus targets. To reconstruct the incoming neutrino energies from the observed particles, we need to construct more reliable models of the neutrino-nucleus interactions that give good agreement with experimental data. In recent years, many experiments measuring neutrino interactions are making efforts to achieve this, and the NINJA experiment also sets our goal to give insights into the complicated nuclear effects.

In this section, three nuclear effects are discussed: nuclear modeling, correlations between nucleons inside a nucleus, and re-interaction of final state particles.

3.2.1 Nuclear modeling

In the previous discussions, the nucleons are treated in the rest frame. However, in reality, they are in a bound state and moving in a nucleus. The cross section of the neutrino interactions and the kinematics of the outgoing particles depend on nuclear models, which describe the initial kinematics of nucleons in a nucleus. Three nuclear models used in NEUT, relativistic Fermi gas (RFG) [98], local Fermi gas (LFG) [99, 100], and spectral function (SF) [101, 102] models, are introduced below.

The RFG model is the simplest nuclear model among the tree models, and it has been widely used in neutrino interaction simulators. In this model, the nucleons are assumed to behave as an ideal Fermi gas uniformly spreading in a nucleus. All momentum states are filled up from the ground state to the highest state, which is called Fermi momentum (p_F). Interactions scattering off nucleons with momenta below p_F are not allowed, because the nucleons obey the Pauli exclusion principle. Therefore, only nucleons with momenta above p_F are emitted. Considering the nuclear binding energy (E_B), the momentum-energy distribution of a nucleon can be written as

$$P(\mathbf{p}, E) = \theta(p_F - |\mathbf{p}|)\delta(E + \sqrt{M_N^2 + |\mathbf{p}|^2} - E_B) \tag{3.9}$$

where θ is a step function, and M_N is the mass of a nucleon. The Fermi momentum p_F is measured by electron scattering experiments as $217\,\mathrm{MeV}/c$ for ^{12}C and $225\,\mathrm{MeV}/c$ for ^{16}O. The nuclear binding energy E_B is also measured as $25\,\mathrm{MeV}/c$ for ^{12}C and $27\,\mathrm{MeV}/c$ for ^{16}O. In the nucleon momentum distribution, there is a sharp cut off, which is a feature of the RFG model, around p_F.

The RFG model assumes that the spatial density distribution inside a nucleus is uniform, but a nucleus has a local density, in fact. The LFG model was developed as an alternative nuclear model that implements the local density depending on a radial position inside a nucleus. The local density function $\rho(r)$ is determined from electron scattering measurements. In this model, p_F depends on the radial position r in a nucleus. Thus it follows $p_F(r) \propto \rho(r)^{1/3}$, and the cut off seen in the RFG model does not appear in the nucleon momentum distribution of the LFG model.

While the LFG model is more realistic than the RFG model, it still assumes that nucleons are non-interactive fermions in a nucleus. Interactions between nucleons change their momenta. Thus the SF model was developed to take this effect into account. The SF model by Omar Benhar *et al.* is implemented in NEUT. In this model, momenta of nucleons and nuclear removal energies are prepared two-dimensionally. The nuclear removal energy corresponds to E_B in the RFG model, although it is not a single value. Figure 3.5 shows distribution of initial nucleon momentum in an oxygen nucleus. As short-range correlations of nucleons are considered in the SF model, the momentum distribution of nucleons has a tail in the high momentum region compared to the RFG and LFG models.

In this thesis, the CCQE interactions in the nominal simulation are generated with the Nieves *et al.* model, which uses the LFG model, while samples using the SF model are prepared for comparisons and estimation of systematic uncertainties between models. The SF model is also used in future sensitivity studies shown at the end of this thesis.

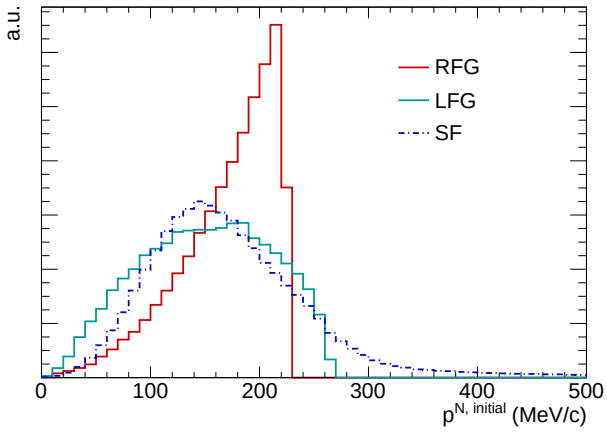

Figure 3.5: Distribution of initial nucleon momentum in an oxygen nucleus. Relativistic Fermi gas (RFG), local Fermi gas (LFG), and spectral function (SF) models are simulated in NEUT.

3.2.2 Nucleon-nucleon correlation

As described in Sec. 3.1.1, neutrino experiments using heavy target nucleus found that their results of the CCQE cross-section measurements are not explained by the M_A^{QE} value obtained from the bubble chamber experiments (M_A=1.03 GeV/c^2). In 2006, the K2K experiment reported that their best fit M_A value is M_A=1.20±0.1 GeV/c^2 by measuring neutrino interactions on oxygen [103]. After that, the MiniBooNE collaboration measured

the cross section of the ν_μ CCQE interactions on a ^{12}C target as a function of neutrino energy, using a mineral oil Cherenkov detector [104]. Figure 3.6 shows the result in which the observed CCQE events are 20% larger than the expected number of events from the M_A^{QE} measured by the bubble chamber experiments. The value $M_A^{\mathrm{QE}} = 1.35 \pm 0.17\,\mathrm{GeV}/c^2$ was obtained from the MiniBooNE result assuming the RFG model, and this "MiniBooNE M_A puzzle" triggered many discussions.

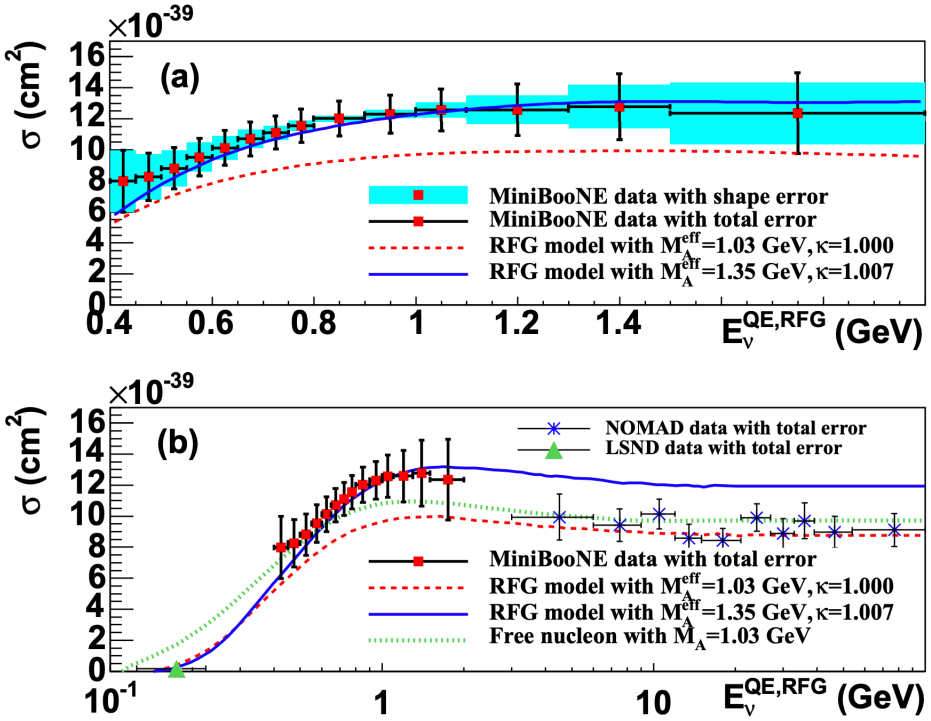

Figure 3.6: Measurement of ν_μ CCQE cross section by MiniBooNE [104]. (a) Colored boxes correspond to shape errors, while the total errors are shown as bars. (b) A wider energy range is shown with results from LSND [105] and NOMAD [106] experiments. Predictions by NUANCE are also shown with various values of the model parameters.

In response to this puzzle, it was pointed out that a neutrino interaction with a couple of interacting nucleons leads to a "CCQE-like" interaction [100, 109]. Such interaction mode scatters off two nucleons and leaves two empty states, thus it is called a two-particle-two-hole (2p2h) interaction (or np-nh in case of multiple nucleons). In this context, the CCQE interaction can be considered as a 1p1h interaction. A charged-current 2p2h interaction produces two nucleons and a charged lepton in its final state. Since most protons do not exceed the Cherenkov threshold, and MiniBooNE only selects events with a single muon-like ring, the CCQE event sample was contaminated by the multiple nucleon interactions of the CCQE-like events, which include several nucleons in the final state.

Figure 3.7 shows diagrams of the 2p2h interactions. The 2p2h interactions mainly contain Meson Exchange Current (MEC), Nucleon-Nucleon correlation (NN), pion in flight, and contact term. Around 20% of nucleons consist of correlated neutron-proton pairs in a nucleus (neutron-neutron and proton-proton pairs are much less than the neutron-proton pairs [107]), and the amount of the total 2p2h interaction is considered to be around 10% of the CCQE interaction. The MEC interaction is the dominant component in the 2p2h

interaction, and the NN interaction is the second dominant, while the components of pion in flight and contact term are considered to be small compared to the MEC and NN components. The problem of these interactions in T2K is described in Sec. 3.3. Besides, we discuss how we reveal the nature of the 2p2h interactions at the end of this thesis, in Sec 10.2.1.

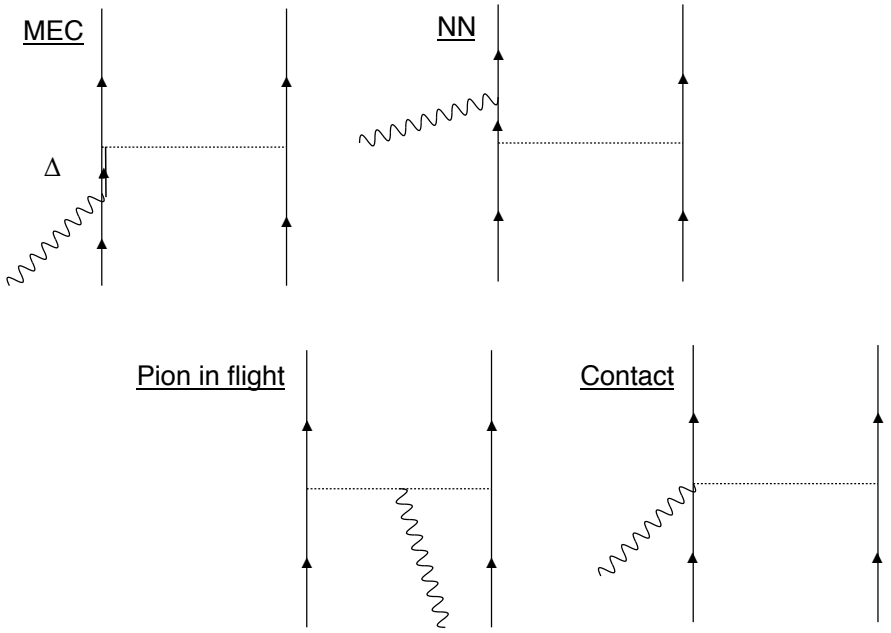

Figure 3.7: Diagrams of the 2p2h interactions. The solid lines are nucleons, the dotted lines are pions, the wavy lines are W bosons, and the double line is Δ.

While the 2p2h interaction is caused by a short-range correlation, a long-range correlation between nucleons is also needed to be considered. This effect is estimated by a long-range random phase approximation (RPA) [100], and a correction factor of the cross section is calculated as a function of Q^2. Figure 3.8 shows the correction factor for the CCQE interactions on a carbon target. By taking into account the multi-nucleon interactions and the RPA correction, the MiniBooNE puzzle is well explained by the RFG model with $M_A^{\mathrm{QE}} \sim 1.0\,\mathrm{GeV}/c^2$.

There are several 2p2h models of neutrino interactions, such as models developed by Nieves *et al.* [100], Martini *et al.* [109], and SuSAv2 [110]. However, the uncertainties of these models are significantly large due to insufficient experimental observations. The most significant feature of the 2p2h interaction is two nucleons in the final state. Therefore, precise measurements of these nucleons using high-resolution detectors would significantly improve the 2p2h model. Since the NINJA experiment can detect short-range tracks by emulsion films, protons from the 2p2h interactions can be measured with a $200\,\mathrm{MeV}/c$ threshold, which will give more clear insights into the 2p2h interactions.

3.2.3 Final state interaction

Hadrons produced by neutrino interactions are likely to re-interact within the nuclear medium before escaping from the nucleus. These re-interactions are called final state interactions (FSI). The most prominent FSI processes in T2K are pion elastic scattering,

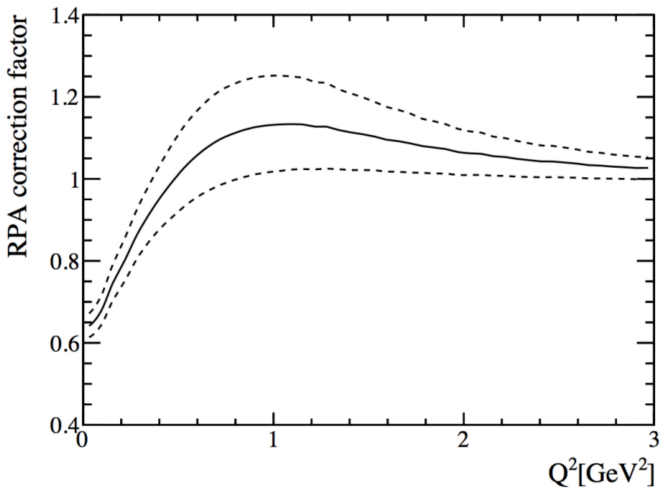

Figure 3.8: Correction factor of RPA for CCQE on a carbon target [108], which is calculated based on Ref. [100]. The broken lines correspond to the $\pm 1\sigma$ uncertainty.

charge exchange, absorption, and production, as shown in Fig. 3.9. The FSI changes their kinematics, as well as the number of final state particles and their charge. Besides, particles escaping from the nucleus also interact with materials before reaching a detector or with the detector itself. Such interactions are known as secondary interactions (SI). Hence, what we can measure is different from the primary interaction, and there is no way to know the primary interaction process (such as CCQE, CCRES, CCDIS) event-by-event from our observation. The construction of reliable FSI models is essential, as well as the neutrino interaction modeling.

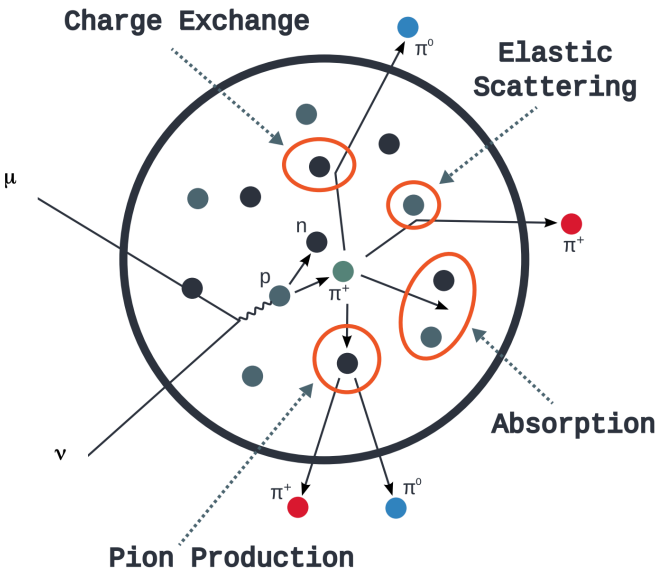

Figure 3.9: Final state interactions of pions inside a nucleus [111]. Elastic scattering, charge exchange, absorption, and production are considered in NEUT.

In many neutrino interaction simulators, intranuclear cascade models are used to simulate the FSI. A hadron from a neutrino interaction is propagated through a nuclear medium step-by-step based on the mean free path, and the probability of every possible re-interaction is computed in each step. This calculation is repeated until the particle reaches the surface of the nucleus. In NEUT, the Oset *et al.* model [112] provides interaction probabilities of elastic scattering, charge exchange, and absorption for pions momentum below 500 MeV/c. For higher momentum pions, productions of multiple hadrons can occur, and they are simulated based on pion scattering data with free protons and deuterons [113]. For nucleon FSI, elastic scattering and production of pions are implemented using the free nucleon-nucleon scattering data [114].

3.3 Neutrino interaction in oscillation experiments

Neutrino interaction simulators provide the cross section of each interaction mode introduced in the previous sections, and they also give the kinematics of all outgoing particles considering the FSI. There are several simulators, such as NEUT [81], GENIE [115], NuWro [116], NUANCE [117], and GiBUU [118]. Each simulator is tuned using a wide range of experimental data to reproduce the measured neutrino events. NEUT is a simulation program library of neutrino interactions used as the nominal simulator in the T2K experiment, covering from 100 MeV to 100 TeV of neutrino energy range. In this analysis, NEUT 5.4.0 is used as the nominal simulator, while GENIE is used for comparison. Below, several important points that we have discussed above are emphasized again, especially from the point of view of T2K.

The CCQE interactions constitute the dominant neutrino interaction process in T2K. The far detector, SK, is insensitive to most nucleons from the neutrino interactions. T2K selects events with a single lepton and no other visible particles as the primary signals. Assuming the two-body scattering of the CCQE interaction, the incoming neutrino energy is reconstructed only from the outgoing lepton. However, the 2p2h interactions can be included in the selected events. Figure 3.10 shows the distribution of the difference between the reconstructed and true neutrino energies in each interaction mode predicted from the neutrino interaction models. The 2p2h interactions, especially the MEC interactions, bias the reconstructed neutrino-energy. This is because the MEC interaction emits protons via a Delta baryon resonance, as shown in Fig 3.7. Although the other interaction modes also distort the reconstructed neutrino energy, still the 2p2h interactions are one of the leading backgrounds. This is because we select events with a single muon-like ring, and an event associated with pions does not pass this selection as far as the muon and pions are correctly detected. In T2K, ND280 is used to measure and study the neutrino interactions [64–71]. However, we have very poor 2p2h measurements at present because most protons from the neutrino interactions are below the detector threshold. Thus, additional measurements of low-momentum protons are important. In addition, precise measurements of low-momentum charged pions from the neutrino interactions are essential. For instance, neutrino interactions with pions also pass the CCQE signal selection at SK when the pions fall short of the Cherenkov threshold in water, although Michel-electron tagging from the pion decay ($\pi^+ \to \mu^+ + \nu_\mu, \mu^+ \to e^+ \nu_e \overline{\nu}_\mu$) can sometimes be used to veto such events. Measurements of protons and pions with low momentum thresholds are

essential to construct reliable neutrino-nucleus interaction models, and they will reduce the systematic uncertainties in T2K.

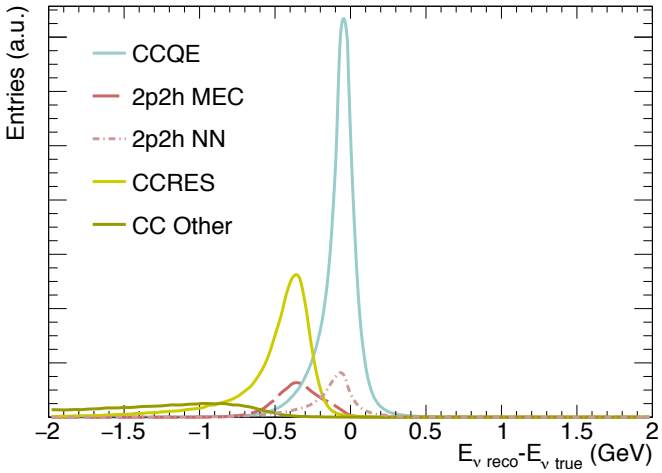

Figure 3.10: Distribution of difference between the reconstructed and true neutrino energies at the 2.5° off-axis. The neutrino energy is reconstructed assuming the two-body scattering of the CCQE interaction.

3.4 Status of the neutrino interaction measurements

3.4.1 CCQE-like cross-section measurements

Cross sections of neutrino interactions have been measured widely with various nucleus targets. Figure 3.11 shows the results of ν_μ and $\overline{\nu}_\mu$ CC inclusive cross sections by various experiments [119]. The measured cross sections follow a linear function of neutrino energy above 10 GeV, where the DIS is the dominant interaction mode. On the other hand, significant discrepancies are observed below 10 GeV because of the nuclear effects discussed in Sec. 3.2. Since most accelerator-based neutrino oscillation experiments use neutrino beams below 10 GeV, the poor understanding of the neutrino interactions in this region leads to considerable systematic uncertainties.

Many neutrino interaction experiments focus on measurements of charged leptons in the CC interactions. However, to probe the nuclear effects and give stronger constraints on the neutrino interaction models, observing hadrons produced by the neutrino interactions plays an indispensable role in addition to measuring the outgoing leptons. While we are especially trying to utilize the CCQE interactions, we found that perfectly identifying the CCQE events from data is impossible even with a perfect detector because the outgoing particles are distorted by the nuclear effects. Therefore, CC interactions without pions in the final state, called CC0π (or CCQE-like) events, are defined as the signals in recent years. Moreover, experiments with low momentum thresholds can measure the number of protons. Thus CC interactions without pions with N protons (CC0πNp) can be measured explicitly. Proton measurements are very important to provide more useful information to construct the neutrino interaction model not only for the CCQE interaction, but also for

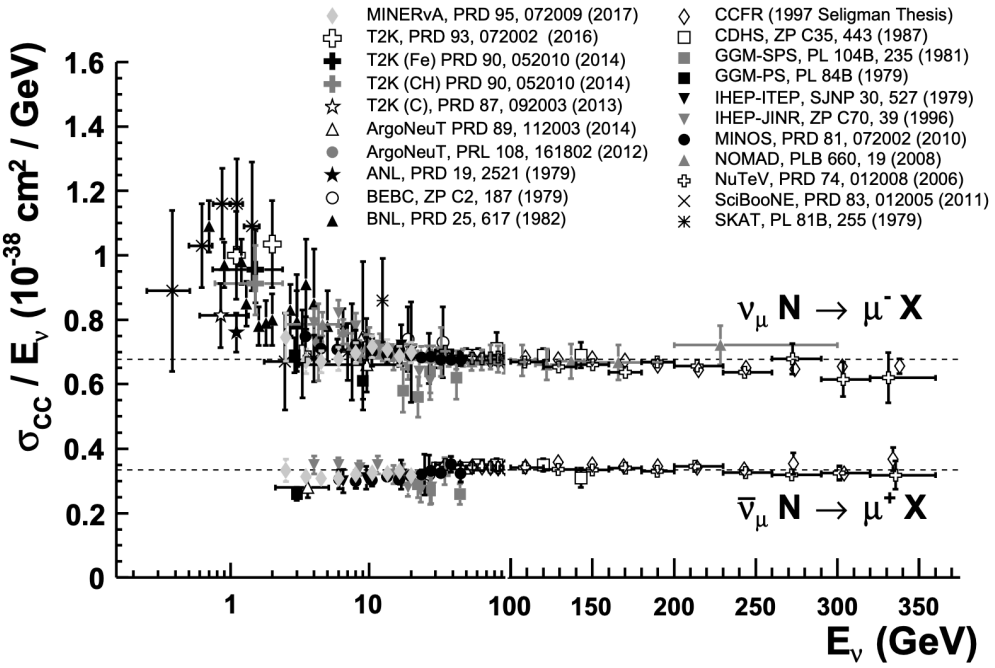

Figure 3.11: Various measurements of ν_μ and $\overline{\nu}_\mu$ CC inclusive cross sections on various nucleus targets [119].

other types of interaction and nuclear effects. In the following sections, modern approaches to the measurement of the CC0π interactions accompanying protons are described.

3.4.2 Measuring short hadron tracks from neutrino interactions

In the 1970s, bubble chambers were useful detectors to measure protons with low momentum thresholds. Recently, instead of the bubble chambers, liquid argon time projection chambers (LArTPCs) are showing great activities to measure the neutrino interactions precisely [49, 120]. The LArTPCs will be used as main detectors for next-generation experiments, such as DUNE [47]. The LArTPCs are expected to realize kton-scale target masses with few-mm position resolutions. Hence, it suits to detect short proton tracks from the neutrino interactions with sufficient statistics.

ArgoNeuT [122] is the first LArTPC experiment to measure low momentum protons from the neutrino interactions. They reported the detection of "back-to-back" proton pairs in the CC0π interactions using a 240-kg LAr target. It is concerned that neutrino interactions with such pairs induce 2p2h interactions which emit two protons in the opposite directions. Therefore, the opening angle distribution of the proton pairs is one of the powerful observables to characterize the 2p2h interactions. Figure 3.12 left plot shows the relation between the momentum of the lower energetic proton and the opening angle of the proton pairs. The data sample includes only 30 CC0π events with two protons, and four events are found as "hammer events," which have pairs of back-to-back protons with $\cos(\gamma) < -0.95$ for their opening angle γ (Fig. 3.12 right).

ArgoNeuT did not give a strong conclusion due to the limited statistics. Since 2015,

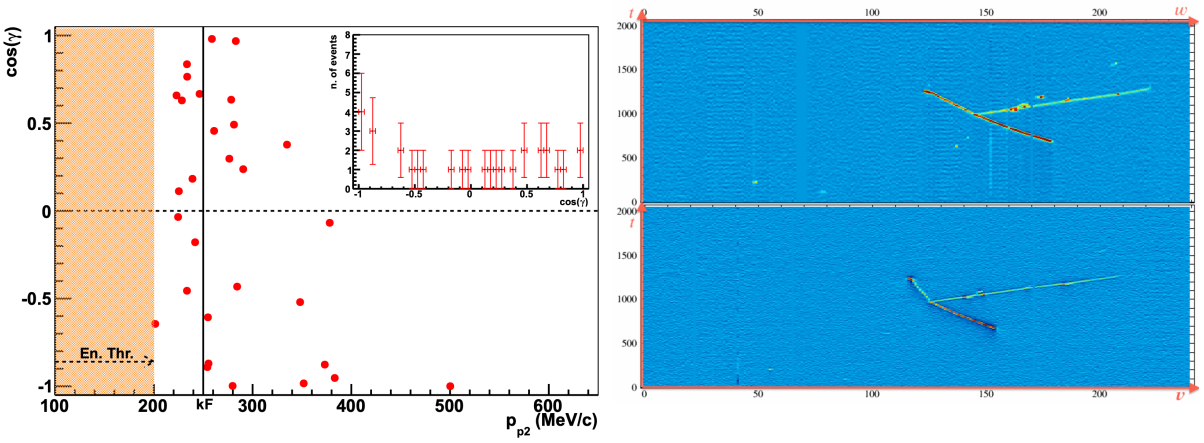

Figure 3.12: Relation between the momentum of lower energetic proton and the opening angle of proton pairs in CC0π interactions (left) and a typical hammer event (right) measured by ArgoNeuT [122].

MicroBooNE [49] has taken data with a 170-ton LArTPC. A similar analysis was performed with a 300 MeV/c proton momentum threshold [121]. The preliminary result is shown in Fig. 3.13. In contradiction to the ArgoNeuT result, there is no tendency of the back-to-back protons so far. The result is going to be updated with more statistics and accurate estimation of systematic uncertainties. The distribution of the proton opening angle depends on the interaction model and is especially sensitive to the 2p2h interactions. Thus, measurement with small uncertainty will give a good constraint on the 2p2h interactions.

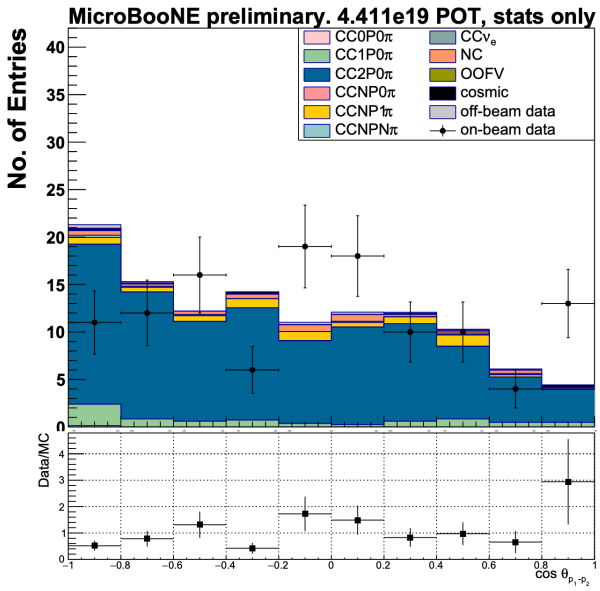

Figure 3.13: Opening angle distribution of proton pairs in CC interactions measured by MicroBooNE [121].

3.4.3 Prospect of the neutrino interaction measurements

There are other modern approaches to probe the nuclear effects using scintillator detectors, although they cannot achieve as low momentum thresholds as LArTPCs. In the absence of the nuclear effects, the kinematics of the outgoing lepton and the proton in a CCQE event should be balanced with respect to the incoming neutrino axis. Hence, their "imbalanced" kinematics directly correlates with the nuclear effects [123]. Such kinematics imbalances were measured by T2K [68] and MINERνA [124]. Another approach similar but different from the kinematics imbalance is inferred kinematics. Assuming the two-body kinematics of the CCQE interaction, kinematics of the outgoing proton can be inferred from the muon kinematics. Differences between the inferred and measured proton kinematics also probe the nuclear effects, and they are also measured by T2K [68]. More details about the kinematics imbalance and inferred kinematics measurements are described in Appendix C.1.

Although T2K and MINERνA are establishing such novel approaches to probe the nuclear effects, the 2p2h model is still not well understood. We need to consider what kind of strategies should be made to reveal the 2p2h model and other nuclear effects in future measurements. Figure 3.14 shows the momentum distribution of protons from the CCQE and 2p2h interactions predicted from the neutrino interaction models. Since the proton momentum threshold of ND280 is around 500 MeV/c, not all protons leaving the nucleus are detected. We need to achieve a much lower proton momentum threshold to cover all the protons from the neutrino interactions. While LArTPCs are promising detectors providing precise measurements of the low-momentum protons, they only measure interactions on the argon nucleus. For T2K (and HK), understanding the neutrino interactions on water, the SK's target material, is essential. Besides, large angular acceptance is essential to cover all protons. In the following section, the physics goals of the NINJA experiment and the features of our detector are introduced.

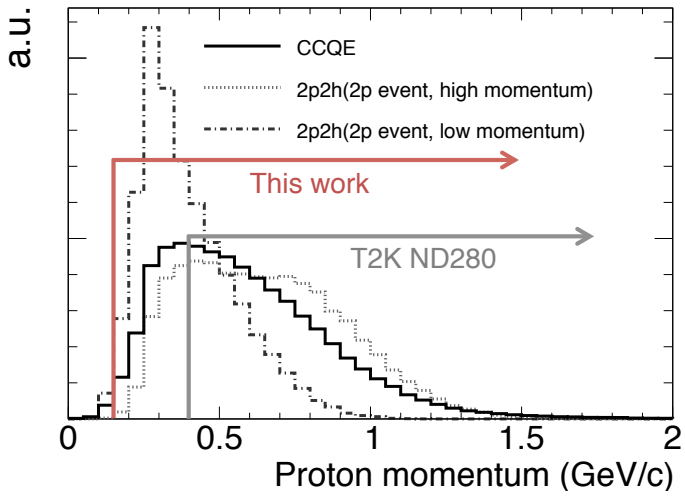

Figure 3.14: Momentum distribution of protons from the neutrino interactions on a water target. Single proton from the CCQE interaction and the higher and lower momentum protons from the 2p2h interactions with two protons in its final state are shown separately. NINJA can cover most protons with a 200 MeV/c momentum threshold.

Chapter 4

The NINJA experiment

As discussed in the previous section, there are important requirements for new experiments to reduce the systematic uncertainty from the neutrino interaction modeling in T2K: detecting low momentum protons with a large angular acceptance and using a water target for the measurement. Hence, we have carried out a new experiment, NINJA. In this section, an overview of the NINJA experiment and features of the nuclear emulsion are described, as well as the other detectors used in the NINJA pilot run.

4.1 Motivation of the NINJA experiment

The NINJA experiment measures the charged-current (CC) interactions on a water target using the T2K neutrino beam. We attempt to realize multi-differential cross-section measurements with low momentum thresholds to give insights into the neutrino-nucleus interaction. Our detector can measure the kinematics of muons, charged pions, and protons as well as their correlation, including the protons with momentum down to 200 MeV/c. As introduced in Chapter 3, low-momentum protons produced by the neutrino interactions have been measured by bubble chambers containing hydrogen or deuterium [79, 125, 126] as well as liquid argon time projection chambers [122]. By contrast, recent long-baseline neutrino oscillation experiments use carbon and oxygen as their targets. The proton momentum thresholds achieved for these nuclei are down to only around 400 MeV/c [68, 124]. As already shown in Fig. 3.14, we achieved a much lower threshold using a nuclear emulsion detector.

We use a nuclear emulsion detector as our main detector. The nuclear emulsion detector is a three-dimensional tracking device with very high granularity. The emulsion detectors have contributed to advances in fundamental particle physics such as the discovery of the charm particles in cosmic rays [127], the direct observation of ν_τ in DONUT [4], and the discovery of ν_τ appearance in neutrino oscillation measured by OPERA [128]. The detection of extremely short tracks was a key to these observations. The high granularity of the nuclear emulsion allows clear detection of short-range tracks from interaction vertices. Measurements with various target materials are enabled by preparing an alternating structure of emulsion films and thin target layers. Figure 4.1 shows a candidate event of ν_τ appearance in the $\nu_\mu \to \nu_\tau$ neutrino oscillation observed in the OPERA experiment, where an alternating structure of the emulsion films and lead target layers is used. Owing to this structure, a few-mm range tracks can be detected.

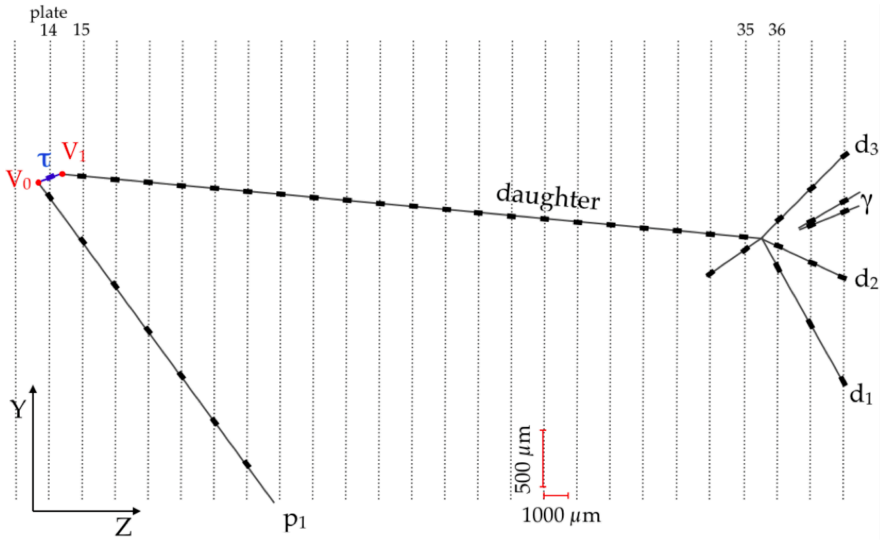

Figure 4.1: Candidate event of ν_τ appearance in $\nu_\mu \to \nu_\tau$ neutrino oscillation observed in OPERA [128]. Owing to the high granularity of nuclear emulsion films, very short tracks of τ were detected.

In our case, thin water-layers are used as the target layers. The main detector is called the water-target emulsion cloud chamber (ECC), which records all charged particles from the neutrino interactions. The ECC is not sufficiently large to fully contain the muon tracks in it. Thus the ECC is installed upstream of a T2K near detector which has an alternating structure of iron plates and scintillator layers (INGRID is used for the pilot run, and Baby MIND is used for the physics run, which is described in Sec. 9). The T2K near detector is used as a muon range detector (MRD), which detects muons from the neutrino interactions in the ECC to identify the CC interactions. The emulsion accumulates all the tracks after the production of the films without any timing information, whereas the MRD records the tracks with timing information. The position and angular resolutions of the MRD are not sufficient to identify corresponding tracks between the ECC and the MRD. Therefore, another device was installed between them and used for timestamping. Using the ECC, the MRD, and the timestamping device, we measure CC neutrino interactions on water.

4.2 Nuclear emulsion

Since the nuclear emulsion film is often used in photography, it is also referred to as a photographic film. The nuclear emulsion is sensitive to charged particles, and these tracks appear on the film after a development process. Figure 4.2 shows a neutrino interaction occurring in the nuclear emulsion. Owing to the very high granularity of the nuclear emulsion, it can record short tracks and measure the interaction vertices clearly.

The mechanism of the nuclear emulsion is shown in Fig. 4.3. An emulsion film is a plastic base film coated with emulsion gel on both surfaces. The plastic base and the single emulsion gel layer are around 200-μm and 70-μm thicks, respectively. The emulsion gel is made of gelatin in which silver bromide (AgBr) crystals are doped. Charged particles passing through the nuclear emulsion generate electrons, and these electrons are collected

at the surface of the AgBr crystals. Then the sensitive nucleus gets negatively charged, and silver atoms are created by deoxidizing neighboring silver ions. Several silver atoms, typically more than four, form a latent image, and all the silver ions in the AgBr crystal are deoxidized to form a grain by the development process. Although the typical size of the AgBr crystal is about 0.2 μm, the position resolution of the emulsion films is around 0.4 μm due to the precision of a microscope that scans the tracks on the emulsion films. The angular resolution of the emulsion films depends on the track angle, and it is typically 2 mrad for the tracks perpendicular to the films. Details of the track reconstruction of the emulsion films are described in Sec. 6.1.

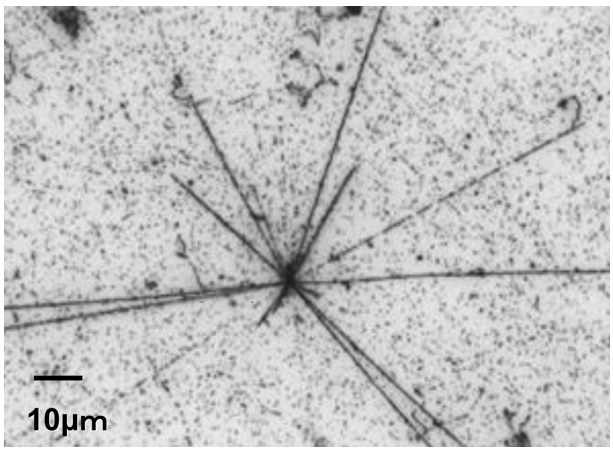

Figure 4.2: Microscopic view of a neutrino interaction on a nuclear emulsion film. Owing to the very high-granularity of the emulsion, tracks shorter than 100 μm can be detected clearly.

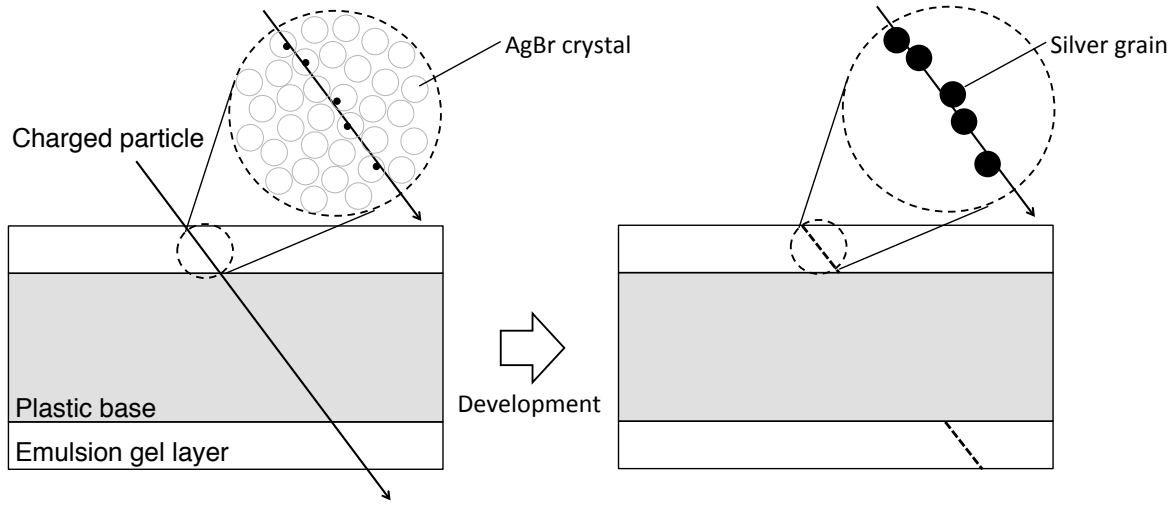

Figure 4.3: Mechanism of the nuclear emulsion film. Charged particles passing through the nuclear emulsion generate a latent image, and all the silver ions in the AgBr crystal are deoxidized to form a grain by the development process.

4.3 Overview of the NINJA pilot run

A series of pilot experiments has been carried out since 2014. In 2014 and 2015, a 2-kg iron-target ECC was exposed to the neutrino and antineutrino mode beams. An emulsion shifter [129] was used as a timestamping device. The first detection of neutrino interactions by the ECC was achieved using the T2K neutrino beam, and the results were summarized in Ref. [130]. In 2016, a 60-kg iron-target was exposed to the neutrino and antineutrino mode beams. The inclusive cross section of the neutrino interactions on an iron target was measured and summarized in Ref. [131]. Then, in 2017 and 2018, a measurement of neutrino interactions using a 3-kg water-target ECC was carried out. This water-target pilot run is the main theme of this thesis. Results of this measurement were published in Ref. [132].

The water-target pilot run is the first measurement to detect neutrino interactions on water in NINJA. The experimental site is shown in Fig. 4.4, and one of the INGRID modules is used as the MRD. In the following sections, detectors used in the pilot run are described as well as their data taking results.

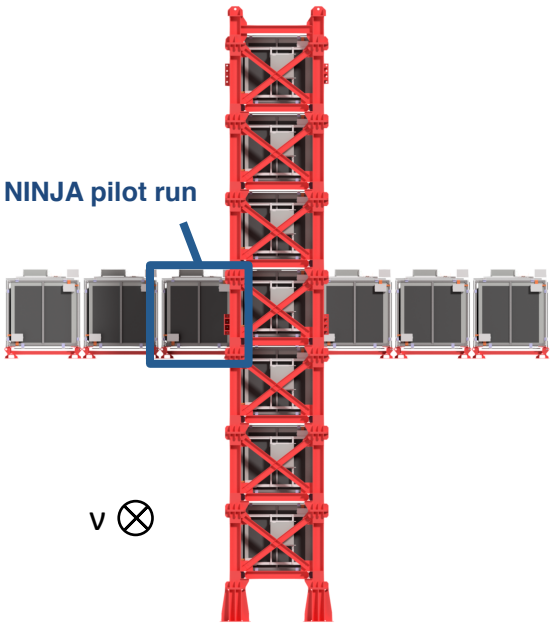

Figure 4.4: Experimental site of the NINJA pilot run. We use one of the INGRID modules next to the central one as an MRD.

4.4 Detector configuration

Figure 4.5 shows a schematic view and a photo of the detectors after the installation. The main detector is the water-target ECC, which records all the charged particles from the neutrino interactions. The ECC was placed upstream of an INGRID module. INGRID is used as an MRD, and it detects muons from the neutrino interactions occurring in the ECC. The emulsion films do not have timing information, and the angular and position resolutions of INGRID are not enough to identify corresponding tracks between the ECC

and INGRID. Thus Scintillating Fiber Tracker (SFT) was newly developed and installed between them as a timestamping device. The ECC and the SFT were placed in a shelter with a cooling unit to maintain the temperature at around 10°C and the humidity below 60%. The cooling shelter prevents the emulsion tracks from fading under high temperature and humidity. It also prevents the emulsion films from warping due to fluctuations in the ambient temperature.

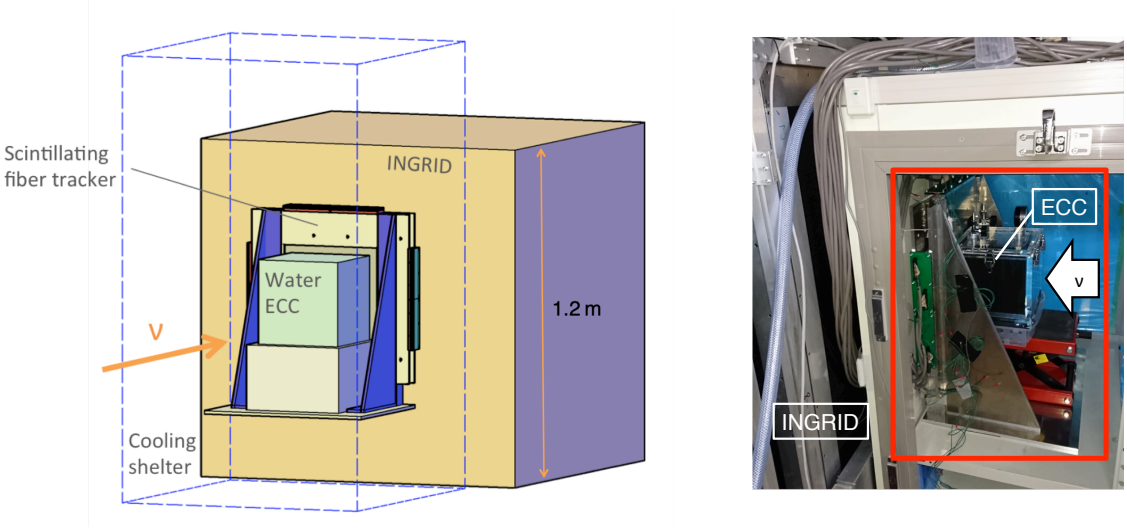

Figure 4.5: Schematic view (left) and a photo (right) of the NINJA detector. ECC and SFT are installed in a cooling shelter, which is placed in front of an INGRID module.

4.4.1 ECC

The ECC is an emulsion-based detector composed of alternating layers of emulsion films and target materials. The target materials and their thickness can be optimized flexibly. Moreover, the alternating structure of the emulsion films and the thin target layers enables us to achieve a low momentum threshold. NINJA is the first emulsion experiment using water as the target of the ECC. The structure of the water-target ECC is shown in Fig. 4.6. The main components of the ECC are placed in a commercial desiccator, which is constructed with 2- cm-thick walls and has inner dimensions of 21 cm × 21 cm × 21 cm.

Two emulsion films and a 500-μm-thick iron plate are vacuum-packed in a 115-μm-thick packing film, as shown in Fig. 4.7. This structure is referred to as a tracking layer, in which the iron plate is sandwiched by the two emulsion films. These iron plates are employed as supporting structures for the emulsion films and also used for the momentum measurement described in Sec. 7. The tracking layers are placed at 2-mm intervals by inserting acrylic frames with a hollow square shape between them. The desiccator is filled with pure water, and 2-mm water layers are formed inside the acrylic frames. Thus, charged particles from neutrino interactions occurring in the water layers leave tracks on the neighboring emulsion films. As the tracks are required to pass through at least one tracking layer in the reconstruction, the momentum threshold for proton tracks is about 200 MeV/c, while that for pions is around 50 MeV/c.

An iron ECC, which consists of five iron plates and six emulsion films, is placed downstream of the water region to measure the momentum of the charged particles using

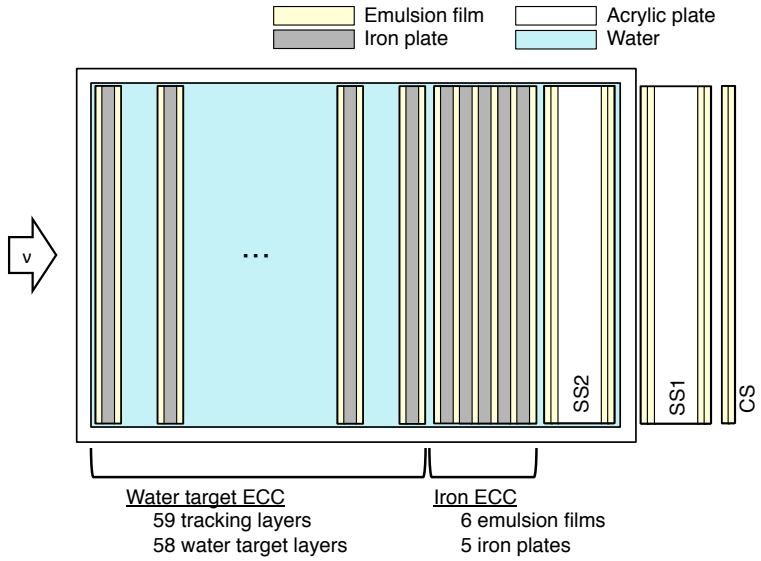

Figure 4.6: Structure of a water-target ECC. The upstream part has alternating layers of 2-mm water layers and tracking layers. A tracking layer has an iron plate and two emulsion films. Charged particles from neutrino interactions in water layers make tracks on the emulsion films. The downstream part consists of an iron ECC, two sets of special sheets (SS1, SS2), and one changeable sheet (CS).

the multiple Coulomb scattering. In addition, two sets of special sheets (SSs) and one changeable sheet (CS) are installed in the most downstream region. SS1 is placed outside the desiccator, while SS2 is inside it. As shown in Fig. 4.7, each SS has four emulsion films with a 2-mm-thick acrylic plate inserted between pairs of the emulsion films. This structure is used to measure the track angle with a good resolution. The CS contains two emulsion films, and they are replaced every month to separate the tracks into several time periods.

Figure 4.8 shows photographs of the ECC construction. After packing the emulsion films at Nagoya University, all the components were transferred to J-PARC. The ECC was constructed just before the installation to prevent the cosmic ray tracks from being accumulated.

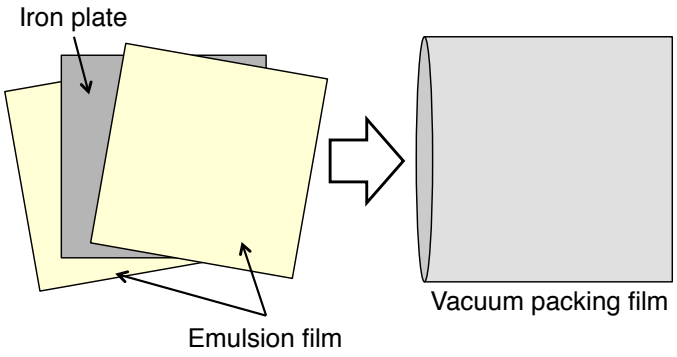

Figure 4.7: Structure of a tracking layer. Two emulsion films and a 500-μm iron plate are vacuum-packed using a 115-μm thick packing film.

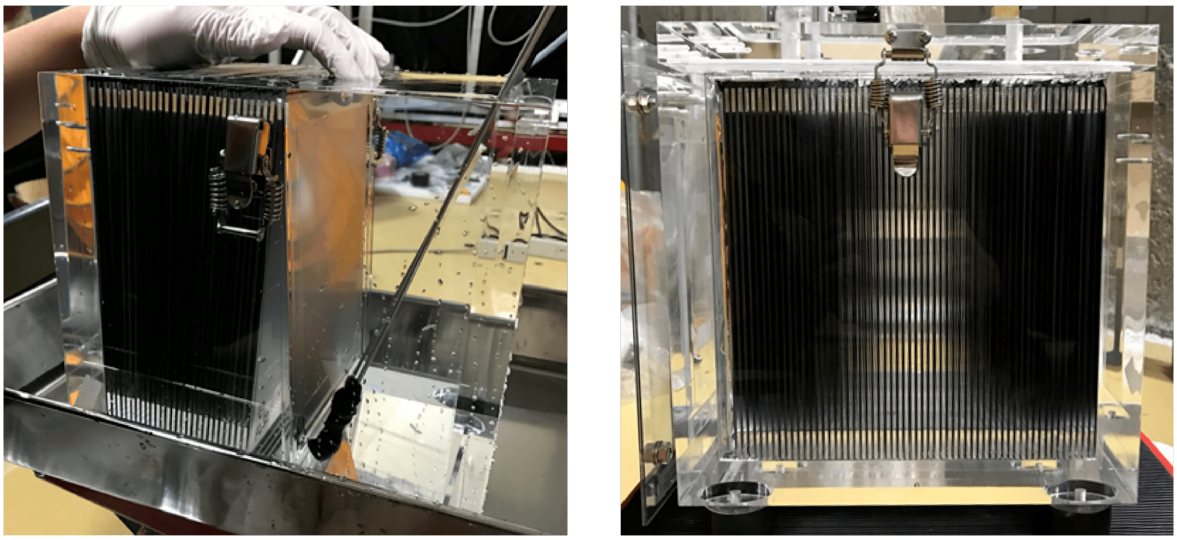

Figure 4.8: Photographs of construction of the ECC (left) and the constructed ECC (right).

4.4.2 SFT

Whereas the emulsion detectors have excellent angular and position resolutions, they do not provide any time information. For track matching between the ECC and INGRID, another device providing both time and precise position information is required because the angular and position resolutions of INGRID are poor to select a track candidate in the ECC to be connected to an INGRID track. In some cases, emulsion shifters [129, 133] are used to give timestamps to tracks in the ECC. The emulsion shifter consists of several moving walls, on which emulsion films are mounted. These walls move in different cycles, thus they give time information similar to a clock's long and shorthand. However, in this pilot run, we employed the SFT as a timestamping device because it can provide more precise time information than the emulsion shifter. The SFT is installed behind the ECC, as shown in Fig. 4.9.

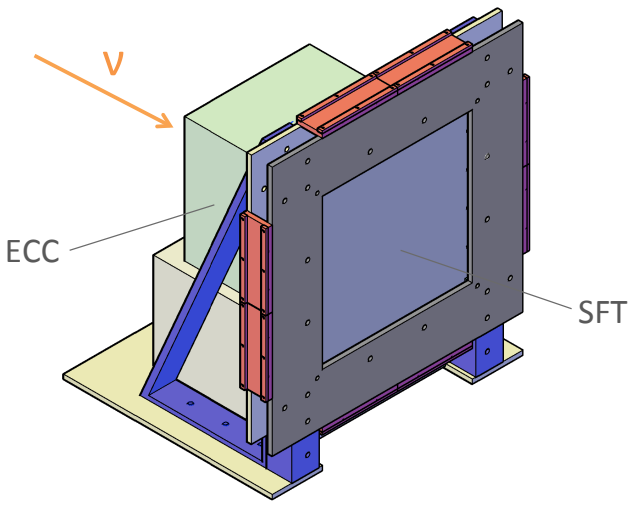

Figure 4.9: Schematic view of the SFT.

Scintillating fiber trackers have been used in several experiments as timestamping devices together with nuclear emulsion detectors since they can provide time information and achieve excellent position and angular resolutions by using the fine cross-sectional size of the fibers. However, the number of readout channels usually becomes enormous. Therefore, we tried a new idea, which helps us to achieve a better position resolution without reducing the cross-sectional size of the fibers.

Figure 4.10 shows the concept of our SFT. By arranging square fibers in a slanting lattice pattern, we can obtain a precise track position from the ratio of the light yields at neighboring fibers. Since the light yield at each fiber is proportional to the path length of a charged particle, the ratio of the light yields changes with the position of the particle. Assuming that the charged particle passes through perpendicular to the fiber plane, track position d is predicted as

$$d = \frac{N_1}{N_1 + N_2} R, \tag{4.1}$$

where R is the fiber interval, N_1 and N_2 are light yields at each fiber. Considering only the statistical fluctuation of the light yield, the expected position resolution is proportional to $1/\sqrt{N_1 + N_2}$ when the light yield ratio is used. Thus, a position resolution better than the typical $A/\sqrt{12}$ can be obtained with the same number of fibers, where A is the fiber cross-sectional size. The position resolution is degraded as the injection angle of the particle increases. However, this effect is not significant for the muons from the neutrino interactions in the ECC. This is because more than 95% of them are emitted forward below 30 degrees, where the resolution is kept good enough. The performance of the SFT is described in Sec. 6.4.

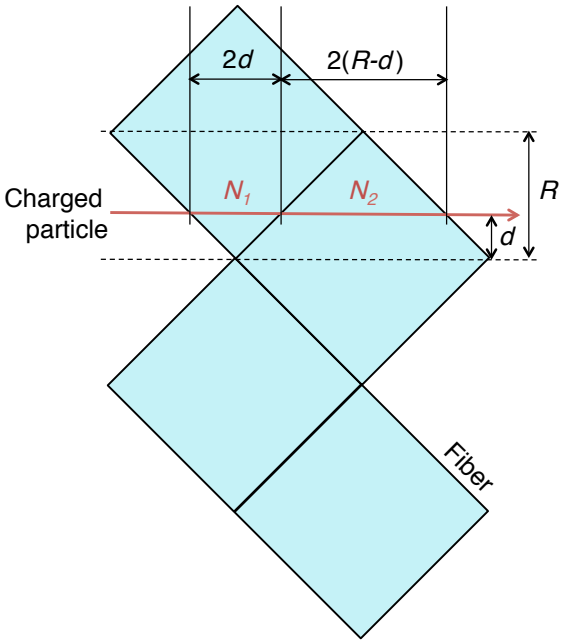

Figure 4.10: Concept of the position measurement using square fibers. The ratio of the light yields at neighboring fibers gives precise position information. Light yields of the fibers are denoted by N_1 and N_2, the fiber interval is written as R, and d is the true hit position.

In this pilot run, 1-mm square scintillating fibers (Kuraray SCSF-78) are used [134]. Figure 4.11 shows a schematic cross-sectional view of the square fiber, and Tab. 4.1 summarizes the specifications. The core of the fiber made of polystyrene is excited by the energy deposit of charged particles, and scintillation light (∼300 nm) is emitted. The scintillation light is absorbed by a fluorescent dye doped in the core, and light with a longer wavelength is emitted. Fibers with two types of fluorescent dyes are widely used for scintillating fibers, and the wavelength is shifted twice with the primary and the secondary dyes. The emission spectrum has a peak of around 450 nm. As described later, this wavelength is well-matched with the sensitive wavelength of the MPPCs we use. A part of the emitted light is propagated within the fiber by total internal reflection. Cladding is used to increase the light trapping efficiency of the fiber by reducing the refraction index between the fiber and the air. Only single cladding fiber is available for the square fiber, and the trapping efficiency is around 4% (cf. a double-cladding round fiber has a 5% trapping efficiency). We did not put any reflector on the fibers, because it will increase the insensitive area and make it hard to align the fibers with good accuracy. The attenuation length of the fiber is more than 2.5 m, thus it is negligible in this SFT.

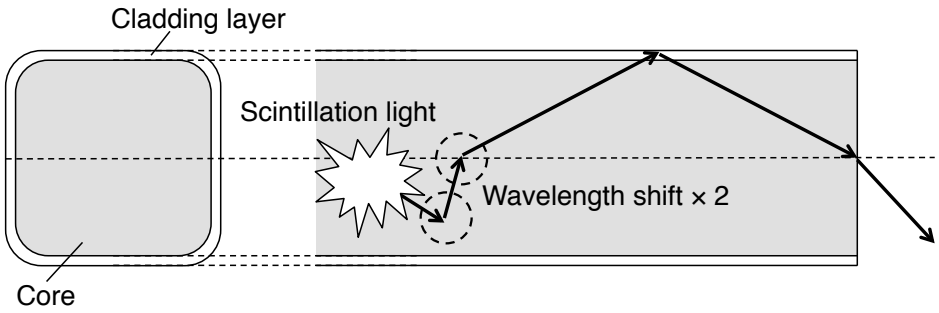

Figure 4.11: Schematic view of a square scintillating fiber. The core of the fiber made of polystyrene is excited by the energy deposit of charged particles, and scintillation light is emitted. The scintillation light is absorbed by a fluorescent dye doped in the core, and the wavelength is shifted twice with the primary and the secondary dyes. A part of the emitted light is propagated within the fiber by total internal reflection.

Table 4.1: Specifications of the scintillating fiber (SCSF-78) [134]

Core	Polystyrene (n=1.59)
Clad	PMMA (n=1.49)
Emission peak	450 nm
Decay time	2.8 ns
Attenuation length	∼2.5 m

The fibers are aligned in 0.725-mm intervals to cover an area of 37 cm × 37 cm. Figure 4.12 shows the structure of aluminum plates on which fibers are aligned. The fibers are glued on the grooved aluminum plates, and two plates make one layer. A horizontal layer and a vertical layer are constructed, and each layer consists of 512 fibers.

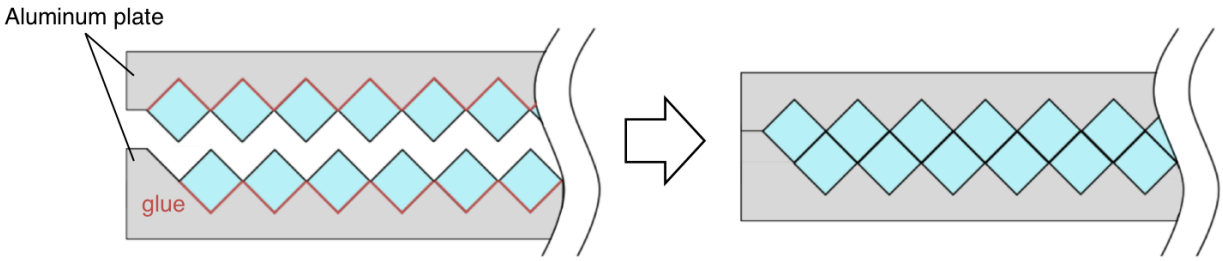

Figure 4.12: Structure of the fiber plate. Fibers are aligned on grooved aluminum plates. Assembling two plates makes a zig-zag structure.

MPPC [135] is a photon-counting silicon sensor using multiple Avalanche Photo-diodes (APDs) operated in Geiger mode. The charge yield of the MPPC has a linear correlation with the number of pixels in which photoelectrons are produced. This leads to an excellent photon-counting capability of the MPPC, thus it suits the position reconstructing method of our SFT. Hamamatsu 16-channel MPPC arrays (S13361-3050AE-04) are employed for the readout of the scintillation light. One MPPC array has 16 MPPCs, and each channel has a 3 mm × 3 mm surface area. Figure 4.13 shows the photograph of the MPPC array and the spectrum of the photon detection efficiency. Table 4.2 summarizes the specification of the MPPC array. The peak wavelength (∼460 nm) is well-matched with the emission spectrum of the scintillating fiber (∼450 nm).

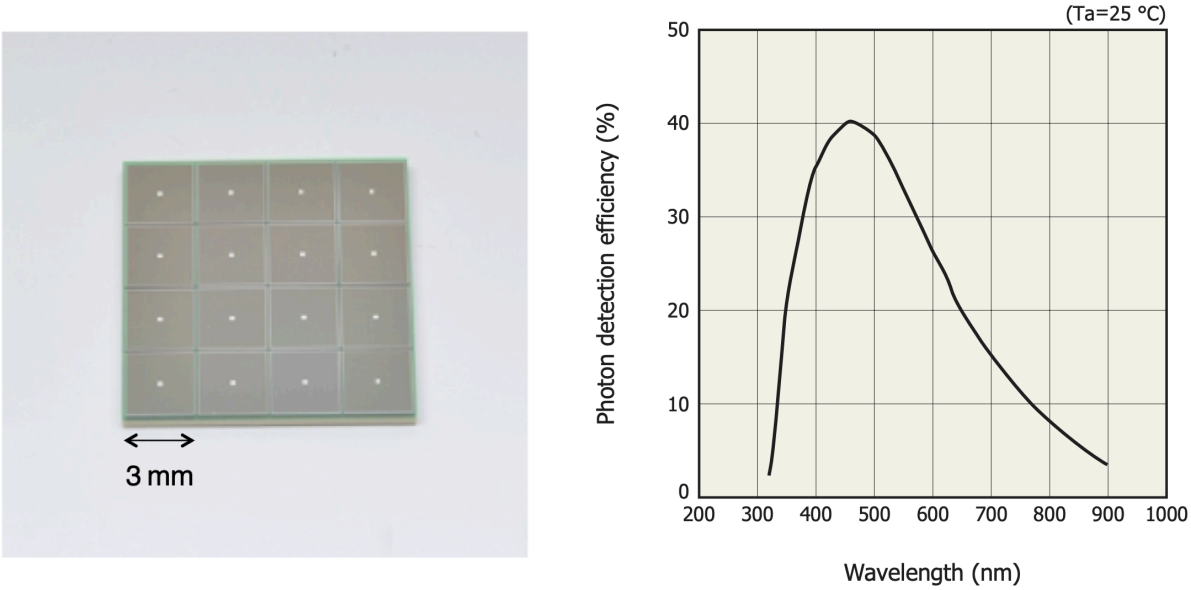

Figure 4.13: Photograph of the MPPC array (left) and the photon detection efficiency as a function of the wavelength (right) [135].

A general MPPC readout module, NIM EASIROC [136], is used as readout electronics. One module can operate 64 MPPCs at once. Thus, eight modules are used for the SFT readout. Figure 4.14 shows a diagram of the trigger timing for the SFT data acquisition. A beam window is produced by a beam trigger which comes 31 μs before the expected neutrino arrival timing. In EASIROC, the signal is divided into slow and fast shapers.

Table 4.2: Specifications of the MPPC array (S13361-3050AE-04) [135]

Number of channels	16 (4×4)
Effective photosensitive area/channel	3 mm × 3 mm
Pixel pitch	50 μm
Number of pixels	3584
Peak sensitivity wavelength	450 nm
Photon detection efficiency	∼40%
Breakdown voltage	53±5 V
Dark count (25°C, typical)	0.5 MHz (0.5 p.e. threshold)

The pulse height of the slow shaper signal is held by a hold signal, which is generated by a coincidence of the fast shaper signals made by hits in the horizontal and vertical layers of the SFT. In this pilot run, only one event per one spill was recorded by the SFT without timing information inside the spill. Therefore, only hits induced by the first track were recorded even if there were several tracks in a spill. For this reason, a veto signal is generated right after the hold signal. If there are no hits in a bunch, a dummy trigger created from the beam trigger makes a fake record, in which pedestals of all the channels are recorded.

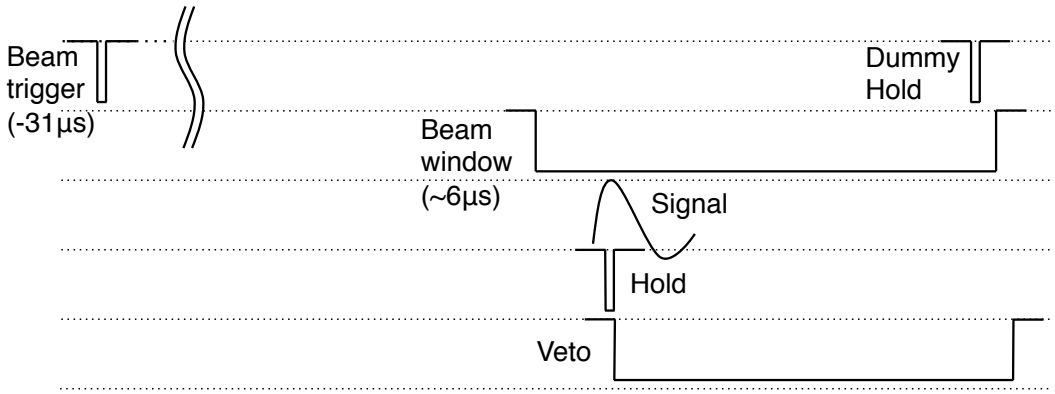

Figure 4.14: Diagram of signal timing for the SFT data acquisition. A beam window is produced by a beam trigger which comes 31 μs before the expected neutrino arrival timing. A hold signal is generated by a coincidence of the fast shaper signals made by hits in the horizontal and vertical layers of the SFT, and right after the hold signal, a veto signal is generated. This is because our DAQ system can record only one data per one spill. If there are no hits in a bunch, a dummy trigger produced from the beam trigger makes a fake record, in which pedestals of all the channels are recorded.

To reduce the number of readout channels, one MPPC reads out four fiber signals, and the signals are read out from both ends of the fibers. As the combinations of the four fibers at the two ends are different, we can identify the hit fibers. Therefore, the total number of readout channels is 512, while the total number of fibers is 1024.

4.5 Data taking

There are two periods of beam exposure during T2K Run9. The first period (Run-a) is from October to December 2017, and the second (Run-b) is from March to May 2018. Both runs are separated into three periods corresponding to different CS films, and each period is roughly one month. Table 4.3 summarizes POT delivered from the J-PARC accelerator and POT recorded by the NINJA detector in each CS period, and Fig. 4.15 shows the accumulated POT. The total POT with both the SFT and INGRID are operating is 7.1×10^{20} POT. The following analysis is performed with this data.

Table 4.3: Summary of the accumulated POT.

Run-a	Period	Recorded (10^{20})	Delivered (10^{20})
CS12	2017/10/12-10/22 (neutrino mode)	0	0.21
CS34	2017/10/22-11/22	0.52	1.53
CS56	2017/11/22-12/22	1.43	2.20
Run-b	Period	Recorded (10^{20})	Delivered (10^{20})
CS12	2018/3/5-4/10	2.07	2.08
CS34	2018/4/10-5/10	1.85	1.86
CS56	2018/5/10-5/31	1.21	1.21
total		7.09	9.10

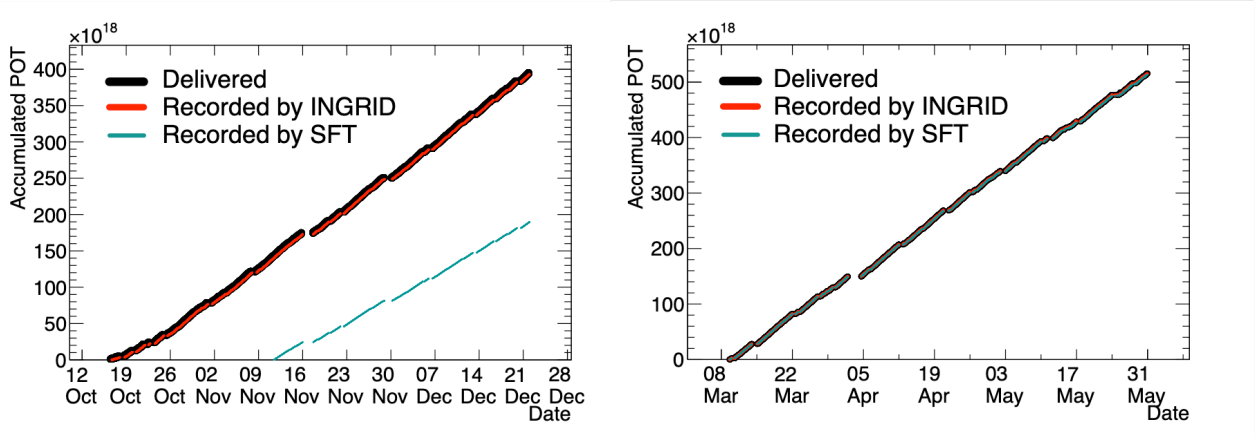

Figure 4.15: Accumulated POT history of INGRID and the SFT in Run-a (left) and Run-b (right) periods.

The operation of INGRID was stable, and the data taking efficiency was more than 99.8%. The SFT was also operated stably, but it started working around one month after the beginning of the beam exposure. The neutrino mode beam was delivered only before the SFT operation, thus only the antineutrino mode data were used for the analysis. In addition, there was an issue of the SFT trigger timing in Run-a. The seventh and eighth bunches were not recorded, because the timing of the beam window was $\sim 1\,\mu$s earlier than expected. This is why the recorded POT in the Run-a period is smaller than the delivered POT. Small differences in the delivered and the recorded POT in the Run-b period mainly come from the DAQ run exchange of the SFT. Figure 4.16 shows the daily

event rate recorded by the SFT normalized by the recorded POT. Most of the hits are induced by the sand muons. The daily event rate is obtained from the recorded POT and the number of SFT hits, which have at least one MPPC channel with 2.5 photoelectrons (p.e.) in both layers. The daily event rates in both periods are consistent within the statistical uncertainty, and they are also consistent with the sand muon rate measured by INGRID.

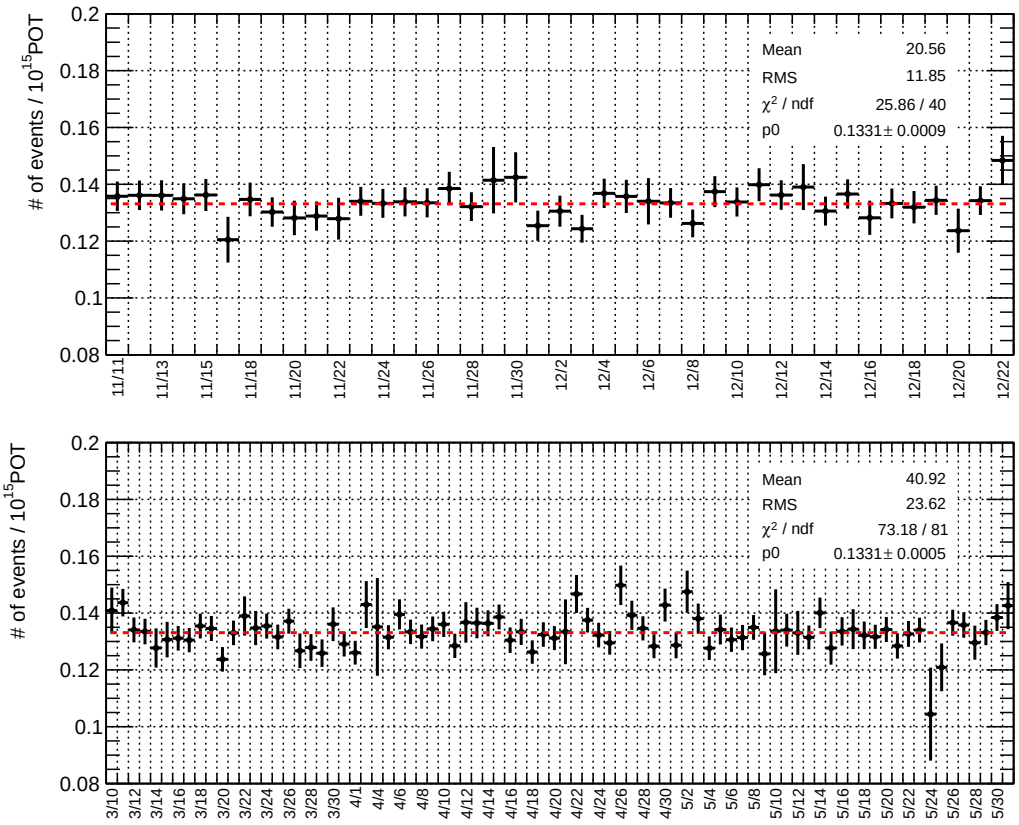

Figure 4.16: Event rate of the SFT hits. Run-a (top) and Run-b (bottom) periods are shown. The daily event rate was stable during the operation period.

Figure 4.17 shows the stabilities of the temperature and humidity inside the cooling shelter during the beam exposure. Spikes in the temperature plots correspond to the periods in which the door of the cooling shelter was open for hardware works during beam-off periods. The daily spikes in the humidity plots are the defrosting operation of the cooling unit, and these spikes do not affect the data quality of the emulsion films.

4.6 Goal of the pilot run analysis

In the following chapters, neutrino interactions on the water are measured using the detectors introduced above. Multiplicity, angular, and momentum distributions of the outgoing charged particles from the neutrino-water interactions are reported. Since it was an antineutrino mode dataset, about 25% of all the recorded interactions are ν_μ interactions in the antineutrino mode beam. Thus, our signal is defined as charged-current $\overline{\nu}_\mu$ and ν_μ inclusive interactions. As the outgoing particles, we consider muons,

charged pions, and protons. The muons are identified by matching tracks between the ECC and INGRID. The angle and momentum of each outgoing particle are measured by the ECC using its excellent resolutions. In this thesis, a measurement of protons from the neutrino-water interaction in the 200–400 MeV/c region is reported for the first time in measurements of neutrino-water interactions.

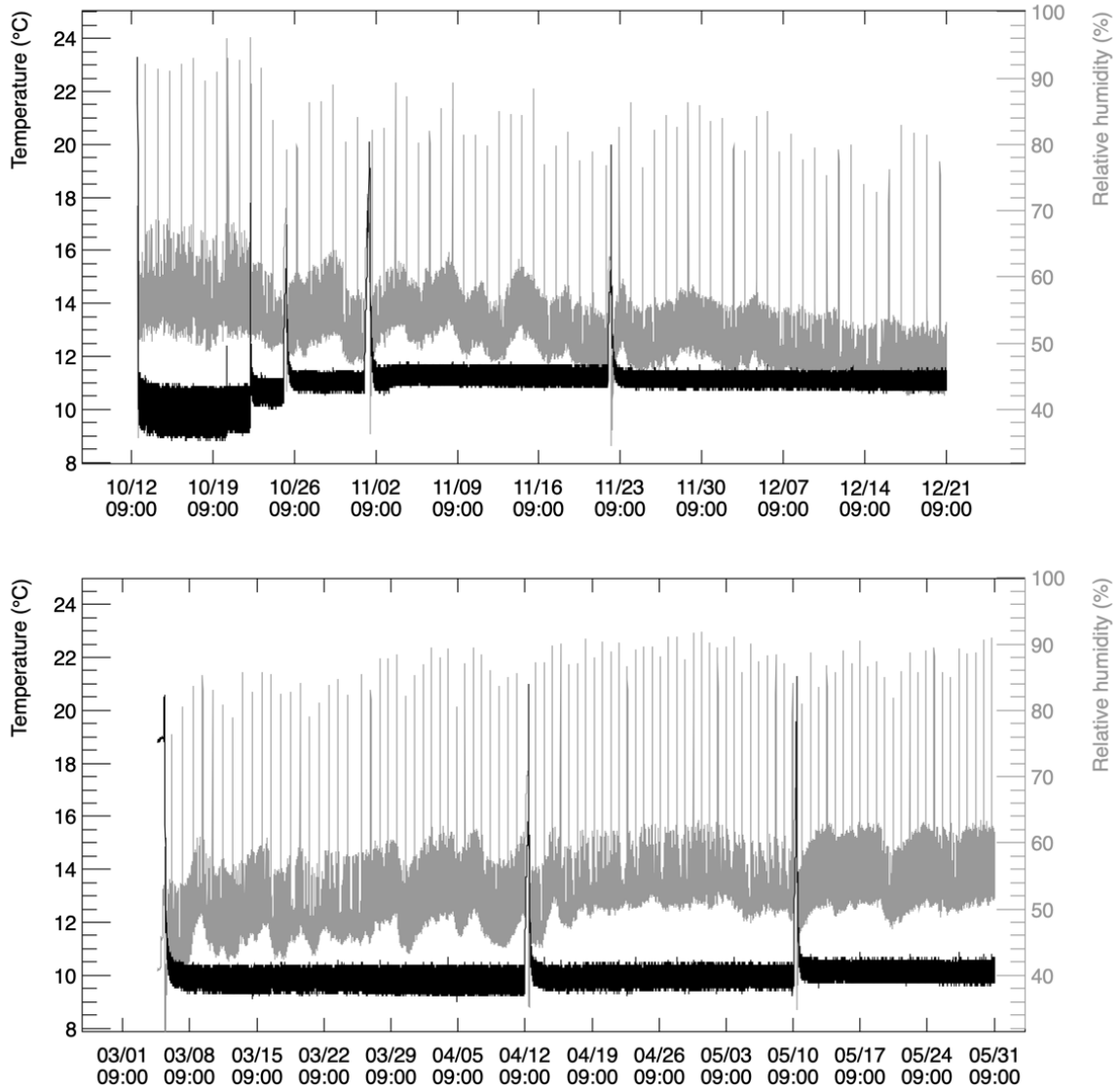

Figure 4.17: Stabilities of the temperature and humidity inside the cooling shelter during Run-a (top) and Run-b (bottom) periods. Spikes in the temperature plots correspond to the door-opening for several hardware works during beam-off periods. The daily spikes in the humidity plots are defrosting operation of the cooling unit, and those spikes do not affect the data quality of the emulsion films.

Chapter 5

Monte Carlo simulation

The expected signals and backgrounds are generated by Monte Carlo (MC) simulations. Figure 5.1 shows an overview of the MC simulation. Three software packages are used: JNUBEAM [137] for the simulation of the neutrino flux, NEUT [81] for the neutrino-nucleus interactions, and a Geant4 [138] based framework for the simulation of the detector response. In this analysis, we generated $\overline{\nu}_\mu$ and ν_μ interactions on H_2O and Fe in the antineutrino mode beam by JNUBEAM and NEUT. Since $\overline{\nu}_e$ and ν_e components of the flux are less than 1%, $\overline{\nu}_e$ and ν_e interactions in the ECC are not simulated. In the pilot run analysis, the MC predictions are normalized by POT and corrected by the detector efficiencies estimated using the true data and the MC data.

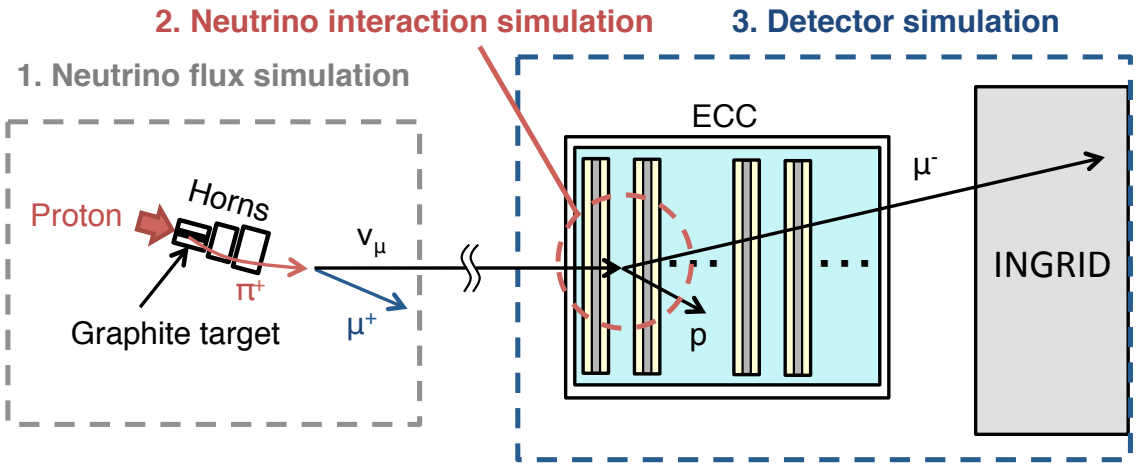

Figure 5.1: Overview of the Monte Carlo simulation. JNUBEAM [137] for the neutrino flux simulation, NEUT [81] for the neutrino-nucleus interactions, and a Geant4 [138] based framework for the simulation of the detector response are used to produce the signal and background MC data.

5.1 Neutrino flux prediction

JNUBEAM is a GEANT3 [139] based neutrino flux simulator developed by T2K. Interactions of the primary protons from the accelerator hitting the graphite target are simulated by FLUKA2011.2 [140, 141], and secondary particles are generated. JNUBEAM

simulates the propagation, interaction, and decay of these secondary particles transferred from FLUKA. Neutrinos are generated from the decay of the hadrons. The hadron interactions are tuned by external measurements of hadron production, such as CERN NA61/SHINE [73–75]. Most pions exiting the graphite target are tuned by their 2009 data taken with a T2K replica target [76]. Figure 5.2 shows the predicted flux in the antineutrino mode at the location of the NINJA detector. The mean energy of the $\overline{\nu}_\mu$ component is 1.3 GeV, and that of the ν_μ component is 2.0 GeV. The fraction of $\overline{\nu}_\mu$ (ν_μ) in the antineutrino mode is 92.5% (6.7%), and the fractions of ν_e and $\overline{\nu}_e$ are less than 1%.

Figure 5.3 shows the total flux uncertainties of the $\overline{\nu}_\mu$ and ν_μ components in the antineutrino beam mode. Although the NA61/SHINE measurements significantly reduce the uncertainty on the hadron production at the target, it is the current dominant uncertainty source. There are also uncertainties in the proton beam and the beamline, such as the proton beam profile used as an input to the simulation, fluctuation in the horn current, imperfection of geometrical modeling in the simulation, and the total number of protons incident on the graphite target.

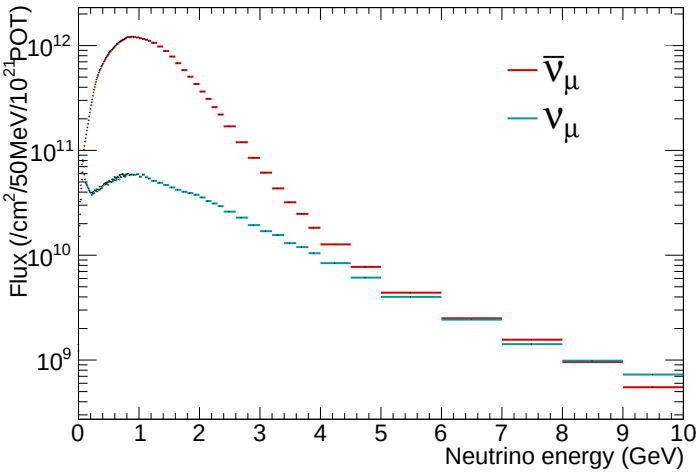

Figure 5.2: Predicted $\overline{\nu}_\mu$ and ν_μ fluxes in the antineutrino mode beam at the location of the NINJA detector.

5.2 Neutrino interaction prediction

The neutrino flux calculated by JNUBEAM is transferred to NEUT to generate $\overline{\nu}_\mu$ and ν_μ interactions on H_2O and Fe targets. Besides, neutrino interactions in the upstream wall and INGRID are generated as background sources. Table 5.1 summarizes the neutrino interaction models used in this analysis, and the details of the models were introduced in Sec. 3. The nominal MC predictions are generated using NEUT version 5.4.0. We use the 1p1h model by Nieves *et al.* with correction by random-phase approximation (RPA) [142, 143] for the CCQE interactions. The axial vector mass M_A^{QE} is set to 1.05 GeV/c^2. The LFG model is employed as the default nuclear model, while the SF model is prepared as an alternative model. For the 2p2h interactions, the model by Nieves *et al.* [100] is used. The resonant pion production is modeled by the Rein-Sehgal model [88], and the

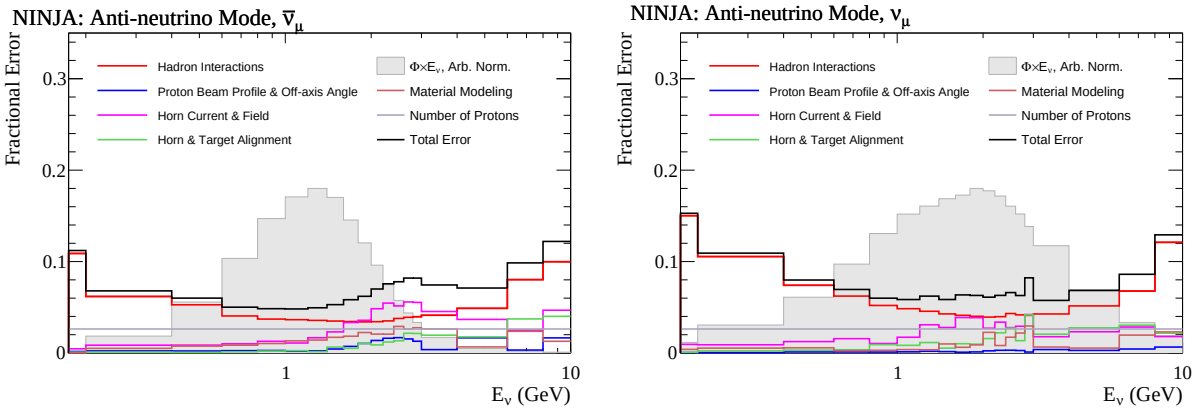

Figure 5.3: Flux uncertainty at the NINJA detector. The gray histograms correspond to fluxes in an arbitrary normalization. The $\overline{\nu}_\mu$ (left) and ν_μ (right) components in anti-neutrino beam mode are shown.

Table 5.1: Neutrino interaction models used in the nominal MC simulation.

Mode	Model
CCQE	Nieves 1p1h [142]
	LFG with the RPA correction (M_A^{QE}=1.05 GeV/c^2)
2p2h	Nieves *et al.* [100]
CCRES	Rein-Sehgal [88] (M_A^{RES}=0.95 GeV/c^2)
Coherent π	Barger-Sehgal [94]
DIS	GRV98 PDF with Bodek-Yang modifications [97]
FSI	Semiclassical intranuclear cascade model [81]

axial mass M_A^{RES} is set to 0.95 GeV/c^2. The Barger-Sehgal model [94] is used for the coherent pion production, and the deep inelastic scattering (DIS) is described by the parton distribution function GRV98 and a cross-section model modified by Bodek and Yang [97]. A semiclassical intranuclear cascade model [81] is used to simulate the final state interactions (FSI) in the nuclear medium. Samples with other parameters are studied to compare and to evaluate the size of the systematic error as described in Sec. 8.2.

Uncertainties on the neutrino interaction and FSI models in the pilot run analysis are based on Ref. [144] and are described in Sec. 8.2. However, the models and their uncertainties are updated year by year. Thus, we use the latest models and uncertainties used in Ref. [30] in the studies described in Sec. 10, and the detail of these models are described in Appendix F.

5.3 Detector simulation

The behavior of the particles from the neutrino interactions is simulated by a Geant4-based detector MC framework. This framework was originally developed for INGRID, and it was updated for the NINJA pilot run. Figure 5.4 shows the NINJA detector, INGRID, and the wall of the detector hall constructed in the GEANT4 framework. Position

(x, y, z), angle (tanθ_x, tanθ_y), momentum, and energy deposit at each emulsion film are recorded. On the other hand, the scintillating fibers of the SFT are constructed as polystyrene sheets, and the hit information of the SFT is not recorded for simplification. All the matching efficiencies are estimated from the sand muon data, and the estimated efficiencies are used to give weights to the events in the MC simulation.

In the Geant4 framework, QGSP BERT [145] is used as the default physics list. Muons, charged pions, and protons from the neutrino interactions generated by NEUT and their secondary particles are simulated. In addition to the neutrino interactions in the ECC, we also generate interactions in the INGRID modules and the upstream wall of the detector hall for the background study. The background from cosmic rays is evaluated using the track data in the off-beam timing instead of using the MC simulation.

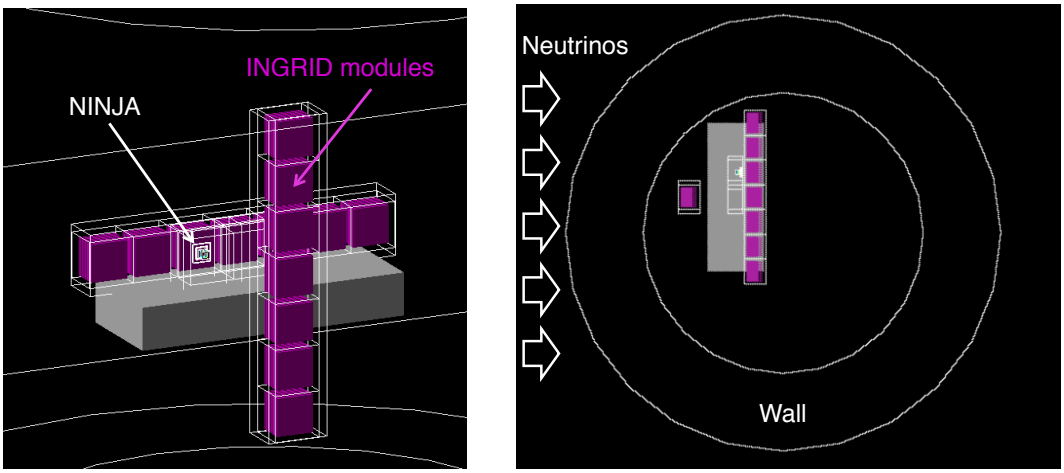

Figure 5.4: NINJA detector, INGRID, and the wall of the detector hall constructed in the GEANT4 framework

5.4 Summary of the MC simulation

Table 5.2 summarizes the signal and the backgrounds generated in the MC simulation. All the MC data are processed through the Geant4 simulation. The MC predictions are normalized by the recorded POT, and they are also corrected by the detector efficiencies, except for the interactions in the upstream wall.

Table 5.2: Signal and backgrounds generated in the MC simulation. The target material of the upstream wall is assumed as water instead of concrete and soil for simplification.

	Target	Flavor	Normalization
Interactions in the ECC			
	water	$\overline{\nu}_\mu$, ν_μ	POT, efficiency
	iron	$\overline{\nu}_\mu$, ν_μ	POT, efficiency
Background			
Upstream wall	water	$\overline{\nu}_\mu$, ν_μ	Number of sand muons in the real data
INGRID modules	iron	$\overline{\nu}_\mu$, ν_μ	POT, efficiency

Chapter 6

Event reconstruction

For the reconstruction of the neutrino interactions, track reconstructions in the ECC and INGRID, as well as hit position reconstruction at the SFT, are carried out first. After that, track matching between all the detectors enables us to reconstruct the neutrino interactions using the whole NINJA detector.

6.1 Track reconstruction in the ECC

In this section, film treatments such as development are introduced. Then, we describe scanning and reconstruction of the tracks in the films.

6.1.1 Emulsion film treatments before scanning

After the beam exposure, the following procedures were applied before scanning the films by a microscope.

Development

Development of the emulsion films was carried out at Nihon University. In a light-tight room, the films were unpacked from the vacuum packing and put into a solution for the development. While being put in the developing solution, silver ions in the AgBr crystals are deoxidized. Silver latent images, which were made by the energy deposits of charged particles, absorb the deoxidized silver ions to form silver grains. The silver grains grow large enough to be observed by microscopes. The growing of the silver grains is stopped by putting the films into an acid solution to prevent the growing of noise grains induced by random chemical reactions. The rest of the AgBr crystals, which were not excited by the energy deposits of the charged particles, are eluted by a fixing procedure using a dedicated solution. After the fixing procedure, the emulsion films do not need to be treated in a dark environment. In the end, the films were put in running water to remove all remaining chemicals, then dried for a whole day. Typically, these processes are done within two or three days for the pilot run ECC ($\sim$150 films). The development process was carried out immediately after the beam exposure to prevent accumulating extra cosmic rays.

Removing extra surface silver

After the development, extra silver grains were deposited on the surface of the films. These films look black, and it affects the scanning process. Thus, both surfaces of the films were wiped out by tissues with ethanol.

Swelling

The film thickness became about half of that in the beam exposure by the developing because most AgBr crystals were removed during the fixing process. When the films are scanned by a microscope, this difference in thickness distorts the original angles of the tracks in the films. Thus the films were swelled and restored to their original thickness. In this procedure, the films were put in water for about one hour. After that, they were put in a glycerin solution to replace water with glycerin.

6.1.2 Scanning of the emulsion films

Hyper Track Selector (HTS) [146] at Nagoya University was used to scan the entire films of the pilot run. Figure 6.1 is a photo of HTS, in which optical systems and computer clusters are shown. For each emulsion gel layer, HTS takes 16 layers of images to detect silver grains by changing the focusing depth in the perpendicular direction to the film plane. These images are composed of pixels with their size of around 5 μm. Hit pixels are defined by binarizing the image, and if the hit pixels are detected in more than a certain number of layers (typically seven or eight out of the 16 layers) as shown in the Fig. 6.2 right figure, they are recognized as a track.

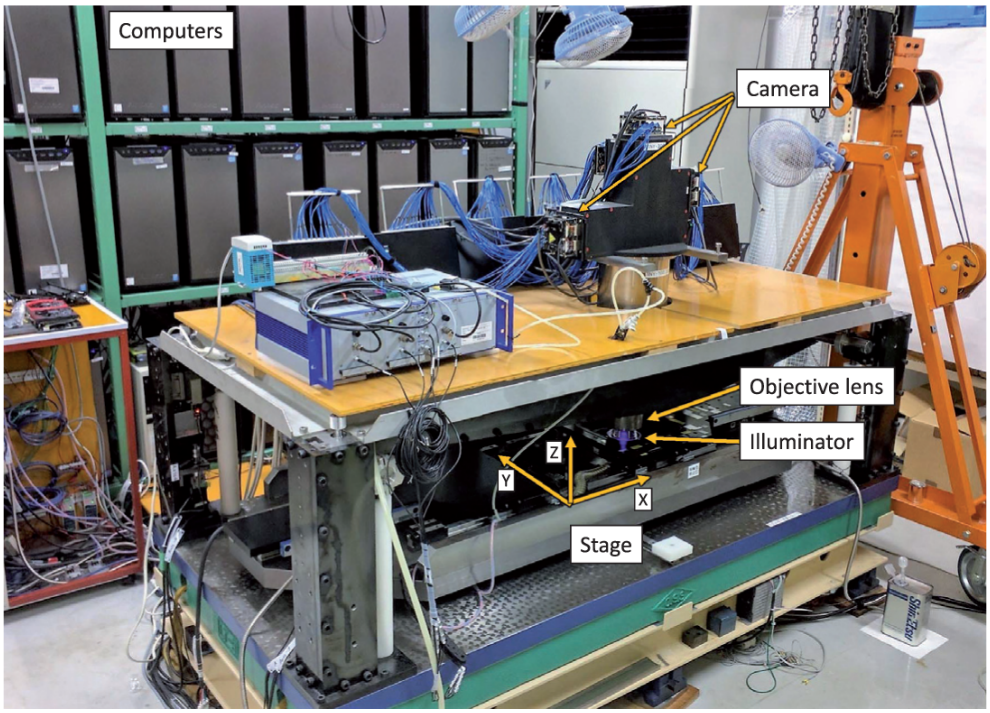

Figure 6.1: Hyper Track Selector (HTS) used for the scanning of the emulsion films [146].

A track on the emulsion gel layer is called a "microtrack." As shown in Fig. 6.2, the microtrack angle is obtained by shifting the 16 layers so that the hit pixels are aligned in the perpendicular direction to the film. The shifted distance d determines the track angle as $\tan\theta = d/L$ (L is the emulsion gel thickness) in x-z and y-z views. The scanned tracks are in the right-handed coordinates whose z-axis is perpendicular to the film. Thus, the z-axis is corresponding to the direction of the neutrino beam. The number of hit layers is defined as Pulse Height (PH), and the number of hit pixels summed over the 16 layers is defined as Volume Pulse Height (VPH). While the PH is used as the threshold of recognizing the tracks, the VPH is used as a parameter proportional to the energy deposit of the track.

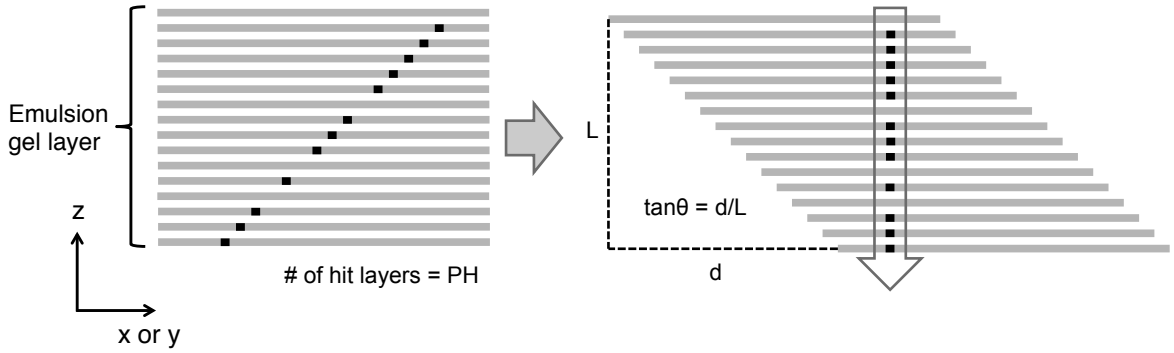

Figure 6.2: Track angle reconstruction of the emulsion films. The microtrack angle is obtained by shifting the 16 layers so that the hit pixels are aligned vertically.

After reconstructing the microtracks, a "basetrack" is formed from a pair of microtracks over the plastic base. Figure 6.3 shows the relation between a pair of microtracks and a basetrack, as well as their angles. The reconstruction is carried out automatically for each film using a process called "NETSCAN" [147]. This process is widely used in emulsion experiments. Pairs of microtracks within 20-μm positional differences are connected if the angular differences between $\tan\theta_{\mathrm{micro1}}$ and $\tan\theta_{\mathrm{micro2}}$ shown in Fig. 6.3 are within $0.04 + 0.12 \times |\tan\theta_{\mathrm{base}}|$. To reconstruct the basetrack angle (θ_{base}), the microtrack positions at the plastic base surfaces are used. This is because the plastic base is more solid than gel, thus we can obtain a better angular resolution using the basetrack angle. The angular resolution becomes worse if the microtrack angles are used because the thickness of the emulsion gel is affected by the environment of the development, swelling, and change in the temperature and humidity.

The basetracks require the microtracks on both sides of the film. Therefore, very low-momentum tracks induced by radioactive backgrounds are not reconstructed as the basetracks. The PH and VPH of a basetrack are the sums of those in two microtracks constituting the basetrack. Besides, to reduce the chance coincidence of the microtracks, a selection based on the VPH and the angular difference of a pair of microtracks is applied [148]. The detail of this selection is described in Appendix D.1. The microtrack angle of the pilot run is limited to $|\tan\theta_{\mathrm{micro}}| \lesssim 1.5$. Tracks satisfying $|\tan\theta_{\mathrm{micro}}| < 1.3$ are used in the analysis because the microtrack detection efficiency becomes low near the scanning angle limit. The track density is $\mathcal{O}(10^3)$ per cm^2, where the main components of the tracks in the emulsion films are cosmic rays and environmental radiations.

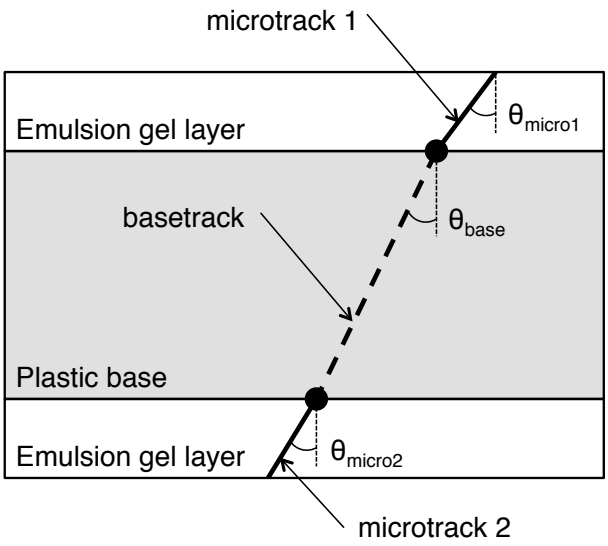

Figure 6.3: Definition of reconstructed tracks on a film. Microtracks are reconstructed on each side of films. Basetracks are formed by connecting two microtracks over the plastic base.

One scanning area covered by HTS is limited to about 10.0 cm × 12.5 cm at once, thus each film is separated into four scanning areas. Since many tracks escape from the edge of the scanning areas, an inter-area connection process is applied to all the films. There are overlapping areas between each scanning area, and the tracks in these areas are scanned and reconstructed twice. The relative positions of the overlapped areas are determined using these double-scanned tracks. After merging four areas, tracks within the 10-μm positional difference and the 100-mrad angular difference are considered the same track, and one of the tracks constituting the same track is put forward to the next step.

6.1.3 Track connection between the emulsion films

Following the track reconstruction in each film, a connection process between the films is applied. After the beam exposure, the emulsion films consisting of the ECC are disassembled into each film for the development and scanning. Thus, the relative positions and angles between the films during the beamtime need to be inferred from the positions and angles of the basetracks in each film. NETSCAN is also used for the emulsion track reconstruction over the films. The distance between the two films, positional shifts in the X and Y directions, shrink and rotation of the films are considered using affine transformation parameters:

$$\begin{pmatrix} x' \\ y' \end{pmatrix} = \begin{pmatrix} a & b \\ c & d \end{pmatrix} \begin{pmatrix} x \\ y \end{pmatrix} + \begin{pmatrix} p \\ q \end{pmatrix}, \tag{6.1}$$

where the first term of the right side corresponds to the shrink and rotation, and the second term corresponds to the positional shifts. This track connection process is applied not only to adjacent films but also to those separated by one or two other films. The angular and position tolerances are defined as functions of the track angle, and the tolerances are

based on the scattering angle of minimum ionizing particles (MIPs). The connected two basetracks over a couple of films are referred to as "linklets."

Figures 6.4 and 6.5 show the distributions of position and angle differences between pairs of basetracks in linklets. Tracks are extrapolated from both films, and the position and angle differences at the middle of the two films are calculated. The position differences of linklets over a water gap are broader than those over an iron gap, while the angular differences are almost the same in the water and iron gaps. This is because the distance of the two films over the water gap is longer ($\sim$2000 μm) than that over the iron gap ($\sim$500 μm). The differences between the x (horizontal) and y (vertical) directions in both position and angular distributions are induced by the track angle dependency of the angular resolution. The angular resolution of the emulsion films is worse for the large-angle tracks. Most of the tracks in the emulsion films are cosmic rays, thus there are many large angle tracks in the y-direction. Hence, the distributions in the y-direction are broader than those in the x-direction.

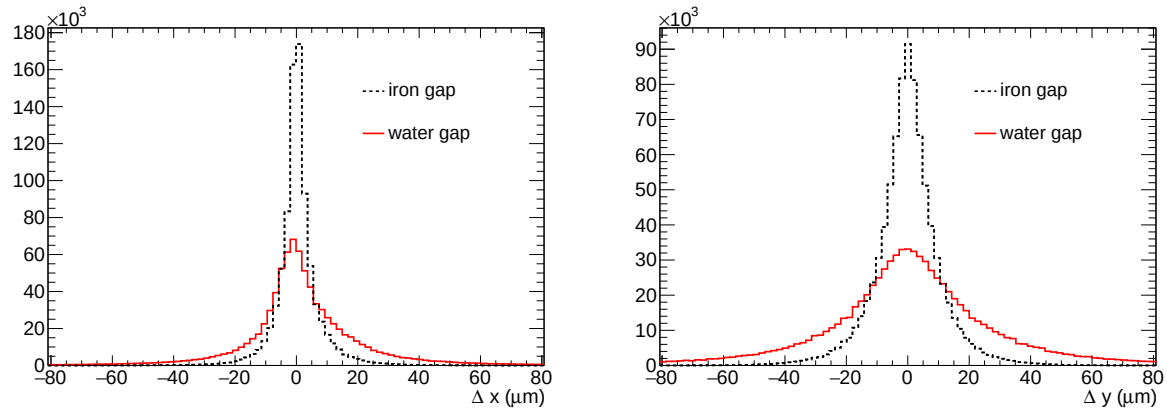

Figure 6.4: Distributions of position differences between two basetracks in each linklet over a single water or iron gap in x (left) and y (right) directions.

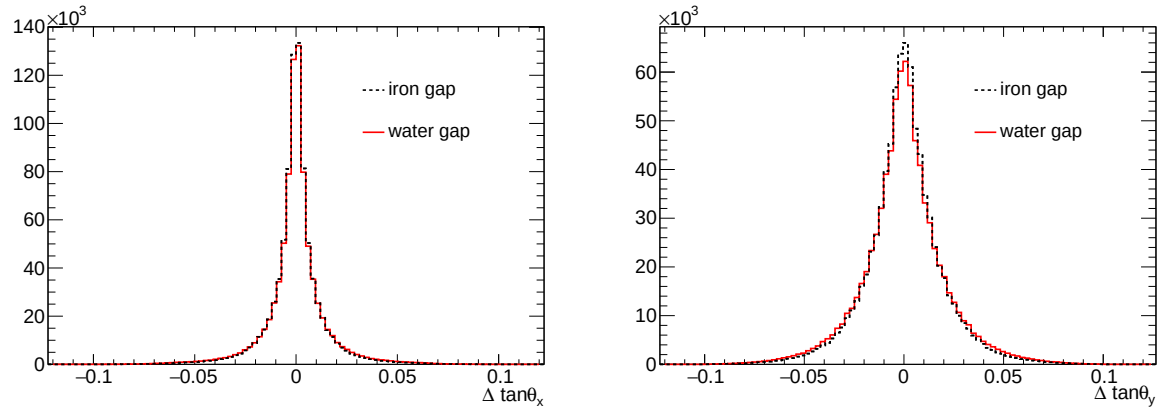

Figure 6.5: Distributions of angular differences between two basetracks in each linklet over a single water or iron gap in x (left) and y (right) directions.

After reconstructing the linklets between each pair of the films, they are connected using NETSCAN. A group of linklets constituting the same basetrack is collected to form a track called a "chain." In the following analysis, chains are used as tracks reconstructed in the ECC. More details of the reconstruction process can be found in Appendix D.1.

6.1.4 Efficiency of the emulsion films

The detection efficiency of each film is estimated using muon-like tracks. Two types of detection efficiencies are defined in this analysis. One is basetrack pickup efficiency, which is the detection efficiency of the basetracks in each emulsion film. The basetrack pickup efficiency is affected by hardware issues, such as film damages, distortion of the emulsion gel, contamination of impurity materials, and failure of scanning. It does not depend on the tolerances of the track reconstruction. The other efficiency is connection efficiency, which is determined by the reconstruction tolerances. Although the connection efficiency cannot be estimated by the data directly, we can measure the basetrack pickup efficiency and its product with the connection efficiency. The product of the basetrack pickup efficiency and the connection efficiency is called a chain reconstruction efficiency. Figure 6.6 shows a schematic view of the evaluation method of the basetrack pickup efficiency and the chain reconstruction efficiency.

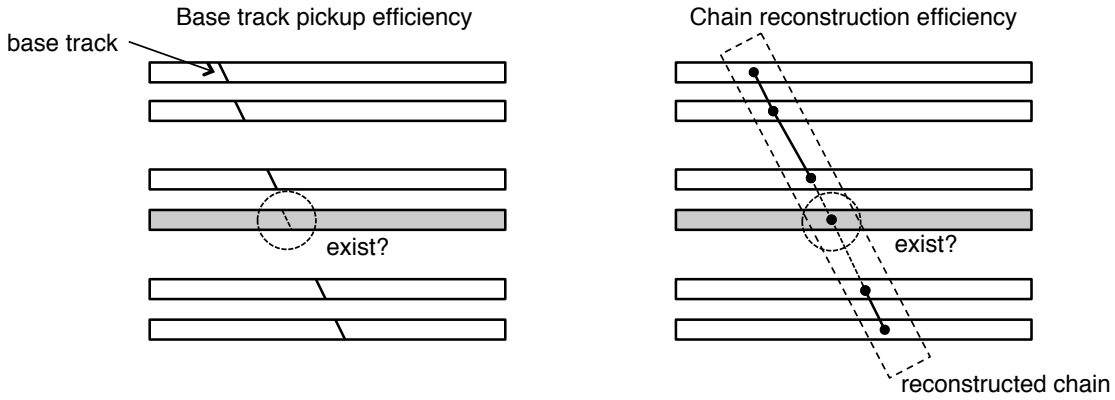

Figure 6.6: Schematic view of the evaluation method of the efficiencies. The base track pickup efficiency is evaluated using basetracks, and the chain reconstruction efficiency is evaluated using reconstructed chains.

The basetrack pickup efficiency is estimated using tracks on both upstream two films and downstream two films. For instance, there are five films (Film 1–5), and when we evaluate the Film 3 efficiency, the linklets reconstructed between Film 1-2, 2-4, 4-5 are used to select the track sample. The basetracks on the upstream films are extrapolated to the target film, and it is checked if there is a track within a tolerance. The tolerance for the angular difference is fixed to $|\Delta\tan\theta| < 0.2$, which is larger compared to the tolerances used for the later analysis. In contrast, the tolerance of the positional difference is varied from $5\,\mu$m to $100\,\mu$m. As shown in Fig. 6.7, the saturated efficiency where the efficiency stops increasing (the broken red line in the plot) is defined as the basetrack pickup efficiency. Figure 6.7 shows the basetrack pickup efficiency evaluated as a function of the track angle.

For all the films used in the pilot run, the basetrack pickup efficiency of a single emulsion film is around 97%–99%.

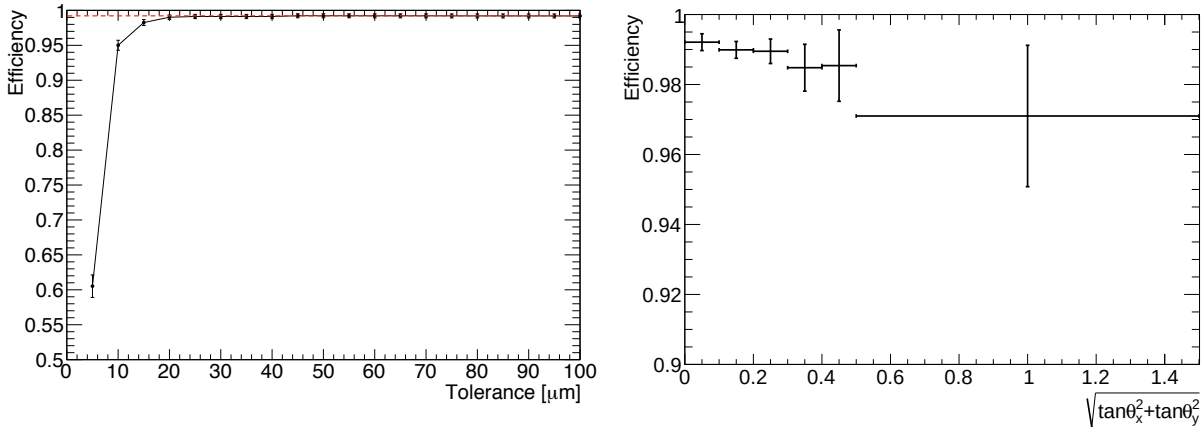

Figure 6.7: Basetrack pickup efficiency of an emulsion film. The left plot shows efficiency over position tolerance (example of $0.2 < \sqrt{\tan^2\theta_x + \tan^2\theta_y} < 0.3$). Where the efficiency stops increasing (the broken red line) is defined as the basetrack pickup efficiency. The right plot shows the efficiency as a function of the track angle. For all the films used in the pilot run, the basetrack pickup efficiency of a single emulsion film is around 97%–99%.

The chain reconstruction efficiency is evaluated using the same track sample as used to evaluate the basetrack pickup efficiency. Using NETSCAN, the reconstruction of chains is carried out. Linklets are reconstructed not only for the adjacent films but also for those separated by one or two films. Thus, a reconstructed chain may not include basetracks in all the films. The chain reconstruction efficiency is evaluated by checking if there is a basetrack on the target film. The result is around 97%–99% in each film, and this efficiency is almost the same as the basetrack pickup efficiency. Since the chain reconstruction efficiency is a combination of the basetrack pickup efficiency and the connection efficiency, the connection efficiency is evaluated as more than 99.8%. Therefore, by connecting tracks between both adjacent films and the films separated by one or two films, the track reconstruction efficiency becomes higher than 99.99%.

6.1.5 Corrections applied to the emulsion films

The VPH value varies with each film because the VPH depends on several factors other than the energy deposit of charged particles, such as the AgBr volume occupancy in the emulsion gel, development treatment, and scanning parameters. To eliminate the fluctuation of the VPH value of the films, scaling factors among the films are calculated based on the VPH peak value of MIP tracks. Figure 6.8 shows the typical VPH distribution, in which two peaks are shown: tracks with sufficiently large energy deposits, such as the proton tracks, have large VPH values, while the MIP tracks have small VPH values. The peak with smaller VPH values is called the MIP peak, and the peak with larger VPH values is called the black peak. The black peak is broadly distributed since the VPH value in the black peak strongly depends on the momentum and the angle of the track sample. Thus, the MIP peak value is used to calculate the scaling factor. However, the VPH of the

MIP peak also depends on the track angle. The scaling factors are evaluated separately in nine angle bins: [0.0, 0.1, 0.2, 0.3, 0.4, 0.5, 0.7, 0.9, 1.1, 2.5] in $\tan\theta$ ($=\sqrt{\tan^2\theta_x + \tan^2\theta_y}$). The VPH values are scaled in each angle bin so that the MIP peaks have the same value.

In addition to the VPH variation between the films, the VPH decreases over time due to a fading of the emulsion gel. Figure 6.9 shows the average VPH of the sand muons as a function of time to the development. The newer tracks have larger VPH values, and the VPH values decrease a few % per week. The degree of the fading in each film is measured using the sand muon samples, and a correction is applied to the beam timing events in the data.

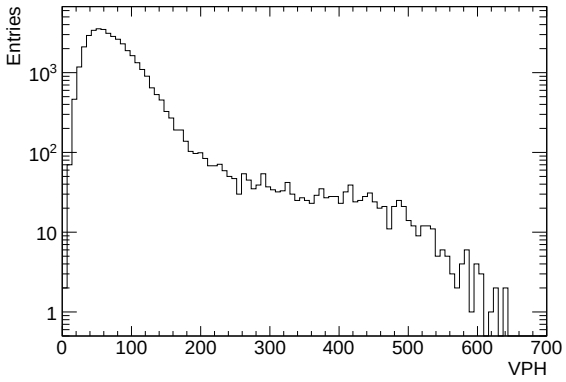

Figure 6.8: Typical VPH distribution of an emulsion film. The peak with smaller VPH is called the MIP peak, and the peak with larger VPH is called the black peak.

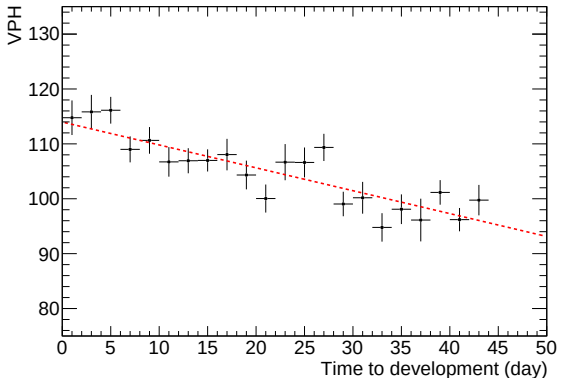

Figure 6.9: Average VPH of the sand muons as a function of time to the development. The VPH values decrease a few % per week.

6.2 Track reconstruction in INGRID

Muons from the neutrino interactions in the ECC penetrate it, and we cannot identify muons for the CC interaction selection only by the ECC. Therefore, tracks in INGRID are used to select the CC interactions by matching them with the tracks in the ECC. The track reconstruction method of INGRID is almost the same as the INGRID beam profile measurement. It is well established and used in several measurements [50, 149, 150]. The following is a summary of the INGRID reconstruction process.

(1) Time clustering

MPPC channels with more than 2.5 p.e. are counted as hits. If the INGRID module has more than three hit channels within 100 nsec, all hits within ± 50 nsec from the average hit time are clustered. This clustering reduces accidental hits induced by MPPC dark noise, which is an avalanche generated by a thermal carrier in the MPPC even in the absence of photons.

(2) Number of active planes selection

To reduce the accidental noise hits further, an active plane is defined as a plane with hits in both x and y layers. Events with at least three continuous active planes are selected.

(3) Two-dimensional track reconstruction

Two-dimensional tracks in x-z and y-z views are reconstructed. Cellular automaton is used for the track reconstruction algorithm [151].

(4) Three-dimensional track reconstruction

After reconstructing two-dimensional tracks, a pair of the x-z and y-z plane tracks is combined into a three-dimensional track. Here, the difference of the upstream z-position of the pair of the two-dimensional tracks should be smaller than three layers. Pairs of two-dimensional tracks matching this criterion are used in the following analysis.

(5) Vertex reconstruction of the INGRID tracks

The upstream edge of a three-dimensional track is defined as a vertex. If there are more than two tracks, those satisfying the following two criteria are considered to originate from the same vertex; the sum of the z-position differences at the upstream of the tracks is less than two; position difference between two vertices is less than 150 mm. For the NINJA analysis, we only need tracks starting upstream of INGRID. Thus, tracks with vertices at the most upstream plane are selected.

(6) Beam timing cut

The neutrino events should be within ± 100 nsec from the expected timing of each beam bunch. The timing of an event is defined by the hit timing of the largest yield channel. This cut reduces cosmic-ray backgrounds.

After the reconstruction, the angular and position resolutions of the INGRID tracks are around 3.8° and 2.7 cm, respectively [152]. As described in the process (5), tracks need to start at the most upstream plane to select the neutrino interactions occurring in the ECC. Figure 6.10 shows the hit efficiency of a scintillator layer as a function of the track angle. The hit efficiency is more than about 97% in all angle regions. Thus the probability of missing hits at the upstream plane in both x and y layers due to the hit inefficiency is less than $(1-0.97)^2 < 0.1\%$.

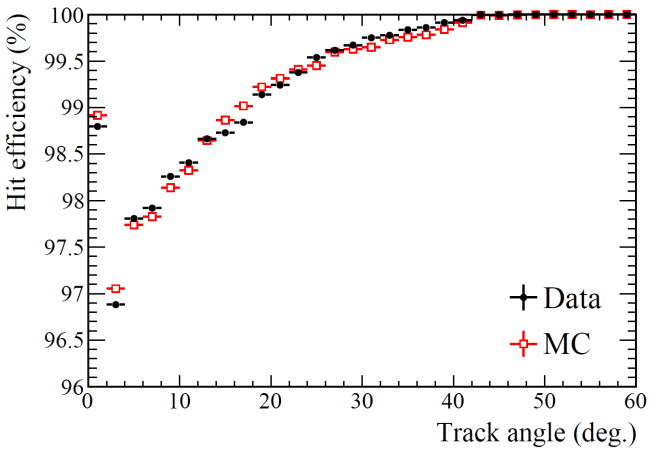

Figure 6.10: Hit efficiency of a scintillator layer at INGRID [149]. The hit efficiency is more than about 97% in all angle regions.

6.3 Hit reconstruction in the SFT

As described in Sec. 4.4.2, the SFT fiber hits are identified using the channel combinations at both-end readouts of the fibers. The hit threshold of the SFT is set at 2.5 p.e., and at least one hit channel is required in each layer. Figure 6.11 shows two types of SFT hits. The SFT hit cluster consisting of two fiber hits is defined as a normal hit, and the hit position is reconstructed from the light yield ratio of the neighboring fibers. If there is only one hit fiber, it is defined as a single hit, and the particle is considered to have passed through exactly the center of the fiber because there is an insensitive area of the fiber cladding.

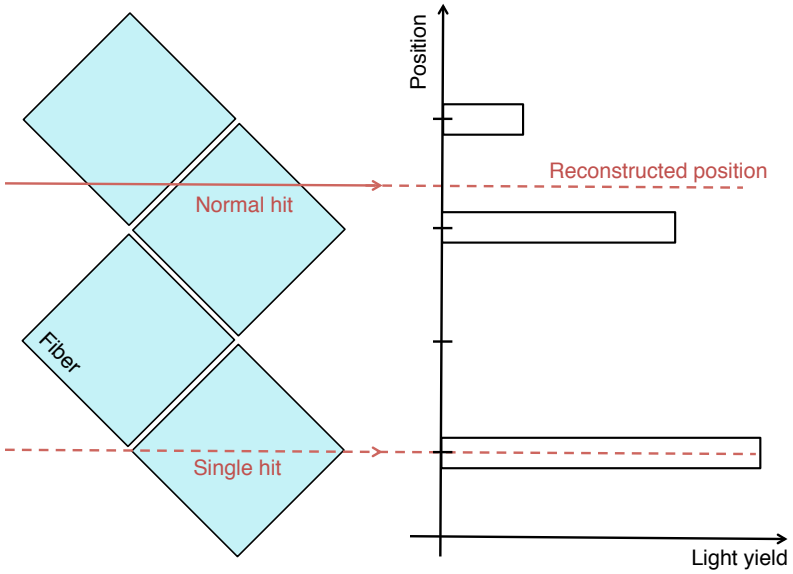

Figure 6.11: SFT hit type: a normal hit has two hit fibers, while a single hit has only one hit fiber due to the insensitive area of the fiber cladding.

Figure 6.12 shows the light yield distributions of the SFT x and y layers. The sum of the light yield at each layer has a Landau-convoluted Gaussian distribution. It has a peak around 60 p.e., which is consistent with the designed value. Crosstalks between the neighboring fibers are checked using events having more than two continuous hit fibers. In this SFT, the number of hit fibers is usually one or two, thus events with more than three hit fibers are likely induced by crosstalk of the fibers. It is evaluated that the hit induced by the crosstalk is less than 1.5% of all reconstructed hits.

We checked two effects to evaluate the track reconstruction efficiency: accidental noise hits and bunch pileups. The accidental noise hits are induced by MPPC dark noise. The SFT DAQ system records only one hit per channel in a spill. If a hit by the dark noise is recorded before a beam signal, we cannot record the hit caused by a beam-induced particle. The inefficiency due to the accidental noise hits is estimated to be 0.2%. The bunch pileup inefficiency is also induced by the limitation of the DAQ system. If there are multiple tracks in one spill, the second or later tracks cannot be recorded. The efficiencies are calculated to be 99.67% in Run-a and 99.41% in Run-b using the sand muon events. The difference between Run-a and Run-b comes from the number of recorded bunches in a spill (There are no seventh and eighth bunch data in Run-a due to the DAQ trouble).

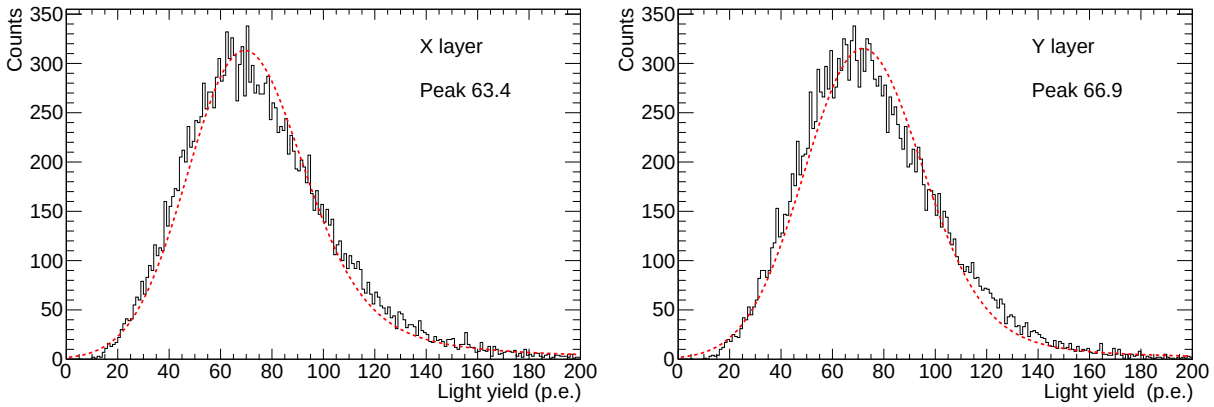

Figure 6.12: Light yield distributions of the x (left) and y (right) layers of the SFT. It has a Landau convoluted Gaussian distribution which has a peak around 60 p.e.

The pileup inefficiency increases as the number of bunches in a spill increases. Thus, the Run-b efficiency is lower than that in Run-a.

6.4 Track matching

After reconstructing the tracks and the hit positions of the detectors, track matching processes are applied to connect tracks between the ECC and INGRID. Matching between the INGRID tracks and the SFT hits is carried out first. Following this, matching between the SFT-INGRID tracks and the ECC tracks is performed using the SFT hit position and the INGRID track angle.

6.4.1 Track matching between the SFT and INGRID

Track matching between the INGRID tracks and the SFT hits is performed using the position and timing information recorded at each detector. A track reconstructed at INGRID is extrapolated to the SFT location. If the extrapolated position is within ± 10 cm from the reconstructed SFT hit in the same spill, they are regarded as the same track. Figure 6.13 shows the position differences of the SFT hits and INGRID tracks extrapolated to the SFT position. The bunch distributions of the matched tracks are also shown. Although there are no seventh and eighth bunches in Run-a, the matched tracks are uniformly observed in the other bunches. If there are several INGRID track candidates for one SFT hit, the INGRID track in the earliest bunch is selected. This is because the SFT records hits induced by the first track in each spill. By contrast, if there are several INGRID track candidates in the same bunch, or one INGRID track has several SFT hit candidates, all of them are put forward to the neutrino event selection.

The connection efficiency between the SFT and INGRID is evaluated using INGRID high momentum tracks. Tracks penetrating more than four iron plates are selected as the high-momentum track sample. The INGRID tracks are extrapolated to the SFT position, and check if there are SFT hits in the same spill. Tracks with reconstructed positions near the SFT center (12 cm$\times$ 12 cm) are used. The reason we use the INGRID high momentum tracks is tracks penetrating only a small number of iron plates have a

poor angular resolution, and tracks not passing through the SFT may contaminate to the sample by extrapolating such short tracks. As shown in Fig. 6.14, the matching efficiency becomes lower in the large-angle region, but it is higher than 95% in the forward region where most muon tracks exist. The 5% inefficiency mainly comes from the inefficiency of the SFT hit reconstruction.

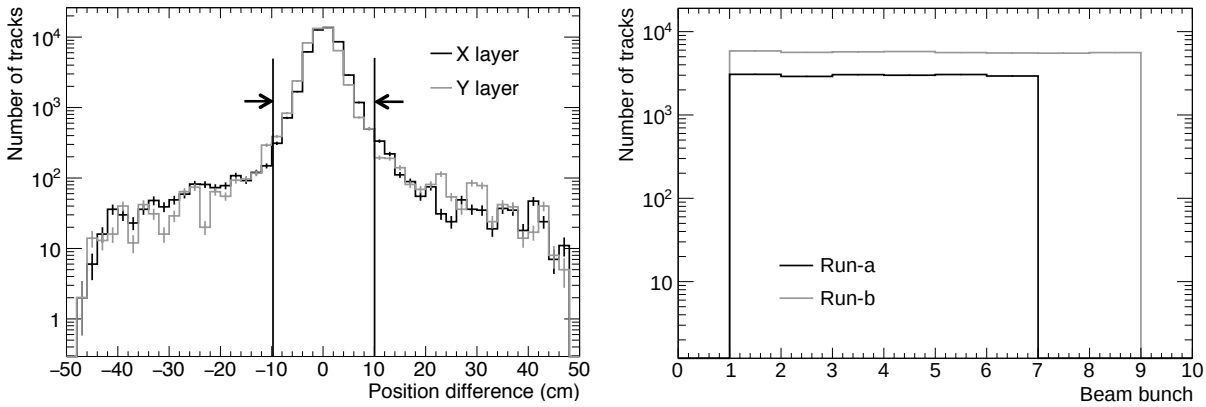

Figure 6.13: Position differences of SFT hits and INGRID tracks extrapolated to the SFT position (left) and bunch distribution (right). Extrapolated INGRID tracks within ± 10 cm from the reconstructed SFT hit in the same spill are regarded to belong to the same track. Although there are no seventh and eighth bunches in Run-a, tracks are uniformly selected in the other bunches.

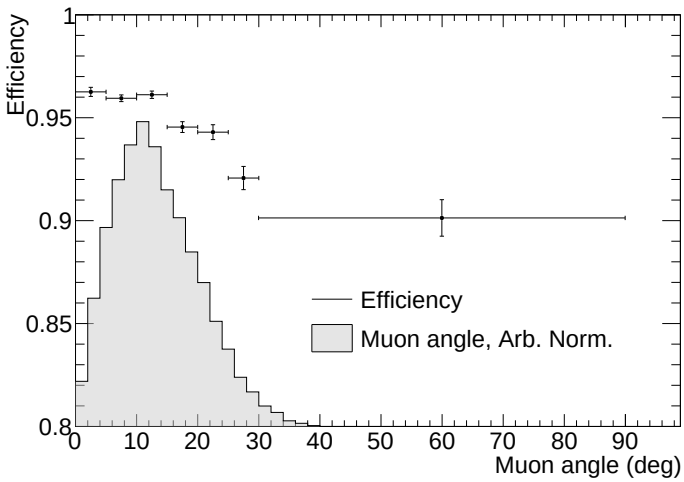

Figure 6.14: Track matching efficiency between the SFT and INGRID evaluated as a function of the track angle.

6.4.2 Track matching between the SFT-INGRID tracks and the ECC tracks

The matched tracks between the INGRID tracks and the SFT hits are called SFT-INGRID tracks, which have the SFT hit position and the INGRID angle information. In this sec-

tion, a track matching between the SFT-INGRID tracks and the ECC tracks is described. Tracks recorded on the SS emulsion films are extrapolated to the SFT location, as shown in Fig. 6.15. These tracks are called SS prediction tracks. We require basetracks at least one of the two films on both sides of SS1. We also require basetracks on both CS films. When tracks are extrapolated from the SS films, these angles are reconstructed not by basetracks but by pairs of two basetracks in the films over the 2-mm-thick acrylic plate. This is because they give a better angular resolution, which is about 1 mrad, while the angular resolution of a basetrack is typically 2 mrad. If the difference between the position of the SFT-INGRID track and that of the extrapolated SS track is less than 600 μm, and the difference of their angles is less than 0.2 in $\tan\theta$ in both horizontal and vertical directions, that track is regarded as a matched track. If there are several matching candidates, all candidates remain until the neutrino event selection.

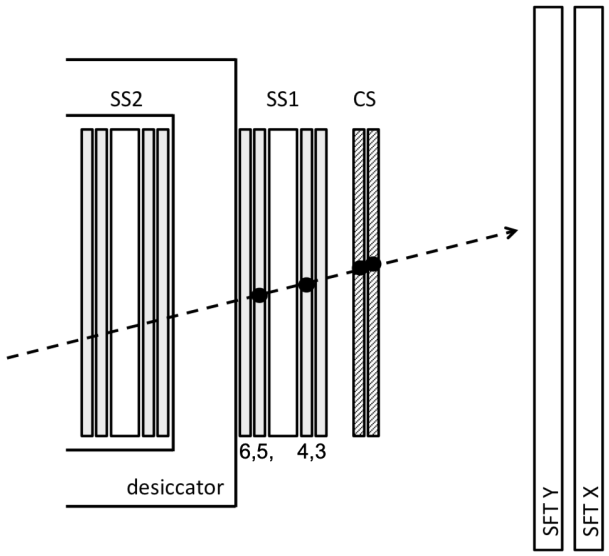

Figure 6.15: Definition of the SS prediction tracks. Neutrinos come from the left side of the figure. The SS prediction tracks are extrapolated to the SFT position.

Figure 6.16 shows position differences between the SFT-INGRID tracks and the ECC tracks extrapolated to the SFT position. Figure 6.17 shows angular differences between them. These distributions correspond to the position resolution of the SFT and the angular resolution of INGRID because the position and angular resolutions of the emulsion films are much better than those of the other detectors. The position and angular resolutions after the matching are evaluated as 240 μm and 0.03 in $\tan\theta$, respectively.

Track matching efficiency between the SFT-INGRID tracks and the ECC tracks is also evaluated by the INGRID high momentum tracks. The number of ECC-SFT connected tracks against the total track sample is considered as the matching efficiency. Figure 6.18 shows the result. The efficiency in Run-b is lower than that in Run-a because the CS films were slightly bent in the Run-b period. Thus, the distance between the SS and CS films varied depending on the position in the films, and the accuracy of the matching between these films got worse. The track sample used for the evaluation of the ECC-SFT connection is limited. Therefore, the statistical uncertainty of the track sample is assigned to the uncertainty of the ECC-SFT connection efficiency, as discussed in the later section.

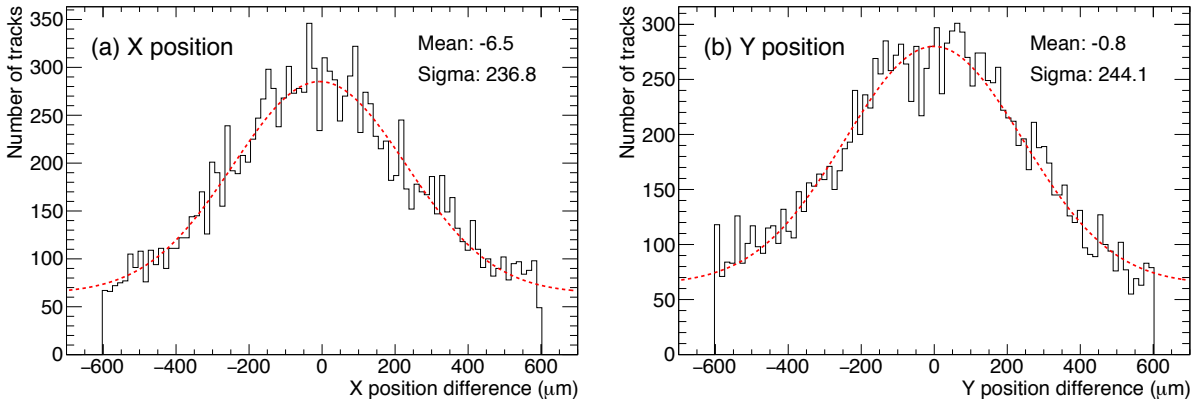

Figure 6.16: Position differences of the SFT hits and the ECC tracks extrapolated to the SFT location. The x (left) and y (right) position differences are shown.

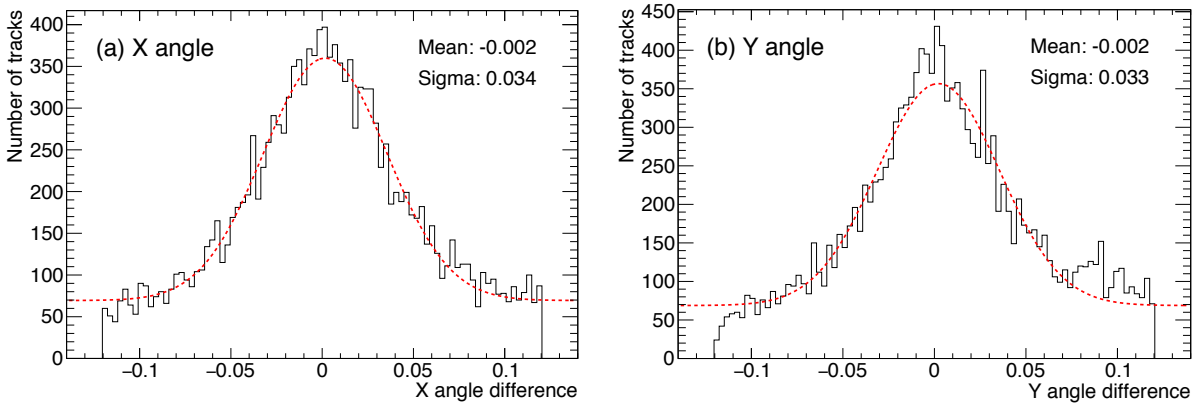

Figure 6.17: Angular differences of the SFT-INGRID tracks and the ECC tracks extrapolated to the SFT location. The x (left) and y (right) angular differences are shown.

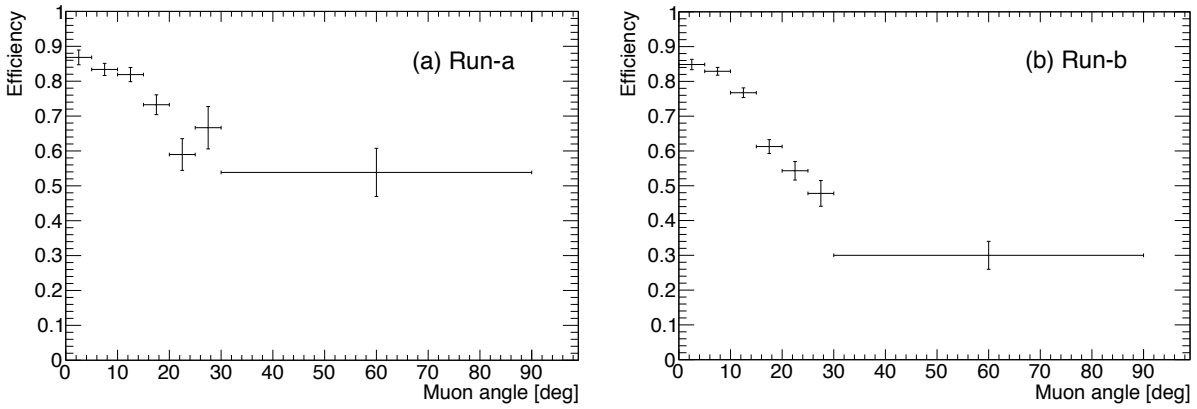

Figure 6.18: Track matching efficiency between the ECC and the SFT in each period. The CS films were bent in the Run-b, and it is considered as a cause of the difference between the two periods.

6.4.3 Summary of the track matching

Figure 6.19 shows the total muon detection efficiencies in the Run-a and Run-b periods. The difference between the two periods comes from the matching efficiency between the SFT-INGRID tracks and the ECC tracks.

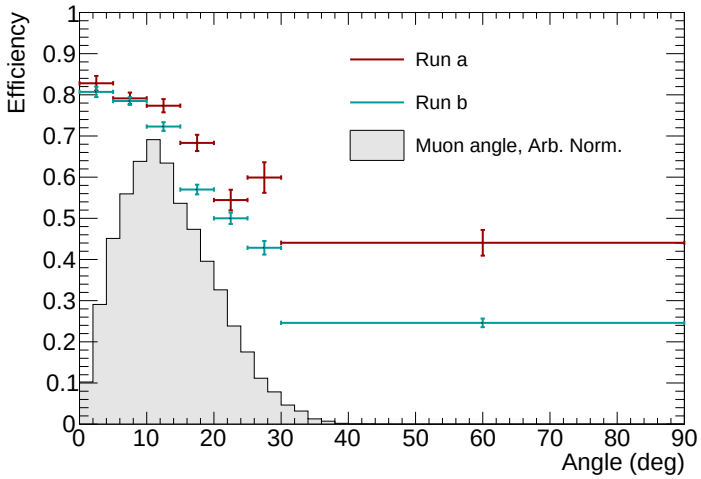

Figure 6.19: Total muon detection efficiencies as a function of angle. Vertical bars are the statistical errors. The gray histogram is the expected angular distribution of muons within the INGRID acceptance.

Chapter 7

Momentum reconstruction and Particle identification

The INGRID matched track is selected as a muon candidate, and a track constructing the vertex with the muon candidate is considered a proton or a charged pion. In this chapter, momentum reconstruction of these tracks is described as well as the separation of protons and pions, while the selection of the protons and pions is described in Chapter 8.

7.1 Overview of the momentum reconstruction and the particle identification

In emulsion detectors, momentum of a charged particle can be measured from scatterings in a material. A charged particle passing through the material is scattered many times mainly due to Coulomb scattering by nuclei. This process is called multiple Coulomb scattering (MCS), and the charged particle gradually changes its direction. The momentum $P\beta$ can be obtained from the scattering angle, the radiation length, and the thickness of the material independently from the kind of particle. Here, P is the momentum, and β is the velocity of the particle. Hence, the momentum of the particle can be measured without using a magnetic field. The momentum reconstruction using MCS requires good angular and position resolutions of a detector. Thus, the emulsion detectors suit this reconstruction method. There have been two methods developed for measuring the momentum by MCS: a coordinate method [153] and an angular method [154]. The coordinate method uses the positional displacement of a track on three films, while the angular method uses the scattering angle measured by the angular difference of a track between two films.

Figure 7.1 shows the flow chart of the momentum reconstruction and particle identification (PID). Although the muon momentum can be measured by INGRID track range or MCS in the ECC, we can measure higher muon momentum only by MCS in the ECC. In this analysis, the coordinate method is used to reconstruct the muon momentum as described in Sec. 7.2.2, while the momenta of protons and pions are obtained by the angular method as described in Sec. 7.3. The reason why we use the different methods is these methods have advantages and disadvantages in the capable momentum range and the statistical precision. We need to select an appropriate method to suit the momentum range we measure. The PID is performed using $P\beta$ measured above and the VPH value,

which is proportional to the energy deposit of the particle. Moreover, the track range is used to measure the momentum of protons fully contained in the ECC.

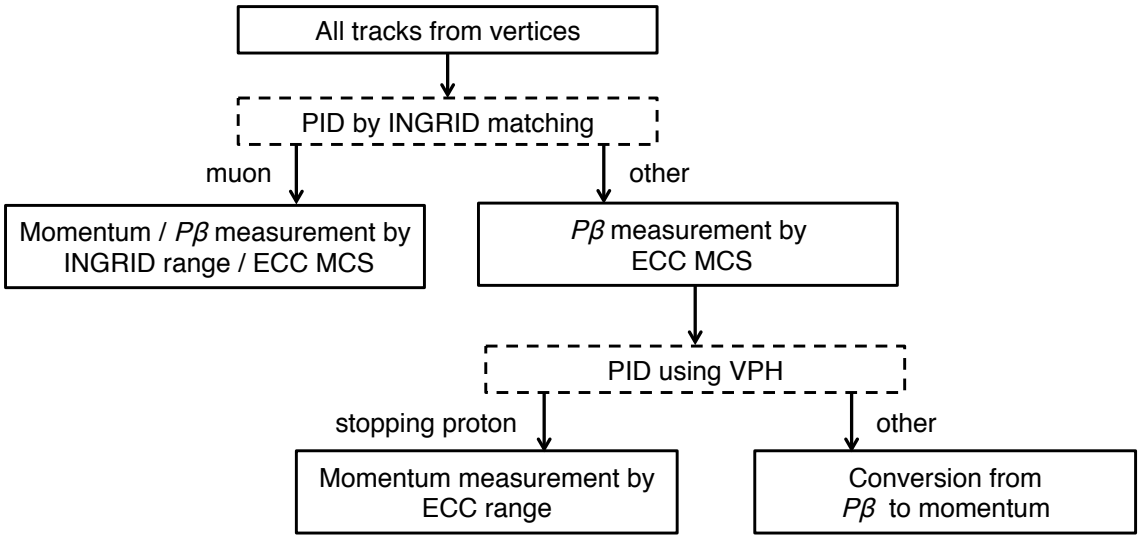

Figure 7.1: Flow chart of the momentum reconstruction and the PID. Muon momentum is measured by the INGRID range and the ECC MCS. Momenta of protons escaping from the ECC and pions are measured by the ECC MCS. Momenta of stopping protons in the ECC are measured by the range in the ECC after the PID.

7.2 Momentum reconstruction of muon tracks

In this section, we introduce two methods of momentum reconstruction for muon candidates, which are tracks matched with INGRID in the previous section.

7.2.1 Momentum reconstruction using the INGRID range

The first method is using an INGRID range, which is obtained from the number of penetrated iron plates. We calculate the range of a particle passing through the iron plates by considering the track angle. The correlation between the muon momentum and the INGRID range is shown in Fig. 7.2. When a track stops in INGRID, the range is easily measured. However, we cannot measure the momentum of side escaping tracks or tracks penetrating all the iron plates of INGRID. Therefore, with this method, we can measure momenta only up to around 1 GeV/c. Since our detector is placed near the on-axis position, the muon momentum peak is around 1.2 GeV/c. Therefore, most tracks penetrate INGRID as shown in Fig. 7.2 right plot, and we need another method to measure the muon momentum.

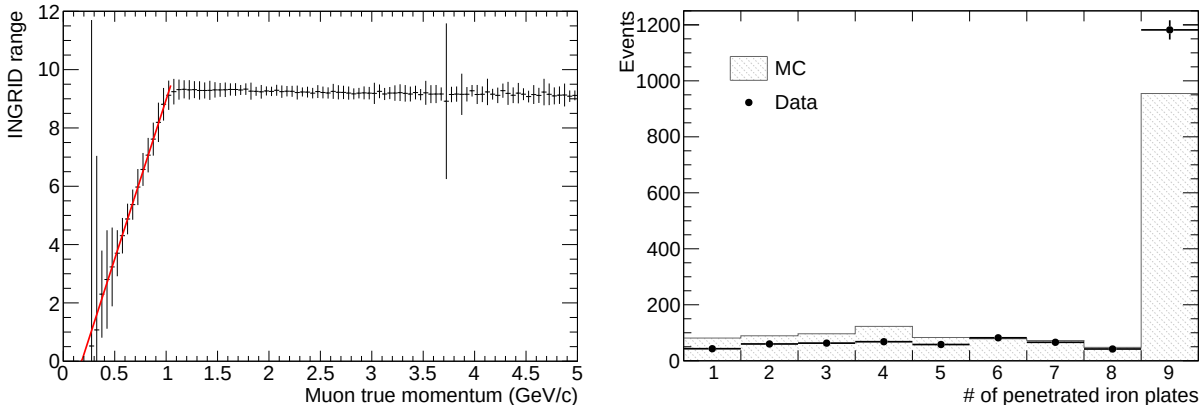

Figure 7.2: Correlation between the muon momentum and the INGRID range in the MC simulation (left) and the distribution of the number of penetrated iron plates (right). The neutrino interactions in the ECC and the sand muons are included. Most muons penetrate all the nine iron plates, thus their momenta cannot be measured by the INGRID range.

7.2.2 Momentum reconstruction using the MCS in the ECC

As described in the previous section, INGRID measures muon momentum up to 1 GeV/c. However, in our measurement, most muons have higher momenta, and they penetrate all the iron plates of INGRID. Therefore, we adopt the MCS coordinate method using the ECC to reconstruct the muon momentum. In this method, we use positional displacements of the track by MCS. Three films are used to calculate the positional displacement. We use the first and second films to reconstruct the track angle. Using the reconstructed angle, the track on the second film is extrapolated to the third film. Then, the positional displacement at the third film is used to reconstruct the momentum.

The maximum momentum that can be measured by this method is determined by the measurement error because the scattering angle of a high momentum particle becomes smaller than the measurement error. The positional displacement is proportional to $x^{3/2}$ due to the nature of MCS, while its measurement error is proportional to x, where x is the thickness of the material between the second and third films. Hence, two films that are placed further apart can measure higher momentum than adjacent films because the measurement error becomes smaller compared to the scattering angle. Figure 7.3 shows the definition of the positional displacement used for the coordinate method. In this analysis, the second and third films are separated by five iron plates. The distance between the second and third films is around 1.5 cm, and it enables us to measure the momentum up to around 5 GeV/c.

The coordinate method used in this analysis is slightly different from that in Ref. [153]. In the original coordinate method, three films placed at the same interval are used. In this analysis, films separated by a single water gap are used as the first and second films to reconstruct the track which is extrapolated to a film placed over five iron plates away. This is applied for all available combinations of three films because the number of films in our detector is limited, and we want to increase the number of film combinations for a precise reconstruction of the momentum. Then, the positional displacement from the predicted position at each combination y_{i} (i=1, 2, 3...) is measured in both x-z and y-z views. The quadrature sum of y_{i} is taken as y^2_{meas}, which includes both the positional

displacement by MCS (y_0) and the measurement error (y_{err}):

$$y_{\mathrm{meas}}^2 = y_0^2 + y_{\mathrm{err}}^2. \tag{7.1}$$

Therefore, the measurement error needs to be subtracted.

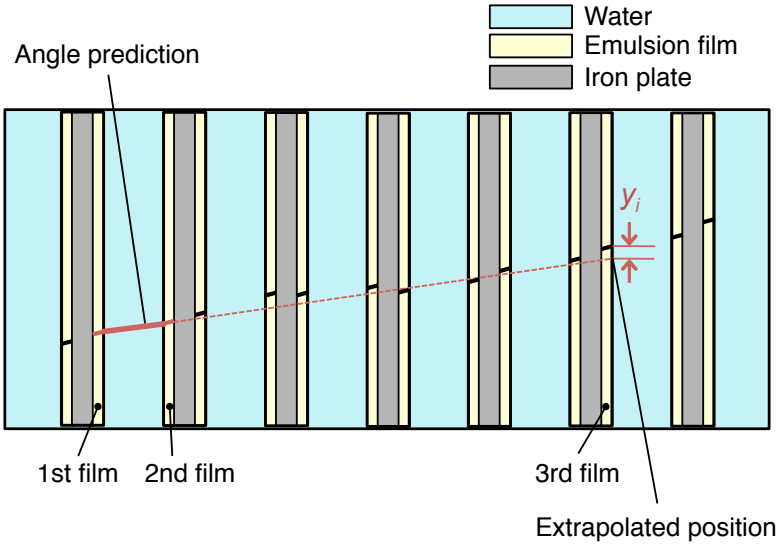

Figure 7.3: Definition of the positional displacement used for the coordinate method. The first and second films are used to reconstruct the track angle. Using the reconstructed angle, the track on the second film is extrapolated to the third film. Then, the positional displacement at the third film is measured.

The measurement error depends on the alignment accuracy of the films over a water gap. The uncertainty of the reconstructed angle σ_θ in a two-dimensional view is written by

$$\sigma_\theta^2 = \frac{2}{\Delta z^2}(\delta x^2 + \delta z^2 \times \tan^2\theta), \tag{7.2}$$

where Δz is the distance between the two films over a water gap, δx is the alignment accuracy of positions in the x or y direction, δz is the uncertainty of Δz, and $\tan\theta$ is the track angle. We use lateral and radial directions introduced below instead of the x and y directions to reduce σ_θ and to achieve the reconstruction of higher momentum. Figure 7.4 shows the definition of the lateral and radial directions of a track. Assuming that particles are passing in the z-direction (beam direction), the coordinates are rotated in the x-y plane for each track. The radial axis corresponds to the track direction projected in the x-y plane, while the lateral axis is the transverse direction. In the lateral direction, the uncertainty from $\delta z^2 \times \tan^2\theta$ in Eq. 7.2 vanishes because $\tan\theta = 0$, thus we use only the lateral direction. The estimated y_{err} is typically less than $10\,\mu$m depending on the distance between the two segments of the track. The uncertainty of the measurement error is evaluated for the momentum reconstruction uncertainty, and it is added to the systematic error from the detector response in Sec. 8.2.

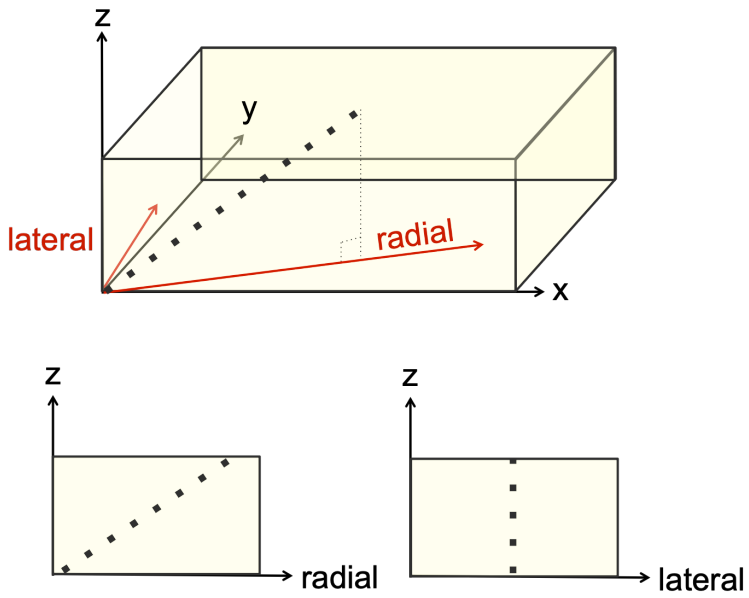

Figure 7.4: Definition of the lateral and radial directions of a track. The radial axis is defined along with the track direction, while the lateral axis is transverse to the radial axis.

Finally, $P\beta$ is calculated from the following relation [155]:

$$y_0 = \frac{C}{\sqrt{3}} z \frac{13.6\,\mathrm{MeV}/c}{P\beta} \sqrt{\frac{x}{X_0}} \left(1 + 0.038\,\ln\left(\frac{x}{X_0}\right)\right), \tag{7.3}$$

where z is the distance between the second and third films, x is the total thickness of the iron plate, X_0 is the radiation length in iron, and C is a correction factor for the effect of passing through several materials. It is assumed that only the iron plates affect the scattering of a particle when we assign values to x and X_0. If the ECC is a simple structure of a single target material and emulsion films, and the mass of the emulsion films is much smaller than that of the target material, the scattering in the emulsion films can be ignored. However, the water ECC contains several layers of different materials such as iron, water, emulsion film, and the vacuum-packing film. Thus scattering in each material is considered, and C is estimated using the MC simulation. Figure 7.5 shows the result. The parameter $\mathrm{N_{cell}}$ denotes the number of iron plates crossed by a particle. In this analysis, $\mathrm{N_{cell}} = 5$ is used. Mono-energetic muons in momentum 0.5, 1.0, 2.0, 3.0, 4.0, 5.0 GeV/c are injected in the MC simulation. At $\mathrm{N_{cell}} = 1$, the factor is almost 1 since it only includes one iron plate between films. The small discrepancy from 1 is considered due to the scattering at the emulsion films. The factors are expected to be independent of momentum because it only depends on the radiation length determined by the detector structure. According to the MC simulation, they show similar factors at each momentum as expected.

Figure 7.6 shows the relation between the true and reconstructed momenta of muons from the neutrino interactions calculated by the MC simulation. With this method, our detector can reconstruct the muon momentum with a resolution of 30%–40%.

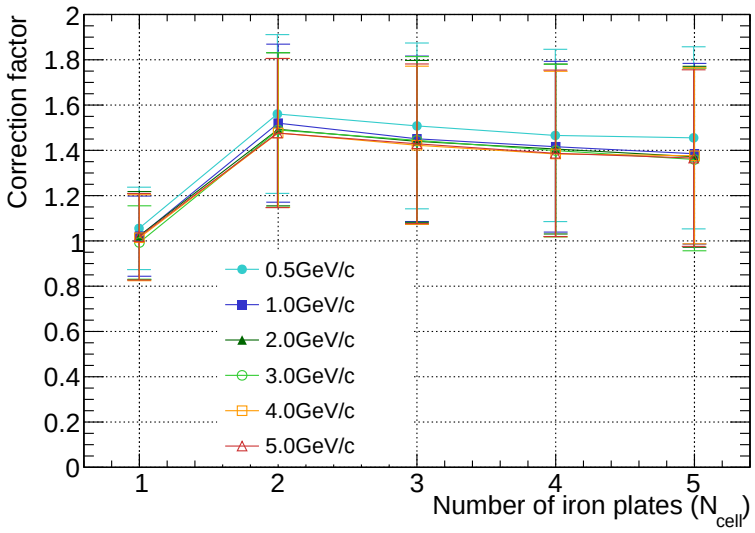

Figure 7.5: Correction factor of the coordinate method in the water-target ECC estimated by the MC simulation. Monoenergetic muons from 0.5 to 5.0 GeV/c are injected. The correction factor corresponds to C in Eq. 7.3, and the error bar corresponds to the root mean square of the reconstructed momentum distribution.

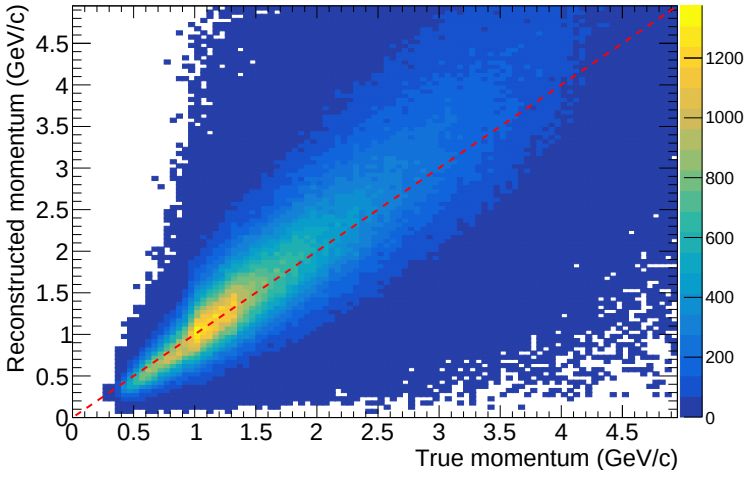

Figure 7.6: Relation between the true and reconstructed momenta of muons from neutrino interactions in the MC simulation.

7.3 Momentum reconstruction of proton and pion tracks

Another way to reconstruct momentum by MCS is the angular method. Figure 7.7 shows the definition of the scattering angle used for the angular method. The angular difference between two basetracks on different films is measured instead of the positional displacement. This method enables us to increase the statistics of the combination of films and

reconstruct the momentum of short tracks. However, the angular method is not suitable for the muon momentum measurement, because the measurable momentum is limited by the angular resolution of the films, which is typically 2 mrad for the forward angle tracks. In this analysis, the maximum $P\beta$ measured by the angular method is around 1.5 GeV/c, while $P\beta$ up to 5 GeV/c can be measured by the coordinate method.

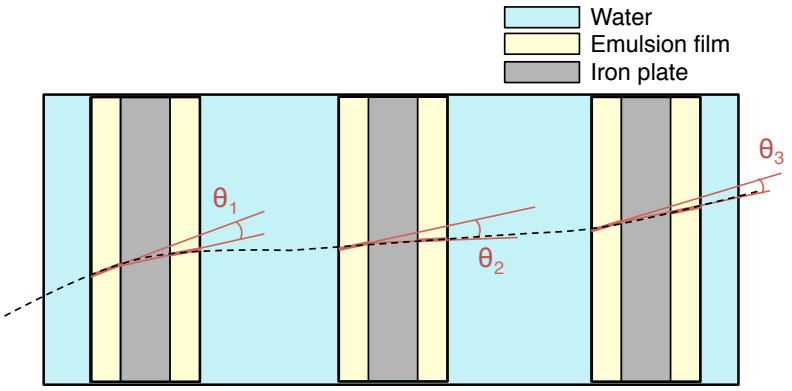

Figure 7.7: Definition of the scattering angle used for the angular method. The angular difference between the two films over iron plates is measured.

The root mean square of the scattering angle θ_{i} is denoted as θ_0, and it is related to $P\beta$ as follows [155]:

$$\theta_0 = \frac{13.6\,\mathrm{MeV}/c}{P\beta}\sqrt{\frac{x}{X_0}}\left(1 + 0.038\,\ln\left(\frac{x}{X_0}\right)\right). \tag{7.4}$$

In the angular method, the angular differences are measured in the lateral–radial coordinates, which is introduced in the coordinate method. The angular resolution of the basetracks is also written by Eq. 7.2, in this case, Δz is the thickness of the plastic base, δx is the positional resolution of the films ($\sim 0.3\,\mu$m), δz is the focusing depth of HTS ($\sim 4\,\mu$m), and $\tan\theta$ is the track angle. The typical angular resolution of the films is 2 mrad. The uncertainty from this angular resolution is also evaluated, and it is added to the systematic error from the detector response in Sec. 8.2.

As already discussed in the coordinate method, the ECC has a complex structure of several materials. The total scattering angle is considered as the quadrature sum of the scattering angle in each material. The measurement error is also considered and subtracted from the measured scattering angles. Figure 7.8 shows the relation between the true and reconstructed momenta. The momentum of protons and pions are reconstructed by the angular method with a resolution of 30%–40%.

In addition to the reconstruction using MCS, we can measure the momenta of protons stopping in the ECC by the track range. This measurement is used only for the track identified as a proton. Therefore, the momentum measurement using the range information should be applied after the PID process described in the next section. Figure 7.9 shows the relation between the true and reconstructed momenta of protons reconstructed by the range method. By this method, the momentum is reconstructed with a 5% resolution. Most of the low-momentum protons (typically below 400 MeV/c) are measured with this good momentum resolution by the range method.

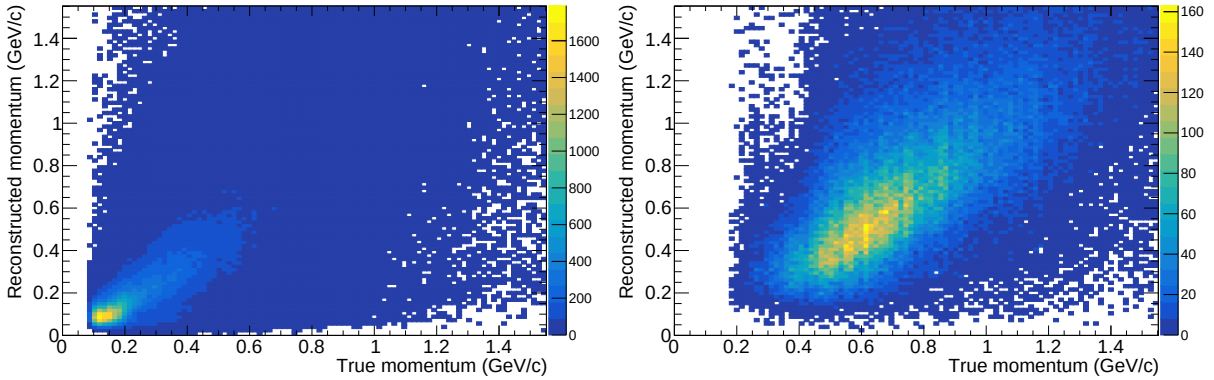

Figure 7.8: Relation between the true and reconstructed momenta estimated by the MC simulation. The left plot is pion momentum distribution, and the right plot is proton momentum distribution. Only proton momenta measured by the MCS are included.

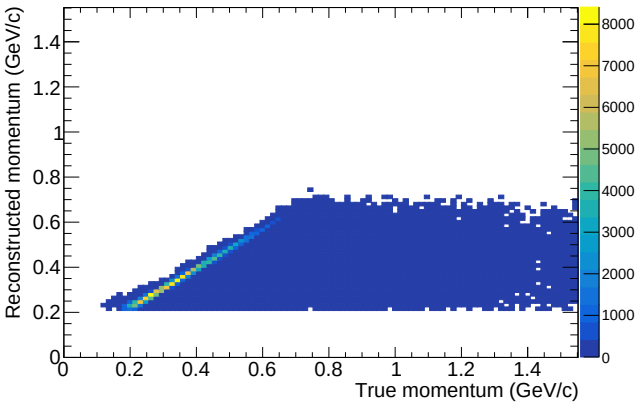

Figure 7.9: Relation between the true and reconstructed momenta of protons reconstructed by the range method, estimated by the MC simulation. While momenta reconstructed by MCS spread both in higher and lower than the true momenta, momenta reconstructed by range spread only to lower region. This is because tracks may stop or interact before reaching their expected range while they usually do not become longer than expected.

7.4 Particle identification

Muon-like tracks are identified by the track matching with INGRID. This section describes the PID of the other tracks. After $P\beta$ estimation, all tracks are separated into nine angle bins: [0.0, 0.1, 0.2, 0.3, 0.4, 0.5, 0.7, 0.9, 1.1, 2.5] in $\tan\theta$ and the nine momentum bins: [0.0, 0.1, 0.2, 0.3, 0.4, 0.5, 0.6, 0.8, 1.0, 10.0 (GeV/c)]. Separation of the proton-like and pion-like particles in each bin is performed based on the VPH, which corresponds to energy deposit in the emulsion films. Figure 7.10 shows the VPH distribution, which has two peaks as described in Sec. 6.1.5. In this figure, the MC distribution includes only tracks from the neutrino interactions, while the data plot contains off-beam timing tracks

as well as the tracks from the neutrino interactions. The MIP and black peaks are fitted by Gaussian to obtain the means ($\mu_{\mathrm{MIP}}, \mu_{\mathrm{black}}$) and the deviations ($\sigma_{\mathrm{MIP}}, \sigma_{\mathrm{black}}$).

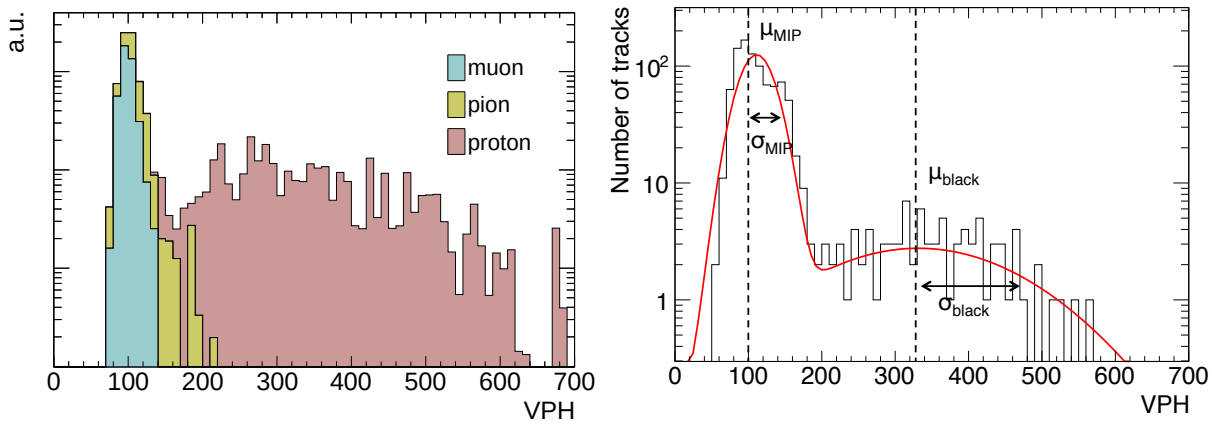

Figure 7.10: VPH distributions in the MC simulation (left) and the data (right). This is an example of tanθ 0.5–0.7, $P\beta$ 0.2–0.3 GeV/c.

The proton-like likelihood L_{proton} and the pion-like likelihood L_{pion} are defined as follows:

$$L_{\mathrm{proton}} \equiv \frac{1}{\sigma_{\mathrm{black}}} \exp\left(\frac{-(v-\mu_{\mathrm{black}})^2}{2\sigma_{\mathrm{black}}^2}\right), \tag{7.5}$$

$$L_{\mathrm{pion}} \equiv \frac{1}{\sigma_{\mathrm{MIP}}} \exp\left(\frac{-(v-\mu_{\mathrm{MIP}})^2}{2\sigma_{\mathrm{MIP}}^2}\right). \tag{7.6}$$

where v is the VPH of the track. The pion-like likelihood ratio $\mathcal{R}$ is defined as:

$$\mathcal{R} \equiv \frac{L_{\mathrm{pion}}}{L_{\mathrm{proton}} + L_{\mathrm{pion}}}. \tag{7.7}$$

According to this parameter, particles with $\mathcal{R}$ more than 0.5 are identified as pions, and those with $\mathcal{R}$ less than 0.5 are identified as protons. Figure 7.11 shows the distribution of the likelihood ratio evaluated by the MC simulation. The proton selection efficiency is evaluated as 76.0% with 98.5% purity, while the pion selection efficiency is evaluated as 98.7% with 78.8% purity for the tracks from the neutrino interactions. The proton identification efficiency is lower than that of pion because high momentum protons contaminate the MIP peak. The separation criteria are determined so that we can get high proton purity to precisely study the proton momentum distribution. This PID process is applied after the VPH corrections described in Sec. 6.1.5.

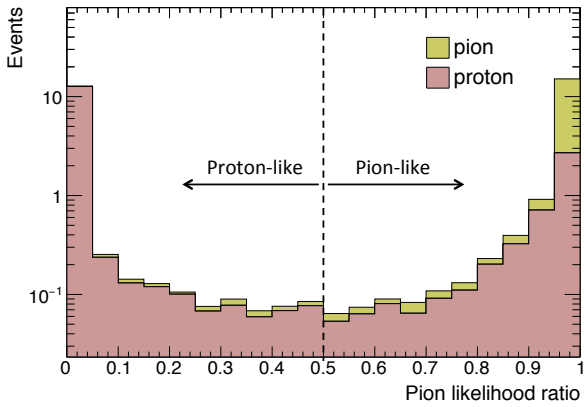

Figure 7.11: Pion-like likelihood ratio evaluated by the MC simulation. Particles with likelihood ratios more than 0.5 are identified as pions, and those with likelihood ratios less than 0.5 are identified as protons.

Chapter 8

Results

This chapter describes the selection of the neutrino interactions in the ECC as well as systematic uncertainties on the selection. Following this, we report multiplicity, angular, and momentum distributions of the outgoing charged particles from the neutrino-water interactions and discuss the results.

8.1 Event selection and background estimation

8.1.1 Event selection

Our signals are CC $\overline{\nu}_\mu$ and ν_μ inclusive interactions on the ECC water target. Muon-like tracks are reconstructed and identified in INGRID, and the track matching between the ECC and INGRID selects the CC interactions in the ECC. This subsection describes the event selection and the determination of the track multiplicity for measurements of the kinematics distributions of protons and pions.

(1) INGRID matching

Track matching between the ECC and INGRID is performed using the SFT hits as described in Sec. 6.4. After the track matching, a total of 14495 events remain as CC interaction candidates. Figure 8.1 shows the angular distributions of the ECC-INGRID matched tracks.

(2) Fiducial volume cut

Most of the tracks selected by the INGRID matching are sand muons. To select neutrino interactions occurring in the ECC, we define a fiducial volume (FV) as the central $16\,\mathrm{cm} \times 17\,\mathrm{cm}$ area from the second-most upstream water gap to the most downstream gap, as shown in Fig. 8.2. The starting points of the muon candidates are required to be in the FV. After the FV cut, 350 events remain as candidates for the interactions in the ECC.

(3) Viewer check

Basetracks on the films might fail to be connected, or wrong basetracks might be connected due to the inefficiency of track detection on the emulsion films or the failure of the automatic reconstruction process. Therefore, all the event candidates are checked by the event display to find the misconnections and properly determine

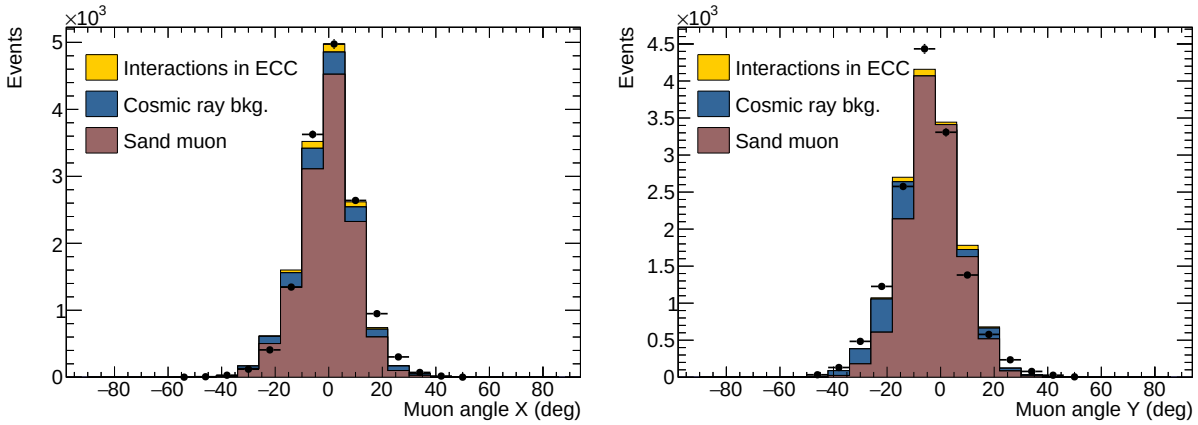

Figure 8.1: Angular distributions of the selected muon candidates after the INGRID matching in the x (left) and y (right) directions.

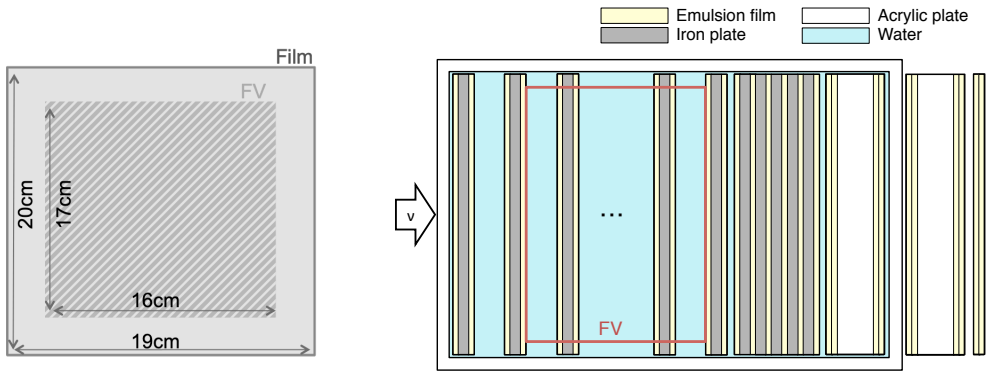

Figure 8.2: Definition of the ECC Fiducial Volume (FV). It is defined as the central 16 cm × 17 cm area from the second-most upstream water gap to the most downstream gap.

the muon starting point. Basetracks near the muon starting point are checked whether they are connected to the starting point.

There is also a possibility of misidentifying large-kink of the sand muons as neutrino events with a forward-going muon and a backward-going pion. Additional selections are applied to such kink event candidates found in the viewer check based on the angle, momentum, and VPH of tracks upstream and downstream of the kink position. Efficiencies of these additional selections and backgrounds of the kink events are evaluated using the sand muons in the MC simulation.

(4) Manual check

After the viewer check, the interaction vertex position is confirmed using a microscope manually. The vertex position of an event with multiple tracks can be determined as the crossing point of the extrapolated tracks. By contrast, the starting positions of events with one track cannot be determined by the data. Therefore, events with single track are contaminated by the interactions on the emulsion films and packing films because the data scanned by HTS do not contain track segments starting in the middle of the emulsion films. To exclude interactions on the emul-

sion films, the upstream emulsion film of the vertex position is manually checked by a microscope. If a track starts in the middle of the emulsion film, that event is considered as an interaction in the emulsion film and excluded. On the other hand, the interactions on the packing films cannot be excluded by this check, because there are no films between the packing films and the water layers. Therefore, the background from the interactions on the packing films is evaluated using the MC simulation.

After the viewer and manual checks, 97 events remain as interactions on water (and the packing films), and 182 events remain as interactions on iron, while 71 events are excluded as interactions in the emulsion films or misconnected tracks. In the MC simulation, we assume that the efficiencies for the viewer and manual checks are 100%.

(5) Momentum consistency check

Cosmic rays coming from the downstream may stop in the ECC and could be connected to the INGRID tracks induced by the neutrino interactions by chance. Besides, the protons and pions from the neutrino interactions also contaminate the muon candidates. To exclude such tracks, the consistencies of the muon momentum measured by MCS in the ECC and that measured by the INGRID range are checked event by event. Since cosmic rays stopping in the ECC have low momenta, the momentum measured by the INGRID range becomes larger than that measured by MCS. By contrast, in the case of the proton or pion, the INGRID range becomes shorter than that expected from the momentum measured by MCS. If the momentum measured by MCS is greater (smaller) than 175% (25%) of that measured by the INGRID range, these events are excluded. In the case of the INGRID-penetrating track, the maximum limit is not set, because a momentum above $1\,\mathrm{GeV}/c$ cannot be measured by the INGRID range.

Figure 8.3 shows the result of the selection, in which momenta measured by the MCS and the INGRID range are compared. By this selection, 11 events are excluded from the neutrino-water event candidates. Figure 8.4 shows angular distributions of the muon candidates before and after the cut, estimated by the MC simulation. The contamination of the protons and pions is around 1.7% of the event candidates before the momentum consistency check, while it is expected to be reduced to around 0.6%.

The events selected above are considered as the candidates for muons from the neutrino interactions on the ECC water target. Two-dimensional detection efficiency is shown in Fig. 8.5, and the number of selected events after each step is summarized in Tab. 8.1. In this pilot run, a total of 86 events are selected as candidates of the CC interactions on the water target, while the MC predicts 91.6 events. The observed number of events is consistent with the MC prediction within the statistical error.

Following the selections described above, the precise vertex position and track multiplicity of each event are determined as below.

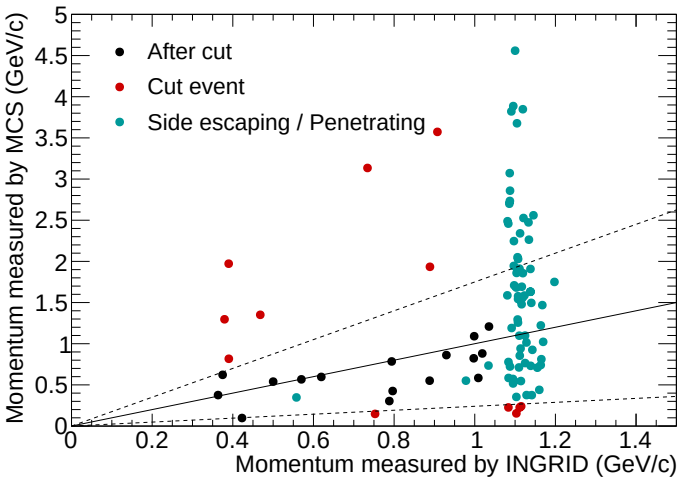

Figure 8.3: Result of the muon momentum consistency check. Momenta measured by the MCS and the INGRID range are compared. The black and green points remain after the check, while the red points are excluded. The green points are corresponding to the INGRID side escaping or penetrating tracks, and only the lower limits of their momenta are set by the INGRID range measurement. The solid line in the plot is the $x = y$ line, and the broken lines correspond to the maximum and minimum limits.

Table 8.1: Number of selected events after each step.

Step	MC (background)	data
INGRID matching	-	14495
FV cut	-	350
Viewer/Manual check	102.4 (25.3)	97
Momentum consistency check	91.6 (21.4)	86

(6) Determination of the vertex

After confirming the muon candidates, the precise vertex positions are determined. First, minimum distances between the muon candidate and tracks around the muon starting point are calculated, and tracks that have a minimum distance shorter than 600 μm are clustered. The midpoint between the closest points of each track and the muon candidate is calculated. We regard the center of mass of these midpoints as a temporary vertex. Then, tracks that have a minimum distance shorter than 100 μm from the temporary vertex are clustered again, and their center of mass is regarded as the reconstructed vertex position.

(7) Partner track determination

Finally, partner tracks that make a vertex with the muon track are selected to determine the track multiplicity. Tracks with a minimum distance less than 50 μm from the vertex calculated in the previous step are selected as the partner tracks. Figure 8.6 shows the distribution of impact parameter (IP) between the reconstructed vertex point and the partner track. The data distribution is consistent with the MC prediction.

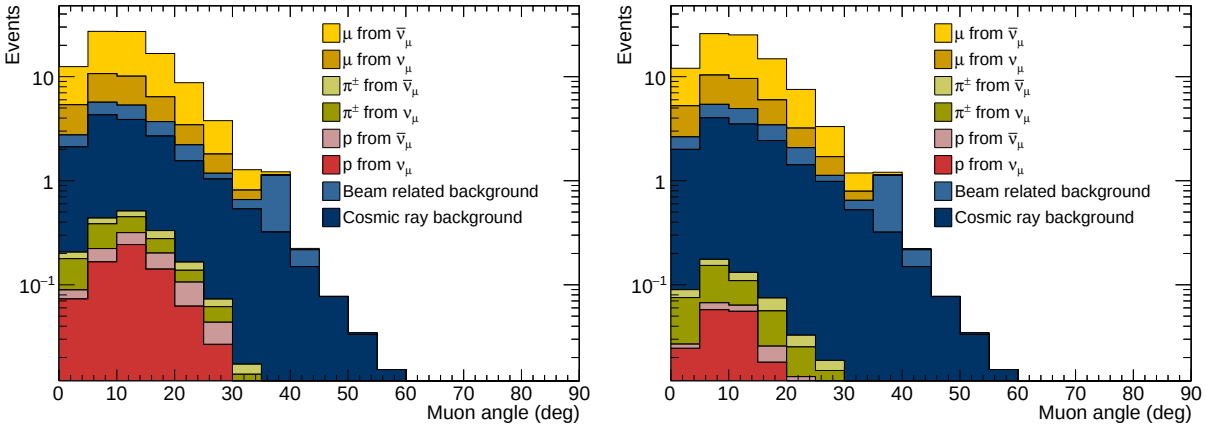

Figure 8.4: Muon angle distributions before (left) and after (right) the momentum consistency check, obtained by the MC simulation.

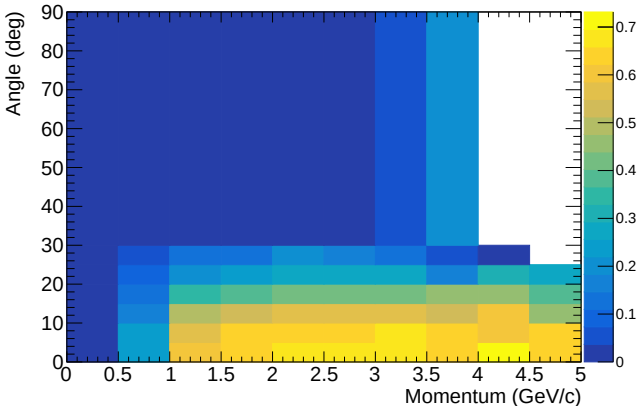

Figure 8.5: Two-dimensional muon detection efficiency estimated by the MC simulation after all selections.

We also applied track length selections to exclude very short tracks from nuclear spallations. It is required that the lengths of tracks with large VPH (black) are two or more layers, and those with small VPH (MIP) are nine or more layers.

After the determination of the multiplicity, the momentum reconstruction and PID processes introduced in Sec. 7.4 are applied. Figure 8.7 shows the distribution of the pion-like likelihood ratio. Particles with likelihood ratios more than 0.5 are regarded as pions, and those less than 0.5 are regarded as protons. The data distribution is consistent with the MC prediction.

After the selections, 18 proton candidates and 13 pion candidates remain as tracks from the CC neutrino interactions on water. The selection efficiencies of the protons and pions from the neutrino interactions are evaluated by the MC simulation. Figure 8.8 shows each selection efficiency, which is defined as the number of selected tracks divided by the number of tracks within the scanning angular acceptance. In all momentum regions above 200 MeV/c, more than 50% of protons are expected to be detected.

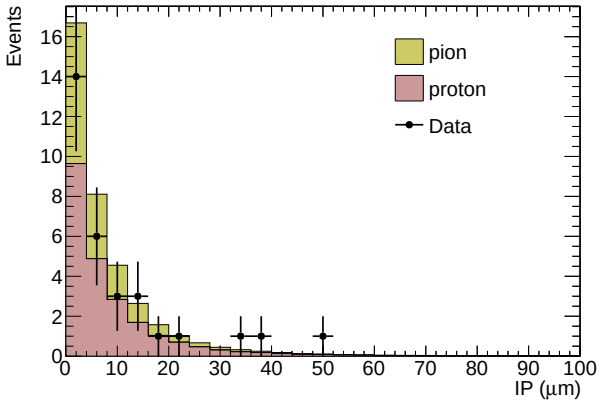

Figure 8.6: IP distribution of the neutrino-water interactions observed in the ECC.

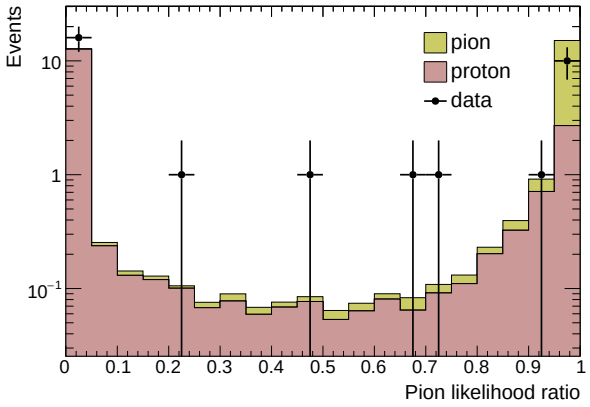

Figure 8.7: Distribution of the pion-like likelihood ratio. Particles with likelihood ratios more than 0.5 are identified as pions, and those with likelihood ratios less than 0.5 are identified as protons. The data distribution is consistent with the MC prediction.

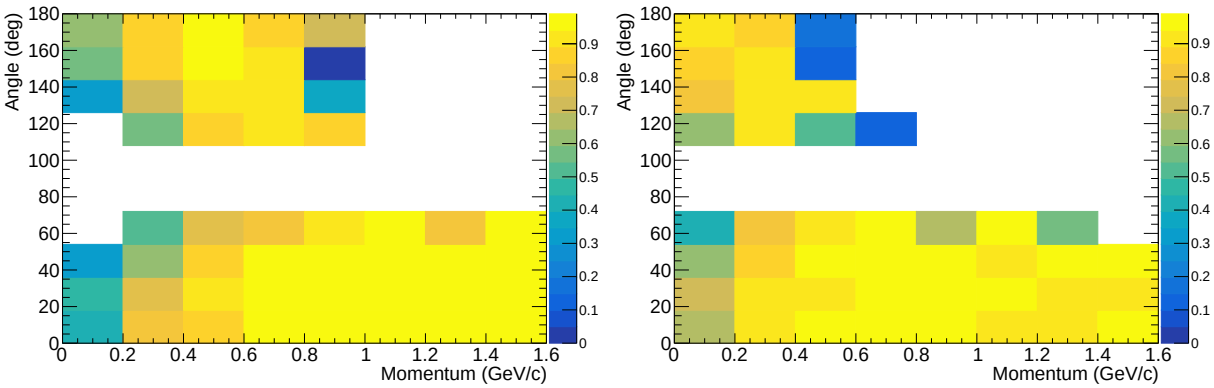

Figure 8.8: Proton (left) and pion (right) detection efficiencies estimated by the MC simulation. Empty bins around 90° are the region out of the scanning acceptance.

8.1.2 Background estimation

The event candidates selected above include backgrounds. To estimate the amount of the background contamination, the following background sources are considered.

Beam-induced backgrounds

Although interactions in the emulsion gel or the plastic base are excluded by the manual check, interactions on the packing films remain and cannot be separated. If vertices have multiple tracks, z-points of the interaction can be reconstructed. This corresponds to determining the target material of the events, thus the interactions on the packing films are excluded. For single-track events, the interactions on the packing films cannot be separated since there is no way to estimate the interaction z-point. The total amount of the interactions on the packing films is estimated by the MC simulation. The 11.5% of the single-track events are estimated as the interactions on the packing films. This fraction corresponds to 5.0% of the total predicted number of events.

In addition to the interactions on the packing films, events induced by misconnection of the sand muons or secondary interactions of tracks from the outside the FV are also evaluated using the MC simulation. These backgrounds are estimated to be smaller than 2.0% of the total predicted number of events.

Cosmic rays

Cosmic muons misconnected by the SFT are the most severe background in our measurement. Many cosmic rays stop in the ECC FV, and if they are matched to the SFT-INGRID tracks by chance, they become backgrounds to the neutrino events. To estimate this effect, mock data are prepared. First, the positions of all the SS prediction tracks in the real data are shifted a few mm in both x and y direction (shifted data). Then, the shifted data is merged into the real data. In this mock data, the number of backgrounds is doubled while it includes the original amount of signals. The event selection is applied to the mock data, and the number of extra events compared to the events selected in the nominal data is treated as the cosmic ray background. According to this estimation, the cosmic background in the selected 86 events is expected to be 15.0 events.

Chance coincidence in the partner track search

Besides the contamination to the muon candidates, cosmic rays which stop in the ECC may be selected as proton or pion candidates by chance. Another set of mock data is prepared to estimate the chance coincidence with cosmic ray tracks. In the mock data, positions of all the muon track candidates are shifted by a few mm in the x and y directions, while the other tracks remain in their original positions. The partner track search is applied to the mock data, and the PID process is also applied to the partner tracks. Since the number of muon tracks in the data is limited, the shifted data is generated 20 times by changing the amount of shifts to reduce the statistical uncertainty. These backgrounds are estimated to be 2.6 out of 18 proton candidates and 1.5 out of 13 pion candidates.

8.1.3 Summary of the event selection

In this pilot run, a total of 86 candidate events of CC interactions on the water target are selected, while the MC prediction is 91.6 events. Table 8.2 shows the observed and predicted numbers of events with a breakdown by the signal and background sources. Figures 8.9 and 8.10 show the vertex position distributions of the selected events on the water and iron targets. The observed number of events is consistent with the MC prediction within the statistical error. In the MC prediction, 58.7% of the events are $\overline{\nu}_\mu$ interactions, while 18.0% are ν_μ interactions. The remaining 23.4% are expected to be background events, in which cosmic-ray backgrounds are dominant. The amount of the background events can be precisely predicted in this measurement. The detection efficiency of the CC neutrino interactions within the acceptance of the INGRID matching is 63.2%. This fraction corresponds to a detection efficiency of 26.8% for all the CC neutrino interactions on the water target in the ECC FV.

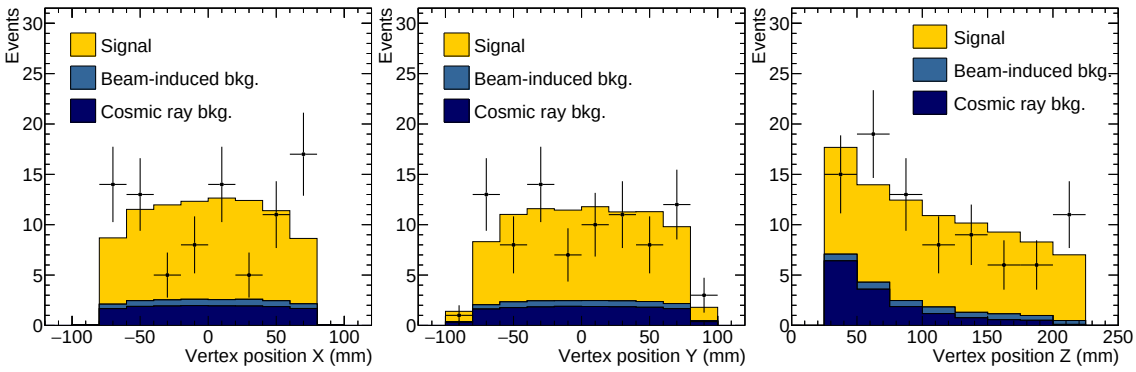

Figure 8.9: Vertex position distributions of the selected events on water target. The position distributions for x (left), y (middle) and z (right) are shown.

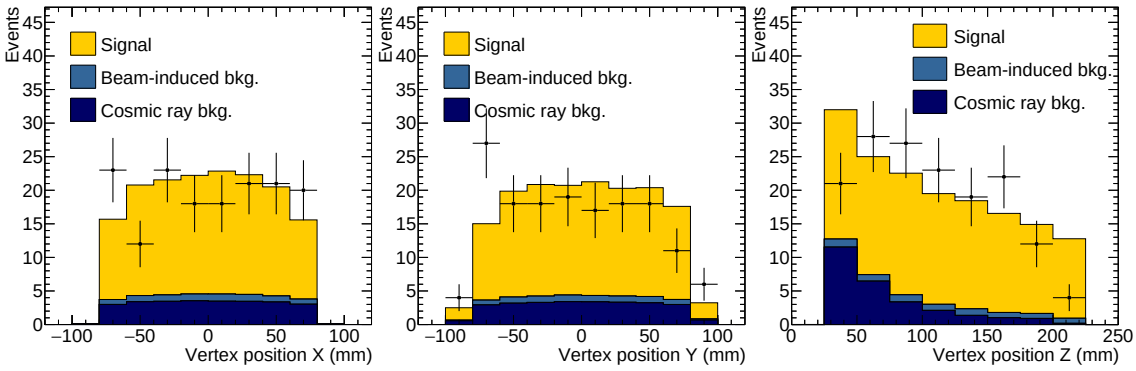

Figure 8.10: Vertex position distributions of the selected events on iron target. The position distributions for x (left), y (middle) and z (right) are shown.

Table 8.2: Observed and predicted numbers of events with a breakdown by the signal and background sources.

Event category	Number of events	Fraction
Observed event	86	-
MC prediction	91.6	-
$\overline{\nu}_\mu$ CC interactions	53.8	58.7%
ν_μ CC interactions	16.5	18.0%
Beam induced background	6.4	7.0%
Cosmic ray background	15.0	16.4%

8.2 Systematic uncertainty

The systematic uncertainty sources are classified into three categories: the neutrino flux, the detector response, and the background estimation. In this analysis, comparisons between the data and the MC predictions are shown without unfolding the detector effects. Therefore, the uncertainty of the neutrino interaction modeling only changes the MC predictions, and it does not affect the results except for a small change in the detection efficiency. The systematic error from each source is evaluated from the data and the MC simulation as follows.

Neutrino flux

Figure 8.11 shows covariance matrices, in which the neutrino flux uncertainty and correlations between each neutrino energy bin of both $\overline{\nu}_\mu$ and ν_μ components at the detector position are described. This matrix is obtained from the uncertainties of the hadron interaction and the J-PARC neutrino beamline configurations. The total flux uncertainties of the $\overline{\nu}_\mu$ and ν_μ components in the antineutrino mode beam are already shown in Fig. 5.3. In our analysis, systematic errors from the neutrino flux are calculated using a set of toy MC simulations. Weighting factor for each set is thrown according to the flux covariance matrix. Then, the change in the number of predicted neutrino interactions from the nominal value is estimated at each bin of the final results. This process is repeated 10^5 times, and the 68% range of the distribution is regarded as the size of the systematic error.

Detector response

Systematic errors from the detector response are evaluated using the sand muon data and the MC simulation. The reconstruction efficiency and the matching efficiency between the detectors are evaluated using the sand muons, and their statistical errors are taken as the systematic error. The systematic error of the muon momentum reconstruction is evaluated in the MC simulation by varying the measured position within the position error ($\sim$1.5 μm), which can be obtained from the alignment accuracy of the automatic reconstruction process. The systematic error from the partner-track search, the momentum reconstruction, and the PID performance is checked by varying the selection criteria in the MC simulation based on the emulsion angular resolution ($\sim$2 mrad). For the PID performance, the difference in the VPH distribution between the data and the MC simulation is also taken into account.

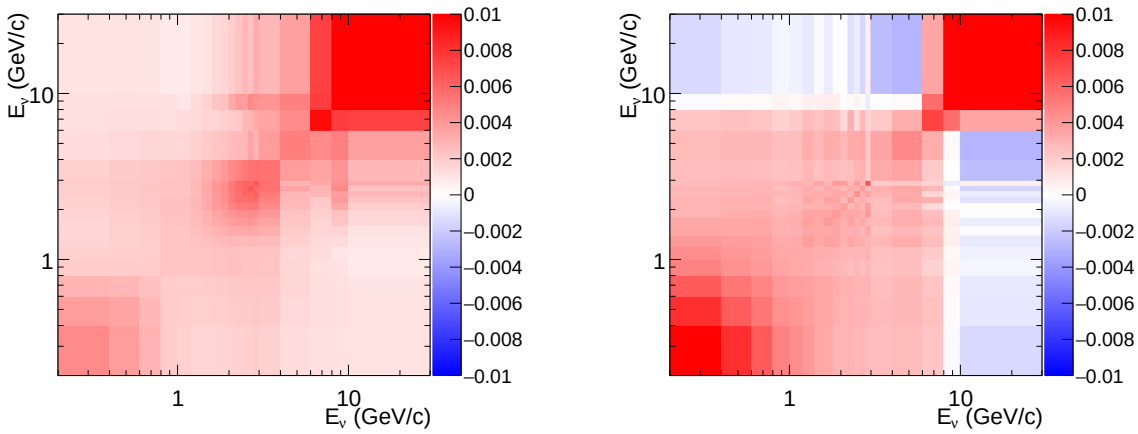

Figure 8.11: Covariance matrices of the flux uncertainties of the $\overline{\nu}_\mu$ (left) and ν_μ (right) components in the antineutrino mode beam.

The dip positions between the MIP and black peaks are checked. There is around a 11% difference at maximum between the data and the MC prediction; thus, the VPH distribution in the MC simulation is varied based on the deviation to see how the PID efficiency and purity change. The systematic error from the GEANT4 physics list is evaluated by trying various physics lists. The detector modeling uncertainty in the GEANT4 simulation is also checked by varying the thickness of materials based on the measured errors. The systematic error from the target mass is calculated from the error of the water layer thickness estimated by the automatic reconstruction process.

Overall, the dominant systematic error for the muon detection is the connection between the ECC and the SFT, which has around a 3% error size. The dominant systematic error for the kinematics measurements of the protons and pions is the PID performance, which has around a 7% error size.

Background estimation

Cosmic rays and beam-induced particles from outside the ECC are considered as background sources for the muon candidates and the partner track candidates. The cosmic background comes from misconnections in the track matching; however, the error size is less than 1%, as the contamination is precisely estimated using the mock data. The uncertainty of the beam-induced background mainly originates from the normalization of the sand muons. There is around a 30% difference between the MC prediction and the data. Thus, the number of sand muons in the MC simulation is normalized with the data. The original 30% difference is taken as the uncertainty of the sand muon, and it corresponds to only 0.5% for the total selected events. Besides, the systematic error from the background of the partner track candidates is also evaluated as less than 1%, as described in Sec. 8.1.2. As above, the total systematic error of these backgrounds is sufficiently small compared to the other

Table 8.3: Summary of the nominal values of the parameters and their 1σ uncertainties used in NEUT [69, 144].

Parameter	Nominal value	1σ uncertainty
M_A^{QE}	$1.05\,\mathrm{GeV/c^2}$	$0.20\,\mathrm{GeV/c^2}$
M_A^{RES}	$0.95\,\mathrm{GeV/c^2}$	$0.15\,\mathrm{GeV/c^2}$
C_5^A	1.01	0.12
Isospin$_{\frac{1}{2}}$ background	1.30	0.20
CCother shape	0	0.40
CCcoh normalization	100%	100%
NCother normalization	100%	30%
NCCoh normalization	100%	30%
2p2h normalization	100%	100%
Fermi momentum	225 MeV/c	31 MeV/c
Pion Absorption	1.1	50%
Pion Charge Exchange (low E)	1.0	50%
Pion Charge Exchange (high E)	1.8	30%
Pion Quasi Elastic (low E)	1.0	50%
Pion Quasi Elastic (high E)	1.8	30%
Pion Inelastic	1	50%

systematic errors in most regions.

Besides the uncertainties above, the uncertainty of the neutrino interaction models changes the MC predictions. Although it does not affect the results, we checked if the model uncertainty covers our results. We also compared the size of the neutrino interaction uncertainty to the other systematic errors since if the total error of our measurement is smaller than the model uncertainty, it means we can give constraints on the neutrino interaction models.

Neutrino interaction

There are various uncertainties in the neutrino interaction and FSI models used in NEUT. Uncertainties from these sources are evaluated by changing parameters in the model based on the current understanding of the neutrino interactions and the FSI. Table 8.3 shows the nominal value and the 1σ error size of each parameter. These parameters and uncertainties are based on Refs. [69,144]. In this analysis, the uncertainty of the nuclear binding energy is not evaluated. However, the uncertainty is covered by the comparison with an alternative nuclear model discussed in Sec.8.3. After evaluating the uncertainty induced by each parameter, the effect of the 2p2h normalization to the selected CC candidate events on the water target is found to be about 8%.

The neutrino interaction uncertainty slightly changes the detection efficiency. The change of the detection efficiency by the change of the parameters in the neutrino interaction model is separately estimated. The typical value is around 1%–2% in each bin. It is added to the systematic error of the detector response.

Figures 8.12 and 8.13 show the systematic errors of each measurement with a breakdown by the uncertainty sources. The fractional error of the expected number of selected events in each bin is plotted. An error of only 5%–8% is derived from the flux uncertainty owing to the significant improvement in the hadron interaction modeling using the NA61/SHINE data. The current detector error is slightly larger than the flux error and is desired to be improved in future analysis. The quadrature sums of the errors from the neutrino flux, the detector response, and the background estimation are smaller than the uncertainty of the neutrino interaction model in almost all bins. This fact shows that our measurements with sufficient statistics will give constraints on the neutrino interaction models.

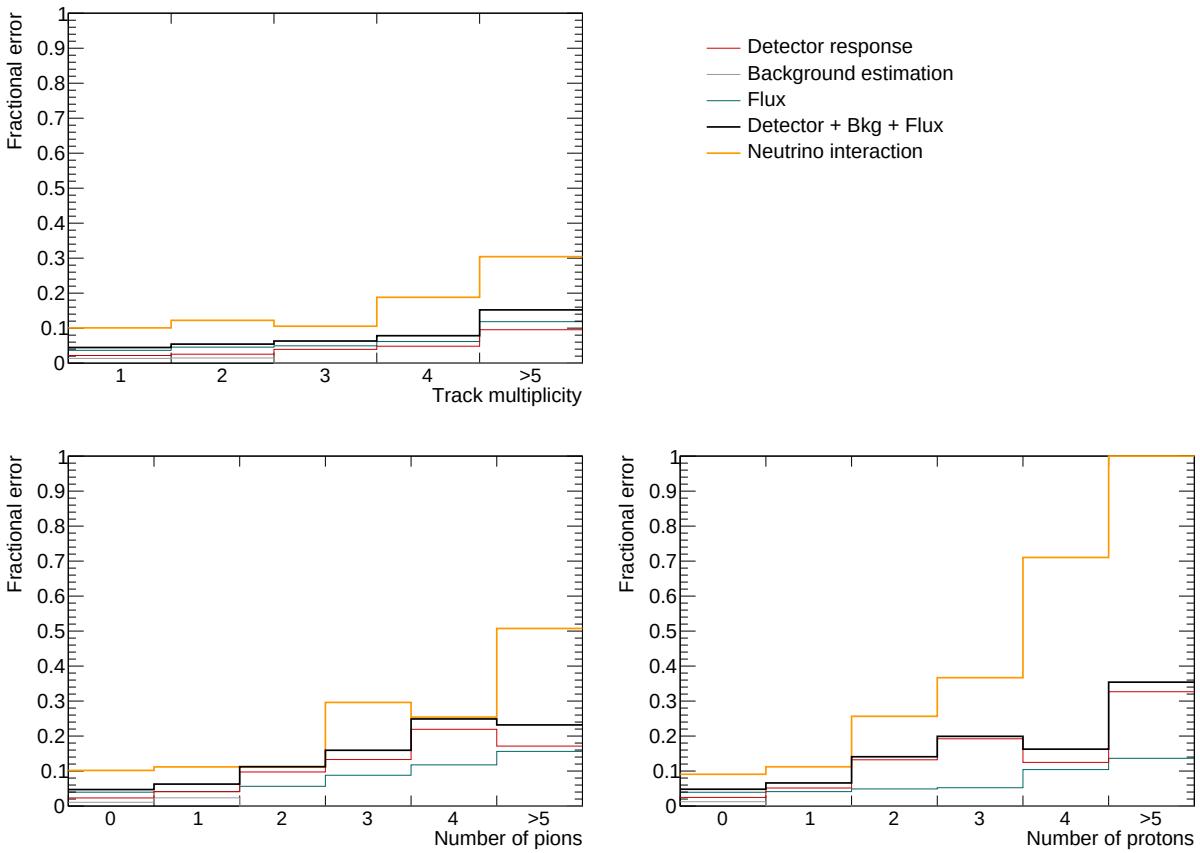

Figure 8.12: Summary of the fractional errors of charged particle multiplicity (top) with a breakdown by the systematic errors from the neutrino flux, the detector response, and the background estimation. The uncertainty of the neutrino interaction model is compared to the other errors. The bottom plots show the fractional errors of the number of pions (middle) and protons (bottom).

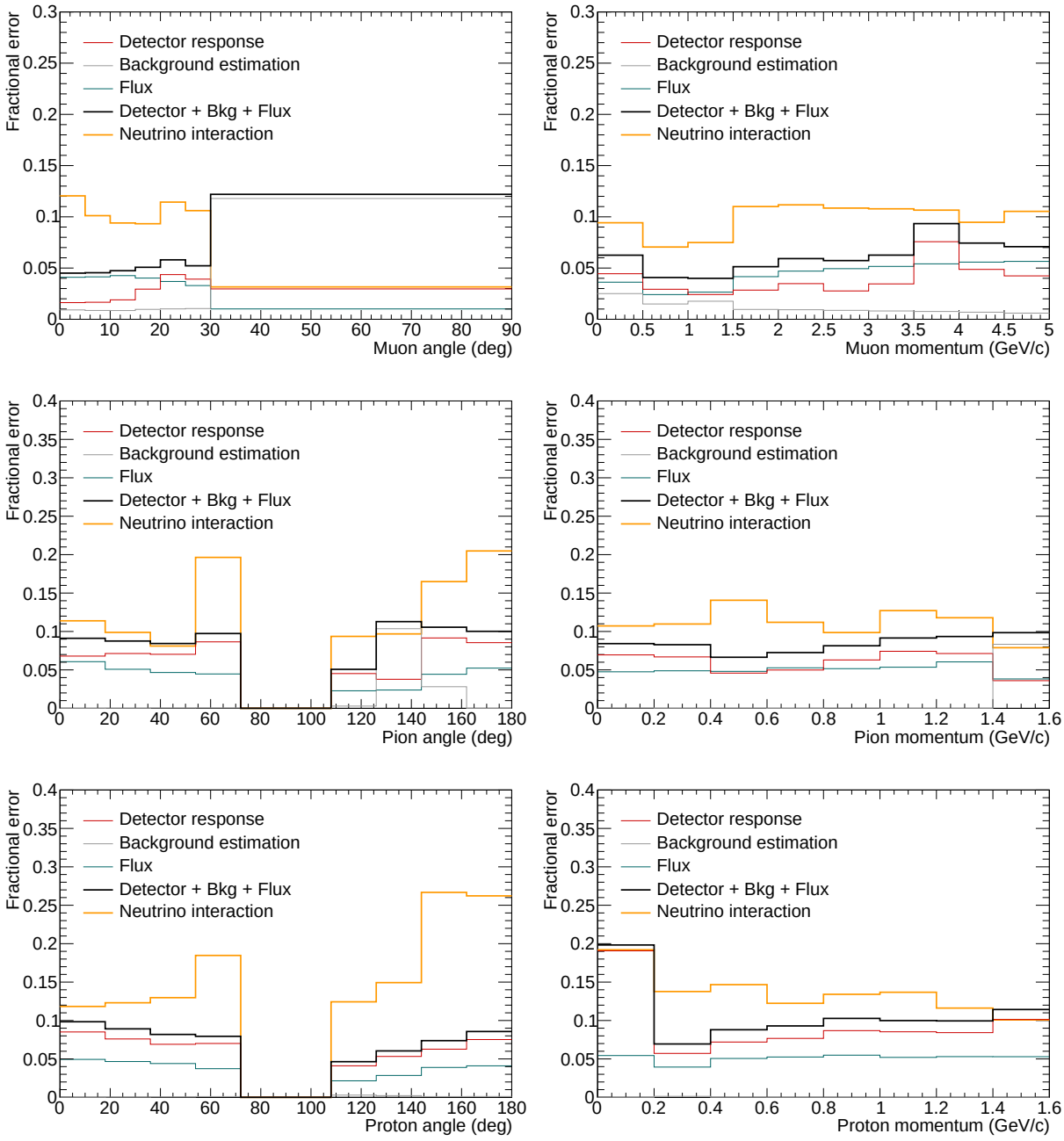

Figure 8.13: Summary of the fractional errors of muon, pion, and proton kinematics with a breakdown by the errors from the neutrino flux, the detector response, and the background estimation. The uncertainty of the neutrino interaction model is compared to the other errors. The left column corresponds to the fractional errors of angular distributions, while the right column corresponds to those of momentum distributions.

8.3 Results

This section describes the results of the multiplicity and kinematics measurements of the neutrino-water interactions in the pilot run. In these measurements, the statistics are insufficient to precisely extract the cross section from the reconstructed distributions. Thus, distributions of the charged particles from the neutrino interactions are compared with model predictions to get insights into the model validity and demonstrate the feasibility of the NINJA detector for future measurements. Below, three types of plots are prepared:

- Raw data distributions without subtracting the backgrounds.
- Signal distributions after subtracting the backgrounds. A breakdown by the interaction mode is shown for the prediction.
- Signal distributions after subtracting the backgrounds, compared with various models.

In each type, the charged particle multiplicity, the numbers of pions and protons, and the momentum and angular distributions of muons, pions, and protons are shown. Note that our results include low-momentum charged particles, especially protons with momenta of 200–400 MeV/c, owing to the high granularity of the emulsion films.

First, we compare raw data distributions to the sums of the neutrino event prediction estimated with the MC simulation and the cosmic-ray background prediction estimated with the off-beam timing data. Figure 8.14 shows the multiplicity of the charged particles and the numbers of pions and protons. The red boxes on the prediction correspond to the quadrature sums of the systematic errors from the neutrino flux, the detector response, and the background estimation. Since it was the antineutrino mode beam, the CCQE interaction ($\overline{\nu}_\mu + p \to \mu^+ + n$) primarily emits a neutron in addition to a muon. Therefore, the selected events contain a large fraction of single-track events, which has only a muon track. Figure 8.15 shows distributions of the reconstructed kinematics of muons, pions, and protons. While the angular resolution for all particles is sufficiently small compared to the bin width in the angle plots, the momentum resolution is typically larger than the momentum binning, especially for high-momentum muons. In the proton momentum distribution, protons with momentum 200–400 MeV/c are successfully detected for the first time in measurements of neutrino-water interactions. Moreover, we also confirmed that the proton data distributions are consistent with the MC predictions within the statistical error, even including these low-momentum protons.

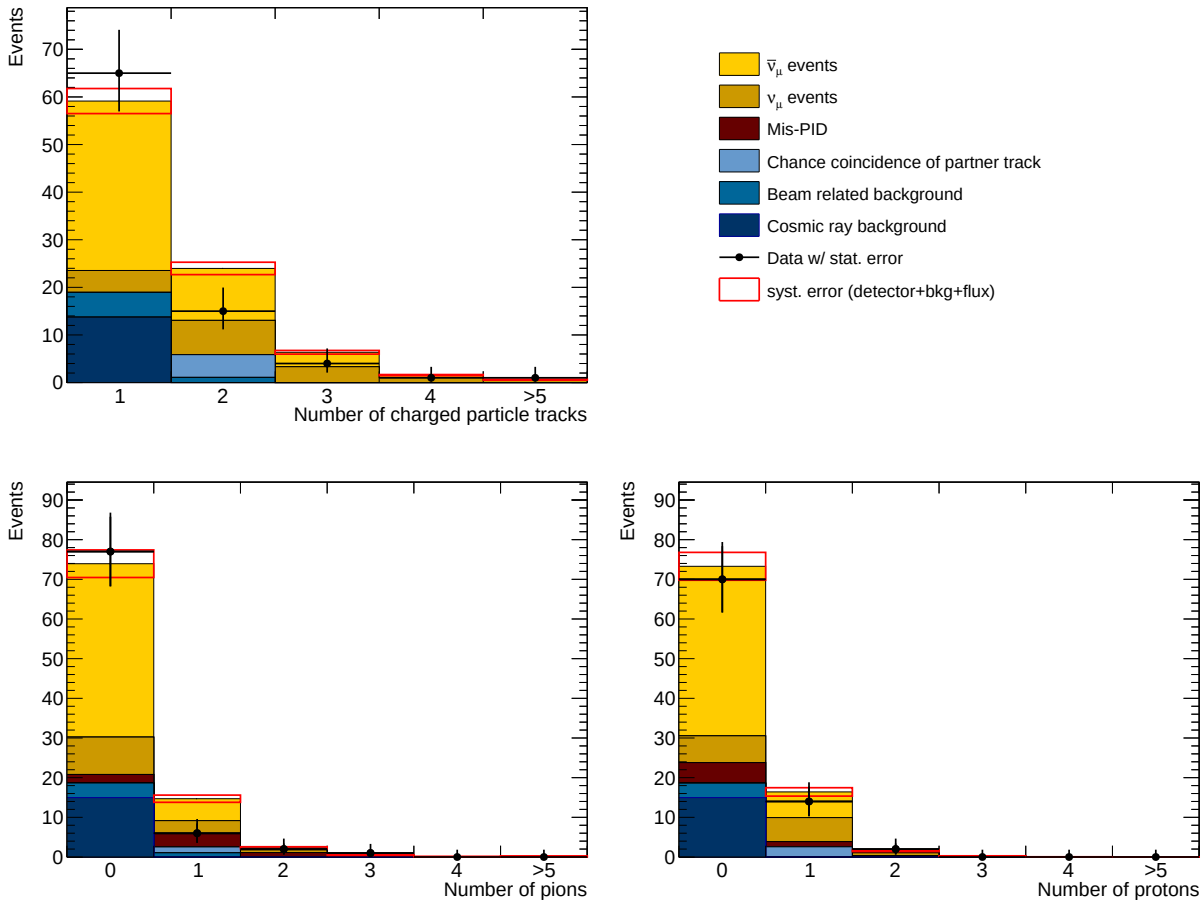

Figure 8.14: Multiplicity of charged particles from neutrino-water interactions and backgrounds (top). The bottom plots show the numbers of pions (left) and protons (right). The data points are shown by marker points with the statistical error bars, and the predictions are shown by histograms with systematic errors as red boxes, which are the quadrature sums of the systematic errors from the neutrino flux, the detector response, and the background estimation.

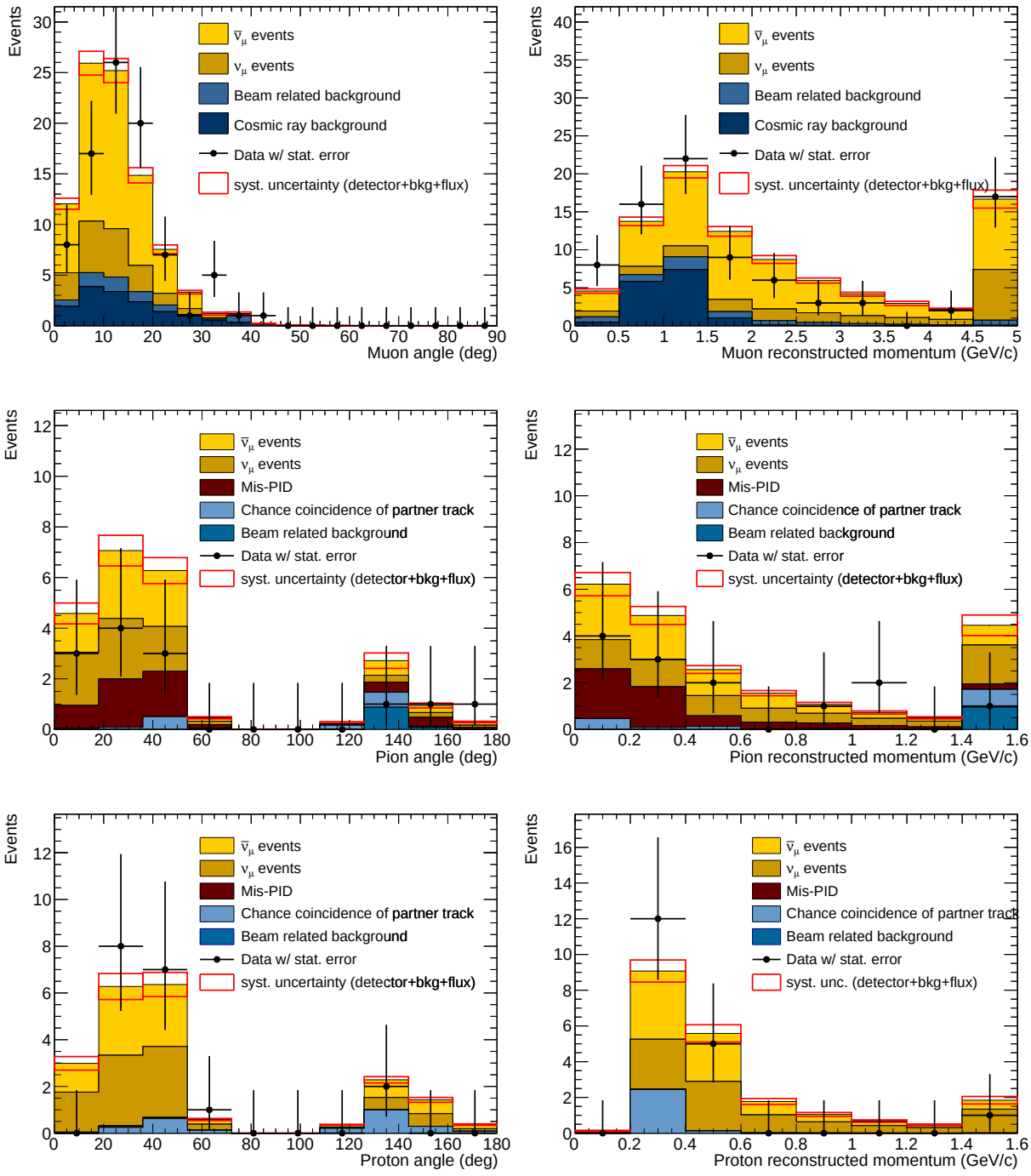

Figure 8.15: Distributions of muon, pion, and proton kinematics from the neutrino-water interactions and backgrounds. The left column shows angular distributions, while the right column shows reconstructed momentum distributions. The angular resolution is sufficiently small compared to the bin width, while the momentum resolution is not especially for the muons with high momentum. The data points are shown by marker points with the statistical error bars, and the predictions are shown by histograms with systematic errors as red boxes, which are the quadrature sums of the systematic errors from the neutrino flux, the detector response, and the background estimation.

Second, in order to extract the signal distributions from our data and compare them with the MC predictions from the neutrino interaction model, backgrounds from neutral-current interactions, interactions on the packing films, cosmic rays, and chance coincidence of the off-beam timing tracks are subtracted from the data using the background prediction. Figures 8.16 and 8.17 show the results, in which the signal distributions are compared with the predictions. In Fig. 8.17, contaminations by misidentification between protons and pions are also subtracted. In these plots, the systematic errors from the flux, the detector response, and the background estimation are included in the error bars of the data points, while the hatched regions correspond to the uncertainty of the neutrino interaction model. We assigned the uncertainty of the neutrino interaction model to the MC prediction because it is exactly what we want to measure in the future, and it is not regarded as a source of the systematic error in this measurement. The small effects of the neutrino interaction models to the detection efficiency is included in the detector error. The systematic errors shown in the red boxes were originally applied to the MC predictions in Figs. 8.14 and 8.15. The absolute values of the error on the bin-by-bin MC predictions are transferred to the data points to show our measurement errors clearly. The measurement's systematic error is smaller than the current model uncertainty. Hence, measurements with the NINJA detector can be expected to constrain neutrino interaction models given more statistics.

Although the statistical error is considerable, the measurement result shows a slightly lower multiplicity of charged particles than the MC prediction. It mainly attributed to an overestimation of pions in the MC simulation, as shown in the bottom plots of Fig. 8.16. The total number of detected pions in all the data is 4.9 ± 3.6 (stat.) $\pm$ 0.6 (syst.), while 14.5 tracks are expected in the MC prediction. By contrast, 15.2 ± 4.2 (stat.) $\pm$ 0.8 (syst.) protons are detected, and this observation is consistent with the nominal MC prediction of 17.7 protons. These tendencies may be induced by the inaccuracy of the modeling of the neutrino interactions and the FSI. Besides this overestimation, the muon distributions have slightly higher angle and lower momentum shapes than the MC prediction. In the other plots, the predictions explain the data well.

In addition to the one-dimensional kinematics distributions, Fig. 8.18 shows the relation between the angle and the momentum of protons and pions. These plots also show good agreement between the data and the MC predictions.

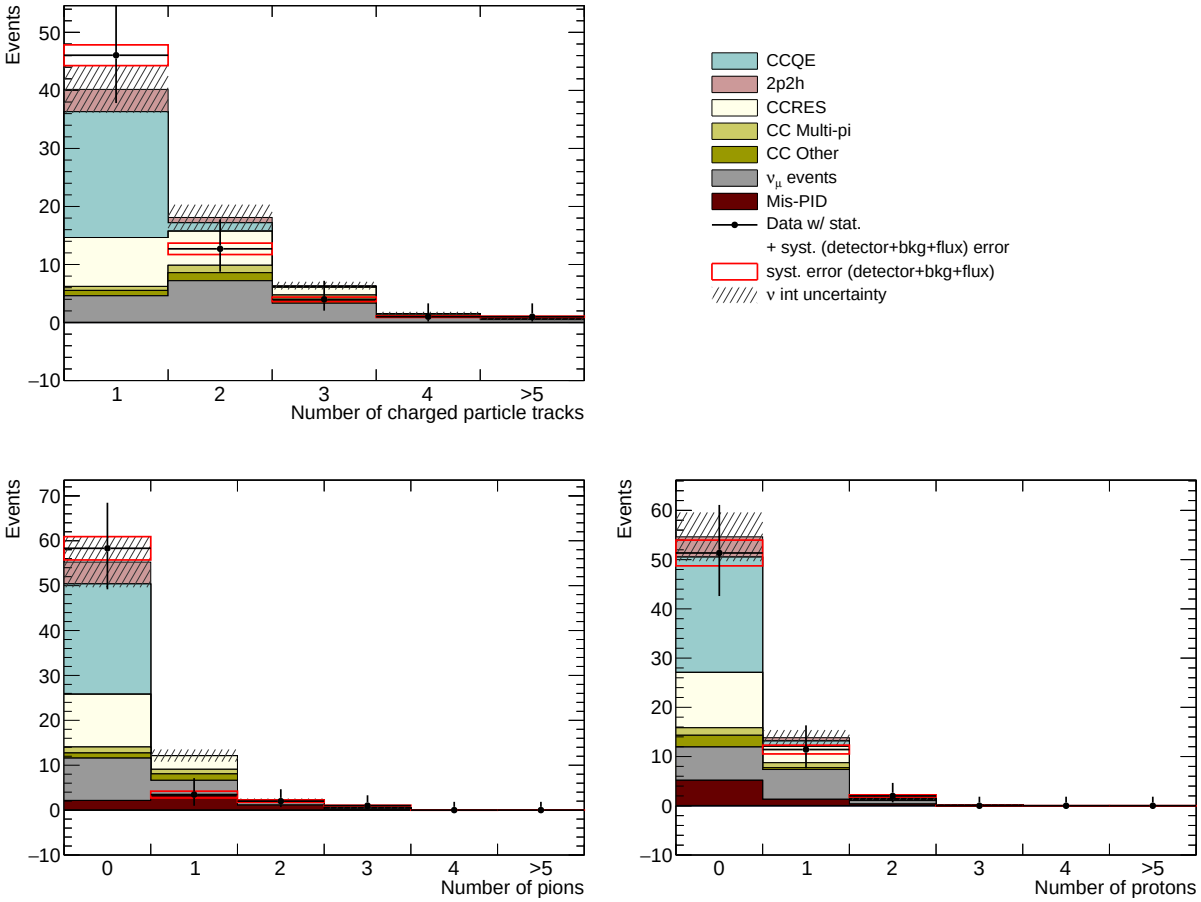

Figure 8.16: Multiplicity of charged particles from the neutrino-water interactions (top). Backgrounds are subtracted from the data and the prediction. The bottom plots show the number of pions (left) and protons (right). The systematic errors from the flux, the detector response, and the background estimation are included in the error bars of the data points, while the hatched regions correspond to the uncertainty of the neutrino interaction model.

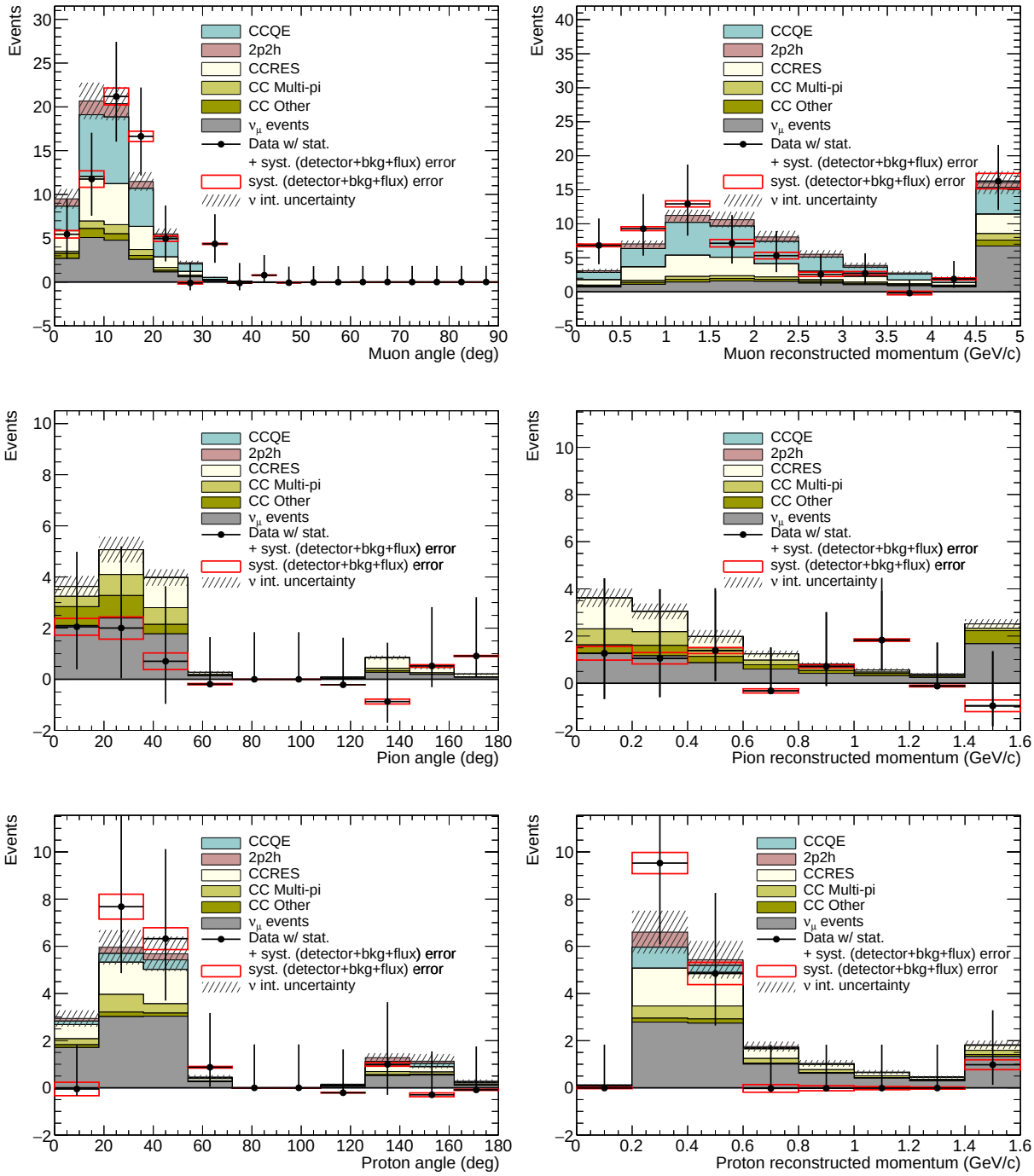

Figure 8.17: Distributions of muon, pion, and proton kinematics. Backgrounds are subtracted from the data and the prediction. The left column shows angular distributions, while the right column shows momentum distributions. The angular resolution is sufficiently small compared to the bin width, while the momentum resolution is not especially for the muons with high momentum. The systematic errors from the flux, the detector response, and the background estimation are included in the error bars of the data points, while the hatched regions correspond to the uncertainty of the neutrino interaction model.

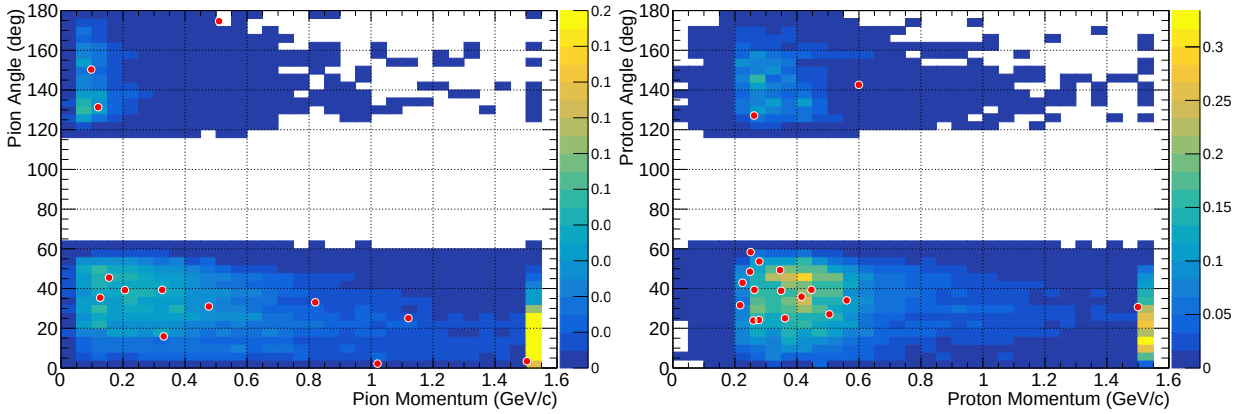

Figure 8.18: Two-dimensional kinematics distributions of pions (left) and protons (right) from the neutrino-water interactions. The red points correspond to the data and the colored histograms represent the MC predictions.

Finally, an alternative model of NEUT using the SF model, and another generator, GENIE [115, 156], are studied for comparisons with the nominal model of NEUT using the LFG model. Figures 8.19 and 8.20 show the results. The interaction models used in the nominal MC simulation are summarized in Tab. 5.1. The alternative model of NEUT is almost the same as those in Tab. 5.1, but the nuclear model is changed to the SF model, and M_A^{QE} is changed from $1.05\,\mathrm{GeV}/c^2$ to $1.21\,\mathrm{GeV}/c^2$. This is because the available M_A^{QE} value for the SF model was limited to $1.21\,\mathrm{GeV}/c^2$ (but now we can also use $1.03\,\mathrm{GeV}/c^2$, and it is recommended in the latest NEUT version). GENIE v3.0.6 with G18_10b_02_11a tuning is used as an alternative generator. In GENIE, M_A^{QE} is set to $0.96\,\mathrm{GeV}/c^2$. The Berger–Sehgal model [157], in which the lepton mass effect (see Sec. 3.1.2) is implemented in the model, is used for the resonant pion production instead of the Rein–Sehgal model. For the FSI simulation, the GENIE hN cascade model [158] is employed. Reduced χ^2 values are evaluated by a log-likelihood method assuming a Poisson distribution in each bin. The results are summarized in each plot in Figs. 8.19 and 8.20. Only the statistical errors are used for the evaluation.

In all the plots, the predictions by the LFG and SF models using NEUT show similar distributions, while the GENIE prediction shows a slightly small number of events. It is difficult to compare the agreement between the data and each MC prediction due to the statistical limitation. However, none of the models explain the data perfectly, especially in the distributions of the number of pions and the muon kinematics. We need more statistics to make a definitive conclusion.

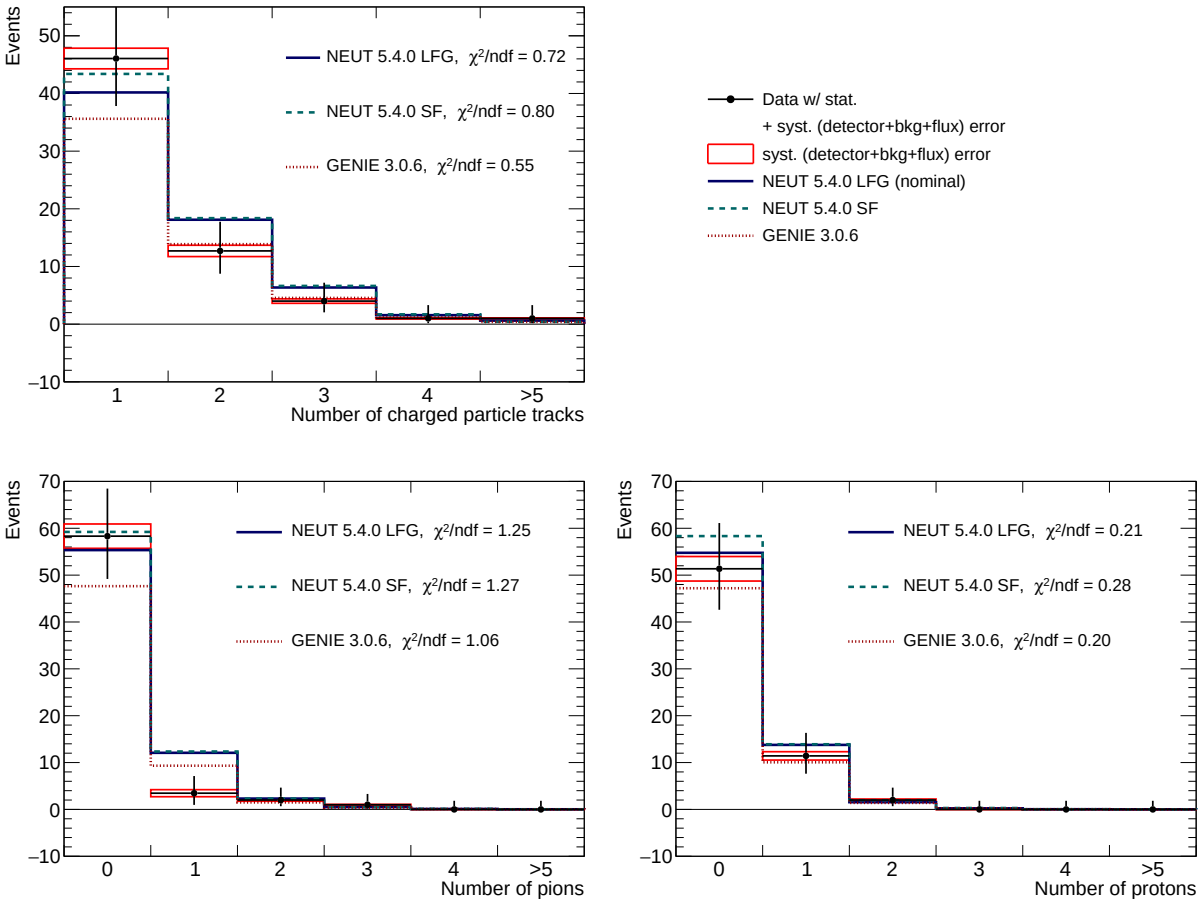

Figure 8.19: Multiplicity of charged particles from the neutrino-water interactions (top) in comparison with NEUT LFG (nominal), NEUT SF, and GENIE predictions. Backgrounds are subtracted from the data and the MC prediction. The bottom plots show the number of pions (left) and protons (right). The systematic errors from the flux, the detector response, and the background estimation are included in the error bars of the data points.

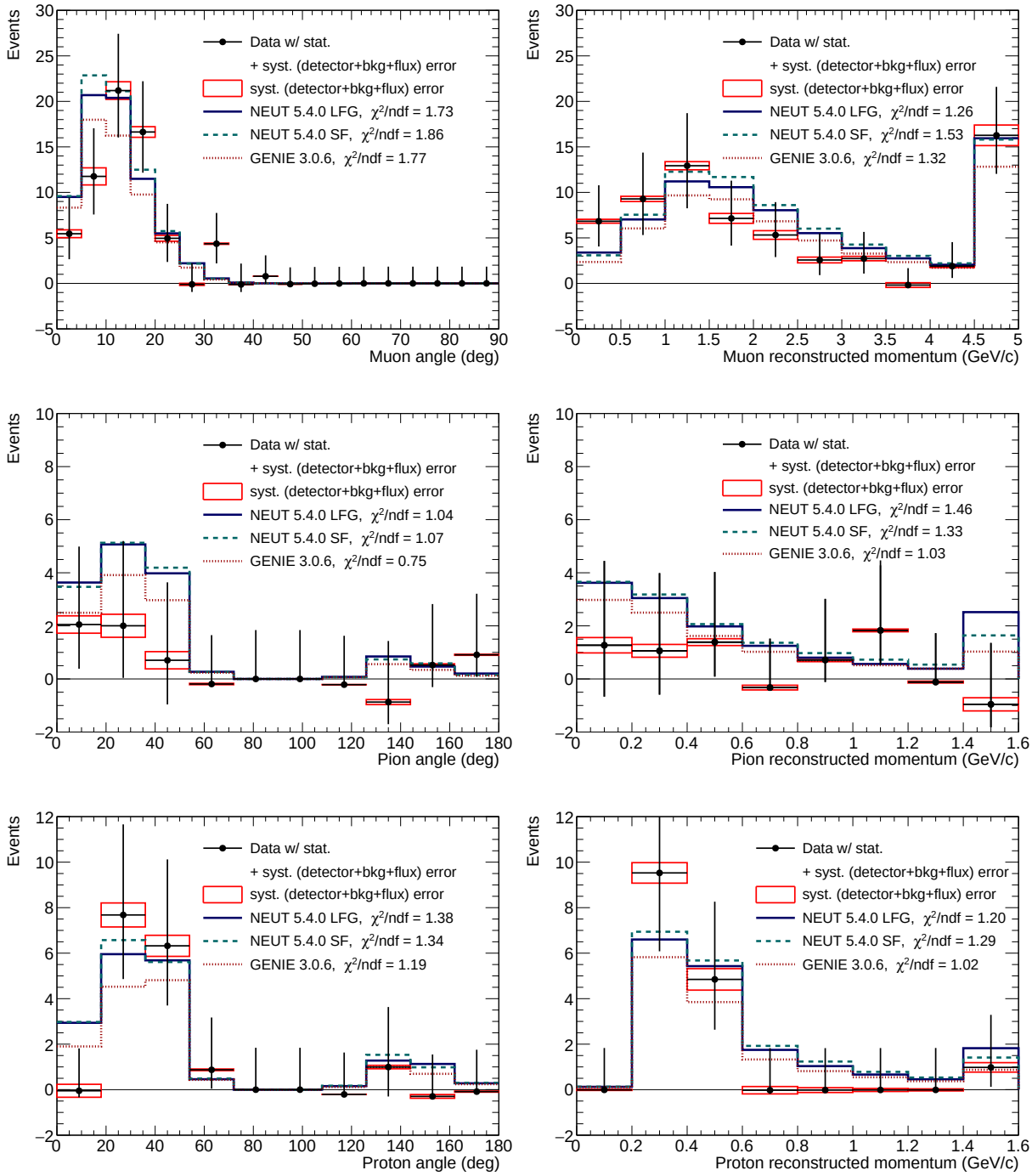

Figure 8.20: Distributions of muon, pion, and proton kinematics. Backgrounds are subtracted from the data and the MC prediction. The left column shows angular distributions, while the right column shows momentum distributions. The angular resolution is sufficiently small compared to the bin width, while the momentum resolution is not sufficiently small especially for the muons with high momenta. The systematic errors from the flux, the detector response, and the background estimation are included in the error bars of the data points.

8.4 Discussion

Discrepancies between the data and the MC prediction

The results show that the shapes of the muon kinematics and the number of pions are different from the MC predictions. Figure 8.21 shows muon angular and momentum distributions separated by the numbers of protons and pions: 0π0p, 0π1p, and 1πNp interactions. The number of events in each sample is summarized in Tab. 8.4. The observed numbers of events are consistent with the MC prediction within the statistical error for the 0π0p and 0π1p samples. In contrast, that in the 1πNp sample is about half of the MC prediction. Besides, the shapes in the 0π1p sample are consistent with the MC predictions, while the shapes in the 0π0p sample do not tend to be explained by the MC predictions well. This fact indicates that our CCQE model may have some issues because the CCQE interactions are dominant in the 0π0p sample. For instance, Q^2 dependency of the CCQE cross section may change such distributions, as described below.

Table 8.4: Breakdown of the number of events after subtracting the backgrounds.

Sample	0π0p	0π1p	1πNp	Other	total
MC	40.2	12.5	10.3	7.4	70.4
Data	44.9	11.0	4.9	4.0	64.8

Q^2 distribution

The momentum transfer (Q^2) of the CCQE interaction can be reconstructed from the muon kinematics. The Q^2 value can be written as follows:

$$Q^2 = -m_\mu^2 + 2E_\nu(E_\mu - p_\mu \cos\theta_\mu), \tag{8.1}$$

where m_μ is the muon mass, E_μ, p_μ, and θ_μ are the energy, momentum, and angle of the reconstructed muon respectively, and E_ν is neutrino energy reconstructed using Eq. 3.1. Figure 8.22 shows the reconstructed Q^2 distribution of the 0π0p sample. Several neutrino-scattering measurements show that there are significant suppressions in data at the small Q^2 region (Q^2 <0.2 GeV$^2/c^2$) [71, 173, 178]. However, the distribution in our data seems consistent with the MC prediction within the statistical error due to the lack of statistics.

The Q^2 distribution is strongly affected by the resolution of the muon momentum reconstruction. As shown in Sec. 7.2.2, the resolution in the pilot run is around 30%–40%. Thus the momentum resolution should be improved to measure the Q^2 distribution precisely. In the NINJA physics run discussed in the next chapter, momenta of roughly a half of all muons can be measured by MRD range (∼5% resolution) because we use a larger muon detector, Baby MIND.

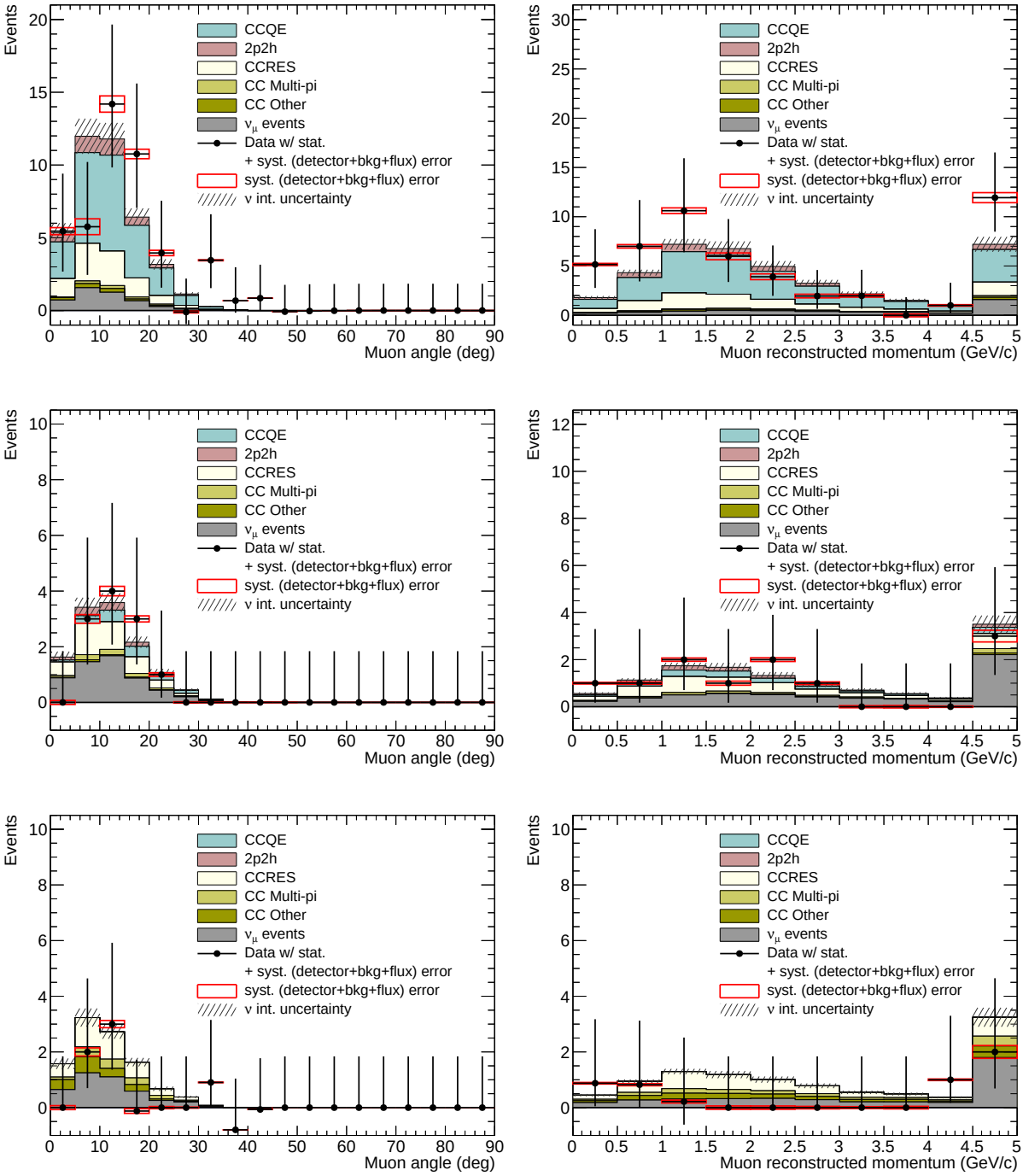

Figure 8.21: Muon angle (left) and momentum (right) distributions for the $0\pi0p$ (top), $0\pi1p$ (middle), and $1\pi Np$ (bottom) interactions.

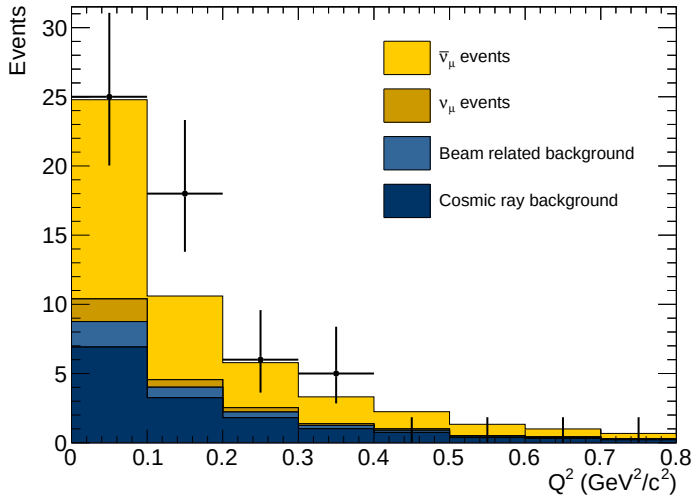

Figure 8.22: Distribution of Q^2 in the CC0π0p sample

Toward a precise measurement

In the pilot run analysis, the systematic error from the detector response is the largest in the measurements of the proton and pion kinematics, as shown in Fig 8.13. There are several ideas to reduce the systematic error from the detector response in the proton and pion kinematics measurements. Figure 8.23 shows fractional error from the detector response with a breakdown by uncertainty sources. In the pilot run measurement, the uncertainty of the PID performance is the largest systematic error source. This error comes from the uncertainty in the relation between the VPH and the energy deposit in the emulsion films. Although the VPH value is proportional to the energy deposit, it has an angle dependency. Besides, there is a significant saturation in a large energy deposit region due to the scanning mechanism. The cause is discussed further in Appendix D.3. More understanding of these effects enables us to estimate the energy deposit from the VPH precisely, and the PID performance will be improved. Then, the systematic error from the detector response in the proton and pion kinematics measurements will be reduced as low as the flux error, and the size of the total systematic error will be similar to that of the muon measurements. In the current measurements, a 10% level total systematic error is assigned in the proton and pion kinematics measurements, while there is around 15%–20% uncertainty from the neutrino interaction modeling in each measurement. Reducing the total systematic error to a 5% level makes it possible to test the neutrino interaction model. Besides, cross sections of neutrino interactions defined by the numbers of protons and pions, such as the CC1π and CC0πNp events, can be measured with a better precision by this improvement.

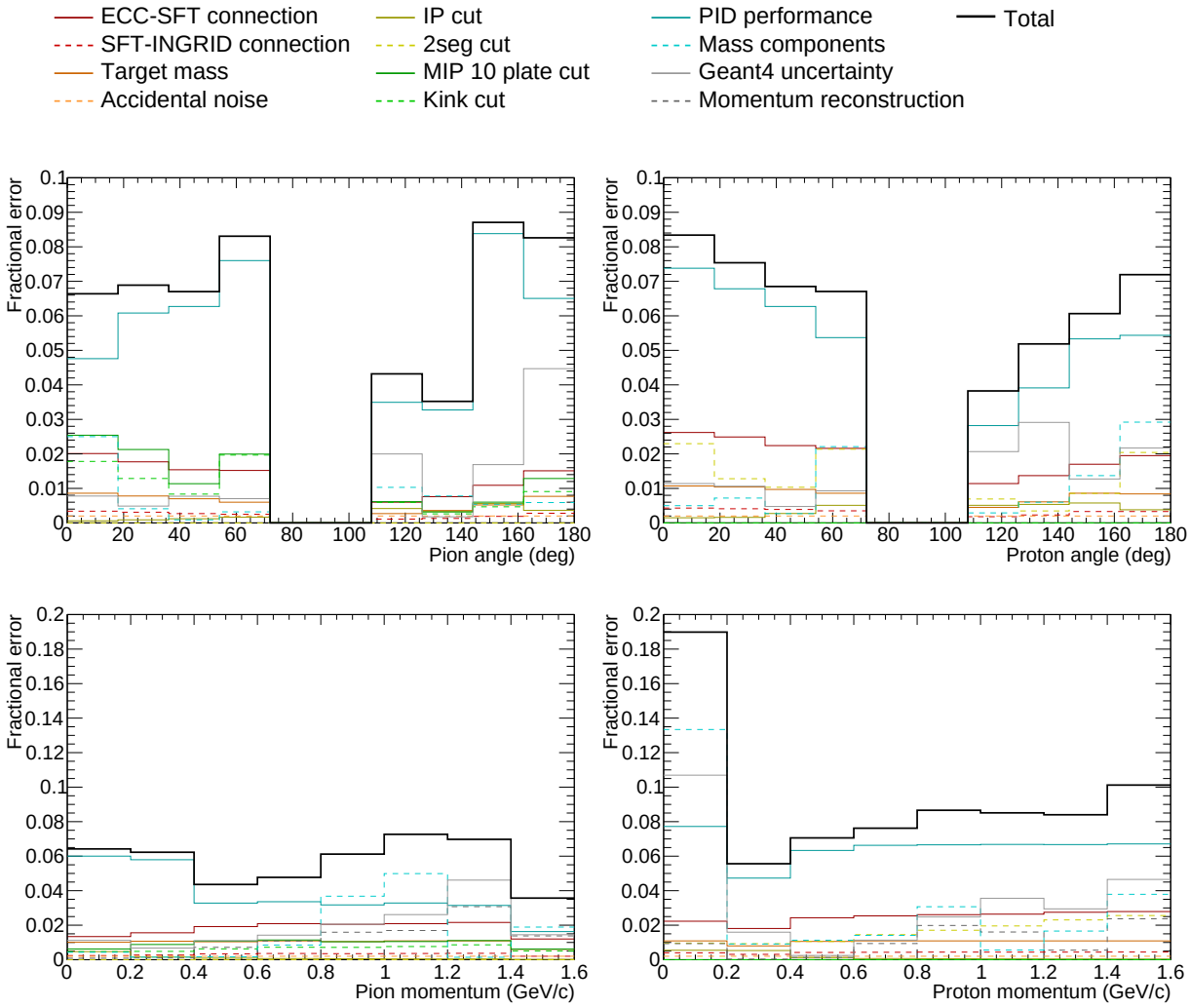

Figure 8.23: Fractional error from the detector response with a breakdown by uncertainty sources.

8.5 Summary of the pilot run results

The first results of the NINJA pilot run using the water-target emulsion detector are reported in this chapter. Multiplicity, angular, and momentum distributions of the outgoing muons, charged pions, and protons from neutrino-water interactions are reported. Protons from the neutrino-water interaction are measured with a 200 MeV/c threshold for the first time in measurements of the neutrino-water interactions. Although the statistical error is large, we found a tendency to overestimate the number of charged pions in the MC simulation. In addition, the muon distributions show slightly higher angle and lower momentum shapes than the MC prediction. Other than these tendencies, the current neutrino interaction models predict the kinematics distributions well within the measurement uncertainty, including low momentum protons down to 200 MeV/c.

The NINJA experiment has finished the first physics beam exposure in early 2020 with the neutrino mode beam, as will be described in the next chapter. We expect a 15 times larger number of neutrino interactions, thus the statistical error will be as small

as the current systematic error. In the current analysis, a relatively large systematic error is applied to the measurements of pions and protons due to the uncertainty of the PID performance. This error can be reduced by further understanding of our detector response, and the size of the total systematic error for the pion and proton measurements will be similar to that of the muon measurements. Then, we will measure the differential cross section with about 10% uncertainty. Using the physics run data, we aim to give a constraint especially on the 2p2h normalization, which has the largest uncertainty in the current analysis. Moreover, differential cross section measurements with respect to the number of protons as well as the measurements of kinematics correlations allow us to give more insights into the nuclear effects. The results of this pilot run have clearly demonstrated the capability of the emulsion detector to achieve these goals.

Chapter 9

NINJA physics run

In the previous sections, we presented the excellent performance of the emulsion detector to precisely measure the neutrino-water interactions. However, we could not give strong constraints on the neutrino interaction models because of the lack of statistics. Thus, the NINJA physics run was carried out to gain higher statistics. In this section, an overview of the NINJA physics run (J-PARC E71) is described.

9.1 Detectors for the physics run

The first beam exposure of the NINJA physics run was carried out from November 2019 to February 2020. While the pilot runs were carried out near the on-axis position using INGRID as the MRD, the physics run was carried out at 1.5° off-axis, which is the same experimental location as WAGASCI [159]. In the physics run, we use Baby MIND, which is one of the WAGASCI detectors, as the MRD. Baby MIND is a magnetized MRD, which covers a larger area than INGRID. Thus, we can access a larger angle acceptance for muons compared to the pilot run. The reason we selected this location is not only to use Baby MIND, but also to access a wide range of analyses by combining our data to the WAGASCI data in the future. For instance, NINJA can use the WAGASCI detectors to exclude external background tracks, and we can also perform combined cross-section measurements using both NINJA and WAGASCI data.

Figure 9.1 shows the experimental setup of WAGASCI and NINJA. The NINJA detector is surrounded by the detectors for the WAGASCI experiment consisting of two WAGASCI modules [159], Proton Module [160], Baby MIND [161], and two Wall MRDs. Baby MIND is composed of magnetized iron plates and scintillator tracking planes. Owing to the magnetized iron plates, Baby MIND gives charge identification, by which neutrino and antineutrino CC interactions are separated. Figure 9.2 shows an exploded view of the NINJA detectors for the physics run. The basic structure of the ECCs is not changed, but the water target mass is significantly increased by arranging nine ECCs in a 3×3 array. Since a larger timestamping device is required to cover the nine ECCs, a scintillator tracker and an emulsion shifter are newly developed to give time information to emulsion tracks in the ECCs.

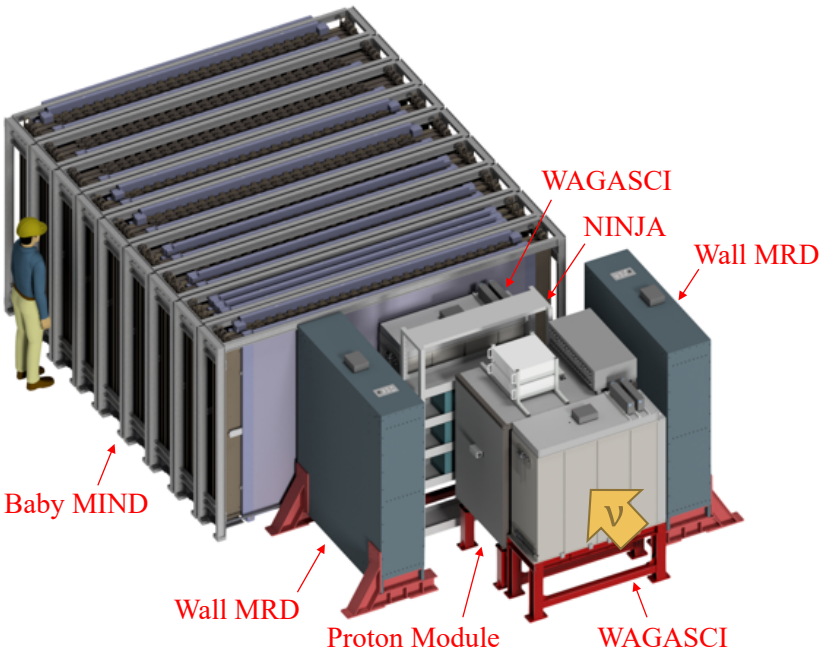

Figure 9.1: Schematic view of the detector configuration of the WAGASCI and NINJA experiments

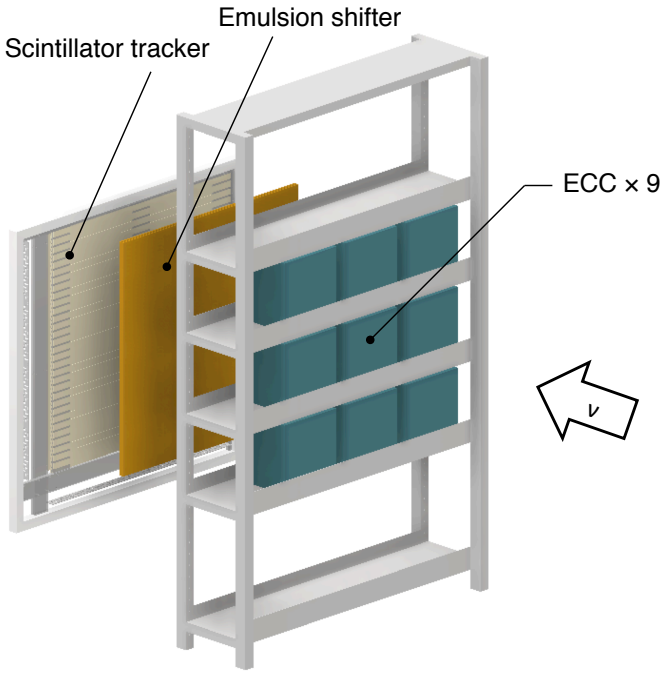

Figure 9.2: Exploded view of the detectors for the NINJA physics run.

Details of the NINJA detector components and Baby MIND are summarized below.

- ECC: The same structure as the pilot run ECC, but larger emulsion films (25 cm × 25 cm) are used. Accordingly, the size of the desiccator also becomes larger. In addition, the thickness of the water target layers is increased from 2,0 mm to 2.3 mm to increase the water target mass. This does not affect the proton momentum threshold, because the iron plate thickness determines the threshold. The ECCs consist of water, iron, polystyrene (plastic base of the emulsion film), and emulsion gel. The total mass of each component is summarized in Tab. 9.1.

Table 9.1: Total mass of the components in the physics run ECCs. The ECCs consist of water, iron, polystyrene (plastic base of the emulsion film), and emulsion gel.

Material	Mass (kg)
Water	75
Iron	130
Polystyrene	15
Emulsion	30

- Baby MIND: It is composed of 18 scintillator tracking modules and 33 magnetized iron plates. Each iron plate has a 3-cm thickness, and it provides a 1.5-T magnetic field. Charge identification of muons is possible by reconstructing the curvature of the tracks. Baby MIND covers an area of 3.5 m horizontally and 2 m vertically, thus it has a larger muon angle acceptance than INGRID. The horizontal scintillator has a 3-cm width, while the vertical scintillator has a 21-cm width. Thus the position resolutions of Baby MIND in both horizontal and vertical directions are not sufficient for the track matching between the ECCs and Baby MIND. Therefore, two types of timestamping devices are installed as follows.

- Emulsion shifter: Emulsion shifters have been used in previous pilot runs [129, 131] and other experiments [133]. In this physics run, emulsion films are mounted on two moving walls and a fixed wall, and the films cover a 1 m×1 m area. Time information is given by two moving walls, which shift 2 mm in different cycles, four days and four hours. Thus, the emulsion shifter gives time information to the tracks in the ECCs with a four-hour resolution.

- Scintillator tracker [162]: This tracker is composed of scintillator bars with wavelength shifting fibers. The scintillator tracker also covers an area of 1 m×1 m. The same scintillators used in the WAGASCI detector are used. The scintillator bars have dimensions of 0.3 cm×2.5 cm×102 cm, and they are mutually staggered in four layers. The total number of the scintillators are 248, and scintillation light is read out by MPPCs. Tracks are reconstructed by the hit or unhit patterns of the scintillators, thus the tracker gives a better position resolution than the scintillator width. It gives spill by spill time information to the tracks in the ECCs separated every four hours by the emulsion shifter. Thus, it allows us to connect these tracks to the tracks reconstructed in Baby MIND.

WAGASCI uses the Wall MRDs to measure large-angle muons. However, NINJA does not use the Wall MRDs, because we have the timestamping devices only downstream of the NINJA detector. Another timestamping device covering the side of the NINJA detectors is required to measure the large-angle muons using the Wall MRDs. Although the NINJA analysis can be performed without the Proton Module or WAGASCI Module data, using these data may improve track matching efficiency between the ECCs and Baby MIND as well as background rejection capability.

Table 9.2 summarizes the differences between the pilot run and physics run detectors. Compared to the pilot run, the physics run detector has the larger target mass and the wider muon acceptance. Therefore, we significantly increase the statistics of observed neutrino interactions. In the physics run, Baby MIND can measure higher momentum muons than INGRID by range because the total iron thickness is thicker than that in INGRID. Momenta of roughly half of all muons can be measured by Baby MIND range with a 5% resolution.

Table 9.2: Comparison between the pilot run and the physics run detectors. The water target masses are values before the fiducial volume cut.

	Physics run	Pilot run
Water target mass (kg)	75	4
Muon acceptance	$-1.5 < \tan\theta_{x(y)} < 2.5(1.5)$	$\lvert\tan\theta\rvert<1$
Charge identification	Yes	No
Momentum measured by MRD range (GeV/c)	<1.5	<1.0

9.2 Status of beam exposure and data analysis

The first beam exposure of the NINJA physics run was carried out from November 2019 to February 2020. A total of 75-kg water target was exposed to 4.8×10^{20} POT of the neutrino mode beam. This beam exposure is referred to as J-PARC E71a. During the beam exposure, all the detectors were operated stably. Considering periods in which all the detectors, including Baby MIND, were collecting data, a total of 4.2×10^{20} POT will be used for the analysis. The total number of the emulsion films is around 1500, and all the emulsion films were developed immediately after the exposure. Scanning of the emulsion films is currently ongoing, and it is planned to be finished in middle 2021.

Another beam exposure (E71b) is planned in 2022, after the J-PARC MR upgrade. In total, at least 1.0×10^{21} POT will be accumulated in E71 (=E71a+E71b). After that, we also plan to increase the target mass and measure ν_e cross section as well as the ν_μ cross section. To achieve measurements with an even larger target mass, mass production of the emulsion films and a high-speed scanning system are essential. At Nagoya University, the development of a large-scale machine for emulsion gel production is ongoing, as well as a next-generation scanning machine (HTS2).

9.3 Goals of the physics run

In the physics run, we expect 15 times more neutrino-water interactions passing the event selection than that observed in the pilot run. The first goals of the physics run are the measurement of the track multiplicity and the kinematics of muons, pions, and protons, as well as measurements of differential cross-sections with respect to the numbers of protons and pions. Through these measurements, we aim to contribute to developing better neutrino interaction models. The rest part of this thesis describes the expected performance of our physics run and prospects for the improvement of the neutrino interaction models.

9.4 MC simulation

Expected outcomes of the NINJA physics run are estimated using an MC simulation. In this simulation, only flux simulation by JNUBEAM and neutrino interaction simulation by NEUT are performed, and detector responses are not simulated. Thus, selections based on the angle and momentum acceptance are applied to the NEUT outputs. Neutrino interaction models used in the MC simulation are summarized in Tab. 9.3. The used models are almost the same as those in the pilot run, but the nuclear model is changed from the LFG model to the more sophisticated SF model.

Table 9.3: Neutrino interaction models used in the E71 simulation

Mode	Model
CCQE	Nieves 1p1h, SF model (M_A^{QE}=1.03 GeV/c^2)
2p2h	Nieves *et al.*
1π	Rein-Sehgal
Coherent	Barger-Sehgal
DIS	GRV98 PDF with Bodek-Yang modifications
FSI	Semiclassical intranuclear cascade model

With E71 total statistics, around 3300 CC events are expected to be measured. Figure 9.3 shows the expected number of CC neutrino interactions observed in E71. The observed number of events with a breakdown by interaction modes is summarized in Tab. 9.4. In this MC simulation, detector efficiency is assumed to be 80%. In E71b, it is assumed that the number of ECCs will be increased to 12, and the accumulated POT is 5.2×10^{20} POT, while 4.8×10^{20} POT is already accumulated in E71a with the nine ECCs.

Table 9.4: Breakdown of the expected number of events observed in E71

Mode	CCQE	2p2h	CCRES	CC DIS	CC other	Total
E71a	497.5	112.3	467.3	136.7	134.5	1348.3
E71b	718.6	162.2	675.0	197.5	194.3	1947.5
E71 total	1216.1	274.5	1142.3	334.2	328.8	3295.8

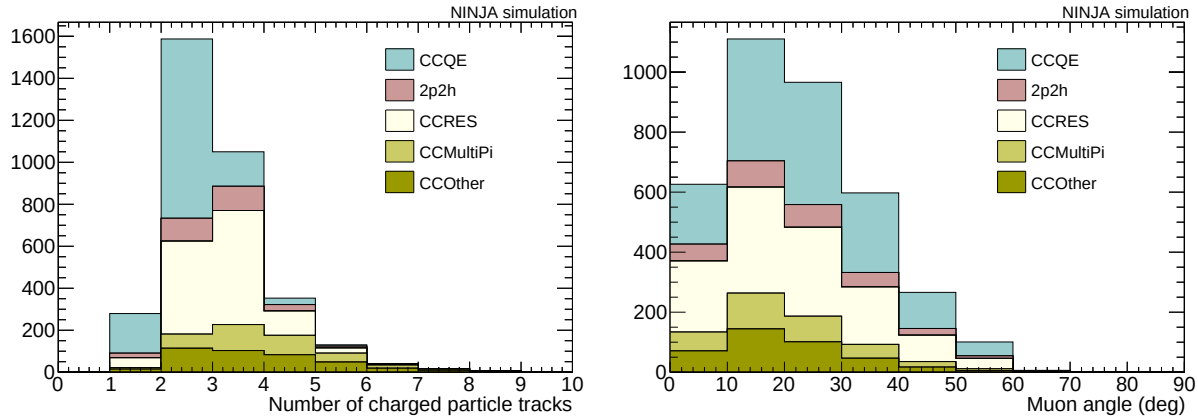

Figure 9.3: Expected number of the events of NINJA physics run (E71). Track multiplicity (left) and muon angular distribution (right) are shown.

We aim to measure protons and pions precisely. There is an important change from the pilot run analysis regarding the detection of protons and pions. In the pilot run analysis, the micro track angle used in the analysis was limited $|\tan\theta_{\mathrm{micro}}|< 1.3$. This is because HTS was usually used to scan tracks with angle $|\tan\theta_{\mathrm{micro}}|\lesssim 1.5$. After many tunings, now the limitation is extended up to $|\tan\theta_{\mathrm{micro}}|\lesssim 4.0$. This change is critical to cover more protons and pions from the neutrino interactions. Figure 9.4 shows the angular distribution of protons from neutrino-water interactions. In the physics run, 86.7% of all the protons above 200 MeV/c are detected, while only 57.0% of them were covered in the pilot run acceptance.

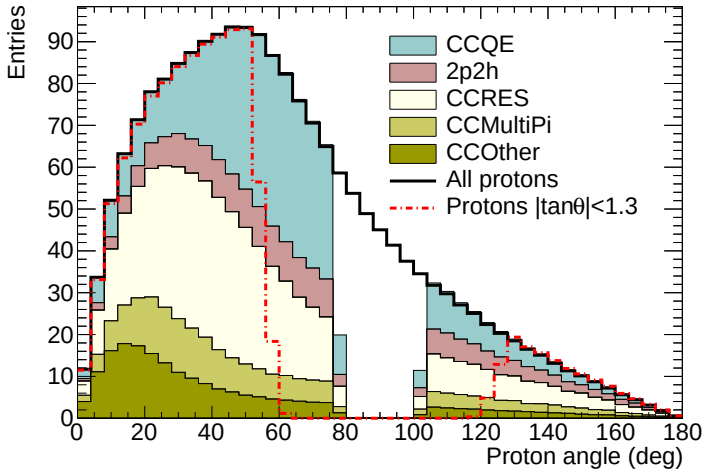

Figure 9.4: Angular distribution of protons from the neutrino-water interactions detected within the HTS angle acceptance. The acceptance is extended to $|\tan\theta_{\mathrm{micro}}|\lesssim 4.0$, thus 86.7% of all the protons above 200 MeV/c are covered.

In the measurements of neutrino interactions, observed events are classified based on the numbers of protons and pions. Although we cannot separate the observed events into each interaction mode in the data, separating them based on the number of tracks makes it easy to see the effects in specific interaction modes. For instance, the CC0π2p

(CC interactions with no pion and two protons) sample will be a 2p2h enriched sample. Owing to the low momentum threshold of the emulsion detector, we can measure most of the protons from 2p2h interactions, and they are categorized into the CC0π2p sample, in which about one-third of the events are expected to be the 2p2h interactions. We can clearly see the relation between the proton pairs, such as opening angle distributions, and measurement of such observables will be a different approach from the T2K near detectors.

Figure 9.5 left shows the opening angle distribution of the two protons in the CC0π2p sample. As described in Sec. 3.4.2, the current 2p2h models predict back-to-back protons ($\cos\theta \sim -1$ in the plot). The hatched region corresponds to the normalization uncertainty of the 2p2h interactions. The systematic errors from the detector response, the flux, and all the other uncertainties of the neutrino interaction model are shown by the red boxes. The error bars show the total errors including both systematic and statistical errors. The fact that the measurement error is much smaller than the 2p2h normalization uncertainty means the NINJA measurements will constrain the 2p2h uncertainty beyond the current knowledge. Figure 9.5 right plot shows the pion momentum distribution. The uncertainties from the pion FSIs are shown in the hatched regions. Pion scattering in the nuclear medium changes its momentum. Besides, absorption, production, and charge exchange of a pion change the total number of pions, and this change corresponds to the normalization of the plot. Thus, measurement of pion momentum will give constraints on the FSI models.

The reason why the 2p2h and the FSI still have significantly large uncertainties in the current models is the lack of measurements of low momentum protons and pions. The NINJA physics run provides proton and pion information with sufficiently low momentum thresholds, which was achieved in the pilot run. Hence, we can probe the characteristics of the neutrino interactions, such as the 2p2h interactions and the FSI effects. In the next chapter, we discuss how we contribute to the neutrino interaction modeling using the NINJA results, as well as impacts on the T2K neutrino oscillation analysis.

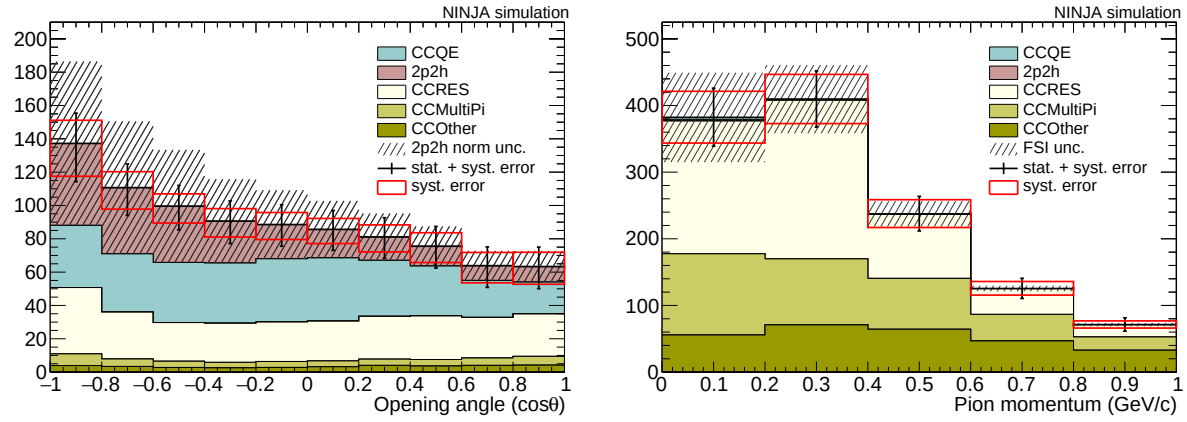

Figure 9.5: Examples of the MC simulation results with measurement errors. Left plot shows the opening angle of two protons in the CC0π2p sample. Right plot shows momentum distribution of pions in the CC inclusive events.

Chapter 10

Prospects of neutrino interaction modeling

In this chapter, we discuss how we apply the NINJA measurements to T2K. Firstly, we check the impact of our measurements on the T2K oscillation analysis when the fitting to the NINJA data is performed in the same way as the ND280 to constrain the neutrino interaction models. Secondly, we consider the method to validate the interaction models using a multivariate analysis to the NINJA data. Finally, we introduce several ideas of other measurements by NINJA to improve the interaction models.

10.1 Impact on the oscillation analysis using an internal constraint method

10.1.1 Analysis overview

In the T2K oscillation analysis, the measurements at ND280 give a prediction of the neutrino events at SK with constraints on the flux and neutrino interaction uncertainties, as discussed in Sec. 2.5. The simplest way to use the NINJA data is to perform a fitting similar to the ND280 fit. We call such a NINJA fitting as an internal constraint method because the same neutrino interaction model as T2K is used for the fitting. Figure 10.1 shows a flow chart of a possible constraint method by the NINJA data. The flux and interaction models constrained by the ND280 measurements are further constrained by the NINJA measurement. If NINJA can give more substantial constraints even after the ND280 fitting, systematic errors of the oscillation analysis will be reduced.

In the following section, MC distributions are fitted using neutrino interaction parameters used in the ND280 fit, and the constraints by the NINJA measurements are checked. After that, systematic errors on the numbers of events observed in SK are evaluated as well as the errors on the oscillation parameters by performing a sensitivity study with simulated data.

10.1.2 Simulated data fit

In Sec. 9.4, we found that the several uncertainties of the neutrino interaction are larger than the total size of the measurement error. Since many parameters are used in the

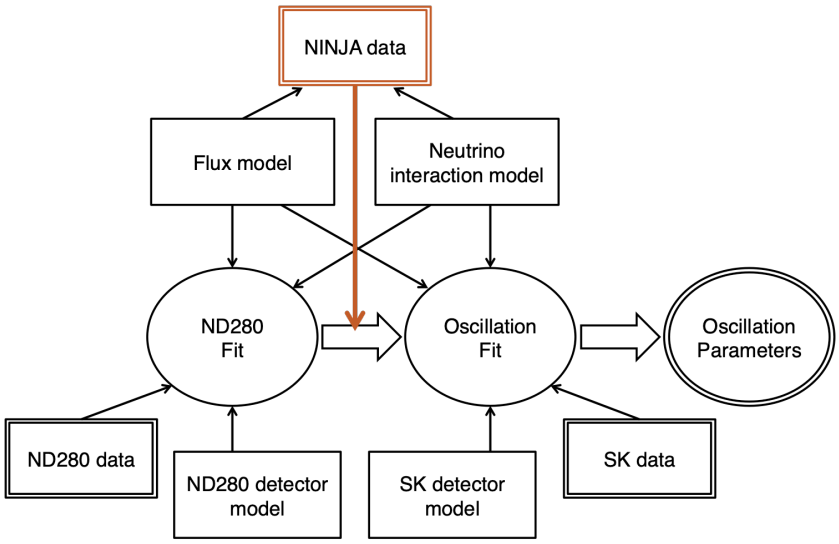

Figure 10.1: Constraint by the NINJA measurement in the T2K neutrino oscillation analysis. The flux and interaction parameters constrained by the ND280 measurements are further constrained by the NINJA measurement.

neutrino interaction model, all the parameters related to the neutrino interaction model need to be fitted simultaneously.

In the ND280 fitting, CC events are separated into three samples based on their number of charged pions: CC0π, CC1π, and CC Other. The muon momentum-angle distribution is prepared for each sample, and they are fitted simultaneously to maximize a dedicated likelihood function, which is based on the flux, neutrino interaction, and detector systematic parameters. Currently, distributions of protons and pions are not used in the ND280 fitting yet. This is because the momentum thresholds for protons and pions are not low enough to detect all of them and the observed events are not categorized effectively in ND280. Therefore, the proton and pion information is not sensitive enough to give constraints on the neutrino interaction models. In NINJA, protons and pions are measured with sufficiently low momentum thresholds, thus we set the distributions to be fitted as below.

- CC0π0p+CC0π1p, Muon momentum (p_μ)-angle (θ_μ) distribution (20 bins):
  p_μ [0, 0.4, 0.8, 1.4, 3.0, 10.0] (GeV/c)
  θ_μ [0, 15, 30, 40, 90] (deg)

- CC0π2p, Proton opening angle ($\cos\theta_{\rm open}$) vs Muon angle (θ_μ) distribution (20 bins):
  $\cos\theta_{\rm open}$ [-1.0, -0.6, -0.2, 0.2, 0.6, 1.0]
  θ_μ [0, 15, 30, 45, 60] (deg)

- CCNπ (N>0), Momentum of all pions from the neutrino interactions (p_π) vs Pion multiplicity (N_π) distribution (30 bins):
  p_π [0, 0.2, 0.4, 0.6, 0.8, 1.0, 1.2, 1.4, 1.6, 1.8, 2.0] (GeV/c)
  N_π 1, 2, >2

To determine these distributions, several combinations of kinematics distributions are tested, and the combination giving the best constraints is selected. Figure 10.2 shows

the kinematics distributions used for the fitting. In the fitting below, we assume the E71 statistics in the neutrino mode and the same statistics in the antineutrino mode. Thus, it corresponds to a data set with 2.0×10^{21} POT. We first check how the nominal distributions change by varying neutrino interaction parameters. Then, the distributions are fitted, and the error size of each parameter and their correlations are obtained.

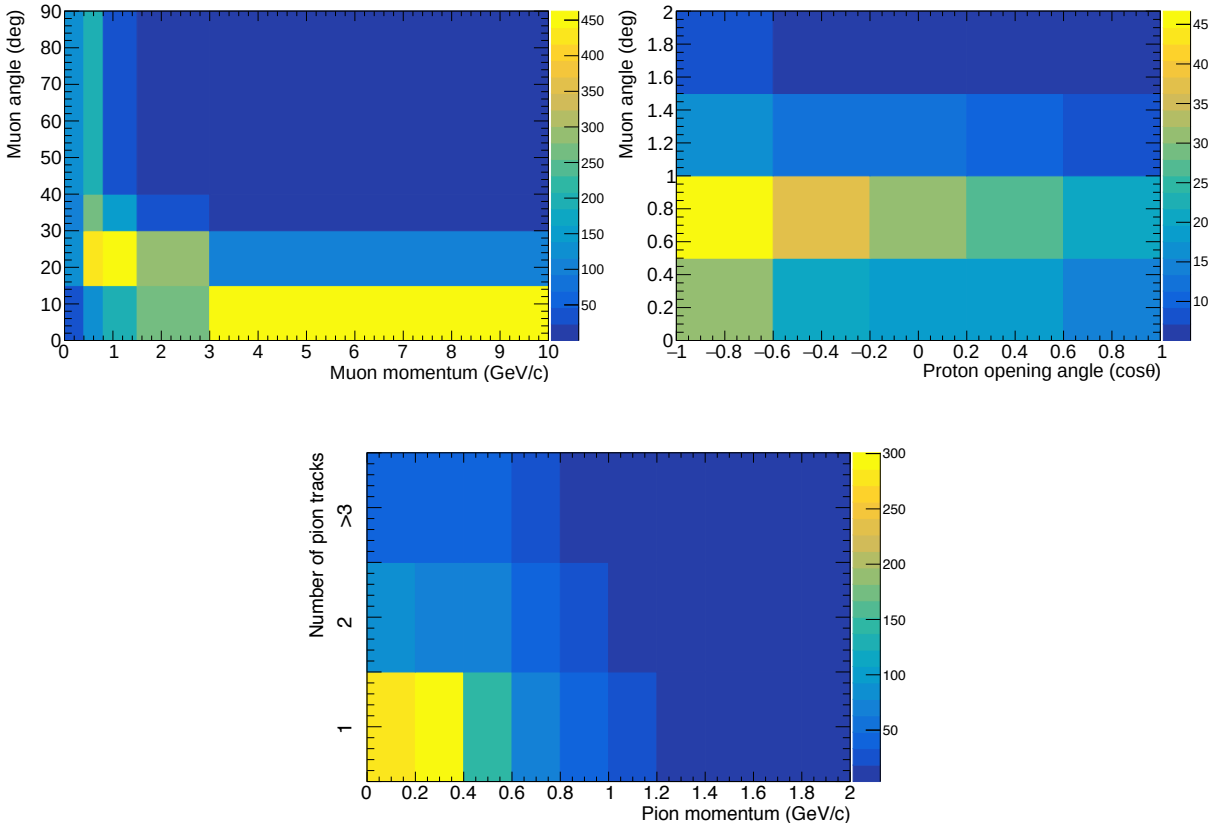

Figure 10.2: Kinematics distributions used for the fitting of the neutrino interaction parameters. Top left plot is sum of two-dimensional distributions of muon momentum and angle in the CC0π0p and CC0π1p samples. Top right plot is the relation between proton opening angle and muon angle in the CC0π2p sample. Bottom plot is the two-dimensional distribution of pion momentum and the number of pions in the CCNπ sample. Distributions in the neutrino mode beam with the E71 total statistics are shown.

A multivariable fitting is performed using MINUIT2 [163] to minimize a χ^2 value defined below:

$$\chi^2 = \sum_{i,j} \Delta N_i^{\mathrm{MC}} (V_{\mathrm{stat}} + V_{\mathrm{syst}})^{-1}_{ij} \Delta N_j^{\mathrm{MC}} + \sum_{i,j} \Delta x_i (V_{\mathrm{int}})^{-1}_{ij} \Delta x_j. \tag{10.1}$$

Here, ΔN_i^{MC} is a change of the entry from the nominal MC prediction in the i-th bin when parameters are changed by $\Delta\mathbf{x}$. This corresponds to the difference of simulated data from the expectation. The matrices V_{stat} and V_{syst} are covariance matrices of statistical and systematic errors of the measurement bins, respectively. The matrices V_{int} corresponds to a covariance matrix of the neutrino interaction model, which includes 47 parameters used in the T2K fitting. The 47 parameters are summarized in Tab. 10.1, and more details are

Table 10.1: Summary of the neutrino interaction parameters used in the sensitivity study. The parameters with parentheses have two parameters, such as parameters for $\nu_\mu/\overline{\nu}_\mu$ and carbon/oxygen.

Parameter	
MAQE	Axial-vector mass for the CCQE interactions
2p2h_norm_nu (nubar)	Normalizations of the 2p2h interactions, separately assigned for ν and $\overline{\nu}$
2p2h_normCtoO	Normalization of the 2p2h interactions, covering difference between ^{12}C and ^{16}O
2p2h_shape_C (O)	Changing the 2p2h kinematics based on two contributions from different mechanisms, separately assigned for ^{12}C and ^{16}O
2p2h_Edep_lowEnu (nubar)	E_ν dependent difference (E_ν <600 MeV) in the 2p2h cross-section models
2p2h_Edep_highEnu (nubar)	E_ν dependent difference (E_ν >600 MeV) in the 2p2h cross-section models
Q2_norm	Normalization of the CCQE cross section as a function of Q^2
EB_dial_C_nu (nubar)	Binding energy (nuclear removal energy) for ^{12}C
EB_dial_O_nu (nubar)	Binding energy (nuclear removal energy) for ^{16}O
CA5	Form factor parameter for the resonant pion production
MARES	Axial-vector mass for the resonant pion production
ISO_BKG_LowPPi	Normalization of the non-resonant background in antineutrino mode ($P_\pi < 0.2\,\mathrm{GeV}/c$)
ISO_BKG	Normalization of the non-resonant background
CC_norm_nu (nubar)	Normalizations for all the CC interactions
nue_numu (nuebar_numubar)	Normalizations between ν_e and ν_μ cross sections
CC_BY_DIS	Switching on/off the Bodek-Yang correction in DIS
CC_BY_MPi	Switching on/off the Bodek-Yang correction in multi pi production
CC_AGKY_Mult	Multiplicity reweighting in the multi pi production
CC_Misc	Normalization for CC1γ, CC1K, CC1η interacrions
CC_DIS_MultPi_Norm_Nu (Nubar)	Normalizations for CC DIS and multi pi production
CC_Coh_C (O)	Normalizations for CC coherent production, separately assigned for ^{12}C and ^{16}O
NC_Coh	Normalization for NC coherent production
NC_1gamma	Normalization for NC single γ production
NC_other_near (far)	Normalizations for the other NC interactions, separately assigned for near and far detectors
FEFQE	FSI QE pion scattering ($P_\pi < 500\,\mathrm{MeV}/c$)
FEFQEH	FSI QE pion scattering ($P_\pi > 500\,\mathrm{MeV}/c$)
FEFINEL	FSI pion production
FEFABS	FSI pion absorption
FEFCX	FSI pion single charge-exchange

described in Appendix F. This fitting is performed after the ND280 fit, thus the post-ND280 fit covariance matrix, obtained by fitting simulated ND280 data, is used as V_{int}.

In the ND280 fit, fitting is performed simultaneously for both flux and neutrino interaction parameters. In this analysis, the flux uncertainty is treated as an independent systematic uncertainty for simplicity. Although the NINJA detectors are located at a different off-axis angle from the ND280, the flux at the NINJA position strongly correlates with the fluxes at ND280 and SK. Thus, the covariances between the flux and neutrino interaction parameters can be transformed from the ND280 fit. For further analysis, the correlations between these fluxes are better to be considered.

Figure 10.3 shows the post-fit correlation matrix of the flux and neutrino interaction parameters using the ND280 and NINJA data. Bins 0–50 correspond to the flux parameters at SK, and bins 51–97 correspond to the neutrino interaction parameters. Each parameter has correlations with others, and especially the flux and neutrino interaction parameters have negative correlations. These negative correlations are important because they reduce the total uncertainty in the oscillation analysis as discussed later. In Fig. 10.4, error sizes of the neutrino interaction parameters are compared before and after the fitting. Unfortunately, NINJA does not give strong constraints. However, parameters related to the 2p2h interactions and the FSI are constrained. This is because we use measured proton and pion kinematics in the fitting, while the ND280 fitting only uses muon kinematics.

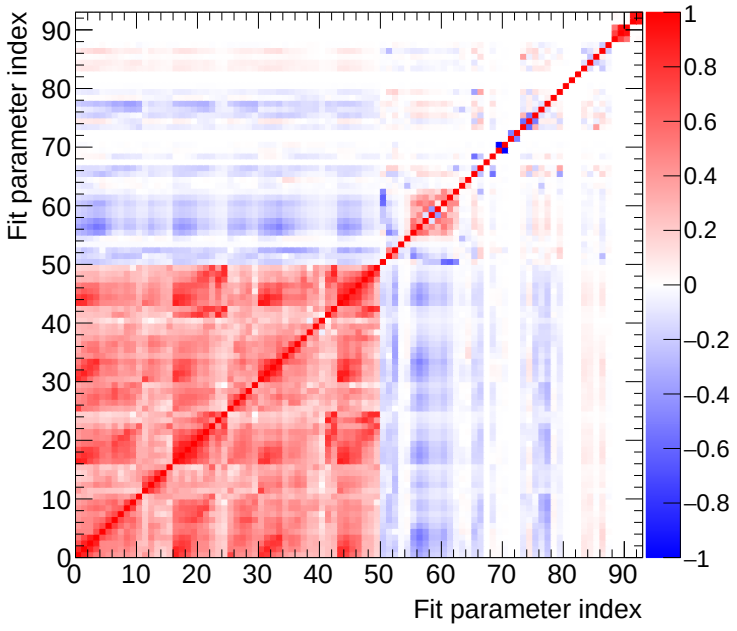

Figure 10.3: Correlation matrix of the flux and the neutrino interaction parameters after the ND280 and NINJA constraints

The statistical limitation is one significant cause of the relatively weak constraints by NINJA, however, there is another crucial point to be considered; the current parameters used in T2K may not be able to cover (or sensitive to) the NINJA observables, and changes

in the NINJA distributions may not change the fitting result so much. This is because the current ND280 fitting does not use hadron kinematics information. This point is closely related to the validation and construction of neutrino interaction models, which is one of the vital roles of NINJA, and it is discussed later. Before discussing that, the impact of the NINJA constraints shown above on the T2K oscillation analysis is checked in the next section.

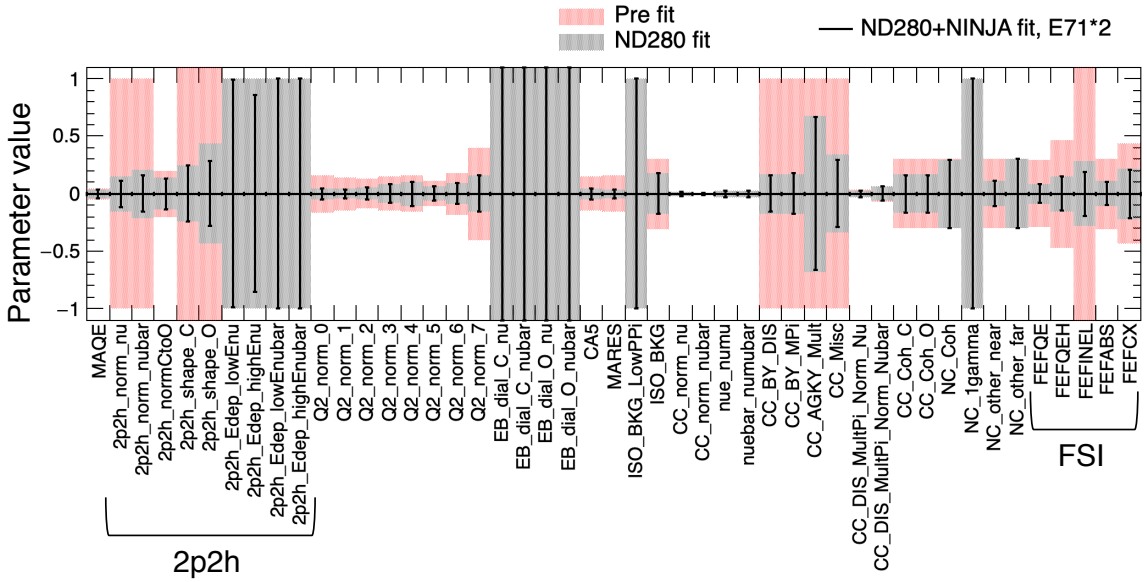

Figure 10.4: Error size of the parameters in comparison before and after the fitting. Parameters related to the 2p2h interactions and the FSI are constrained by NINJA. Red bands correspond to error size before fitted by ND280, gray bands correspond to ND280 post-fit error size, and NINJA constraints are shown by error bars.

10.1.3 Physics sensitivity

A neutrino oscillation analysis with simulated data is performed using the constraints on the flux and neutrino interaction models given by NINJA in addition to ND280. We use a software package used in the T2K analysis. Details of the T2K oscillation analysis method are described in Refs. [164, 165]. Here, we do not use the actual events observed in SK. We use simulated data to check the future sensitivity of our analysis.

First, systematic errors on the predicted numbers of events at SK are estimated using the constrained parameters by ND280 and NINJA. Table 10.2 shows the systematic error on the number of predicted events for each sample. The last column in the table is the error on the ratio of ν_e to $\overline{\nu}_e$, which is important to compare $\nu_\mu \to \nu_e$ and $\overline{\nu}_\mu \to \overline{\nu}_e$ for the δ_{CP} measurement. The error size of Flux+Xsec (cross section) becomes smaller than the individual Flux or Xsec error size. This is because the flux and cross-section parameters have negative correlations as shown in Fig. 10.3, owing to the constraints by ND280 and NINJA. Several neutrino interaction parameters are not constrained by the ND280 fitting, thus these errors are separately considered. The total error size is obtained from the quadrature sum of the "Flux+Xsec (ND280+NINJA constr)", the unconstrained

neutrino interaction parameters, and the error on the SK detector response. Several lines in the table show error sizes without the NINJA constraint (only ND280 constraint) for comparison. Unfortunately, the Xsec+Flux errors and the total errors are not reduced so much, although the Xsec errors are slightly reduced.

Table 10.2: Systematic errors on the numbers of events observed in SK in units of %. These values are obtained only using the MC simulation.

Error source	ν_e1R	ν_μ1R	$\overline{\nu}_e$1R	$\overline{\nu}_\mu$1R	ν_e1R+1d.e.	ν_e1R/$\overline{\nu}_e$1R
Flux	3.0	3.0	3.2	3.1	3.0	1.6
Xsec (ND+NINJA constr)	3.3	3.1	3.3	3.1	4.3	1.6
(cf.) Xsec w/o NINJA	3.4	3.2	3.5	3.3	4.4	1.8
Flux+Xsec (ND+NINJA constr)	2.2	2.2	2.7	2.6	4.0	1.8
(cf.) Flux+Xsec w/o NINJA	2.2	2.2	2.7	2.6	4.0	1.8
2p2h Edep	0.2	0.4	0.3	0.5	0.0	0.3
IsoBkg low-p_π	0.1	0.5	2.7	3.4	0.1	2.5
$\sigma(\nu_\mu)/\sigma(\nu_e)$, $\sigma(\bar{\nu})/\sigma(\nu)$	2.5	0.0	1.4	0.0	2.6	3.0
NC γ	1.7	0.0	2.6	0.0	0.0	0.9
NC Other	0.2	0.3	0.4	0.2	0.7	0.2
SK	3.2	2.9	4.3	2.5	13.5	1.3
All	5.1	3.8	6.7	4.3	14.2	4.6
(cf.) All w/o NINJA	5.1	3.7	6.7	4.3	14.3	4.6

As a next step, to extract the oscillation parameters, one or two-dimensional fitting is performed by calculating the negative log-likelihood, which corresponds to χ^2, as a function of each oscillation parameter of interest ($\delta_{\rm CP}, \sin^2\theta_{23}, |\Delta m^2_{32}|$). Other oscillation parameters and systematic uncertainty parameters are marginalized over. Negative log-likelihood values as a function of a single parameter or 68% confidence level contours are obtained. Figure 10.5 top plots show negative log-likelihoods of $\delta_{\rm CP}$ and a confidence level contours of $\sin^2\theta_{23}$ and $|\Delta m^2_{32}|$ calculated with constraints on θ_{13} from reactor experiments. In each plot, results with and without the NINJA constraint and with and without systematic error (stat. only) are compared using statistics corresponding to the T2K Run1–10 data (3.6×10^{21} POT). There are no significant differences in the plots with and without the NINJA constraint. This is mainly because the current statistical error is significantly larger than the systematic error. With the current statistics, reducing the systematic error does not significantly affect the total error size. However, as already discussed, the reduction of the systematic uncertainty is essential to reach 3σ and 5σ observations of the CP violation in the future, where the statistical error is reduced and the systematic error becomes dominant. The case increasing the data statistics up to 20×10^{21} POT, which corresponds to the extended T2K goal [166], is shown in the bottom plots of Fig. 10.5. With these high statistics, the effect of the NINJA constraint can be seen in the $\sin^2\theta_{23}$–Δm^2_{32} plot, while it does not affect $\delta_{\rm cp}$ so much.

10.1.4 Discussion

From the above, we found that the internal constraints by NINJA may not effectively work. Conversely speaking, it means that the current constraint by ND280 has already been well

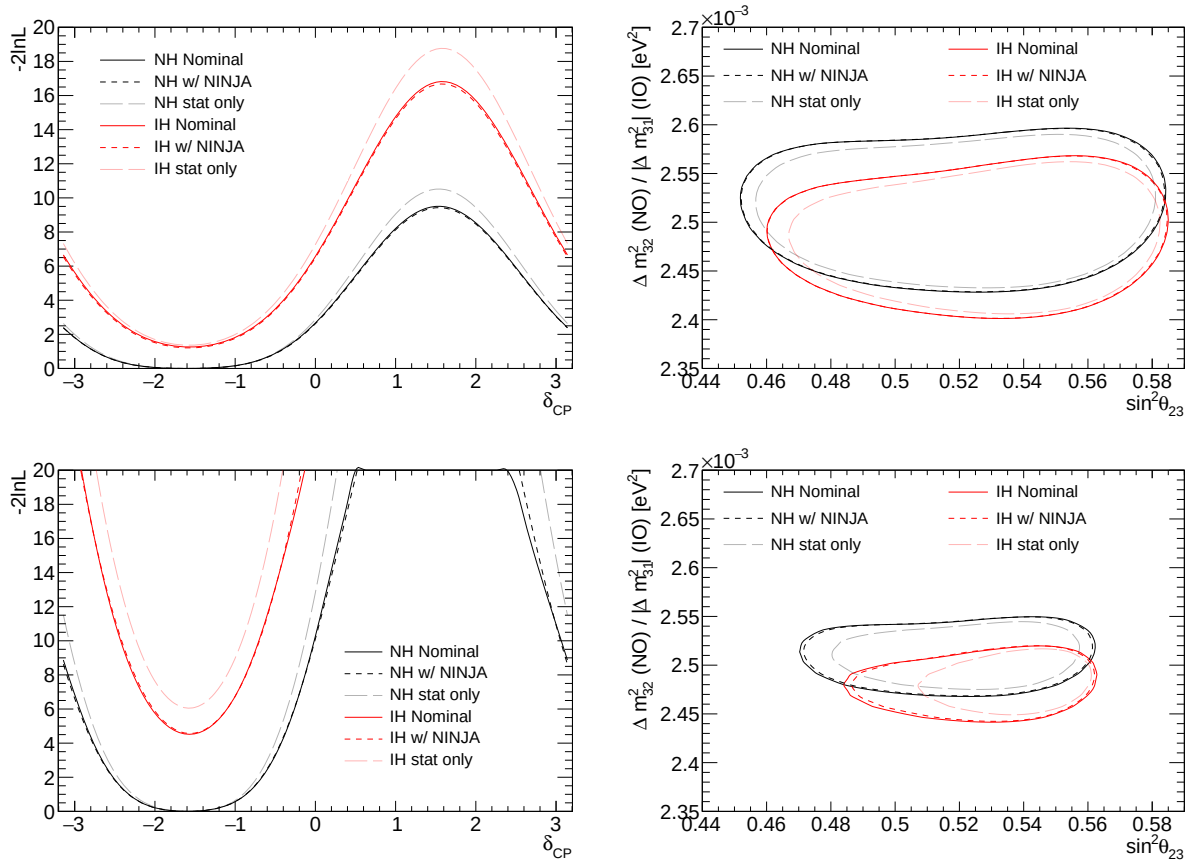

Figure 10.5: Contours of the 68% confidence level of $\sin^2\theta_{23}$-$|\Delta m^2_{32}|$ and negative log-likelihoods of δ_{CP} calculated with constraints on θ_{13} from reactor experiments. Top plots are for the current T2K statistics (3.6×10^{21} POT), while the bottom plots are the case of data with 20×10^{21} POT. In each plot, results with and without the NINJA constraint and with and without systematic error (stat. only) are compared. The black lines correspond to the plots assuming the normal hierarchy (NH) and the red linea correspond to those assuming the inverted hierarchy (IN).

established. Of course, we can improve the NINJA constraints by reducing systematic uncertainties on the NINJA measurements or considering the correlation between the flux and neutrino interaction parameters in the NINJA fitting, but it seems they are not effective ways. However, it never means that the NINJA measurement does not contribute to the T2K systematics. The most important role of NINJA is validating the neutrino interaction models themselves, which correspond to the models before constrained by ND280. Although the ND280 constraint works well, the current evaluation method of the systematic error is built on the assumption that the neutrino interaction model we use is well modeled. If the current neutrino interaction model is perfect, and the parameters in Tab 10.1 cover all uncertainties, the current evaluation method of the systematic error is fine. However, the neutrino interaction models still have many uncertainties, thus the parameters may not cover all of them. This fact means that if the models are not correct, it may cause bias on the oscillation analysis results. Hence, it is crucial to validate the neutrino interaction models by external measurements, such as NINJA.

To evaluate possible biases, studies with a set of “fake” data are carried out in the

T2K oscillation analysis [165]. The fake data are generated by varying parts of the interaction model in the MC simulation. Oscillation analyses are performed with these fake data, and changes in the final results are included in the systematic error. Related to this, possible fake data studies by NINJA are discussed in Appendix G.1. However, this method may still not be perfect if the difference in models appears beyond the ND280 measurement phase space, such as a low momentum or a high angle region. The high-angle region which is not covered by ND280 is especially important because SK has 4π angle acceptance. Therefore, validating neutrino interaction models with a different phase space from ND280 is essential. We test the existing (and future) neutrino interaction models and validate the parametrization used in T2K. We call such validations as an external constraint. In the following section, a possible validation method by NINJA is discussed with an MC simulation study.

10.2 External constraint

In this section, we consider a method to validate the neutrino interaction models. Each interaction mode such as CCQE, CCRES, and CCDIS has uncertainty, but we focus on the uncertainty in the 2p2h interactions. This is because the 2p2h interaction is one of the largest systematic error sources in the current oscillation analysis, and NINJA is the only measurement which is sensitive to most of the protons from the 2p2h interactions on water. There are many parameters related to the 2p2h interactions in the current T2K fit model, as shown in Tab. 10.1. This is reflecting the fact that we still have many unknown factors on the 2p2h interactions. As already shown in Fig. 3.10, understanding the 2p2h interactions is essential because these interactions pass the CCQE signal selection at SK and distort the distribution of the reconstructed neutrino energy. Below, we consider how we reveal the nature of the 2p2h interactions.

10.2.1 Multivariate analysis to test 2p2h models

We can measure the cross section of the 2p2h interaction if we obtain a neutrino event sample in which the 2p2h interactions are highly enriched. Furthermore, we can measure the kinematics of the 2p2h interactions with such a sample. However, extracting the 2p2h interactions from the other interaction modes is not simple. A proton pair in the final state is a characteristic of the 2p2h interaction. Although selecting the CC0π2p events is the first step to make a 2p2h enriched sample, there are backgrounds from the CCQE and CCRES events. This is because the CCQE interaction may have a proton pair due to the proton FSI, and the CCRES interaction also leaves two protons when the pion is absorbed. Therefore, we need to separate these backgrounds based on other observables. As shown in the previous chapter, a possible observable is the proton opening angle, whose behavior is different between the CCQE and 2p2h interactions. Besides, several other observables show different distributions between the CCQE and 2p2h interactions. However, it is difficult to make the 2p2h enriched sample by a cut-based selection using such observables because each parameter does not have a clear discrimination capability.

Even if the difference in each observable is small between the 2p2h and the other interactions, we can combine several observables by using a multivariate analysis. A software package, Toolkit for Multivariate Data Analysis (TMVA) in ROOT [167], is used

to extract the 2p2h interactions. This time, the Boosted Decision Tree (BDT) algorithm is employed. A Decision Tree (DT) is a structure of binary selection. An event sample containing signal and background is separated many times, and at the end of the tree, events are classified into signal or background. The Boosted DT extends the DT to form several trees, and gives weights to misclassified events to improve statistical fluctuation in the training sample.

At the first step of the BDT classification, we define the signal and background in the simulation data. We can assign the whole 2p2h events to the signal, but in this analysis, we try to define a more specific selection. As described in Sec. 3.2.2, there are two main components in the 2p2h interactions: MEC and NN. Strictly speaking, there are also interference terms between MEC and NN. Kinematics of the NN interactions are similar to those of the CCQE interactions, thus they do not give large biases to the neutrino energy reconstruction. On the other hand, the kinematics of the MEC interactions are significantly different from those of the CCQE interactions because protons are emitted via a Delta baryon resonance. Therefore, it results in a large bias in the reconstructed neutrino energy bias. The kinematics of the MEC component is similar to the CCRES interactions rather than the CCQE interactions. In the T2K analysis, the 2p2h shape parameter is introduced in addition to the overall normalization parameter, as shown in Tab. 10.1. The shape parameter changes the fraction of the MEC and NN events in the 2p2h interactions.

We focus on the MEC events in the analysis below. The NN event has similar kinematics to the CCQE interaction, thus separately considering the MEC and NN provides a better classification. However, an event-by-event separation of the MEC and NN interactions is difficult due to their interference. Therefore, we separate the 2p2h interactions based on their reconstructed neutrino energy. Figure 10.6 shows the distribution of the difference between the reconstructed and true neutrino energies. Events with $E_{\nu\,\mathrm{reco}} - E_{\nu\,\mathrm{true}}$ less than $-0.2\,\mathrm{GeV}$ are treated as the MEC-like events, and the rest as the NN-like events. Then, the MEC-like events are used as the BDT signal events, and we attempt to extract the MEC-like events from the other interactions.

10.2.2 Analysis procedure

We applied the BDT to two event categories: one is the CC0π events, and the other is the CC0π2p events. Since there is no requirement in the number of protons for the CC0π events, the CC0π events include the CC0π2p events, and they are not independent. A total of 16 parameters are used as the input variables, as summarized in Table 10.3. Since several parameters cannot be defined depending on the number of protons, availability of the parameters in each sub-sample with respect to the number of protons is also summarized in the table. Besides, for parameters assuming a single proton in the final state, such as the transverse kinematics imbalance and the inferred kinematics, the vector sum of all the protons are considered as the single proton if there are multiple protons in the final state.

The BDT classification is performed with these input variables. The classification using the BDT provides a BDT score for each event as an output. A signal-like event has a positive score, and a background-like event has a negative score. Signal-like events are selected based on the BDT output score, and the number of selected events is denoted as

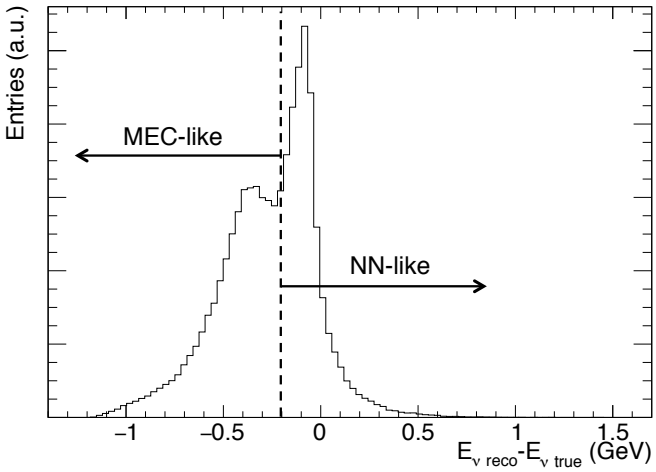

Figure 10.6: Definition of MEC-like and NN-like events of the 2p2h interactions. Events with $E_{\nu\,\mathrm{reco}} - E_{\nu\,\mathrm{true}}$ less than $-0.2\,\mathrm{GeV}$ are treated as the MEC-like events, and the rest as the NN-like events.

N_{sel}. Events other than the MEC-like interactions in the selected events are considered as background, and the expected number of the background events is written by N_{bkg}. The flux-averaged cross section of the MEC-like event per a nucleus (σ_{MEC}) can be obtained by the following formula:

$$\sigma_{\mathrm{MEC}} = \frac{N_{\mathrm{sel}} - N_{\mathrm{bkg}}}{\phi T \epsilon} \tag{10.2}$$

where ϕ is the integrated flux, T is the number of target nuclei, and ϵ is the selection efficiency of the MEC-like events. If the background fraction in the selected events is sufficiently small, we can measure σ_{MEC} with good precision. However, if the background fraction is large, the uncertainty on the number of backgrounds limits the precision. In the next section, we check the possible measurement precision with specific cases.

10.2.3 Results

First, we applied the BDT to the CC0π events. Figure 10.7 shows the distribution of the number of protons used as the input variable for the BDT classification. The MEC-like events have more protons than the other events. Figure 10.8 shows the distributions of the other input variables. As already discussed in Sec. 9.4, the proton opening angle $\cos\theta_{\mathrm{open}}$ has a good separation capability. Besides, the transverse kinematics imbalance and inferred kinematics variables also show different distributions between the signal and the backgrounds. It is crucial to carefully compare these distributions between the data and the model prediction before applying the BDT classification to the data.

Figure 10.9 shows the BDT output score with a breakdown by the interaction mode. If we select events with the BDT output score more than zero, we obtain 62.0 MEC-like events and 269.6 background events in the case of the E71a statistics. The main component of the background is the CCRES interactions. If the CCRES event has a

Table 10.3: Input variables used for the BDT classification. A total of 16 variables are used. Parameters p_{high} and p_{low} are momenta of a higher and lower energetic proton. In the last column, the Np sample includes protons more than two.

Parameter	Description	0p	1p	2p	Np
N_p	The number of protons	✓	✓	✓	✓
δp_T, $\delta\phi_T$, $\delta\alpha_T$	Transverse kinematics imbalance (Appendix C.1)		✓	✓	✓
Δp_p, $\lvert\Delta\boldsymbol{p}\rvert$, $\Delta\theta_p$	Inferred kinematics (Appendix C.2)		✓	✓	✓
$\cos\theta_{\text{open}}$	Opening angle of the proton pairs			✓	
$\lvert p_1 + p_2 + \cdots\rvert$	Absolute value of the proton momenta sum			✓	✓
$\lvert p_1\rvert + \lvert p_2\rvert + \cdots$	Sum of the proton absolute momenta		✓	✓	✓
$p_{\text{high}}/p_{\text{low}}$	Momentum balance of the proton pairs			✓	
θ_p	Measured proton angle		✓	✓	✓
$E_{\nu\,\text{reco}}$	Reconstructed neutrino energy	✓	✓	✓	✓
Q^2	Squared four-momentum transfer	✓	✓	✓	✓
θ_μ	Measured muon angle	✓	✓	✓	✓
p_μ	Reconstructed muon momentum	✓	✓	✓	✓

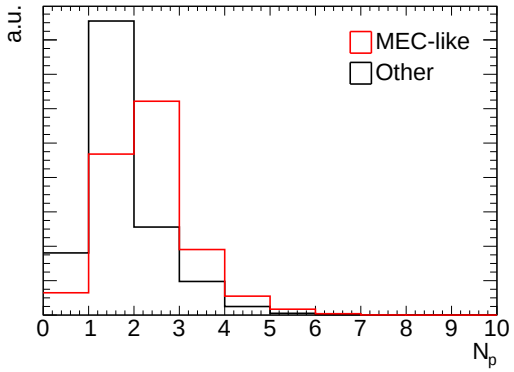

Figure 10.7: Distributions of the number of protons used in the BDT classification of the CC0π events.

neutral pion, or a charged pion is not detected due to the scanning acceptance, that event is categorized as a CC0π event. Moreover, when a π^+ is absorbed in the nuclear medium, a proton pair is emitted. The kinematics of such an event are very similar to those of the MEC event, thus it is difficult to separate them. The purity of the MEC-like event is less than 20%, thus this selection has too much backgrounds, and the uncertainty of the backgrounds makes it difficult to measure the cross section precisely.

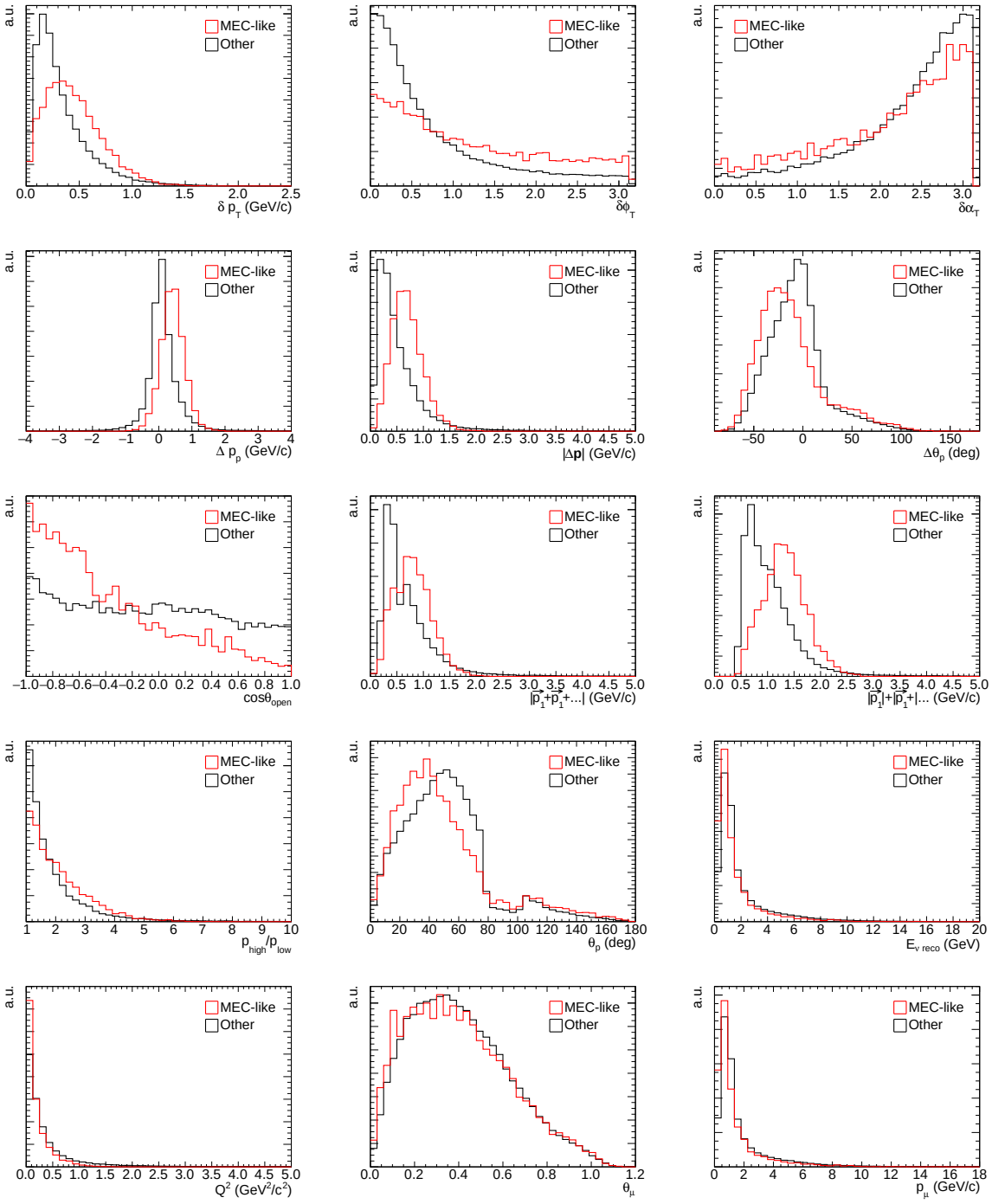

Figure 10.8: Distributions of the input variables used in the BDT classification of the CC0π events.

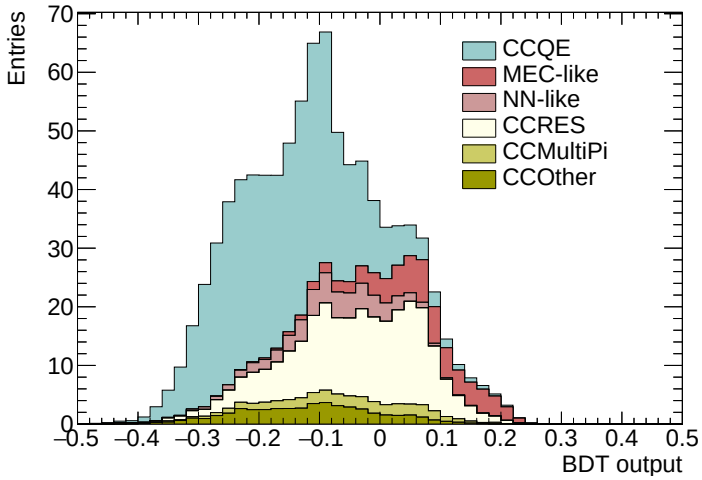

Figure 10.9: BDT output score for the CC0π events with a breakdown by the interaction mode.

Following the CC0π events, we consider the CC0π2p sample below, in which a relatively large fraction of the 2p2h interactions is included. In this sample, an almost equal amount of the CCQE, 2p2h, and CCRES interactions are included. Figure 10.10 shows the distributions of the input variables for the BDT classification of the CC0π2p events. The distributions of the proton opening angle and the momentum balance of the proton pairs are skipped because they are measured only for the CC0π2p events and are already shown in Fig. 10.8. Compared to the case of the CC0π events, the fraction of the MEC-like event increases, and the difference between the MEC-like and the other events becomes more clear.

Figure 10.11 shows the BDT output score with a breakdown by the interaction mode. If we select events with the BDT output score more than zero, we obtain 18.5 MEC-like events and 23.3 background events in the case of the E71a statistics. The purity of the MEC-like event is significantly improved. The background uncertainty from the neutrino interactions is estimated in Tab. 10.4. A 15% level of uncertainty is assigned to the number of backgrounds.

According to analyses of the NINJA pilot runs, the uncertainties on ϕ, T, ϵ are at a 5% level. Thus, the background uncertainty is the dominant error source since the fraction of N_{bkg} in the selected event is more than 50%. The 15% level uncertainty on the N_{bkg} corresponds to roughly a 20% level error on σ_{MEC}. Hence, we can measure the cross section of the MEC-like interaction with around a 20% systematic error. The statistical error of this measurement is roughly 23% for the E71a statistics and 15% for the E71 total statistics.

Figure 10.12 shows comparisons of the 2p2h cross-section models. In the simulation above, we use the model by Nieves *et al.* Compared to this model, the model by Martini *et al.* predicts around three times larger cross section for neutrinos. Hence, the measurement of the MEC-like cross section with a 20% systematic error may rule out either of them. However, as shown in the right plot of Fig. 10.12, other models predict relatively similar cross-section values. Therefore, to test these models, we need to reduce the systematic errors (e.g. 5%) by understanding the other interaction modes. For instance, we can

Table 10.4: Systematic error from the neutrino interaction on the estimated number of backgrounds in the BDT selection.

Parameter	Error (%)
M_A^{QE}	-1.5 / +0.5
CCQE Q^2 normalization	-2.1 / +5.5
E_B	-0.0 / +2.3
C_5^A	-6.2 / +5.6
M_A^{RES}	-3.7 / +4.2
Isospin$_{\frac{1}{2}}$ background	-1.1 / +0.2
CC normalization	-1.9 / +0.0
CC BY DIS	-2.3 / +1.5
CC BY Multipi	-3.7 / +8.2
CC AGKY Multipi	-4.5 / +1.5
CC Misc normalization	-0.0 / +0.6
CC DIS Multipi normalization	-0.0 / +1.3
CC coherent normalization	-0.0 / +0.0
FSI QE ($P_\pi < 500\,GeV/c$)	-0.0 / +3.2
FSI QE ($P_\pi > 500\,GeV/c$)	-2.7 / +0.5
FSI inelastic	-0.0 / +1.4
FSI absorption	-6.2 / +7.6
FSI charge exchange	-0.6 / +2.6
Total	-12.2 / +15.4

reduce the systematic error if we use CC1π events as a control sample and evaluate the background uncertainty in the CC0π sample.

10.2.4 Summary and prospects of the multivariate analysis

We presented the possible measurement of the MEC-like cross section with a 20% systematic error using the CC0π2p events. Since NINJA can use precise proton information compared to the ND280 measurements, the multivariate analysis will be a practical approach to understanding the 2p2h interaction. On the other hand, the approach using the BDT algorithm may have a strong dependence on the neutrino interaction model. Thus not only the BDT classification result but also each kinematics distribution used as the input variables need to be carefully measured. For more reliable measurement of the 2p2h interaction, a lot of validations are still required. However, if such an approach is possible, it will be a unique measurement of the neutrino-water interactions that only NINJA can do. Not only measuring the cross section of the MEC interaction but also measuring kinematics distributions allows us to characterize the MEC and 2p2h interactions and to test the existing (and future) 2p2h models by checking if these models explain our data.

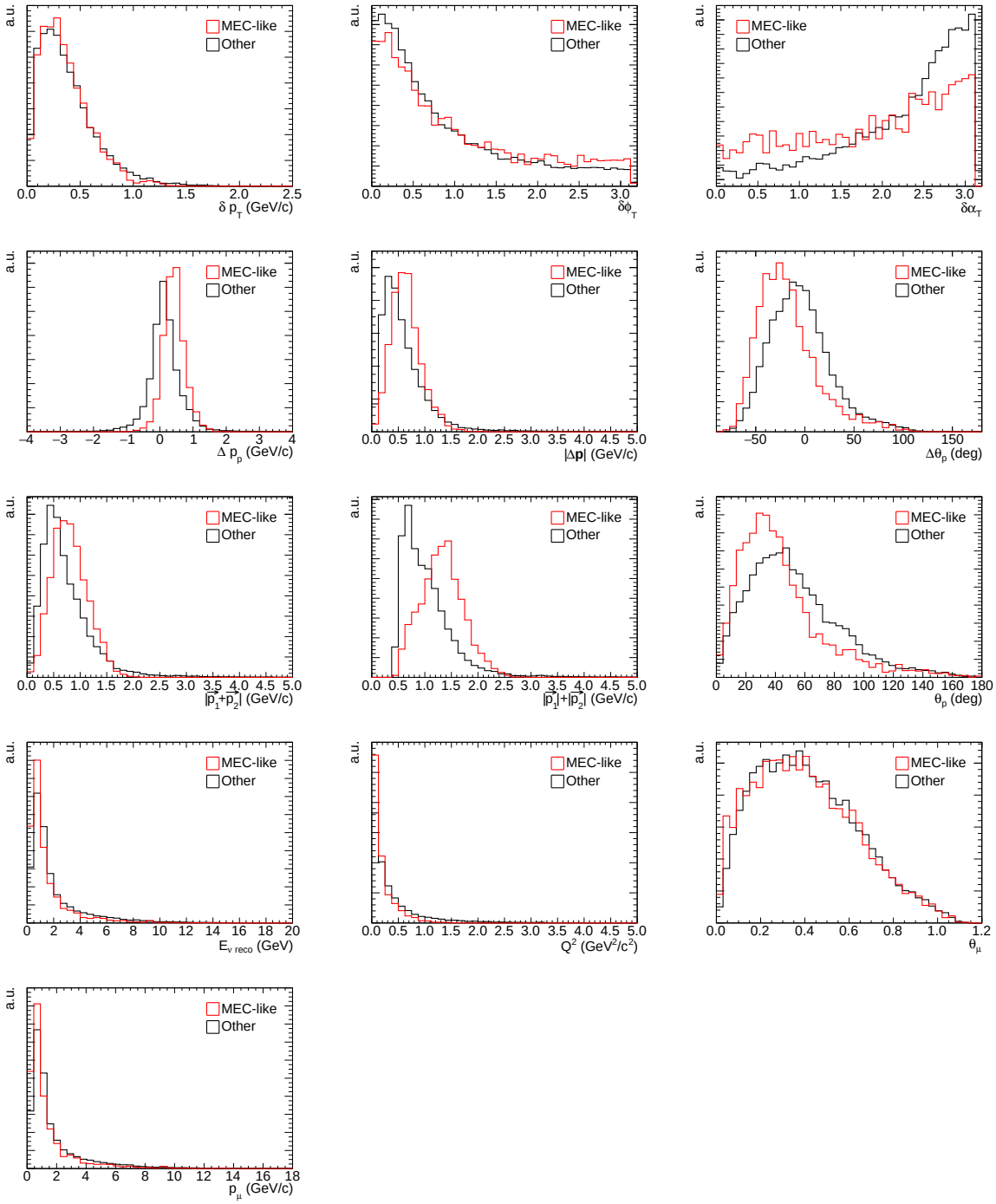

Figure 10.10: Distributions of the input variables used in the multivariate analysis of the CC0π2p events.

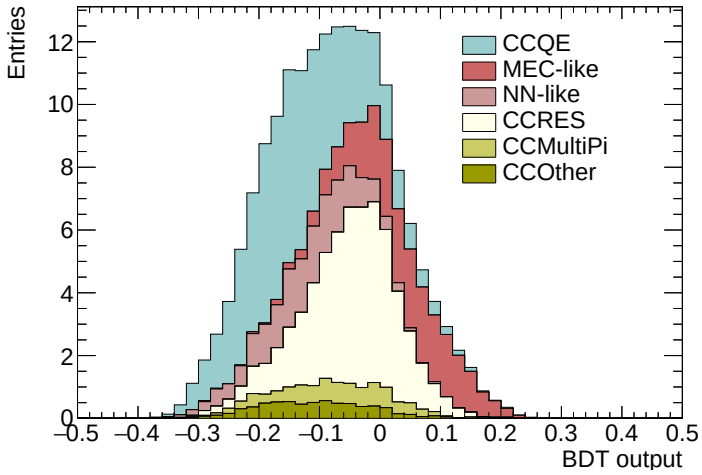

Figure 10.11: BDT output score for the CC0π2p events with a breakdown by the interaction mode

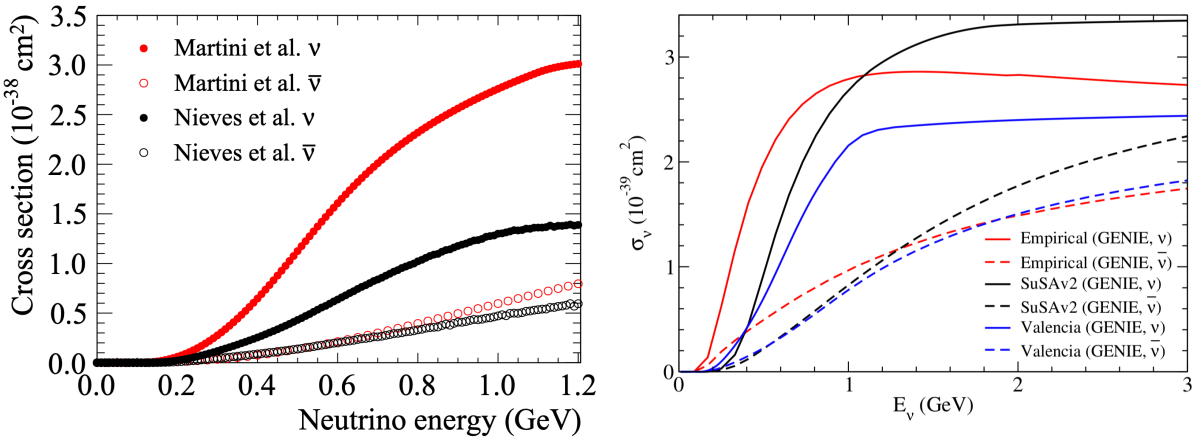

Figure 10.12: Comparisons of the 2p2h cross sections. The left plot shows comparison between the model by Nieves *et al.* and by Martini *et al.* [144], and the right plot shows comparison between the model by Nieves *et al.* (Valencia model) and the other models implemented in GENIE [168].

10.3 Ideas for other possible improvements of the neutrino interaction models

In the previous section, the 2p2h interactions are focused on. However, there are more subjects to which NINJA can contribute. Several possible topics are shown below.

Measurement of low momentum pions in the antineutrino mode

Since the Cherenkov threshold for charged pions in water is around 159 MeV/c, events with low momentum pions may contaminate the ν_μ sample in SK. The non-resonant background in the single pion production emits low momentum pions, but the model used in NEUT is tuned to the neutrino mode data. Therefore, there are large uncertainties on the antineutrino non-resonant background ("IsoBkg low-p_π" in Tab. 10.2). The detection efficiency for pions below 200 MeV/c is not high enough in ND280, thus measuring low momentum pions with a 50 MeV/c momentum threshold by NINJA will reduce the uncertainty.

Electron neutrino cross-section measurement

The cross-section difference between ν_μ and ν_e is not measured precisely. The difference between muon and electron masses changes the cross sections and response to the nuclear effects. The uncertainty of the cross-section ratio ν_e/ν_μ is estimated to be around 3% in theory [169], however it is not confirmed experimentally. It is difficult to measure the ν_e cross section in ND280 because the ν_e flux is only around 1% of the ν_μ flux, and electrons from the ν_e interactions and electrons from gamma rays are not efficiently separated in the current detectors. Although a fine segment detector in the ND280 upgrade [170] will provide a ν_e cross-section measurement in the future, NINJA also can contribute to it. The emulsion detectors have the capability to separate electrons from the ν_e interactions and electrons from gamma rays because the electron-positron pairs from gamma rays can be identified by emulsion's excellent spatial resolution. We plan to prepare a few-ton scale ECCs using an iron (or lead) target to measure the ν_e interactions. A total of around 1000 ν_e events is expected to be observed, thus the ν_e cross-section measurement with a 3% statistical error will be achieved.

Neutral-current cross-section measurements

The NC interaction with a charged pion is a background source for the ν_μ ($\overline{\nu}_\mu$) CCQE selection. If we can separate muons and pions from the neutrino interactions by range with a good purity using Baby MIND, $\nu + n \to \nu + p + \pi^-$ interactions can be measured. Here, detection of $\nu + p \to \nu + n + \pi^+$ is not preferred. Since there is no charged particle other than pion in the final state, background contaminations from cosmic rays and the neutrino interactions on the packing films become large. Even if the separation of muons and pions is difficult, $\overline{\nu} + n \to \overline{\nu} + p + \pi^-$ interactions in the antineutrino mode can be measured with a relatively little background because most of the CCQE interactions in the antineutrino mode ($\overline{\nu}_\mu + p \to \mu^+ + n$) do not have protons in the final states.

10.4 Summary of the NINJA prospects

We know that the current ND280 constraint method significantly reduces the systematic error at SK in T2K. However, testing the validity of the neutrino interaction models, especially the 2p2h interactions and the FSI, might be difficult by just using the ND280 measurement. This is because ND280 is not sensitive to the low-momentum hadrons. Owing to the very low momentum thresholds of the NINJA detector and the different phase space from the ND280, measurements by NINJA are going to reach unexplored regions of the neutrino interactions. Multivariate analyses could be practical methods to validate the neutrino interaction models, as well as simple kinematics measurements, as shown in the pilot run results. We will provide various distributions with low momentum thresholds and small uncertainties, and we test the neutrino interaction models by comparing the data and model predictions. Such validations allow us to contribute to building more robust neutrino interaction models and help to reduce the systematic error in the neutrino oscillation analysis.

Chapter 11

Conclusion

The measurement of the CP violation in the neutrino mixing is an exciting topic in the particle physics, and it attempts to answer the question of the matter-antimatter asymmetry in our universe. The T2K experiment is a long-baseline neutrino oscillation experiment, which precisely measures neutrino oscillation parameters. The latest result from T2K excludes the CP conserving values of δ_{CP} with more than 90% confidence level. To achieve more precise measurements, increasing statistics is essential. However, as the statistics increase, reducing systematic uncertainty becomes more crucial. The uncertainty of the neutrino-nucleus interactions is the dominant systematic error source in the current measurement. Since we need to consider various effects inside the nuclear medium, it is really hard to construct an internally consistent model of neutrino-nucleus interactions to describe all data. There are not sufficient data with good precision in neutrino interaction measurements yet, especially in measurements of low-momentum hadrons. This is because most existing neutrino detectors cannot detect the low-momentum protons and pions due to their high momentum thresholds. Hence, we started a new experiment, NINJA, to precisely measure neutrino interactions using nuclear emulsion detectors. In this thesis, the first measurement of neutrino interactions on water using a nuclear emulsion detector is reported, as well as prospects of future measurements.

We carried out a pilot experiment with a 3-kg water target detector. NINJA is the first emulsion experiment using water as the neutrino interaction target of the emulsion-based detector, ECC. A total of 7.1×10^{20} POT of the antineutrino mode beam was accumulated in 2017 and 2018. Whereas the emulsion detectors have supreme angular and position resolutions, they do not provide any time information. Therefore, a new scintillating fiber tracker (SFT) using 1-mm square fibers was developed as a timestamping device. The SFT we developed has a 240-μm position resolution, and it enables us to connect the tracks in the ECC to INGRID, which is placed downstream of the ECC and used for muon tracking.

For the analysis of the neutrino interactions, we established a momentum reconstruction method using the water-target ECC. Momenta of muon, pion, and protons from the neutrino interactions were measured with a 30%–40% resolution using multiple Coulomb scattering of the particles. Besides, the PID method was also established in this analysis. While the muon tracks are identified by INGRID, separations of protons and pions need to be carried out by the ECC. Using the energy deposit in the emulsion films and the measured momentum, we achieved a 76.0% proton selection efficiency with 98.5% purity and a 98.7% pion selection efficiency with 78.8% purity for the tracks from the

neutrino interactions. Moreover, after the PID process, the momenta of protons stopping in the ECC were measured by the track range in the ECC. This allows us to measure low momentum protons, which are especially important in our study, with around a 5% resolution.

From the above, measurements of the track multiplicity and kinematics of muons, charged pions, and protons from charged-current inclusive $\overline{\nu}_\mu$ and ν_μ interactions on the water target were performed. A total of 86 candidate events were observed. We successfully measured protons from neutrino-water interaction with a 200 MeV/c threshold. Considering that the proton momentum thresholds of ND280 and other scintillator detectors are around 400 MeV/c, this measurement significantly improved the neutrino interaction measurements. We also found a tendency to overestimate the number of charged pions in the current model, and the muon distributions show slightly higher angle and lower momentum shapes than the model predictions. Although the statistical uncertainty was large, the results of this pilot run clearly demonstrated the capability of the emulsion detector to measure various distributions of the charged particles from the neutrino-water interactions with low-momentum thresholds for protons and pions.

We carried out the first NINJA physics run with a 75-kg water target from November 2019 to February 2020. Another run is planned in 2022, and the total CC events are expected to be around 3300. We considered how NINJA measurements with these larger statistics can contribute to the T2K measurements. We found that the current neutrino interaction model used in T2K may not be able to cover the NINJA observables. NINJA needs to validate the models themselves and construct more reliable models together with T2K. Therefore, possible validation methods were considered. It is especially important to characterize the MEC interaction, which is a component of the 2p2h interactions and biases the reconstructed neutrino energy at SK. A multivariate analysis was introduced to extract these interactions from the observed events using an MC simulation. The MEC cross section can be measured from the CC0π2p sample with a 20% systematic error. This approach allows us to measure the kinematics distributions of the MEC interactions as well as the overall cross section, and we can validate the existing models by comparing the data to the model predictions. Although this is one of many possible approaches, such a practical analysis allows us to construct more reliable neutrino interaction models for the neutrino oscillation analysis.

In conclusion, the pilot run results demonstrated that the NINJA measurements achieved an unexplored area in the measurement of neutrino-water interactions, and the simulation studies of the physics run showed our capability of validating and constructing the neutrino interaction models. The NINJA experiment is expected to contribute to reduction of the systematic error in T2K by constructing more reliable neutrino interaction models. The construction of reliable models is a basis for observation of the CP violation in the neutrino oscillation.

Appendix A

Supplementary of the INGRID beam measurement

In this chapter, measurement of the neutrino beam profile in the antineutrino mode is described. We especially focus on the T2K Run9 period, which corresponds to the NINJA pilot run reported in this thesis. Details of the beam profile measurement in the neutrino mode can be found in Ref. [149].

A.1 Reconstruction and event selection

The event reconstruction method in the INGRID modules is described in Sec. 6.2. Neutrino interactions are reconstructed at the 14 individual modules. In the NINJA event reconstruction, only the beam timing cut was applied after the vertex reconstruction. For the beam measurement, the following selections are applied to select neutrino interactions occurring in the INGRID modules in addition to the selection in Sec. 6.2.

Veto cut
: Upstream veto cut is applied to eliminate sand muons and muons from neutrino interactions in upstream materials. On the contrary to the NINJA selection, events having their reconstructed vertices at the most upstream tracking layer are eliminated. Similarly, events with tracks whose upstream edges have hits at the side veto planes are eliminated to exclude muons coming from the sides of the modules.

Fiducial volume (FV) cut
: The FV of each module is defined as $\pm$ 50 cm from the center in the x-y direction from the second to ninth tracking layers. Events with vertices within the FV are selected as neutrino interactions occurring in INGRID.

After selecting neutrino interactions at each module, several corrections are applied as follows to reduce systematic errors induced by the differences between individual modules.

- Iron target mass: there are around 1 % variations in iron target mass between modules. Based on the measured mass at the construction, the number of neutrino interactions at each module is corrected. Mass of each module is summarized at Tab. A.1.

- Background: neutral particles such as neutrons and neutral pions may induce short tracks starting in the INGRID FV. These backgrounds are estimated by the MC simulation and subtracted from the observed number of events. Although the expected number of backgrounds depends on the position of the module, its variation is less than 0.5 %.

- Dead channel: at the end of T2K Run9, there were 68 dead channels in total out of 8360 channels in 14 modules. Those dead channels affect the track reconstruction, thus the effect is estimated by the MC simulation and corrected. This is the largest variation between modules, and the number of dead channels is increasing every year. The number of dead channels and the correction factors are summarized in Tab. A.2.

- Accidental MPPC noise: accidental noise hit may induce misreconstruction or change the number of hit planes. The variation of the noise rate between modules is evaluated, and the correction factors are concluded less than 0.5%.

- Pileup: even if two neutrino interactions occur in the same bunch, these events are basically reconstructed separately. However, event loss may occur when two tracks are overlapped and the vertices are misreconstructed. This effect is called "event-loss constant". It is evaluated based on the beam data, and calculated as a function of POT in a bunch. Event loss constants are summarized in Tab. A.3. The event loss constants at the central modules are about 1% higher than those of edge modules.

Detector systematic errors on the selected number of events in T2K Run9 are summarized in Tab. A.4. Estimation method of each error source is the same as described in Ref. [149], but the values are updated for anti-neutrino measurement.

Table A.1: Iron target mass of each INGRID module and difference from the designed mass

Horizontal module	0	1	2	3	4	5	6
Measured iron mass (kg)	7124	7081	7065	7076	7059	7094	7114
Difference from the designed mass (%)	0.83	0.23	0.00	0.16	-0.08	0.41	0.69

Vertical module	7	8	9	10	11	12	13
Measured iron mass (kg)	7041	7063	7094	6987	7079	6979	6988
Difference from the designed mass (%)	-0.34	-0.03	0.41	-1.10	0.20	-1.22	-1.09

Table A.2: Number of dead channels and the correction factor in each module.

Horizontal module	0	1	2	3	4	5	6
Number of dead channels	8	6	1	1	2	18	6
Correction factor	-3.19	-0.22	0.02	-0.43	-0.25	-3.21	-1.46

Vertical module	7	8	9	10	11	12	13
Number of dead channels	4	0	5	2	8	7	0
Correction factor	-0.75	0	0.13	-0.06	-0.86	-0.57	0

Table A.3: Event loss constant of each INGRID module

Horizontal module	0	1	2	3	4	5	6
Event loss constant (10^{-16}/POT)	3.24	4.92	4.92	5.02	6.09	5.61	4.17

Vertical module	7	8	9	10	11	12	13
Event loss constant (10^{-16}/POT)	4.39	4.42	4.44	5.15	5.39	4.34	4.15

Table A.4: Summary of the INGRID detector systematic errors

Error source	Error size (%)
Iron target mass	0.13
Accidental noise hit	0.13
Hit efficiency	0.43
Event pileup	0.19
Beam-induced background	0.60
Non beam-induced background	0.01
Track reconstruction	1.21
Track matching	0.55
Vertex reconstruction	0.25
Beam timing cut	0.01
Veto cut	0.54
FV cut	0.26
Total	1.67

A.2 Results of the neutrino event rate and the beam profile measurements

As described in Sec. 2.4, the neutrino beam profile can be obtained from the number of observed events at seven modules for each horizontal and vertical modules. The event rate was shown in Fig. 2.12. Beam profile is fitted by Gaussian function, then the beam center and width at the INGRID position are calculated. The fitting result was already shown in Fig. 2.13. There are three systematic error sources: detector error, bias induced by the Gaussian fitting, and the error of the detector position. The detector systematic error is evaluated using a toy MC simulation by propagating the errors in Tab. A.4. To estimate the bias from the Gaussian fitting, the beam center in the MC simulation is varied and the beam center obtained by Gaussian fitting is compared to the true beam center. As the systematic error on the survey of the detector position, 0.2 cm is assigned. The quadratic sum of these three errors is considered as the systematic error. The results of the T2K Run9 period are obtained as follows.

$$\begin{aligned} \text{Horizontal}: &\quad 0.005 \pm 0.017\ (\text{stat.}) \pm 0.122\ (\text{sys.})\ \text{mrad}, \\ \text{Vertical}: &\quad 0.022 \pm 0.019\ (\text{stat.}) \pm 0.140\ (\text{sys.})\ \text{mrad} \end{aligned}$$

These results show that the beam canter was stable enough within the requirement, 1 mrad. Table A.5 summarizes the beam direction measurement in the antineutrino mode. The Run9 results are consistent with the previous results.

Table A.5: Summary of the beam direction measurement in the antineutrino mode

Period	Horizontal (mrad)	Vertical (mrad)
Run5	0.097 ± 0.065 (stat.) ± 0.117 (sys.)	0.185 ± 0.077 (stat.) ± 0.141 (sys.)
Run6	0.069 ± 0.026 (stat.) ± 0.119 (sys.)	0.120 ± 0.029 (stat.) ± 0.139 (sys.)
Run7	0.030 ± 0.026 (stat.) ± 0.120 (sys.)	0.147 ± 0.029 (stat.) ± 0.140 (sys.)
Run9	0.005 ± 0.017 (stat.) ± 0.122 (sys.)	0.022 ± 0.019 (stat.) ± 0.140 (sys.)

A.3 Comparison with proton beam monitors and MUMON

MUMON also measures beam direction from the profile of muons. Neutrino beam profiles measured by INGRID and MUMON have correlations with the proton beam profile. In Fig. A.1, beam center measured by INGRID and MUMON are compared to proton beam information. Proton beam angle measured by proton beam monitors in the beamline is extrapolated to the position of MUMON and INGRID, and the extrapolated positions are subtracted from the measured beam centers at MUMON and INGRID. In the plot, measured positions of the proton beam monitor and MUMON are scaled to easily compare to that of INGRID. One can see that MUMON and proton beam have especially strong correlation, and INGRID also show shift of beam center caused by proton beam direction.

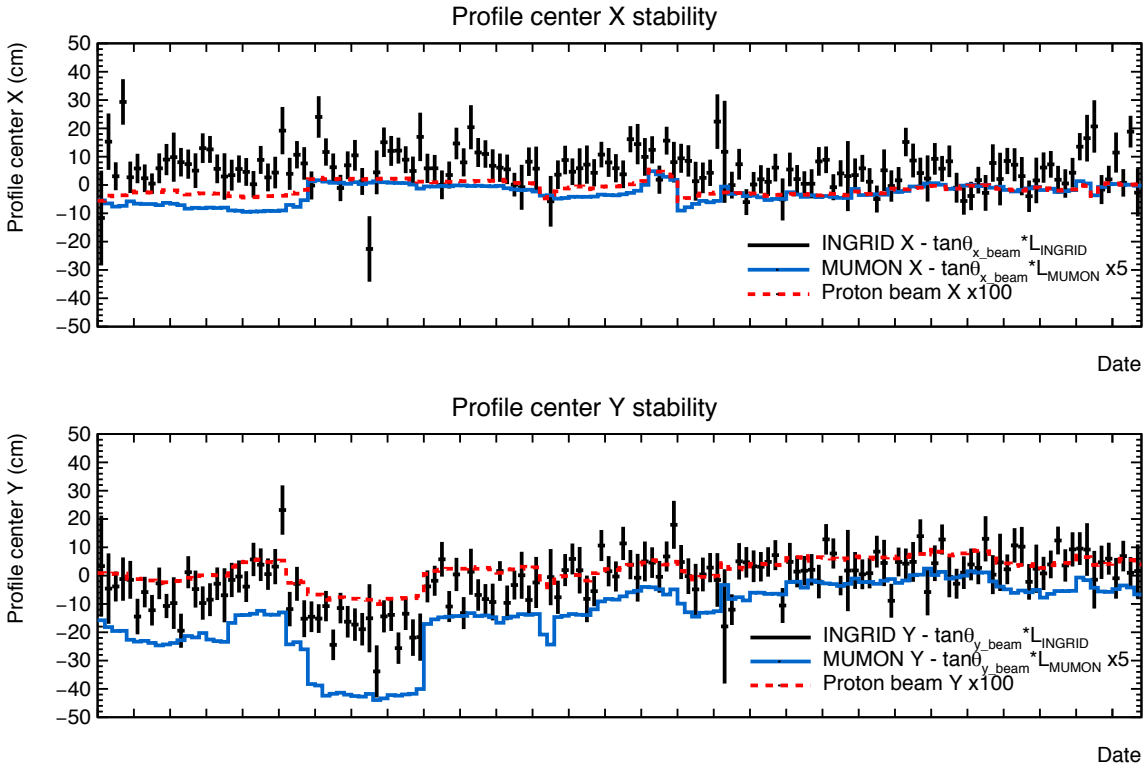

Figure A.1: Comparison of the beam center values measured by the proton beam monitor, MUMOM and INGRID. Each bin corresponds to the daily average of the beam center.

Appendix B

Development and construction of the SFT

In this section, development and construction of the SFT are described.

B.1 Requirement for the SFT

For the pilot run, we developed a new scintillating fiber tracker (SFT), which can cover an enough area to connect tracks between the ECC and INGRID, and can be operated with a small number of readout channels. Requirements are summarized as follows:

- Active size is more than 35 cm×35 cm to cover the size of the emulsion films.
- Thickness is less than around 5 cm to keep the distance between the ECC and INGRID close enough.
- Number of readout channels is less than several hundreds.
- Position resolution is around 200 μm.

As shown in Sec. 4.4.2, we use the ratio of the light yields at the neighboring fibers, and signals from four fibers are read out by one MPPC to reduce the total number of readout channels without reducing the fiber cross-sectional size.

Although the position resolution of the SFT becomes better as the cross-sectional size of the fibers is reduced (e.g. 0.5 mm), the number of readout channels increase in such cases. On the other hand, if we increase the cross-sectional size (e.g. 2 mm), it will be expensive in cost (it is proportional to fiber mass), and handling of the fibers during construction will be harder. This is because we need a longer distance before reaching fiber cookies due to the requirement of the minimum bending diameter. We compared several sizes of fibers, and 1-mm square fiber is employed.

B.2 Construction of the SFT

Construction of the SFT was carried out from April to September 2018. As introduced in Sec. 4.4.2, the SFT is an active tracker which consists of 1024 scintillating fibers. Two layers are constructed to form horizontal and vertical layers, thus the number of fibers for each layer is 512. All the fibers are partially glued on the grooved aluminum plates as shown in Fig. B.1 left photo, and two aluminum plates form one layer. Figure B.1 right photo shows tagged fibers to insert and fixed to fiber cookies. In this SFT, four scintillating fibers are inserted in one hole, which corresponds to one MPPC readout to reduce the total number of readout channels. Since we use combinations of hit MPPC channels to identify the hit fibers, correspondence between the fibers and the cookie holes is carefully checked during the assembly.

Figure B.1: Construction of the tracking layers made of scintillating fibers. Scintillating fibers glued on the grooved aluminum plates (left) and tagged fibers before inserting fiber cookies (right).

Scintillating fibers inserted into the fiber cookies are glued by optical cement. As shown in the left photo of the Fig. B.2, optical cement is poured from the inner side of the SFT. Gluing is carried out only one side at a time. The SFT is rotated after the optical cement is dried (Fig. B.2 left), then, extra part of the fibers were removed and polished up by a company. Figure B.3 shows the polished edge of the fibers.

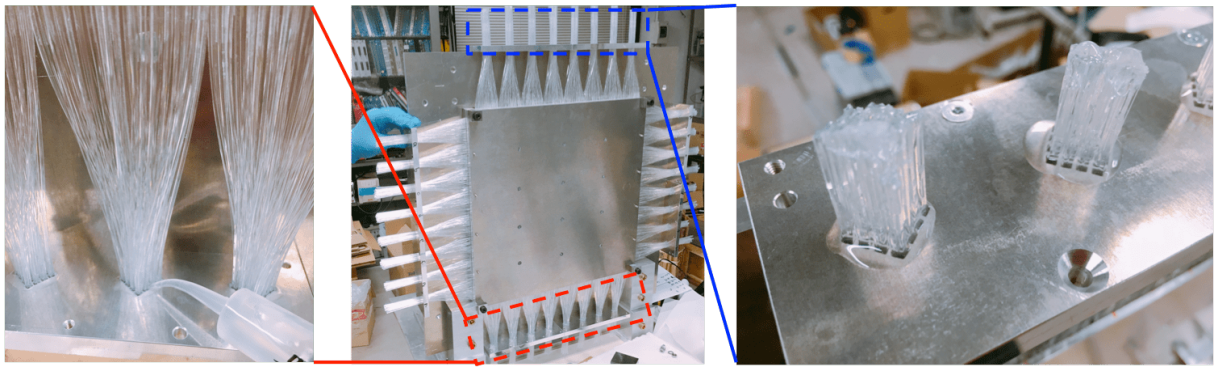

Figure B.2: Gluing of the scintillating fibers inserted into fiber cookies. Optical cement is poured from the inner side of the fiber cookies (right). Glueing one side at a time and the SFT is rotated after the optical cement is dried (right).

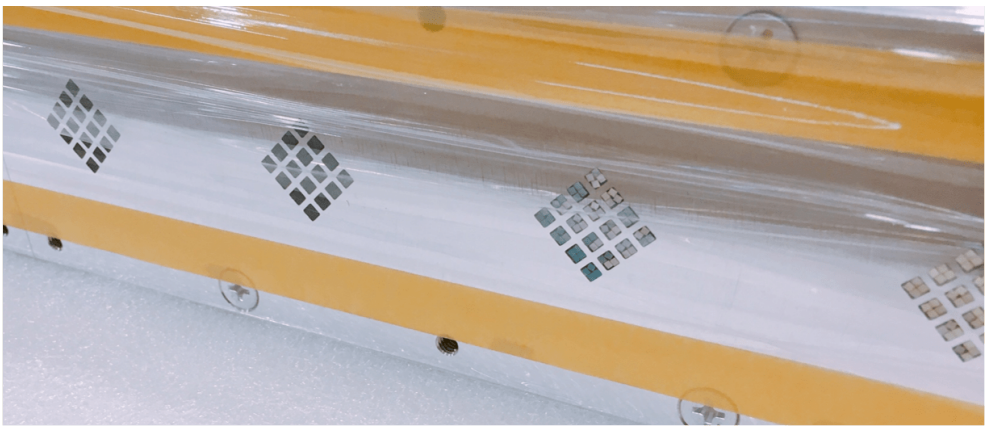

Figure B.3: Fiber cookies after polishing the edges of the fibers by a company.

B.3 Readout system

Scintillation light from the fibers are read out by MPPCs. Dedicated PCBs shown in the left photo of the Fig. B.4 are designed, and four 16-channel MPPC arrays are placed on each PCB. The PCBs are connected to the EASIROC modules using flat cables. In the setup of the pilot run, MPPCs and EASIROCs are placed at about 3 m distance separated by the cooling shelter. Since non-shielded cables shown in top of Fig. B.4 right was affected by significant noise, shielded cables shown bottom are employed.

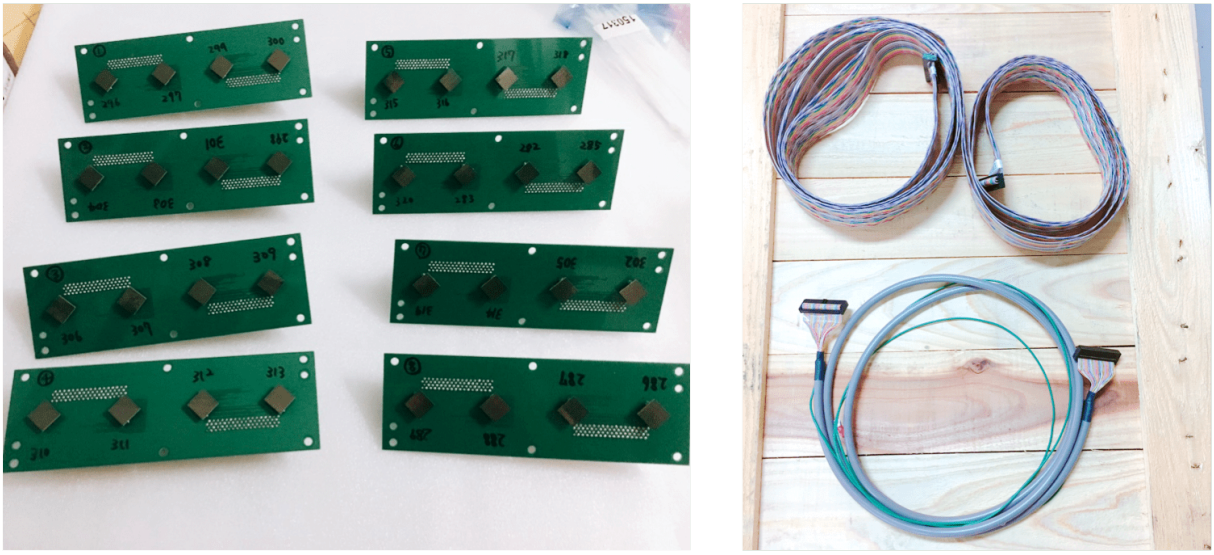

Figure B.4: PCB boards (left) and the flat cables (right) of the SFT.

Appendix C

Supplementary of the neutrino interaction measurements

This chapter describes two approaches to probe the nuclear effects using scintillator detectors, which is mentioned in Sec. 3.

C.1 Transverse kinematics imbalance

To untangle the complicated nuclear effects, three variables shown in Fig. C.1, $\delta p_T, \delta\alpha_T, \delta\phi_T$, are introduced. In the case of the CC0π1p sample, three variables are defined as follows [123]:

$$\delta p_T \equiv |\vec{p}_T^{\,l} + \vec{p}_T^{\,p}|, \tag{C.1}$$

$$\delta\phi_T \equiv \arccos\frac{-\vec{p}_T^{\,l}\cdot\vec{p}_T^{\,p}}{p_T^l p_T^p}, \tag{C.2}$$

$$\delta\alpha_T \equiv \arccos\frac{-\vec{p}_T^{\,l}\cdot\delta\vec{p}_T}{p_T^l \delta p_T}. \tag{C.3}$$

Here, $\vec{p}_T^{\,l}$ and $\vec{p}_T^{\,p}$ are the lepton and proton momenta, while p_T^l and p_T^p refer to their projection to a plane transverse to the incoming neutrino. The first variable δp_T denotes a momentum imbalance. Large δp_T corresponds to the large nuclear effects. The second variable $\delta\phi_T$ is an angular imbalance, which is zero for the CCQE interaction in absence of the nuclear effects. Compared to δp_T, $\delta\phi_T$ does not include so much information, while it can be measured with good accuracy because only the angle information is required. The third variable $\delta\alpha_T$ denotes an acceleration of the final state hadron. $\delta\alpha_T < 90°$ denotes that the proton transverse momentum is increased by the FSI, while it decreases for $\delta\alpha_T > 90°$.

Figure C.2 shows a result of a $\delta\alpha_T$ measurement by T2K [68]. It was measured using a scintillator tracking detector in ND280 with around a 500 MeV/c proton threshold. It was found that any of our current models cannot explain the data well, but more advanced nuclear models such as the SF model are preferred. MINERνA also reported similar measurements using a scintillator tracking detector with a 450 MeV/c proton momentum threshold [124]. Figure C.3 shows the differential cross section as a function of $\delta\alpha_T$. The data and the GENIE prediction show a clear discrepancy, while MINERνA-tuned Monte

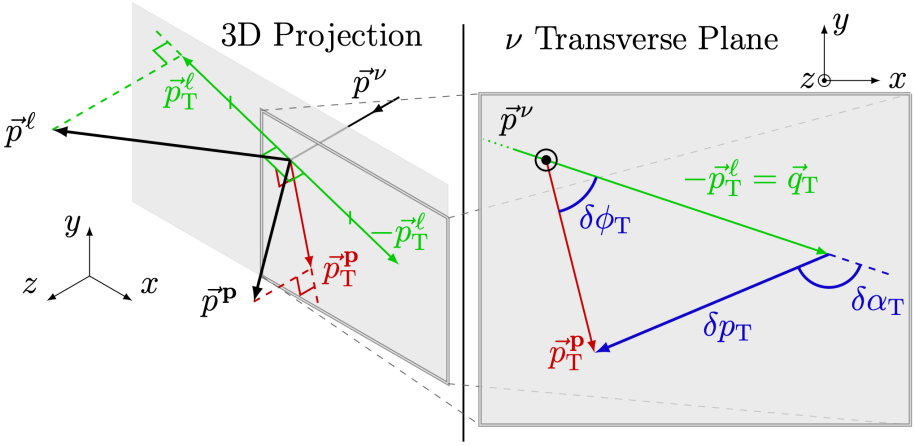

Figure C.1: Schematic view of kinematic variables in a CC0π1p event [174]. The parameter $\vec{p}^{\,\nu}$ is the incoming neutrino momentum, $\vec{p}^{\,l}$ and $\vec{p}^{\,P}$ are the momenta of outgoing lepton and proton respectively. The variables δp_T, $\delta\alpha_T$, $\delta\phi_T$ denote imbalances of projected momenta, which are expected to prove the nuclear effects.

Carlo prediction reproduces the data better. There are also several ideas to probe the nuclear effects in interactions associating pions as well as the CC0π interactions [172,173].

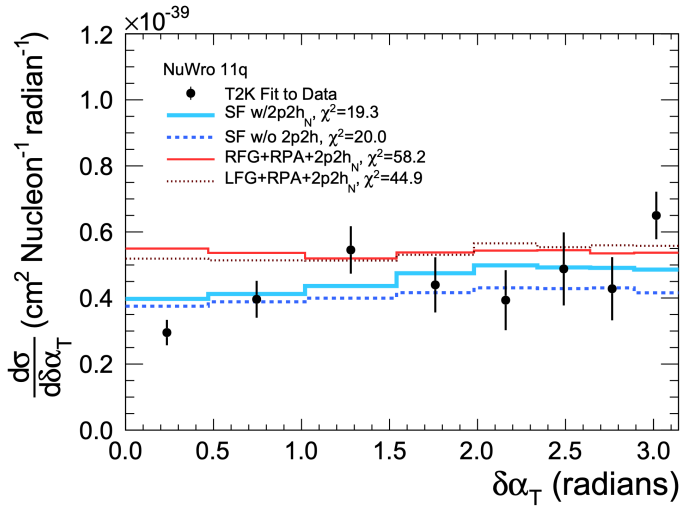

Figure C.2: Differential cross section as a function of $\delta\alpha_T$ measured by T2K ND280 [68].

C.2 Inferred kinematics

The second approach is "inferred kinematics", in which kinematics of the outgoing proton are inferred from the muon kinematics assuming the CCQE interaction. As measured in

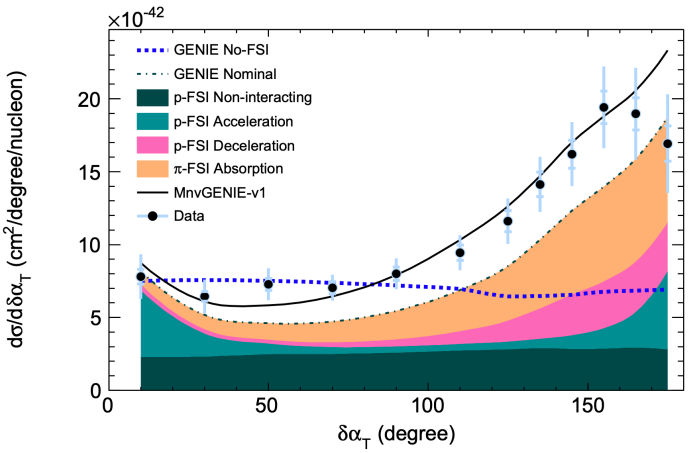

Figure C.3: Differential cross section as a function of $\delta\alpha_T$ measured by MINERνA [124].

T2K [68], three inferred kinematics are defined as:

$$\Delta p_p \equiv |\vec{p}_p^{\,measured}| - |\vec{p}_p^{\,inferred}|, \tag{C.4}$$

$$\Delta\theta_p \equiv \theta_p^{measured} - \theta_p^{inferred}, \tag{C.5}$$

$$|\Delta \boldsymbol{p}| \equiv |\vec{p}_p^{\,measured} - \vec{p}_p^{\,inferred}|. \tag{C.6}$$

Here, $\vec{p}_p^{\,measured}$ and $\theta_p^{measured}$ are measure momentum and angle of the outgoing proton, and $\vec{p}_p^{\,inferred}$ and $\theta_p^{inferred}$ are proton momentum and angle inferred from the muon kinematics. Although they are similar to the transverse kinematics imbalance, these parameters are not projection to a plane transverse to the incoming neutrino.

The parameters of the transverse kinematics imbalance and inferred kinematics are important to see the nuclear effects without using information of low-momentum protons. Related studies and measurements can be found in Refs. [171–173].

Appendix D

Supplementary of the detector performance

This chapter describes reconstruction, resolution, and uncertainties of the pilot run detectors, whose details are not shown in Sec. 4.

D.1 Track reconstruction of emulsion films

Emulsion reconstruction framework, NETSCAN, was originally developed by the DONUT experiment, and since then, it has been updated by many emulsion experiments as a common framework. In our analysis, systematic understanding of the detector and the track reconstruction are especially required. Here, an updated noise cut method which is newly implemented in the pilot run is described first. Following this, remarks on configuration of the linklet reconstruction are described because we need to connect basetracks placed at longer distance than those in the ECCs using only metals such as iron and lead.

D.1.1 Basetrack reconstruction

The basic reconstruction method was described in Sec. 6.1. An update from the previous analysis [130] is the method of selection to reduce accidental noise tracks. Reconstructed basetracks includes noise tracks formed by chance coincidence of tiny tracks of low-energy electrons in emulsion gel induced by environmental radiation. A selection, called "track ranking cut" [130,148], is applied using VPH and angle difference between microtracks and a basetrack. A small angle difference corresponds to two microtracks are aligned straight, and a high VPH value also corresponds to straightness of the microtracks. Thus, tracks with small angle difference and high VPH are selected as signals. In the conventional method, the power of this selection was weak because the angle resolution is worse in high angle region. To reduce noise tracks even for high angle tracks, lateral-radial coordinates (described in Sec. 7.2.2) are introduced in the pilot run analysis. All the tracks are converted into lateral-radial coordinates and the selection is applied using only the lateral angles. Figure D.1 shows the number of tracks after the track ranking cut and the selection efficiency by the cut as a function of the track angle. This new method resulting in more reduction in high angle region without losing the selection efficiency. More details can be found in [176].

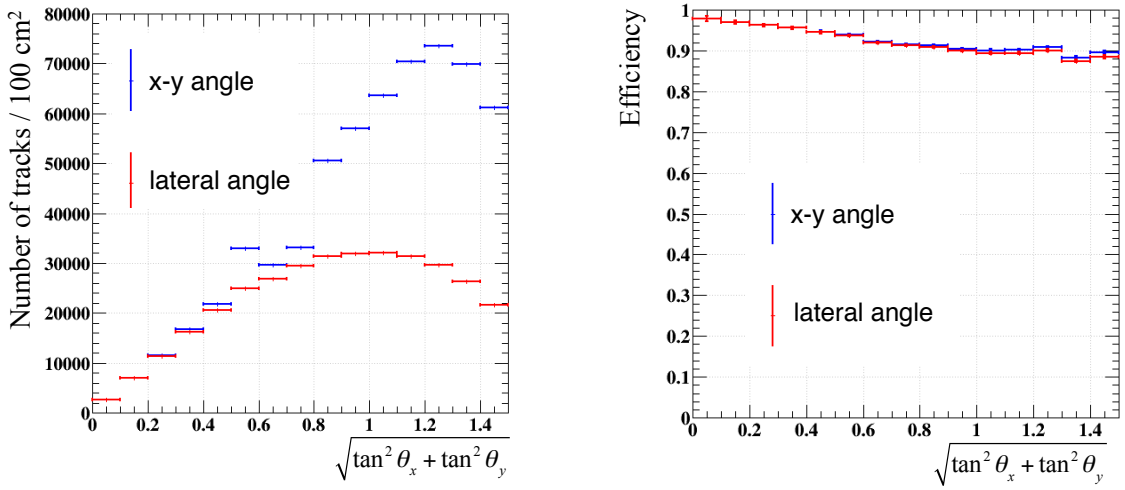

Figure D.1: Number of tracks after the ranking cut (left) and the selection efficiency by the cut (right) as a function of the track angle. The lateral angle method can reduce the number of tracks without losing the selection efficiency.

D.1.2 Linklet reconstruction

A pair of basetracks over two emulsion films is called a linklet. For reconstruction of the linklets, the positional relationship between two films is estimated, and this process is referred to as alignment. A set of affine parameters is varied by an order of μm, and the position where the number of connected tracks will be maximum is selected. A rough alignment between two films is calculated first (Global alignment). Then, alignment of each 2 mm×2 mm is computed (local alignment) because the films are not perfectly flat and the distance between films varies with position due to deflection.

After computing the alignment, linklets are reconstructed. The tolerances of position and angle difference of two basetracks depend on the distance of the two films. Table D.1 summarizes the linklet tolerances used for the chain reconstruction. The parameters δ_{pos}, ϵ_{pos}, δ_{angle}, and $\epsilon_{\mathrm{angle}}$ are used as follows:

$$|dx| < \delta_{\mathrm{pos}} + \epsilon_{\mathrm{pos}} \times |\tan\theta|, \tag{D.1}$$

$$|dax| < \delta_{\mathrm{angle}} + \epsilon_{\mathrm{angle}} \times |\tan\theta|. \tag{D.2}$$

Here, dx and dax are the position and angle tolerances in the x or y direction, respectively. If the two films are adjacent, only an iron plate (Fe in Tab. D.1) or a water layer (Water) exists between the films. However, skipping one or two films are used as well as the adjacent films. Thus, for the case skipping one film, an iron plate and a water layer (Fe-Water) are considered, and for the case of skipping two films, two iron plates and a water layer (Fe-Water-Fe) or an iron plates and two water layers (Water-Fe-Water) are considered. The Fe gap has the closest distance between films, while the Water-Fe-Water gap has the largest.

Sometimes, there are several connection candidates for one basetrack, especially when tracks are connected over a long distance. In such case, only one combination of the

Table D.1: Linklet tolerances used for the chain reconstruction process. Position (μm) and angular allowance are shown.

gap	δ_{pos}	ϵ_{pos}	δ_{angle}	$\epsilon_{\mathrm{angle}}$
Fe	120	20	0.12	0.058
Water	200	20	0.12	0.058
Fe-Water	240	20	0.12	0.058
Fe-Water-Fe	260	20	0.12	0.058
Water-Fe-Water	340	20	0.12	0.058

basetracks is selected on the basis of the position and the angle difference between the basetracks.

D.2 Angular resolution of the emulsion films

Angular resolution of the emulsion films is an important factor affecting not only the reconstruction of tracks and the track angle measurement but also momentum reconstruction. In this section, features of the emulsion angular resolution and measurement method are introduced.

Basetrack angular resolution $\sigma_{\tan\theta}$ can be written as follows:

$$\sigma^2_{\tan\theta} = \frac{2}{\Delta z^2}(\delta x^2 + \delta z^2 \times \tan^2\theta). \tag{D.3}$$

Here, Δz is the thickness of the plastic base, which is fixed as 180 μm (210 μm). δx and δz are free parameters. δx corresponds to the positional resolution ($\sim$0.3 μm) and δz is the depth of focusing of HTS ($\sim$4 μm). Since the angular resolution is a function of track angle, it is measured in angle binning. There are sets of adjacent films included in the SSs at the most downstream of the ECC. For the measurement of the angular resolution, angular differences between basetracks of a linklet in the adjacent films are used. Since low momentum tracks are affected by MCS, sand muons penetrating from the most upstream film to the most downstream one are selected as the track sample to evaluate the angular resolution. Figure D.2 shows the result as a function of track angle fitted by Eq. D.3. At the forward region, the angular resolution is about 2.9 mrad. Note that this value is an angular difference between two films and the resolution of a single film is $1/\sqrt{2}$ of this.

D.3 VPH distribution

The results shown in Sec. 8.3 show that the PID uncertainty is the most dominant error source in the measurements of the proton and pion kinematics. This uncertainty originates from differences of VPH distributions in the data and the MC simulation. Although the MIP peaks are scaled to be 100 in the data and the MC simulation, there still are significant discrepancies in the black peaks. Figure D.3 shows the VPH distributions in each angle range. Tracks with $P\beta$ <0.1 GeV/c are shown. The histograms represent

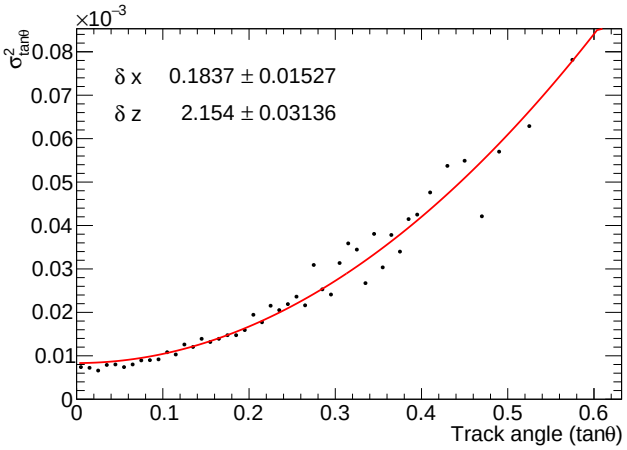

Figure D.2: Angular resolution of the emulsion films as a function of a track angle

the data, while the red broken lines correspond to the prediction by the MC simulation (only the black peaks are shown in the MC simulation). There are especially significant differences in high angle regions.

There are several possibilities that can make such VPH differences between the data and the MC simulation.

- Fading of the tracks
- Linearity between the energy deposit and the number of silver grains
- Saturation due to the scanning

The effect of the fading correction can be estimated by the uncertainty of the correction factor shown in Fig. 6.9. The uncertainty of the correction factor par one week is less than 0.5%, thus the overall uncertainty is smaller than 6% even for the oldest (12 weeks) tracks. The linearity of the relation between the energy deposit and the number of silver grains is discussed in Ref. [177]. It seems there is a very good linearity at least $P\beta > 0.5$,GeV/c although the lower range needs to be confirmed. We are considering that the major difference between the data and the MC simulation seems to come from the scanning by HTS. The VPH is calculated by summing up the number of hit pixels at each scanning layer. However, the number of pixels is limited to 11×11 pixels at once. One scanning layer has about 4 μm thickness while one pixel has 0.45 μm. Therefore, saturation happens for large angle tracks. This effect distorts the relationship between the energy deposit and the VPH, thus the discrepancies between the data and the MC simulation occur at low momentum and high angle regions. To reproduce the VPH distribution in the MC simulation, more understanding of the saturation is necessary.

Effect of the differences in the VPH distributions to the PID performance is evaluated as follows. As the VPH difference between the data and the MC prediction, the dip position between the MIP and the black peaks is used. As shown in Fig. D.4, 2σ from the black peak is defined as the dip position. The difference between the data and the MC prediction are checked at each angle and momentum bin. There is around 11% difference at maximum between the data and the MC prediction; thus, the VPH distribution in the

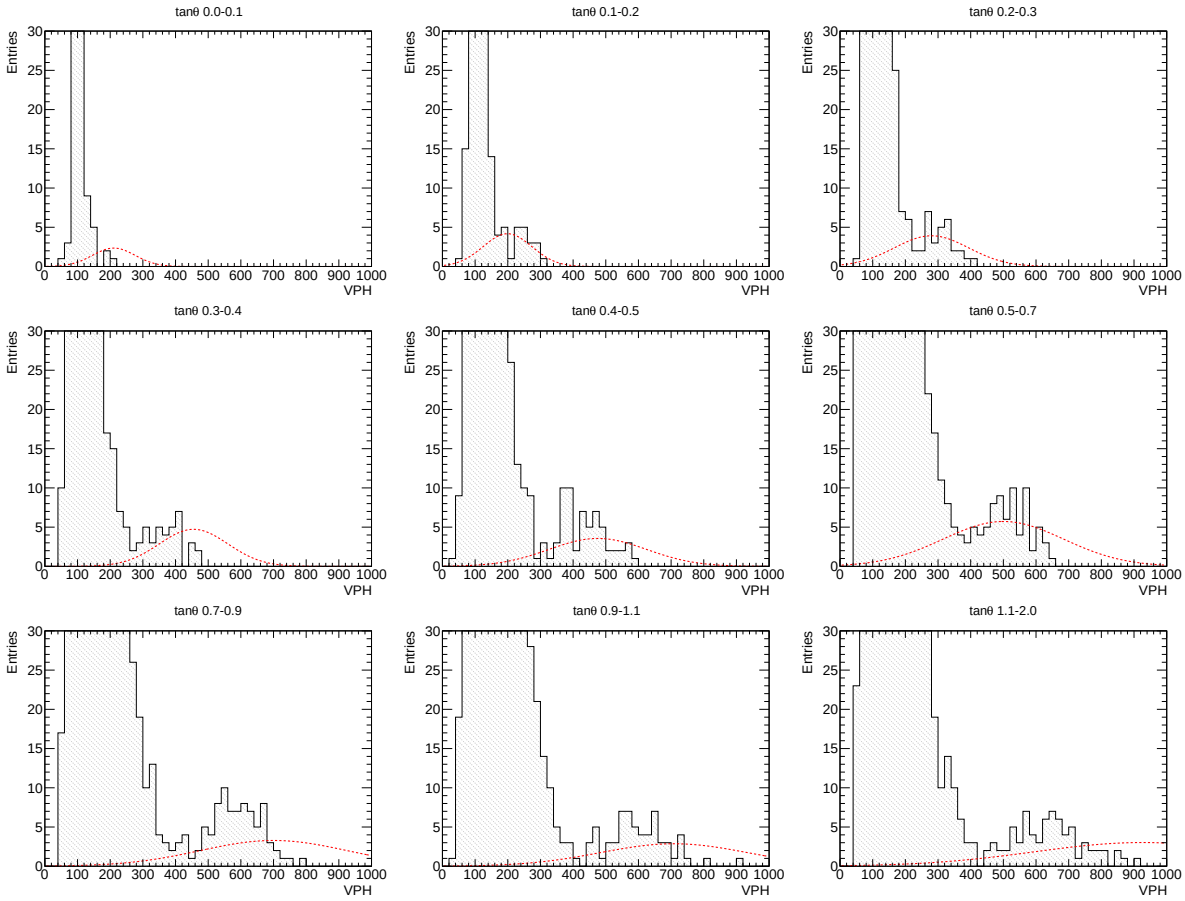

Figure D.3: VPH distributions at each angle range in comparison with the data and the MC simulation. Tracks with $P\beta$ <0.1 GeV/c are used.

MC simulation is varied to see how the PID efficiency and purity change. This estimation method seems conservative, thus we need to consider better estimation with understanding of the VPH behaviour.

D.4 Uncertainties on the ECC components

Uncertainties in thickness of the emulsion films, the iron plates, and the vacuum packing films affect the evaluation of the target mass and the momentum reconstruction. Thus, we carefully measured these variations. Figure D.5 shows measured thicknesses of the emulsion films in Run-a and Run-b periods before developing. Thickness is measured at each corner of the film, and the average is taken as the thickness of the film. The Run-b films have smaller RMS values, while they have larger mean values due to the difference of the base thickness used in each run (180 μm in Run-a and 210 μm in Run-b). Figure D.6 shows measured thickness of the iron plates and the packing films. Six positions in a total of 24 iron plates are measured for the iron thickness, and 36 positions in 10 cm$\times$45 cm are measured for the packing thickness. For the evaluation of the uncertainty to the measurement of neutrino interactions, thickness of each material layer is changed by $\pm 1\sigma$ in the GEANT4 simulation and the change in the final results are checked.

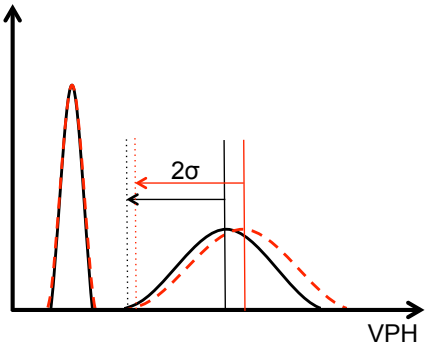

Figure D.4: Definition of the dip position in the VPH distribution. 2σ from the black peak is defined as the dip position.

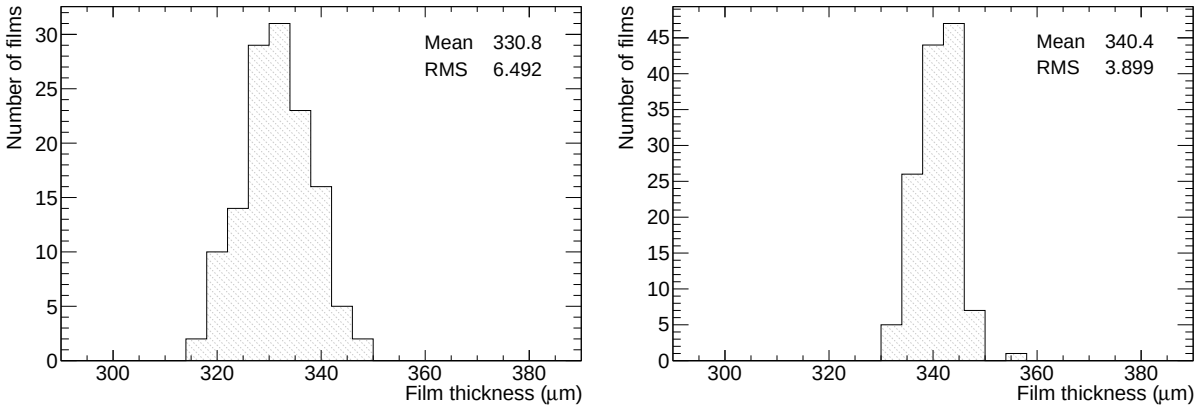

Figure D.5: Measured thicknesses of the emulsion films in Run-a (left) and Run-b (right).

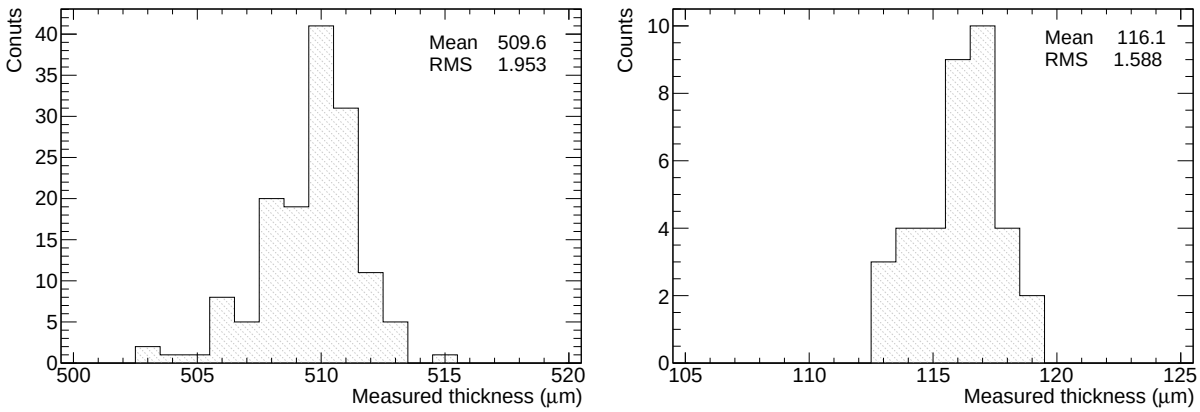

Figure D.6: Measured thicknesses of the iron plates (left) and the packing films (right).

Appendix E

Neutrino interaction measurements on an iron target

In a water target ECC, neutrino interactions occur on the iron plates and the emulsion films as well as the water target layers. In this chapter, measurements of the neutrino interactions on iron plates in the pilot run are described. Compared to water and plastic scintillators (hydrocarbons), iron has more nucleons (even more than argon), thus the nuclear effect may become significant for neutrino interactions on iron. There are several measurements on neutrino-iron cross section and cross-section ratio to other target materials in T2K [69, 160]. Measurement using an iron target will be a good demonstration to check our detector performance since it is easy to increase the target mass and earn the statistics.

As introduced in Sec. 4.4.1, a 500-μm iron plate is sandwiched between two emulsion films in one tracking layer. This corresponds to about the double of the water target mass. Muon track candidates starting at the iron plates are processed to the same analysis as the water interaction candidates. The vertex distributions of the iron target are already shown in Fig. 8.10.

Results of the iron interaction measurements are shown in the following plots. For these results, backgrounds and systematic uncertainties for the iron interaction events are estimated in the same manner of the water targets. In Figs. E.1 and E.2 raw data distributions are compared with the sum of the neutrino event prediction estimated with the MC simulation and the cosmic-ray background prediction estimated with the off-beam timing data. Figure E.1 shows the multiplicity of the charged particles and the number of pions and protons. The red boxes on the prediction correspond to the quadrature sum of the uncertainties of neutrino flux, the detector response, and the background estimation. Figure E.2 shows distributions of the reconstructed kinematics of muons, pions, and protons. The angular resolution is sufficiently small compared to the bin width, while the momentum resolution is not especially for the muons with high momentum.

In Figs E.3 and E.4, backgrounds from neutral-current interactions, interactions on the packing films, cosmic rays, and chance coincidence of the off-beam timing tracks are subtracted from the data using the background prediction. In these plots, the flux, detector response, and background estimation uncertainties are included in the error bars of the data points, while the hatched regions correspond to uncertainty of the neutrino interaction model. There are less forward angle and high momenta muons in the data, and

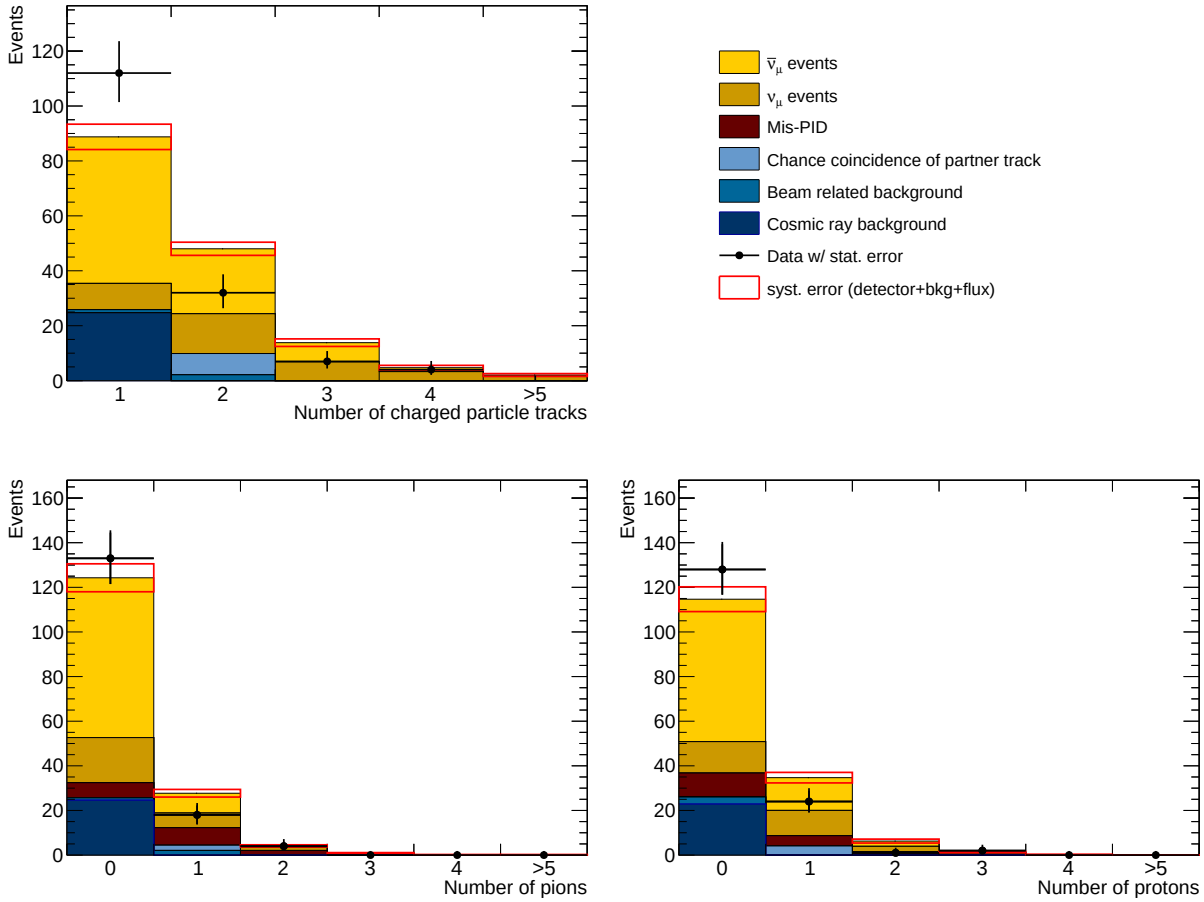

Figure E.1: Multiplicity of charged particles from neutrino-iron interactions and backgrounds (top). The bottom plots show the number of pions (left) and protons (right). The data points are shown by marker points with statistical error bars and the predictions are shown by histograms with systematic uncertainties as red boxes, which are the quadrature sum of the uncertainties of neutrino flux, the detector response, and the background estimation.

the number of measured pions are smaller than expected. These tendencies are similar to the water interaction measurements. Besides these tendencies, the number of measured protons is also smaller than expected. This is because protons from the pion FSI are also reduced due to the small number of pions.

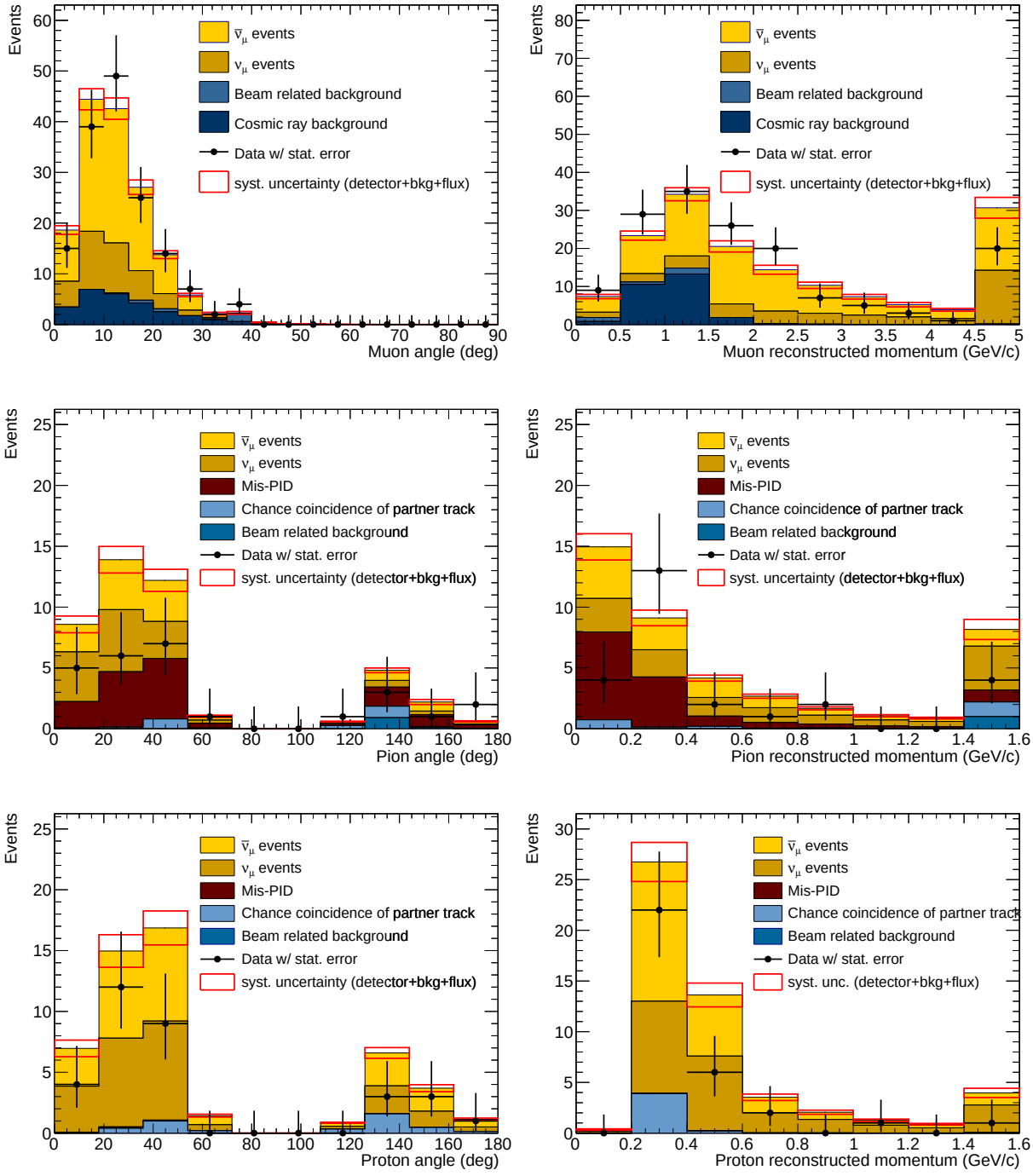

Figure E.2: Distributions of muon, pion, and proton kinematics from neutrino-iron interactions and backgrounds. The left column shows angular distributions, while the right column shows reconstructed momentum distributions. The angular resolution is sufficiently small compared to the bin width, while the momentum resolution is not especially for the muons with high momentum. The data points are shown by marker points with statistical error bars and the predictions are shown by histograms with systematic uncertainties as red boxes, which are the quadrature sum of the uncertainties of neutrino flux, the detector response, and the background estimation.

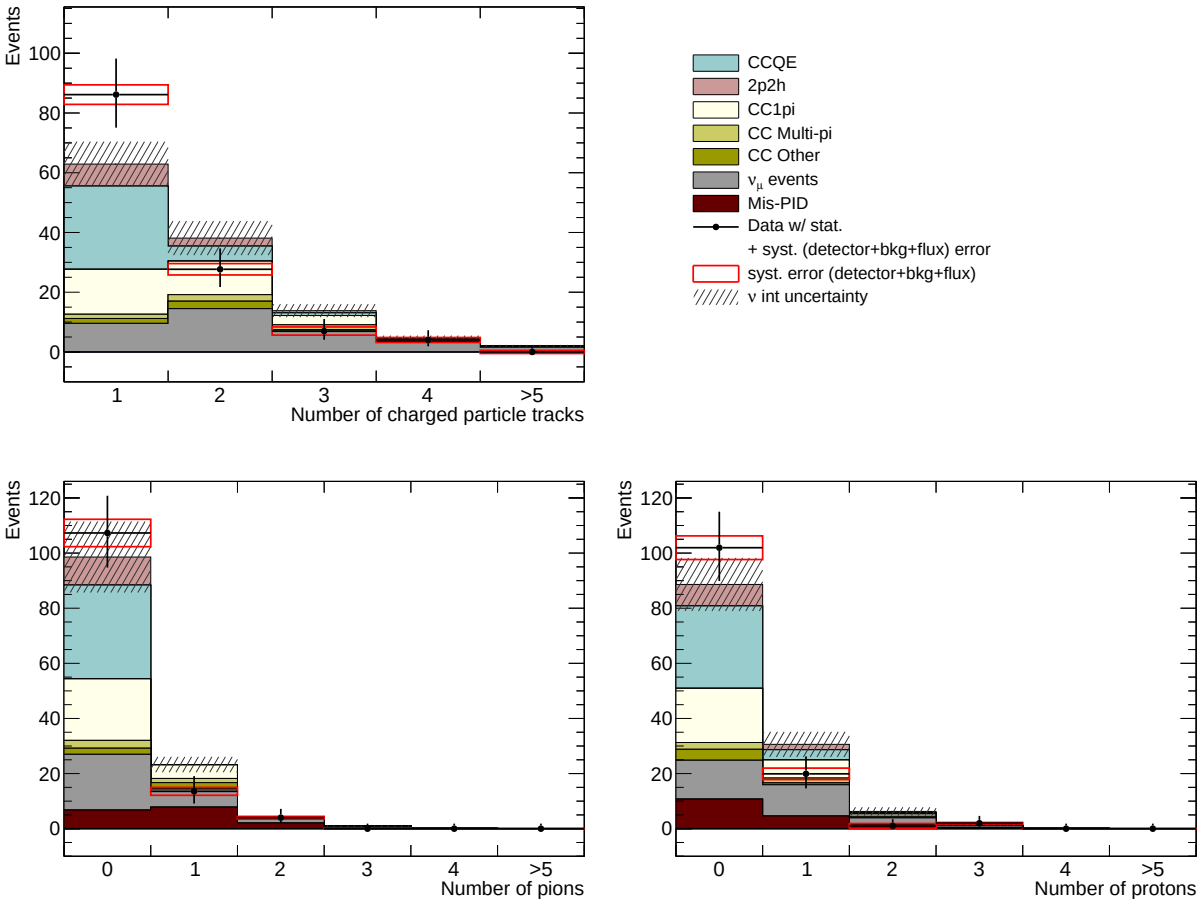

Figure E.3: Multiplicity of charged particles from neutrino-iron interactions (top). Backgrounds are subtracted from the data and the prediction. The bottom plots show the number of pions (left) and protons (right). The flux, detector response, and background estimation uncertainties are included in the error bars of the data points, while the hatched regions correspond to uncertainty of the neutrino interaction model.

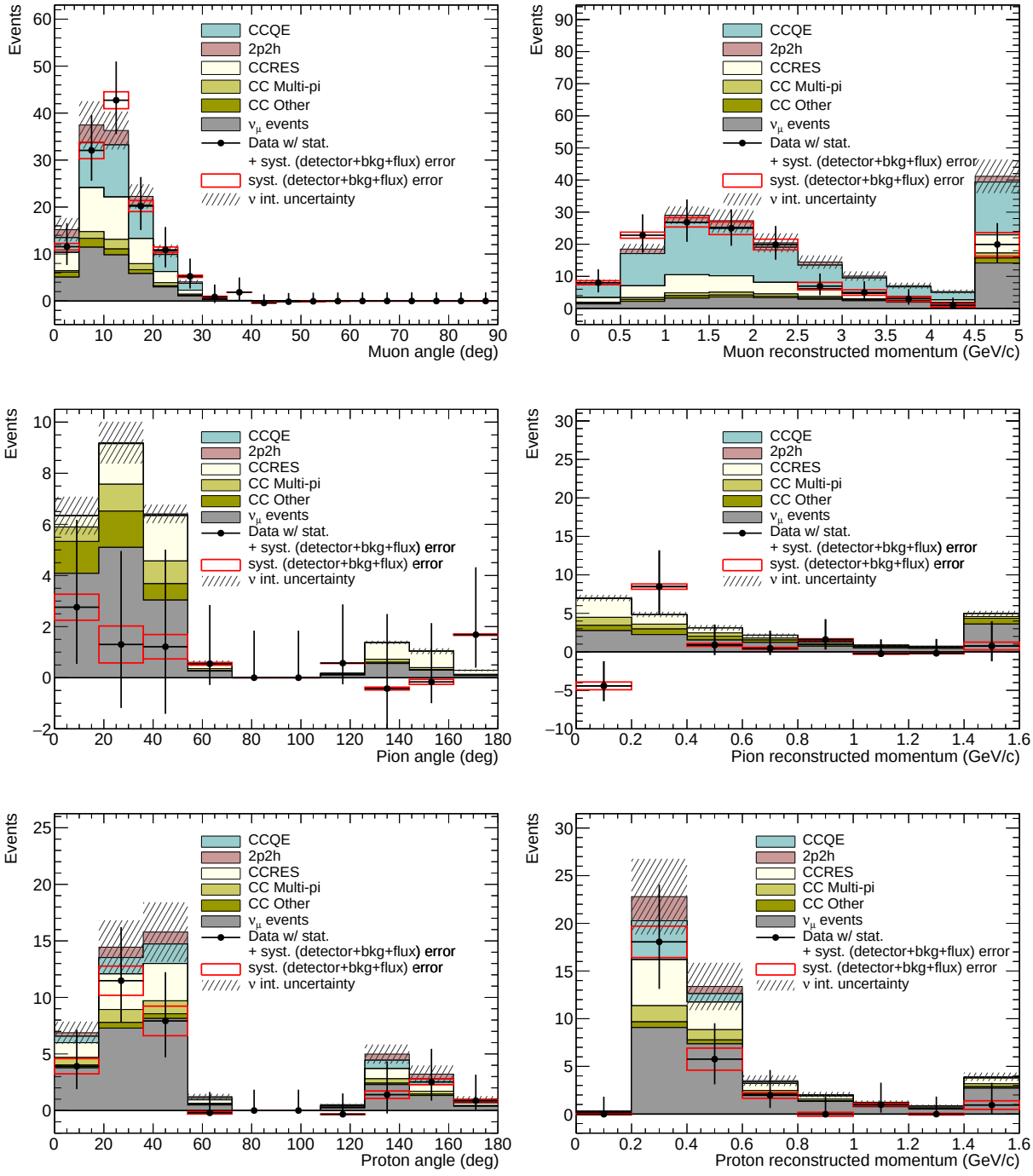

Figure E.4: Distributions of muon, pion, and proton kinematics of neutrino-iron interactions. Backgrounds are subtracted from the data and the prediction. The left column shows angular distributions while the right column shows momentum distributions. The angular resolution is sufficiently small compared to the bin width, while the momentum resolution is not especially for the muons with high momentum. The flux, detector response, and background estimation uncertainties are included in the error bars of the data points, while the hatched regions correspond to uncertainty of the neutrino interaction model.

Appendix F

Supplementary of the neutrino interaction models

This chapter summarizes parameters used in the neutrino interaction model for the latest T2K oscillation analysis, which are already introduced in Tab. 10.1. More details on each parameter and several related topics are discussed. Since the neutrino interaction models and their uncertainties are updated year by year in T2K, some of them are different from the parameters used in the analysis of NINJA pilot run.

F.1 Parameters related to the CCQE interactions

Parameters related to the CCQE and 2p2h interactions are described below.

$M_{\mathrm{A}}^{\mathrm{QE}}$
: Axal vector mass for the CCQE interactions, which is introduced in Sec. 3.1.1. Setting larger $M_{\mathrm{A}}^{\mathrm{QE}}$ value corresponds to increasing the cross section of the CCQE interactions, and it also changes the kinematics of outgoing particles.

Q^2 norm
: Introduced to normalize the CCQE cross section as a function of Q^2. Eight parameters are introduced in the binning of [0, 0.05, 0.10, 0.15, 0.20, 0.25, 0.50, 1.00). Several recent measurements report that measured CCQE-like interactions are less than predictions especially in the low Q^2 region [71, 178, 179]. Figure F.1 is a result from MINERνA which shows differential cross section as a function of Q^2 in comparison with several generator predictions.

2p2h norm
: The 2p2h interactions are not sufficiently measured experimentally thus far, and large discrepancies exist in its cross section among models. For instance, as shown in Fig. 10.12, the model by Martini *et al.* predicts about a factor of two larger 2p2h cross section compared to that of the model by Nieves *et al.* in neutrino mode. However, the discrepancy in the antineutrino interactions is much smaller. Hence, a normalization factor is prepared for each neutrino and antineutrino cross section. Besides, another parameter is prepared to cover difference between carbon and oxygen.

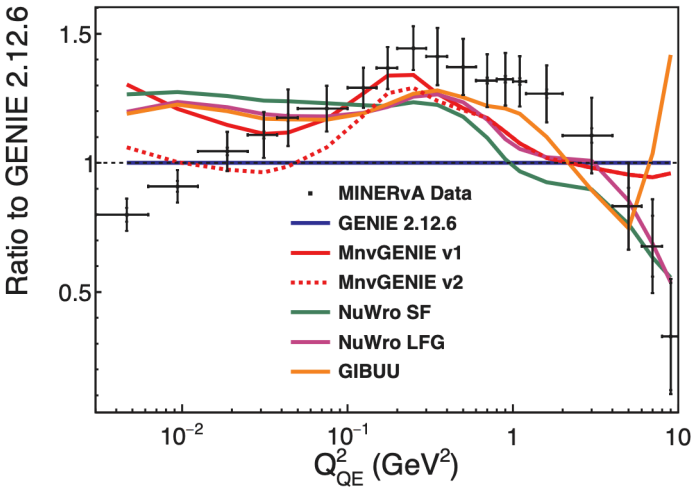

Figure F.1: Differential cross section as a function of Q^2 measured by MINERνA in comparison with several generator predictions [173].

2p2h shape

There are two types of 2p2h interactions, which are separated kinematically as described in Sec. 10.2.1. Figure F.2 shows 2p2h cross section in two dimensional distribution of energy transfer and three-momentum transfer for 3 GeV neutrinos. Two peaks are observed in both neutrino and antineutrino interactions. Interactions in the peak at the higher energy transfer are dominant and referred as Meson Exchange Current (MEC). Another peak is contributed by couplings to a pair of correlated nucleons (NN), and the momentum transfers are as small as they do not create delta resonance. Since the ratio of these two components changes the reconstructed neutrino energies as shown in Fig. 3.10, 2p2h shape parameters are introduced for carbon and oxygen separately to change the ratio of PDD and non-PDD.

2p2h Edep

This parameter covers energy-dependent cross sections between different 2p2h models, which cannot be covered by the overall normalization. Parameters for two energy ranges (above or below 600 MeV) in both neutrino and antineutrino are prepared.

Binding energy, E_B

As described in Sec. 3.2, E_B is introduced for the RFG model. However, the uncertainty of the E_B in the RFG model is not small, and since it changes the kinematics of the outgoing leptons, E_B has given significantly large uncertainty to the oscillation analysis. Since now we use the SF model as the default nuclear model, removal energy in the SF model corresponds to the E_B in the RFG model. More detail of the removal energy can be found at Ref. [181]. The removal energy is not a single value any more, and its spectral can be compared with data from electron scattering experiments. Four parameters are prepared for carbon/oxygen, and neutrino/antineutrino.

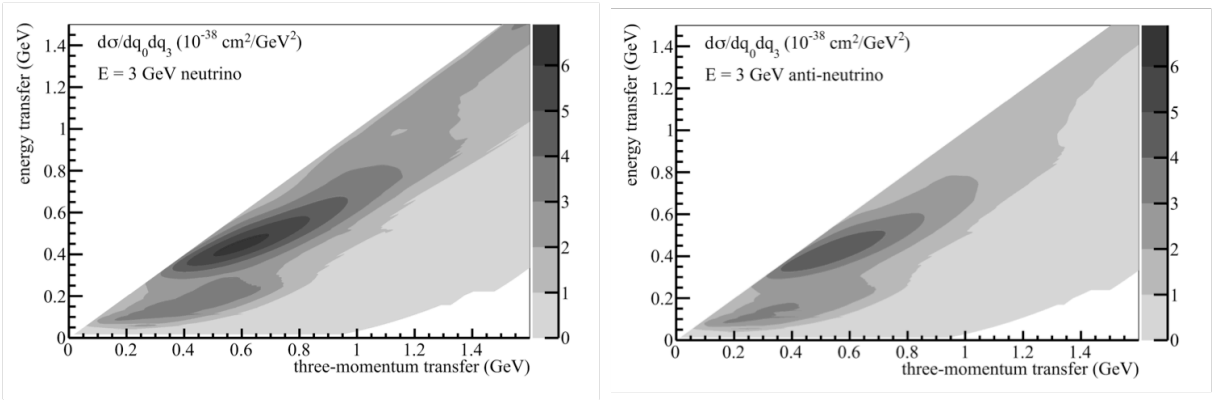

Figure F.2: 2p2h cross section in two dimensional distribution of energy transfer and three-momentum transfer for 3 GeV neutrinos (left) and antineutrinos (right) [180].

F.2 Parameters related to the resonant pion productions

The following parameters are related to the resonant pion production.

C_5^{A}
: Form factor parameter for the resonant pion production introduced in Sec. 3.1.2.

$M_{\mathrm{A}}^{\mathrm{RES}}$
: Axial vector mass for the resonant pion production introduced in Sec. 3.1.2.

$I_{1/2}$ **background low momentum pion**
: Normalization factor of the non-resonant background for pions with momenta below 0.2 GeV/c in antineutrino mode. In recent oscillation analysis, uncertainty of the $I_{1/2}$ background including low momentum pion is especially at issue. Since the Cherenkov threshold of the SK detector is around 145 MeV/c, events with low momentum pions may contaminate the ν_μ single ring sample. We need to understand how much contamination exists, however, the model of the non-resonant background in the resonant pion production in NEUT is tuned to neutrino mode data. Thus, another parameter to cover the case of antineutrino mode is introduced. In the current oscillation analysis, this parameter is not used in the ND fitting since it is not validated that if this parameter can produce a reliable prediction at SK by ND fitting. Therefore, it is treated as an unconstrained parameter which is resulting in a large uncertainty for antineutrino samples.

$I_{1/2}$ **background**
: Overall normalization factor of the non-resonant background separately introduced from the previous parameter.

F.3 Other neutrino interaction parameters

The following parameters are related to the other interaction modes. The multi-pion production is separately treated from the DIS since NEUT 5.4.0, thus there are additional

parameters related to the multi-pion production.

CC norm
Normalization factor for all the CC interactions. Two parameters for neutrino and antineutrino are used.

ν_e/ν_μ, $\overline{\nu}_e/\overline{\nu}_\mu$
Normalization factor between nue and numu because the cross-section difference between ν_μ and ν_e is not understood well. Two parameters for neutrino and antineutrino are used.

CC BY DIS/Multi-Pi
Switching on/off the Bodek-Yang correction in DIS and multi-pion production. In NEUT, the PDF with Bodek-Yang correction is used for the cross sections of the DIS and the multi-pion production. These switching parameters come from a difficulty in treatment of uncertainty for the Bodek-Yang correction.

CC AGKY Multi
Reweighting factor of multiplicity of the multi pion interactions. The AGKY [182] is a model of the multi-pion production used in GENIE. In NEUT, events with two or more pions are treated as the multi-pion production. This parameter covers change in the cross section of the multi-pion production due to the change of pion multiplicity.

CC Misc
Normalization factor for CC1γ, CC1K, CC1η interactions.

CC DIS MultiPi norm
Normalization factor for CC DIS and multi pi interactions. This parameter covers the overall normalization separately from the CC AGKY Multi parameter.

CC coh
Normalization factors for CC coh production. Two parameters for neutrino and antineutrino. A 30% uncertainty is assigned.

NC coh
Normalization factors for NC coh production. Two parameters for neutrino and antineutrino. A 30% uncertainty is assigned.

NC 1γ
Normalization factor for NC single γ production. A 100% uncertainty is assigned.

NC other
Normalization factor for the other NC interactions. A 30% uncertainty is assigned.

F.4 FSI parameters

The intranuclear cascade model used for the FSI simulation in NEUT is tuned by external data. Recent data from DUET experiment [183] is included in the latest oscillation

analysis. In the analysis, correlations between parameters are considered, thus the total uncertainty is smaller than that used in the analysis of the NINJA pilot run.

FEFQE
Quasi-elastic scattering for low momentum pions (<500 MeV/c).

FEFQEH
Quasi-elastic scattering for high momentum pions (>500 MeV/c).

FEFINEL
Pion production

FEFABS
Pion absorption

FEFCX
Single charge exchange

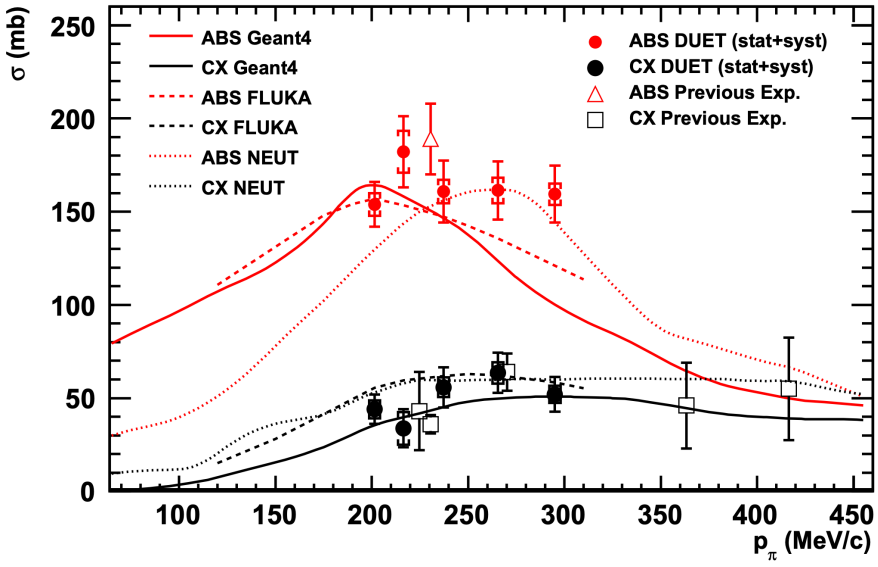

Figure F.3: Cross section of pion absorption and charge exchange measured by DUET compared with previous measurements and several model predictions [183].

Appendix G

Supplementary of the sensitivity study

G.1 Fake data study in NINJA

In the T2K oscillation analysis, validation of the neutrino interaction model is performed by fitting fake data sets, which are generated by varying parts of the interaction model in the MC simulation. Since NINJA covers a different phase space from ND280, fake data study by NINJA may result in different outcomes. In this section, one simple fake data study is performed as an example. In the nominal MC simulation, T2K uses Nieves *et al.* 2p2h model. The Martini *et al.* model is used instead of the Nieves *et al.* model in the fake data study. There is also another 2p2h model, SuSAv2 [110]. An MC simulation with this model will be available soon in GENIE [168] but not used here.

As shown in Fig. 10.12, Nieves *et al.* and Martini *et al.* models show different 2p2h cross sections. They also varied in neutrino or antineutrino interactions. In the fake data, the 2p2h cross section is reweighted as a function of neutrino energy. Figure G.1 shows the result of fitting, which is performed in the same manner shown in Sec. 10.1. If the fitting result shows quite different center values in the 2p2h parameters, it means that the current parameter set does not cover the different model. However, all the parameters are within the pre-fit error size by changing the values of other than the 2p2h parameters.

There are also many possible fake data sets, such as alternative resonant pion production models, different CCQE form factors, and data-driven tunings. We need to develop an application of these fake data used in T2K to perform further fake data study.

G.2 Supplementary for the multivariate analysis

This section describes supplemental remarks on the analysis shown in Sec 10.2.1. First, we discuss transverse kinematics imbalance and the inferred kinematics used in the BDT analysis. Definition of these parameters are described in Appendix. C. For the transverse kinematics imbalance, we extend the definition. Although it was used for the CC0π1p and CC0πNp samples in Sec. 3, we extend it to the CC0π2p sample by taking a vector sum of protons. The vector sum is used as the measured proton kinematics. Figure G.2 shows three parameters of the kinematics imbalances in the CC0π2p sample. There are tendencies that the CCRES δp_t shows slightly different distributions, and the CCQE $\delta\phi_t$

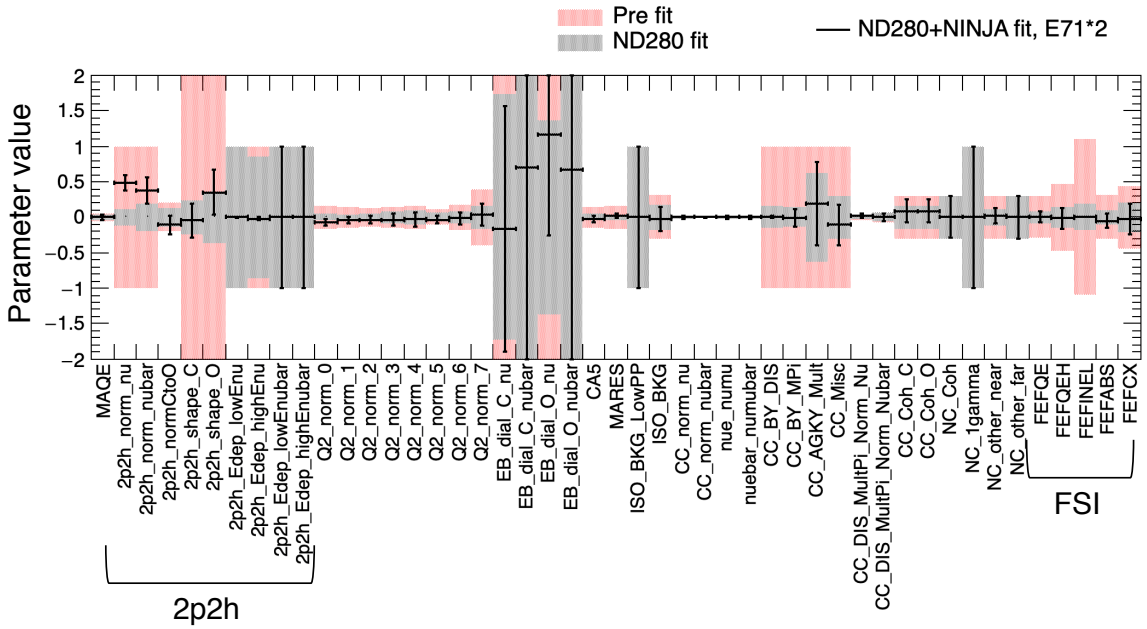

Figure G.1: Error size of the post fit parameters using a fake data with the Martini *et al* 2p2h model.

distribution shows a peak at the small-angle region compared to the 2p2h and CCRES distributions. However, those distributions seem not efficient to extract the 2p2h interactions. Following this, we consider the inferred kinematics distributions. Figure G.3 shows distributions of the inferred kinematics variables in the CC0π2p sample. These parameters also show small differences between the interaction modes.

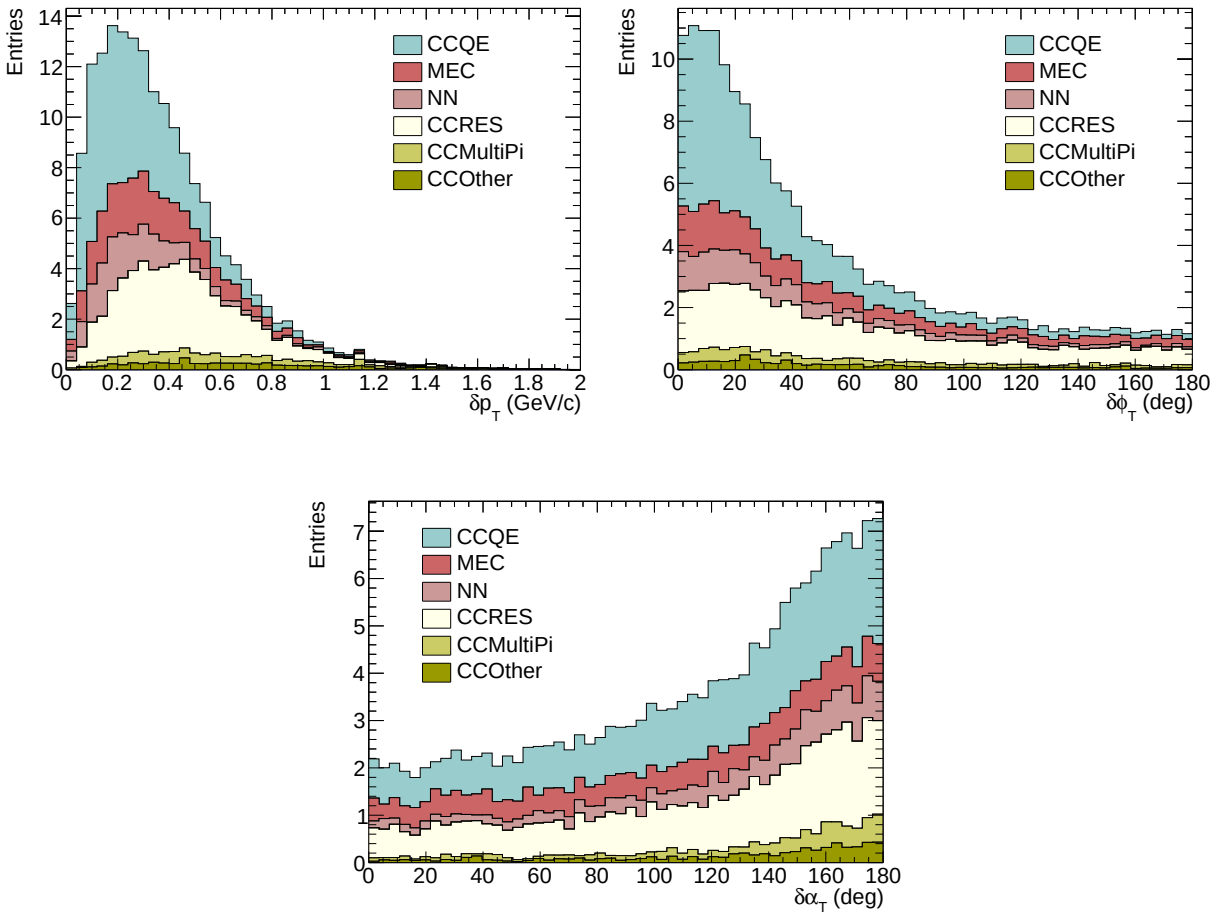

Figure G.2: Distributions of the transverse kinematics-imbalance variables in the CC0π2p sample.

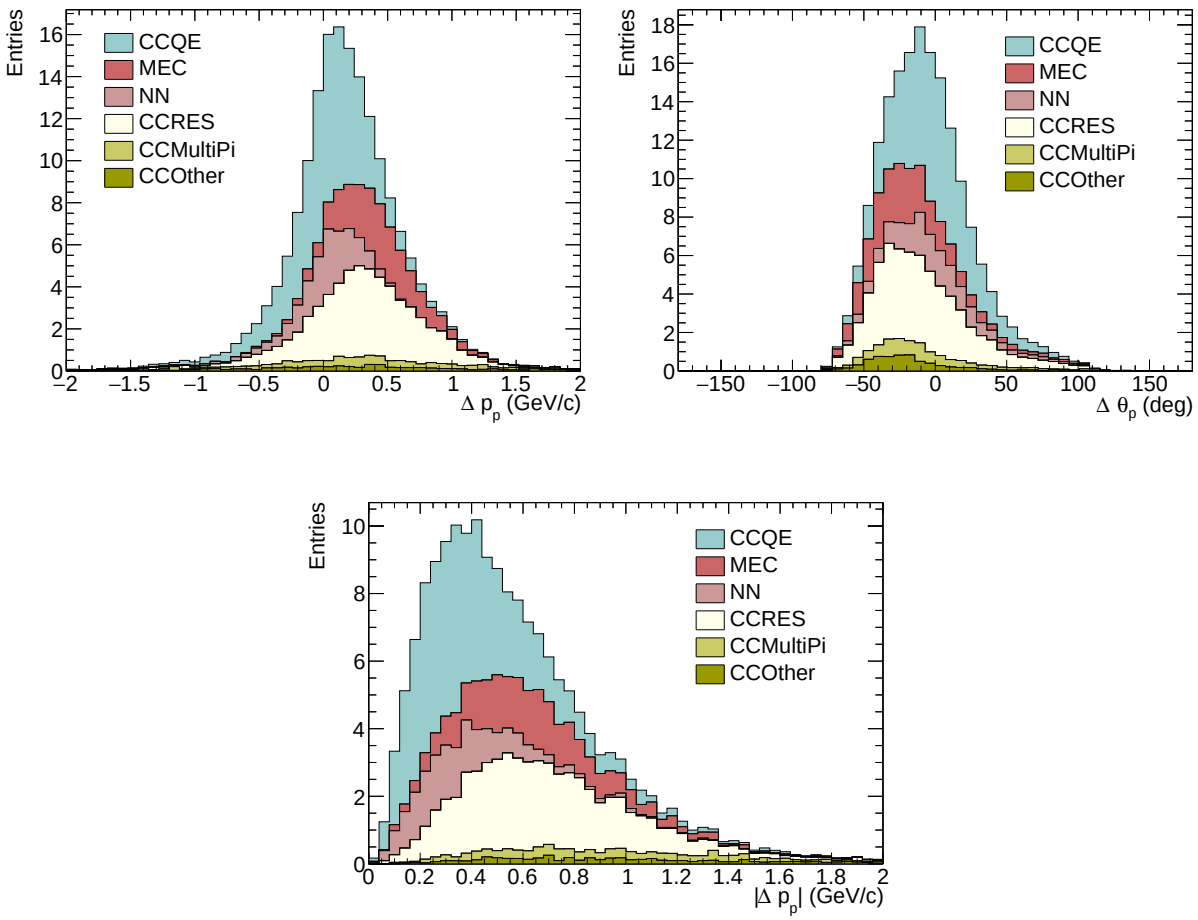

Figure G.3: Distributions of the inferred kinematics variables in the CC0π2p sample.

List of Figures

List of Tables

Bibliography

[1] W. Pauli, "Pauli letter collection", Pauli Archives at CERN

[2] F. Reines and C. L. Cowan *et al.*, "Detection of the free antineutrino", Phys. Rev. **117**, 159 (1960).

[3] G. Danby *et al.*, "Observation of High-Energy Neutrino Reactions and the Existence of Two Kinds of Neutrinos", Phys. Rev. Lett. **9**, 34 (1962).

[4] K. Kodama *et al.* (DONUT Collaboration), "Observation of tau neutrino interactions", Phys. Lett. B **504**, 218 (2001).

[5] D. DeCamp *et al.* (ALEPH Collaboration), "Determination of the number of light neutrino species", Phys. Lett. B **231**, 519 (1989).

[6] The ALEPH Collaboration, The DELPHI Collaboration, The L3 Collaboration, The OPAL Collaboration, The SLD Collaboration, The LEP Electroweak Working Group, The SLD Electroweak and Heavy Flavour Groups, "Precision electroweak measurements on the Z resonance", Phys. Rept. **427** 257 (2006).

[7] N. Aghanim *et al.* (Planck Collaboration), "Planck 2018 results VI. Cosmological parameters", Astron. Astrophys. **641**, A6 (2020).

[8] Z. Maki, M. Nakagawa, S. Sakata, "Remarks on the Unified Model of Elementary Particles", Prog. Theor. Phys. **28**, 870 (1962).

[9] E. Majorana, "Theory of the Symmetry of Electrons and Positrons", Nuovo Cim. **14**, 171 (1937).

[10] L. Wolfenstein, "Neutrino oscillations in matter", Phys. Rev. D **17**, 2369 (1978).

[11] S. P. Mikheyev and A. Yu. Smirnov, "Resonant amplification of neutrino oscillations in matter and solar-neutrino spectroscopy", Nuovo Cim. C **9**, 17 (1986).

[12] W. Hampel *et al.* (GALLEX Collaboration), "GALLEX solar neutrino observations: results for GALLEX IV", Phys. Lett. B **447**, 127 (1999).

[13] M. Altmann *et al.* (GNO Collaboration), "GNO solar neutrino observations: results for GNO I", Phys. Lett. B **490**, 16 (2000).

[14] K. Abe *et al.* (Super-Kamiokande Collaboration), "Atmospheric neutrino oscillation analysis with external constraints in Super-Kamiokande I-IV", Phys. Rev. D **97**, 072001 (2018).

[15] R. Davis, D. S. Harmer, and K. C. Hoffman, "Search for Neutrinos from the Sun", Phys. Rev. Lett. **20**, 1205 (1968).

[16] M. Cribier *et al.* (GALLEX Collaboration), "Results of the whole GALLEX experiment", Nucl. Phys. B-Proc. Sup. **70**, 284 (1999).

[17] K. S. Hirata *et al.*, "Observation of ^{8}B solar neutrinos in the Kamiokande-II detector", Phys. Rev. Lett. **63**, 16 (1989).

[18] J. N. Abdurashitov *et al.* (SAGE Collaboration), "Solar neutrino flux measurements by the Soviet-American Gallium Experiment (SAGE) for half the 22-year solar cycle", J. Exp. Theor. Phys. **95**, 181 (2002).

[19] T. K. Gaisser and M. Honda, "Flux of Atmospheric Neutrinos", Ann. Rev. Nucl. Part. Sci. **52**, 153 (2002).

[20] Y. Fukuda *et al.* (Super-Kamiokande Collaboration), "Evidence for Oscillation of Atmospheric Neutrinos", Phys. Rev. Lett **81**, 1562 (1998).

[21] S. Fukuda *et al.* (Super-Kamiokande Collaboration), "Constraints on Neutrino Oscillations Using 1258 Days of Super-Kamiokande Solar Neutrino Data", Phys. Rev. Lett. **86**, 5656 (2001).

[22] Q. R. Ahmad *et al.* (SNO Collaboration), "Measurement of the Rate of $\nu_e + \mathrm{d} \rightarrow \mathrm{p} + \mathrm{p} + \mathrm{e}$ Interactions Produced by ^{8}B Solar Neutrinos at the Sudbury Neutrino Observatory", Phys. Rev. Lett. **87**, 071301 (2001).

[23] I. Esteban *et al.*, "The fate of hints: updated global analysis of three-flavor neutrino oscillations", J. High Energ. Phys. **2020**, 178 (2020).

[24] K. Abe *et al.* (Super-Kamiokande Collaboration), "Solar neutrino measurements in Super-Kamiokande-IV", Phys. Rev. D **94**, 052010 (2016).

[25] B. Aharmim *et al.* (SNO Collaboration), "Combined analysis of all three phases of solar neutrino data from the Sudbury Neutrino Observatory", Phys. Rev. C **88**, 025501 (2013).

[26] G. Bellini *et al.* (Borexino Collaboration), "Precision Measurement of the ^{7}Be Solar Neutrino Interaction Rate in Borexino", Phys. Rev. Lett. **107**, 141302 (2011).

[27] S. Abe *et al.* (The KamLAND Collaboration), "Precision Measurement of Neutrino Oscillation Parameters with KamLAND", Phys. Rev. Lett. **100**, 221803 (2008).

[28] M. H. Ahn *et al.* (K2K Collaboration), "Measurement of neutrino oscillation by the K2K experiment", Phys. Rev. D **74**, 072003 (2006).

[29] P. Adamson *et al.* (MINOS+ Collaboration), "Precision Constraints for Three-Flavor Neutrino Oscillations from the Full MINOS+ and MINOS Dataset", Phys. Rev. Lett. **125**, 131802 (2020).

[30] P. Dunne (T2K Collaboration), "Latest Neutrino Oscillation Results from T2K", The XXIX International Conference on Neutrino Physics and Astrophysics (2020).

[31] A. Himmel (NOνA Collaboration), "New Oscillation Results from the NOvA Experiment", The XXIX International Conference on Neutrino Physics and Astrophysics (2020).

[32] M. G. Aartsen *et al.* (IceCube Collaboration), "Measurement of Atmospheric Neutrino Oscillations at 6–56 GeV with IceCube DeepCore", Phys. Rev Lett. **120**, 071801 (2018).

[33] M. Apollonio *et al.*, "Limits on neutrino oscillations from the CHOOZ experiment", Phys Lett. B **466**, 415 (1999).

[34] K. Abe *et al.* (T2K Collaboration),"Indication of Electron Neutrino Appearance from an Accelerator-Produced Off-Axis Muon Neutrino Beam", Phys. Rev. Lett. **107**, 041801 (2011).

[35] D. Adey *et al.* (The Daya Bay Collaboration), "Measurement of the Electron Antineutrino Oscillation with 1958 Days of Operation at Daya Bay", Phys. Rev. Lett. **121**, 241805 (2018).

[36] H. de Kerret *et al.* (The Double Chooz Collaboration), "Double Chooz θ_{13} measurement via total neutron capture detection", Nature Phys. **16**, 558 (2020).

[37] G. Bak *et al.* (RENO Collaboration), "Measurement of Reactor Antineutrino Oscillation Amplitude and Frequency at RENO", Phys. Rev. Lett. **121**, 201801 (2018).

[38] N. Cabibbo, "Unitary Symmetry and Leptonic Decays", Phys. Rev. Lett. **10**, 531 (1963).

[39] M. Kobayashi and T. Maskawa, "CP-Violation in the Renormalizable Theory of Weak Interaction", Prog. Theor. Phys. **49**, 652 (1973).

[40] A. D. Sakharov, "Violation of CP invariance, C asymmetry, and baryon asymmetry of the universe", Sov. Phys. Usp. **34**, 392 (1991).

[41] J. H. Christenson, J. W. Cronin, V. L. Fitch, and R. Turlay, "Evidence for the 2π Decay of the K_2^0 meson", Phys. Rev. Lett. **13**, 138 (1964).

[42] B. Aubert *et al.* (BABAR Collaboration), "Measurement of CP-violating Asymmetries in B^0 Decays to CP Eigenstates", Phys. Rev. Lett. **86**, 2515 (2001).

[43] K. Abe *et al.* (Belle Collaboration), "Observation of Large CP Violation in the Neutral B Meson System", Phys. Rev. Lett. **87**, 091802 (2001).

[44] K. Abe *et al.* (T2K Collaboration), "The T2K experiment", Nucl. Instrum. Meth. A **659**, 106 (2011).

[45] K. Abe *et al.* (T2K Collaboration), "Evidence of electron neutrino appearance in a muon neutrino beam", Phys. Rev. D **88**, 032002 (2013).

[46] K. Abe *et al.* (Hyper-Kamiokande Proto-Collaboration), "Physics potential of a long-baseline neutrino oscillation experiment using a J-PARC neutrino beam and Hyper-Kamiokande", Prog. Theor. Exp. Phys. **2015**, 053C02 (2015).

[47] R. Acciarri *et al.* (DUNE Collaboration), "Long-Baseline Neutrino Facility (LBNF) and Deep Underground Neutrino Experiment (DUNE) Conceptual Design Report Volume 2: The Physics Program for DUNE at LBNF", arXiv:1512.06148 [physics.ins-det] (2015).

[48] L. Aliaga *et al.* (MINERνA Collaboration), "Design, calibration and performance of the MINERvA detector", Nucl. Instrum. Meth. A **743**, 130 (2014).

[49] R. Acciarri *et al.* (MicroBooNE collaboration), "Design and Construction of the MicroBooNE Detector", JINST **12**, P02017 (2017).

[50] K. Suzuki, "Measurement of the Muon Beam Properties and Muon Neutrino Inclusive Charged-Current Cross Section in an Accelerator-Produced Neutrino Experiment", Ph.D. Thesis, Kyoto University (2015).

[51] A. K. Ichikawa, "Design concept of the magnetic horn system for the T2K neutrino beam", Nucl. Instrum. Meth. A **690**, 27 (2012).

[52] K. Matsuoka *et al.*, "Development and production of the ionization chamber for the T2K muon monitor", Nucl. Instrum. Meth. A **623**, 385 (2010).

[53] K. Matsuoka *et al.*, "Design and performance of the muon monitor for the T2K neutrino oscillation experiment", Nucl. Instrum. Meth. A **624**, 591 (2010).

[54] Y. Ashida *et al.*, "A new electron-multiplier-tube-based beam monitor for muon monitoring at the T2K experiment", Prog. Theor. Exp. Phys. **2018**, 103H01 (2018).

[55] S. Gomi *et al.*, "Development and study of the multi pixel photon counter", Nucl. Instrm. Meth. A **581**, 427 (2007).

[56] M. Yokoyama *et al.*, "Application of Hamamatsu MPPCs to T2K neutrino detectors", Nucl. Instrm. Meth. A **610**, 128 (2009).

[57] M. Barranco-Luque *et al.* (UA1 Collaboration), "The construction of the central detector for an experiment at the CERN $p^{-}p$ collider", Nucl. Instrum. and Meth. **176**, 175 (1980).

[58] S. Assylbekov *et al.*, "The T2K ND280 off-axis pi-zero detector", Nucl. Instrum. Meth A **686**, 48 (2012).

[59] N. Abgrall *et al.*, "The T2K fine-grained detectors", Nucl. Instrum. Meth. A **696**, 1 (2012).

[60] I. Giomataris *et al.*, "Micromegas in a bulk", Nucl. Instrum. Meth. A **560**, 405 (2006).

[61] P. A. Amaudruz *et al.*, "Time projection chambers for the T2K near detectors", Nucl. Instrum. Meth. A **637**, 25 (2011).

[62] D. Allan *et al.*, "The electromagnetic calorimeter for the T2K near detector ND280", JINST **8**, P10019 (2013).

[63] S. Aoki *et al.*, "The T2K Side Muon Range Detector (SMRD)", Nucl. Instrum. Meth. A **698**, 135 (2013).

[64] K. Abe *et al.* (T2K Collaboration), "Measurement of the ν_μ charged current quasielastic cross section on carbon with the T2K on-axis neutrino beam", Phys. Rev. D **91**, 112002 (2015).

[65] K. Abe *et al.* (T2K Collaboration), "Measurement of the ν_μ charged-current quasielastic cross section on carbon with the ND280 detector at T2K", Phys. Rev. D **92**, 112003 (2015).

[66] K. Abe *et al.* (T2K Collaboration), "Measurement of double-differential muon neutrino charged-current interactions on C_8H_8 without pions in the final state using the T2K off-axis beam", Phys. Rev. D **93**, 112012 (2016).

[67] K. Abe *et al.* (T2K Collaboration), "First measurement of the ν_μ charged-current cross section on a water target without pions in the final state", Phys. Rev. D **97**, 012001 (2018).

[68] K. Abe *et al.* (T2K Collaboration), "Characterization of nuclear effects in muon-neutrino scattering on hydrocarbon with a measurement of final-state kinematics and correlations in charged-current pionless interactions at T2K", Phys. Rev. D **98**, 032003 (2018).

[69] K. Abe *et al.* (T2K Collaboration), "Measurement of the muon neutrino charged-current cross sections on water, hydrocarbon and iron, and their ratios, with the T2K on-axis detectors", Prog. Theor. Exp. Phys. **2019**, 093C02 (2019).

[70] K. Abe *et al.* (T2K Collaboration), "First combined measurement of the muon neutrino and antineutrino charged-current cross section without pions in the final state at T2K", Phys. Rev. D **101**, 112001 (2020).

[71] K. Abe *et al.* (T2K Collaboration), "Simultaneous measurement of the muon neutrino charged-current cross section on oxygen and carbon without pions in the final state at T2K", Phys. Rev. D **101**, 112004 (2020).

[72] Y. Itow, et al., "The JHF-Kamioka neutrino project", arXiv:hep-ex/0106019 (2001).

[73] N. Abgrall *et al.* (NA61/SHINE Collaboration), "Measurements of cross sections and charged pion spectra in proton-carbon interactions at 31 GeV/c", Phys. Rev. C **84**, 034604 (2011).

[74] N. Abgrall *et al.* (NA61/SHINE Collaboration), "Measurement of production properties of positively charged kaons in proton–carbon interactions at 31 GeV/c", Phys. Rev. C **85**, 035210 (2012).

[75] N. Abgrall *et al.* (NA61/SHINE Collaboration), "Measurements of $\pi^\pm$, $K^\pm$, K^0_s, Λ and proton production in proton-carbon interactions at 31 GeV/c with the NA61/SHINE spectrometer at the CERN SPS", Eur. Phys. J. C **76**, 84 (2016).

[76] N. Abgrall *et al.* (NA61/SHINE Collaboration), "Measurements of $\pi^{\pm}$ differential yields from the surface of the T2K replica target for incoming 31 GeV/c protons with the NA61/SHINE spectrometer at the CERN SPS", Eur. Phys. J. C **76**, 617 (2016).

[77] T. Koseki, "Upgrade Plan of J-PARC MR – Toward 1.3 MW Beam Power", In Proceedings, 9th International Particle Accelerator Conference (IPAC 2018): Vancouver, BC Canada, page TUPAK005, (2018).

[78] K. L. Miller *et al.*, "Study of the reaction $\nu_\mu d \to \mu^- pp_s$", Phys. Rev. D **26**, 537 (1982).

[79] T. Kitagaki *et al.*, "High-energy quasielastic $\nu_\mu n \to \mu^- p$ scattering in deuterium", Phys. Rev. D **28**, 436 (1983).

[80] T. Kitagaki *et al.*, "Study of $\nu d \to \mu^- pp_s$ and $\nu d \to \mu^- \Delta^{++}(1232) n_s$ using the BNL 7-foot deuterium-filled bubble chamber", Phys. Rev. D **42**, 1331 (1990).

[81] Y. Hayato, "A neutrino interaction simulation program library NEUT", Acta Phy. Pol. B **40**, 2477 (2009).

[82] C. H. Llewellyn Smith, "Neutrino reactions at accelerator energies", Phys. Rept. **3**, 261 (1972).

[83] M. Gourdin, "Weak and electromagnetic form factors of hadrons", Phys.Rept. **11**, 29 (1974).

[84] R. Bradford, A. Bodek, H. Budd, and J. Arrington, "A New Parameterization of the Nucleon Elastic Form Factors", Nucl. Phys. B Proc. Suppl. **159**, 127 (2006).

[85] S. L. Adler, "Tests of the Conserved Vector Current and Partially Conserved Axial-Vector Current Hypotheses in High-Energy Neutrino Reactions", Phys. Rev. **135**, B963, (1964).

[86] D. Mund *et. al*, "Determination of the Weak Axial Vector Coupling $\Lambda = g_A/g_v$ from a Measurement of the β-Asymmetry Parameter A in Neutron Beta Decay", Phys. Rev. Lett. **110**, 172502 (2013).

[87] V. Bernard *et al.*, "Axial structure of the nucleon", J. Phys. G: Nucl. Part. Phys. **28**, R1 (2001).

[88] D. Rein and L. M. Sehgal, "Neutrino-excitation of baryon resonances and single pion production", Annals of Physics **133**, 79 (1981).

[89] K. M. Graczyk and J. T. Sobczyk, "Lepton mass effects in weak charged current single pion production", Phys. Rev. D **77**, 053003 (2008).

[90] K. M. Graczyk and J. T. Sobczyk, "Form factors in the quark resonance model", Phys. Rev. D **77**, 053001 (2008).

[91] L. Tiator *et al.* "Electroproduction of nucleon resonances", Eur. Phys. J. A **19**, 55 (2004).

[92] D. Rein and L. M. Sehgal, "Coherent π^0 production in neutrino reactions", Nucl. Phys. B **223**, 29 (1983).

[93] D. Rein and L. M. Sehgal, "PCAC and the deficit of forward muons in π^+ production by neutrinos", Phys. Lett. B **657**, 207 (2007).

[94] C. Berger and L. M. Sehgal. "Partially conserved axial vector current and coherent pion production by low energy neutrinos", Phys. Rev. D **79**, 053003 (2009).

[95] A. Higuera *et al.* (MINERνA Collaboration), "Measurement of Coherent Production of $\pi^{\pm}$ in Neutrino and Antineutrino Beams on Carbon from E_{ν} of 1.5 to 20 GeV", Phys. Rev. Lett. **113**, 261802 (2014).

[96] T. Sjöstrand, "High-energy-physics event generation with PYTHIA 5.7 and JETSET 7.4", Comput. Phys. Commun. **82**, 74 (1994).

[97] A. Bodek and U. K. Yang, "Modeling neutrino and Electron Scattering Cross Sections in the Few GeV Region with Effective LO PDFs", AIP Conf. Proc. **670**, 110 (2003).

[98] R. A. Smith and E. J. Moniz, "Neutrino reactions on nuclear targets", Nucl. Phys. B **43**, 605 (1972).

[99] J. Nieves, E. Oset and C. Garcia-Recio, "A theoretical approach to pionic atoms and the problem of anomalies", Nucl. Phys. A **554**, 509 (1993).

[100] J. Nieves, I. R. Simo and M. J. V. Vacas, "Inclusive charged-current neutrino-nucleus reactions", Phys. Rev. C **83**, 045501 (2011).

[101] O. Benhar *et al.*, "Spectral function of finite nuclei and scattering of GeV electrons", Nucl. Phys. A **579**, 493 (1994).

[102] O. Benhar and A. Fabrocini, "Two-nucleon spectral function in infinite nuclear matter". Phys. Rev. C **62**, 034304 (2000).

[103] R. Gran *et al.* (K2K Collaboration), "Measurement of the quasielastic axial vector mass in neutrino interactions on oxygen", Phys. Rev. D **74**, 052002 (2006).

[104] A. A. Aguilar-Arevalo *et al.* (MiniBooNE Collaboration), "First measurement of the muon neutrino charge current quasielastic double differential cross section", Phys. Rev. D **81**, 092005 (2010).

[105] L. B. Auerbach *et al.* (LSND Collaboration), "Measurements of charged current reactions of ν_{μ} on ^{12}C", Phys. Rev. C **66**, 015501 (2002).

[106] V. Lyubushkin *et al.* (NOMAD Collaboration), "A study of quasi-elastic muon neutrino and antineutrino scattering in the NOMAD experiment", Eur. Phys. J. C **63**, 355 (2009).

[107] R. Subedi *et al.* "Probing Cold Dense Nuclear Matter", Science **320**, 1476 (2008).

[108] S. Dolan, "Probing nuclear effects in neutrino-nucleus scattering at the T2K off-axis near detector using transverse kinematic imbalances", Ph.D. Thesis, University of Oxford (2017).

[109] M. Martini *et al.*, "Unified approach for nucleon knock-out and coherent and incoherent pion production in neutrino interactions with nuclei", Phys. Rev. C **80**, 065501 (2009).

[110] R.G.Jimenez *et al.*, "Extensions of superscaling from relativistic mean field theory: The SuSAv2 model", Phys. Rev. C **90**, 035501 (2014).

[111] L. Alvarez-Ruso *et al.*, "NuSTEC White Paper: Status and challenges of neutrino-nucleus scattering", Prog. Part. Nucl. Phys. **100**, 1 (2018).

[112] L. L. Salcedo *et al.*, "Computer simulation of inclusive pion nuclear reactions", Nucl. Phys. A **484**, 557 (1988).

[113] P. de Perio, "NEUT pion FSI", AIP Conf. Proc. **1405**, 223 (2011).

[114] H. W. Bertini, "Nonelastic interactions of Nucleons and π Mesons with Complex Nuclei at Energies Below 3 GeV", Phys. Rev. C **6**, 631 (1972).

[115] C. Andreopoulos *et al.*, "The GENIE neutrino Monte Carlo generator", Nucl. Instrum. Meth. A **614**, 87 (2010).

[116] T. Golan, C. Juszczak, and J. T. Sobczyk, "Effects of final-state interactions in neutrino-nucleus interactions", Phys. Rev. C **86**, 015505 (2012).

[117] D. Casper, "The nuance neutrino physics simulation, and the future", Nucl. Phys. B Proc. Suppl. **112**, 161 (2002).

[118] O. Buss *et al.*, "Transport-theoretical description of nuclear reactions", Phys. Rep. **512**, 1 (2012).

[119] P. A. Zyla *et al.* (Particle Data Group), "Review of Particle Physics", Prog. Theor. Exp. Phys. **2020**, 083C01 (2020).

[120] R. Acciarri *et al.*, "A Proposal for a Three Detector Short-Baseline Neutrino Oscillation Program in the Fermilab Booster Neutrino Beam", arXiv:1503.01520 [physics.ins-det]

[121] MicoBooNE Collaboration, "Selection of ν_μ charged-current induced interactions with N>0 protons and performance of events with N=2 protons in the final state in the MicroBooNE detector from the BNB", MICROBOONE-NOTE-1056-PUB (2018).

[122] R. Acciarri *et al.*, "Detection of back-to-back proton pairs in charged-current neutrino interactions with the ArgoNeuT detector in the NuMI low energy beam line", Phys. Rev. D **90**, 012008 (2014).

[123] X.-G. Lu *et al.*, "Measurement of nuclear effects in neutrino interactions with minimal dependence on neutrino energy", Phys. Rev. C **94**, 015503 (2016).

[124] X.-G. Lu *et al.* (MINERνA Collaboration), "Measurement of Final-State Correlations in Neutrino Muon-Proton Mesonless Production on Hydrocarbon at $\langle E_\nu \rangle = 3\,\text{GeV}$", Phys. Rev. Lett. **121**, 022504 (2018).

[125] S. J. Barish *et al.*, "Study of neutrino interactions in hydrogen and deuterium: Description of the experiment and study of the reaction $\nu + d \to \mu^- + p + p_s$", Phys. Rev. D **16**, 3103 (1977).

[126] N. J. Baker *et al.*, "Quasielastic neutrino scattering: A measurement of the weak nucleon axial-vector form factor", Phys. Rev. D **23**, 2499 (1981).

[127] K. Niu, E. Mikumo, and Y. Maeda, "A Possible Decay in Flight of a New Type Particle", Prog. Theor. Phys **46**, 1644 (1971).

[128] N. Agafonova *et al.* (OPERA Collaboration), "Discovery of τ Neutrino Appearance in the CNGS Neutrino Beam with the OPERA Experiment", Phys. Rev. Lett. **115**, 121802 (2015).

[129] K. Yamada *et al.*, "First demonstration of an emulsion multi-stage shifter for accelerator neutrino experiments in J-PARC T60", Prog. Theor. Exp. Phys.**2017**, 063H02 (2017).

[130] T. Fukuda *et al.*, "First neutrino event detection with nuclear emulsion at J-PARC neutrino beamline", Prog. Theor. Exp. Phys. **2017**, 063C02 (2017).

[131] H. Oshima *et al.* (NINJA Collaboration), "First measurement of the ν_μ charged-current cross section on iron around the 1 GeV energy region using a nuclear emulsion detector", (2020).

[132] A. Hiramoto *et al.* (NINJA Collaboration), "First measurement of $\overline{\nu}_\mu$ and ν_μ charged-current inclusive interactions on water using a nuclear emulsion detector", Phys. Rev. D **102**, 072006 (2020).

[133] H. Rokujo *et al.*, "Multi-stage shifter for subsecond time resolution of emulsion gamma-ray telescopes", Nucl. Instrum. Meth. A **701**, 127 (2013).

[134] Kuraray Co., Ltd., "Plastic Scintillating Fibers"

[135] Hamamatsu Photonics K.K., S13361-3050 series Datasheet

[136] I. Nakamura *et al.*, "A 64ch readout module for PPD/MPPC/SiPM using EASIROC ASIC", Nucl. Instrum. Meth. A **787**, 376 (2015).

[137] K. Abe *et al.*, "T2K neutrino flux prediction", Phys. Rev. D **87**, 012001 (2013).

[138] S. Agostinelli *et al.*, "GEANT4–a simulation toolkit", Nucl. Instrum. Meth. A **506**, 250 (2003).

[139] R. Burn *et al.*, "GEANT: Detector Description and Simulation Tool", CERN-W5013 (1994).

[140] A. Ferrari *et al.*, "FLUKA: A Multi-Particle Transport Code", CERN2005-010, SLAC-R-773, INFN-TC-05-11 (2005).

[141] T. T. Böhlen *et al.*, "The FLUKA Code: Developments and Challenges for High Energy and Medical Applications", Nucl. Data Sheets **120**, 211 (2014).

[142] J. Nieves, I. R. Simo, M. J. V. Vacas, "The nucleon axial mass and the MiniBooNE quasielastic neutrino-nucleus scattering problem", Phys. Lett. B **707**, 72 (2012).

[143] J. Nieves, J. E. Amaro, M. Valverde, "Inclusive quasielastic charged-current neutrino-nucleus reactions", Phys. Rev. C **70**, 055503 (2004).

[144] K. Abe *et al.* (T2K Collaboration), "Measurement of neutrino and antineutrino oscillations by the T2K experiment including a new additional sample of ν_e interactions at the far detector", Phys. Rev. D **96**, 092006 (2017).

[145] J. Allison *et al.*, "Recent developments in GEANT4", Nucl. Instrum. Meth. A **835**, 186 (2016).

[146] M. Yoshimoto *et al.*, "Hyper-track selector nuclear emulsion readout system aimed at scanning an area of one thousand square meters", Prog. Theor. Exp. Phys. **2017**, 103H01 (2017).

[147] K. Hamada *et al.*, "Comprehensive track reconstruction tool NETSCAN 2.0 for the analysis of the OPERA Emulsion Cloud Chamber", JINST **7**, P07001 (2012).

[148] T. Fukuda *et al.*, "The analysis of interface emulsion detector for the OPERA experiment in JAPAN Scanning facility", JINST **5**, P04009 (2010).

[149] T. Kikawa, "Measurement of Neutrino Interactions and Three Flavor Neutrino Oscillations in the T2K Experiment", Ph.D. Thesis, Kyoto University (2014).

[150] T. Koga, "Measurement of neutrino interactions on water and search for electron anti-neutrino appearance in the T2K experiment", Ph.D. Thesis, University of Tokyo (2018).

[151] H. Maesaka, "Evidence For Muon Neutrino Oscillation In An Accelerator-based Experiment", Ph.D. Thesis, Kyoto University (2005).

[152] K. Abe *et al.* (T2K Collaboration), "Measurements of the T2K neutrino beam properties using the INGRID on-axis near detector", Nucl. Instrum. Meth. A **694**, 211 (2012).

[153] K. Kodama *et al.*, "Momentum measurement of secondary particle by multiple coulomb scattering with emulsion cloud chamber in DONuT experiment", Nucl. Instrum. Meth. A **574**, 192 (2007).

[154] A. Agafonova *et al.*, "Momentum measurement by the multiple Coulomb scattering method in the OPERA lead-emulsion target", New J. Phys. **14**, 013026 (2012).

[155] G. R. Lynch and O. I. Dahl, "Approximations to multiple Coulomb scattering", Nucl. Instrm. Meth. B **58**, 6 (1991).

[156] C. Andreopoulos *et al.*, "The GENIE Neutrino Monte Carlo Generator: Physics and User Manual", arXiv:1510.05494 [hep-ph] (2015).

[157] C. Berger and L. M. Sehgal, "Lepton mass effects in single pion production by neutrinos", Phys. Rev. D **76**, 113004 (2007).

[158] S. Dytman, "Final State Interactions in Neutrino–Nucleus Experiments", Acta Phys. Pol. B **40**, 2445 (2009).

[159] K. Abe *et al.* (T2K Collaboration), "Measurements of $\overline{\nu}_\mu$ and $\overline{\nu}_\mu + \nu_\mu$ charged-current cross-sections without detected pions nor protons on water and hydrocarbon at mean antineutrino energy of 0.86 GeV", arXiv:2004.13989 [hep-ex] (2020).

[160] K. Abe *et al.* (T2K Collaboration), "Measurement of the inclusive ν_μ charged current cross section on iron and hydrocarbon in the T2K on-axis neutrino beam", Phys. Rev. D **90**, 052010 (2014).

[161] S. Parsa *et al.*, "Novel Design features of the Baby MIND Detector for T59-WAGASCI experiment", PoS NuFact2017, 152 (2018).

[162] T. Odagawa, "Prospects and status of the physics run of the NINJA experiment", PoS NuFact2019, 144 (2020).

[163] F. James and M. Roos, "Minuit: a system for function minimization and analysis of the parameter errors and correlations", Comput. Phys. Commun. **10**, 343 (1975).

[164] T. Hiraki, "Muon Antineutrino Disappearance Measurement by the T2K Experiment", Ph.D. Thesis, Kyoto University (2016).

[165] K. Nakamura, "Measurement of Neutrino Oscillation with a High Intensity Neutrino Beam", Ph.D. Thesis, Kyoto University (2018).

[166] K. Abe *et al.* (T2K Collaboration), "Proposal for an Extended Run of T2K to 20×10^{21} POT", arXiv:1609.04111 [hep-ph] (2016).

[167] A. Hoecker *et al.*, "TMVA - Toolkit for Multivariate Data Analysis", arXiv:physics/0703039 [physics.data-an] (2007).

[168] S. Dolan *et al.*, "Implementation of the SuSAv2-meson exchange current 1p1h and 2p2h models in GENIE and analysis of nuclear effects in T2K measurements", Phys. Rev. D **101**, 033003 (2020).

[169] M. Day and K. S. McFarland, "Differences in quasielastic cross sections of muon and electron neutrinos", Phys. Rev. D **86**, 053003 (2012).

[170] K. Abe *et al.* (T2K Collaboration), "T2K ND280 Upgrade – Technical Design Report", arXiv:1901.03750 [physics.ins-det] (2019).

[171] X.-G. Lu and J. T. Sobczyk, "Identification of nuclear effects in neutrino and antineutrino interactions on nuclei using generalized final-state correlations", Phys. Rev. C **99**, 055504 (2019).

[172] T. Cai, X.-G. Lu, and D. Ruterbories, "Pion-proton correlation in neutrino interactions on nuclei", Phys. Rev. D **100**, 073010 (2019).

[173] D. Coplowe *et al.* (MINERνA Collaboration), "Probing nuclear effects with neutrino-induced charged-current neutral pion production", Phys. Rev. D **102**, 072007 (2020).

[174] L. Pickering, "Examining Nuclear Effects in Neutrino Interactions with Transverse Kinematic Imbalance", JPS Conf. Proc. **12**, 010032 (2016).

[175] T. Cai *et al.* (MINERνA Collaboration), "Nucleon binding energy and transverse momentum imbalance in neutrino-nucleus reactions", Phys. Rev. D **101**, 092001 (2020).

[176] Y. Suzuki, Master's Thesis, Nagoya University (2019).

[177] T. Fukuda, "Measurement of charged particle ionisation loss with grain counting in the OPERA emulsion films", OPERA Note 179 (2015).

[178] P. Stowell *et al.* (MINERνA Collaboration), "Tuning the GENIE pion production model with MINERvA data", Phys. Rev. D **100**, 072005 (2019).

[179] M. F. Carneiro *et al.* (MINERνA Collaboration), "High-Statistics Measurement of Neutrino Quasielastic-like Scattering at $\langle E_\nu \rangle$=$\sim$6 GeV on a Hydrocarbon Target", Phys. Rev. Lett. **124**, 121801 (2020).

[180] R. Gran *et al.*, "Neutrino-nucleus quasi-elastic and 2p2h interactions up to 10 GeV", Phys. Rev. D **88**, 113007 (2013).

[181] A. Bodek and T. Cai, "Removal energies and final state interaction in lepton nucleus scattering", Eur. Phys. J. C. **79**, 293 (2019).

[182] T. Yang *et al.*, "A hadronization model for few-GeV neutrino interactions", Eur. Phys. J. C **63**, 1 (2009).

[183] E.S.P. Guerra *et al.*, "Measurement of σ_{ABS} and σ_{CX} of $\pi^{\pm}$ on carbon by Dual Use Experiment at TRIUMF (DUET)", Phys. Rev. C **95**, 045203 (2017).